Deep-dive into the environmental drivers of star-formation within dense halos in the early Universe

Boris Sindhu Kalita

Université Paris Cité

École doctorale Astronomie et Astrophysique d'Île-de-France
ED127

Laboratoire AIM, Service d'Astrophysique CEA-Saclay

Deep-Dive into the environmental drivers of star formation within dense halos in the early Universe

Par

Boris Sindhu Kalita

Thèse de doctorat de Astronomie et Astrophysique

Dirigée par Emanuele Daddi

Présentée et soutenue publiquement le 13 Septembre 2022

Devant un jury composé de :

Simona Mei	Professeur	Université Paris Cité	Présidente
Nina Hatch	Professeur	University of Nottingham	Rapporteur
Jeremy Blaizot	Professeur	University of Lyon	Rapporteur
Helmut Dannerbauer	Astronome	Instituto de Astrofísica de Canarias	Examinateur
Matthieu Bethermin	Astronome	Observatoire de Strasbourg	Examinateur
Emanuele Daddi	Astronome	Université Paris-Saclay	Directeur de thèse

Deep-dive into the environmental drivers of star-formation within dense halos in the early Universe

Boris Sindhu KALITA

Deep-Dive into the environmental drivers of star formation within dense halos in the early Universe

Résumé court: L'interaction avec l'environnement est un facteur majeur de l'évolution des galaxies à travers le temps cosmique. Ce facteur est particulièrement important dans les premières phases de formation des galaxies et des amas ($z \sim 2-4$), où les galaxies les plus massives ($> 10^{11}\,M_\odot$) de notre Univers se formaient, évoluaient et mouraient rapidement en l'espace de quelques milliards d'années. Cette thèse vise à caractériser par l'observation le rôle que l'environnement pourrait jouer dans l'évolution des propriétés de ces galaxies, avec un accent particulier sur l'accrétion filamentaire de gaz froid. Ce phénomène essentiel est censé fournir le carburant nécessaire à la formation d'étoiles dans les halos de matière noire traçant des surdensités de matière, qui sont autrement trop chauds (avec des températures de Viriel $\sim 10^6$ K) pour conserver un réservoir de gaz froid ($< 10^4$ K) qui peut être facilement converti en étoiles dans les galaxies membres du halo. La théorie prédit que de tels flux continus de gaz froid sont capables de pénétrer profondément dans les halos dans une gamme de paramètres caractérisée par la masse du halo et le décalage vers le rouge. Ainsi, les halos dont la masse de matière noire est supérieure au seuil de $10^{12}\,M_\odot$, au-delà duquel tout gaz disponible est chauffé par choc, sont encore capables de fournir du gaz froid à leurs galaxies. Étant donné l'importance de ce phénomène, qui a récemment été soutenu soulignée par l'évolution de la luminosité Lyman-alpha des halos à haut décalage vers le rouge (à $1,8 < z < 3,3$), nous avons cherché à trouver des preuves dans des observations très sensibles et bien résolues de galaxies à forte formation d'étoiles dans une telle structure. RO-1001, un groupe de galaxies à z = 2,91 est l'un des rares cas où il existe des preuves convaincantes d'une accrétion filamentaire de gaz froid, tracée par son halo Lyman-alpha. En utilisant une combinaison d'images profondes HST et ALMA, ainsi que d'autres images et spectres en optique et dans l'infrarouge proche, nous trouvons des preuves prometteuses des effets de l'accrétion sur trois galaxies membres de RO-1001 qui forment des étoiles massives. Nous trouvons une interaction entre les disques stellaires ne formant pas d'étoile et les noyaux

fortement formateurs d'étoiles mais obscurcis par la poussière qui est en accord avec les prédictions des simulations de l'évolution des galaxies par accrétion. Cependant, une quatrième galaxie aussi massive mais ne formant aucune étoile est également trouvée dans la même structure riche en gaz, confirmée photométriquement. Ceci peut donc être interprété comme un cas limite de l'accrétion de gaz de rôle, fournissant ainsi une image complète de la formation d'étoiles dans les galaxies au sein de telles structures. De plus, la galaxie ne formant aucune étoile ouvre la voie à la partie suivante de la thèse qui étudie comment la formation d'étoiles est inhibée dans les environnements denses, qui, lorsque nous progressons vers des amas plus évolués, est caractérisée par l'injection d'entropie dans les environnements intra-amas. Une fois encore, l'acteur principal de ce processus : la rétroaction des AGN en mode jet, n'a été étudiée en détail qu'à des décalages vers le rouge inférieurs, mais n'a pas été entièrement comprise à des décalages vers le rouge supérieurs ($z \sim 1.5 - 2.0$ et plus). Nous examinons avons donc examiné ce phénomène dans un amas nouvellement formé, CLJ1449+0856 à z = 1,99, à l'aide d'observations radio profondes JVLA à 3 GHz pour révéler une intense activité de jet d'AGN de faible puissance qui devrait avoir un effet durable sur l'évolution future d'une telle structure. Enfin, une discussion sur l'inhibition de la formation d'étoiles dans les environnements denses serait incomplète sans mentionner le simple effet de la pression dynamique qui est bien étudié à de faibles décalages vers le rouge ($z < 0,5$). Nous discutons dans notre travail de la suppression de la pression dynamique, le méchanisme principal pour éliminer le gaz des galaxies riches en gaz qui entrent dans les amas à des décalages vers le rouge inférieurs, ainsi qu'une brève discussion pour savoir si ce phénomène pourrait jouer un rôle dans l'évolution rapide des galaxies à des décalages vers le rouge aussi élevés que $z \sim 3$.

Mots-clés : formation des galaxies, évolution des galaxies, galaxies formant des étoiles, galaxies ne formant pas d'étoile, galaxies massives, galaxies compactes, accrétion de gaz, formation d'étoiles, extinction dans les galaxies.

Abstract

Boris Sindhu KALITA

Deep-Dive into the environmental drivers of star formation within dense halos in the early Universe

Interaction with the environment is a major driver of galaxy evolution throughout cosmic time. This is especially critical in the first phases of galaxy and cluster formation ($z \sim 2-4$), where the most massive ($> 10^{11}\,M_{\odot}$) galaxies of our Universe were rapidly forming, evolving and dying within the span of a few billion years. This thesis aims to observationally characterize the role environment could be playing to shape the properties of such galaxies, with special emphasis on filamentary cold-gas accretion. This critical phenomenon is expected to provide fuel for star-formation in dark matter halos tracing matter over-densities, that are otherwise too hot (with virial temperatures $\sim 10^6$ K) to sustain cold gas ($< 10^4$ K) which can be readily converted to stars in member galaxies. Theory predicts such sustained streams of cold-gas are capable of penetrating deep into the halos within a parameter range characterized by the halo mass and redshift. This results in halos above the threshold dark matter mass of $10^{12}\,M_{\odot}$, beyond which any available gas is shock heated, to still be capable of providing cold-gas to its galaxies. Given the importance of this phenomenon, which has recently also been supported by the observed Lyman-alpha luminosity evolution of high-redshift halos (at $1.8 < z < 3.3$), we have aimed to find supporting evidence in highly sensitive and well-resolved studies of highly star-forming galaxies within such a structure. RO-1001, a galaxy group at z = 2.91 is one of the handful of cases where there is convincing evidence of filamentary cold-gas accretion, traced by its Lyman-alpha halo. Using a combination of deep HST and ALMA imaging, along with additional optical and near-IR imaging and spectroscopy, we find tantalizing evidence of the effects of accretion on three massive star-forming member galaxies of RO-1001. We find an interplay between lopsided quiescent stellar disks and highly star-forming but dust-obscured cores that is in agreement with predictions of simulations of accretion-driven galaxy evolution. However, a fourth equally massive but fully quiescent galaxy is also found within the same gas-rich structure, confirmed photometrically. This can hence be interpreted as a limiting case of the role gas-accretion, thereby providing a complete picture of star-formation in galaxies within such structures. Moreover, the quiescent galaxy paves the way for the next part of thesis which looks into how star-formation is inhibited within dense environments, which as we progress to more evolved

clusters, is characterized by entropy injection into the intra-cluster environments. Once again, the major player of this process: jet-mode AGN feedback, has only been studied in great detail at lower redshifts but not fully understood at higher redshifts ($z \sim 1.5 - 2.0$ and above). We thus look into this in a newly formed cluster, CLJ1449+0856 at z = 1.99, with deep JVLA 3 GHz radio observations to reveal an abundance of low-powered AGN jet-activity that is expected to have a lasting effect on the future evolution of such a structure. Finally, a discussion on the inhibition of star-formation in dense environments would be incomplete without mentioning the simple effect of ram-pressure which is well studied at low redshifts ($z < 0.5$). We discuss our work on Ram-Pressure stripping, the primary method to remove gas from gas-rich galaxies infalling into clusters at lower redshifts, along with a brief discussion on whether this phenomenon could play a role in the rapid evolution of galaxies at redshifts as high as $z \sim 3$.

Keywords: galaxy formation, galaxy evolution, strar-forming galaxies, quiescent galaxies, massive galaxies, compact galaxies, gas accretion, star formation, galaxy quenching.

Summary

Boris Sindhu KALITA

Deep-Dive into the environmental drivers of star formation within dense halos in the early Universe

This thesis explores various facets of star-formation within dense environments using a multi-wavelength dataset. The availability of gas within these environments is a critical driver of galaxy evolution and various studies have attempted to create theoretical models that predict the availability of cold gas ($< 10^4$ K). This is especially critical since beyond an approximate halo mass of $\sim 10^{12}\,M_\odot$, the majority of gas is expected to be shock heated to virial temperatures $\gtrsim 10^6$ K. It has been predicted however, that streams of cold gas can still survive and penetrate into the centers of halos with otherwise shock-heated gas. This is critical in providing gas that can be readily converted to stars within the central massive galaxies. Only recently have we begun obtaining observational evidence which supports this theory. The first two works of this thesis investigates one such case, a galaxy group RO-1001 at z=2.91.

We first present well-resolved near-IR and submillimeter analysis of the three highly star-forming massive ($> 10^{11}\,M_\odot$) galaxies within the core of the RO-1001 galaxy group at $z = 2.91$. Each of them displays kpc scale compact starbursting cores with properties consistent with forming galaxy bulges, embedded at the center of extended, massive stellar disks. Surprisingly, the stellar disks are unambiguously both quiescent and severely lopsided. Therefore, “outside-in" quenching is ongoing in the three group galaxies. We propose an overall scenario in which the strong mass lopsidedness in the disks (ranging from factors of 1.6 to >3) likely generated under the effects of accreted gas and clumps, is responsible for their star-formation suppression, while funnelling gas into the nuclei and thus creating the central starbursts. The lopsided side of the disks marks the location of impact of accretion streams, with additional matter components (dust and stars) detected in their close proximity directly tracing the inflow direction. The interaction with the accreted clumps, which can be regarded as minor mergers, leads the major axes of the three galaxies to be closely aligned with the outer Lyman-α-emitting feeding filaments. These results provide the first piece of observational evidence of the impact of cold accretion streams on the formation and evolution of the galaxies they feed. In the current phase, this is taking the form of the rapid buildup of bulges under the effects of

accretion, while still preserving massive quiescent and lopsided stellar disks at least until encountering a violent major merger.

Within the same structure, the fourth massive galaxy has a mass-weighted stellar age of 1.6 ± 0.4 Gyr. This galaxy is one of the oldest known at $z \sim 3$, implying that most of its 10^{11} $M_{\odot}$ of stars were rapidly formed at $z > 6$–8. This is a unique example of the predominantly passive evolution of a galaxy over at least $3 < z < 6$ following its high-redshift quenching and a smoking-gun event pointing to the early imprint of an age-environment relation. At the same time, being in a dense group environment with extensive cold-gas reservoirs as betrayed by a giant Lyα halo, the existence of this galaxy demonstrates that gas accretion shutdown is not necessary for quenching and its maintenance.

One of the primary modes of the maintenance of quiescence has been found to be radio AGN-feedback. We investigate this within CLJ1449+0856 at z=2 using 3 GHz VLA observations. We study the effects of radio-jet based kinetic feedback at high redshifts, which has been found to be crucial in low redshift clusters to explain the observed thermodynamic properties of their ICM. We investigate this interaction at an epoch featuring high levels of AGN activity and a transitional phase of ICM in regards to the likelihood of residual cold-gas accretion. We measure a total flux of 30.6 ± 3.3 $^{-}$Jy from the 6 detected jets. Their power contribution is estimated to be 1.2 (± 0.6) $\times 10^{44}$ ergs s^{-1}, although this value could be up to 4.7 $\times$ 10^{44} ergs s^{-1}. This is a factor $\sim$ 0.25 – 1.0 of the previously estimated instantaneous energy injection into the ICM of CLJ1449+0856 from AGN outflows and star formation, that have already been found to be sufficient in globally offsetting the cooling flows in the cluster core. In line with the already detected abundance of star formation, this mode of feedback being distributed over multiple sites, contrary to a single central source observed at low redshifts, points to accretion of gas into the cluster centre. This also suggests a 'steady state' of the cluster featuring non cool-core like behaviour. Finally, we also examine the TIR-radio luminosity ratio for the known sample of galaxies within the cluster core and find that dense environments do not have any serious consequence on the compliance of galaxies to the IR-radio correlation.

The second part of this thesis includes two works on an intermediate redshift cluster to investigate the removal of gas from infalling galaxies. We present and discuss results from the first spatially resolved kinematic study of ram-pressure stripping of a massive late-type galaxy at intermediate redshifts. Our target, the spectacular "jellyfish" galaxy A1758N_JFG1, was previously identified as a fast-moving member of the equal-mass merger A1758N ($z = 0.28$) with a star-formation rate of 48 M yr^{-1}, far above the galaxy main sequence. IFU data obtained by us unambiguously confirm ram-pressure stripping as the physical mechanism driving the optical morphology and high star-formation rate of this system by revealing extended [O2]λ3727Å emission up to 40 kpc (in projection) downstream, as well as an ordered

radial-velocity field generated by (a) conservation of angular momentum of the interstellar gas stripped from the edge of the galactic disk and (b) drag forces exerted by the intra-cluster medium on the “tentacles" of stripped material. We find no evidence of significant nuclear activity in A1758N_JFG1, although an AGN might, at this early stage of the stripping process, be obscured by high column densities of gas and dust near the galactic core. Finally, our exploration of possible trajectories of A1758N_JFG1 found solutions consistent with the notions (a) that the A1758N merger proceeds along an axis that is substantially inclined with respect to the plane of the sky and (b) that A1758N_JFG1 participated in the merger, rather than having been accreted independently from the field.

Prompted by the discovery of A1758N_JFG1, a spectacular case of ram-pressure stripping (RPS) in the galaxy cluster A1758N, we investigate the properties of other galaxies suspected to undergo RPS in this equal-mass, post-collision merger. Exploiting constraints derived from Hubble Space Telescope images and Keck longslit spectroscopy, our finding of apparent debris trails and dramatically enhanced star formation rates in an additional seven RPS candidates support the hypothesis that RPS, and hence rapid galaxy evolution in high-density environments, is intricately linked to cluster collisions. Unexpectedly, we find the vast majority of RPS candidates in A1758N to be moving toward us, and in a shared direction as projected on the plane of the sky. We hypothesize that this directional bias is the result of two successive events: (1) the quenching, during and after the first core passage, of star formation in galaxies with an approximately isotropic velocity distribution within the central region of the merger, and (2) RPS events triggered in late-type galaxies falling into the merging system along a filament, possibly enhanced by a shock front expanding into the outskirts of the south-eastern subcluster. Since this explanation implies that the merger axis of A1758N must be significantly inclined with respect to the plane of the sky, our findings open the possibility of RPS events becoming important diagnostic tools to constrain the geometry of cluster collisions that, due to the orientation of the merger axis, lack the classic observational signatures of face-on mergers.

Résumé

Boris Sindhu KALITA

Deep-Dive into the environmental drivers of star formation within dense halos in the early Universe

Cette thèse explore les différentes facettes de la formation des étoiles dans les environnements denses en utilisant un ensemble de données à plusieurs longueurs d'onde. La disponibilité du gaz dans ces environnements est un facteur critique de l'évolution des galaxies et diverses études ont tenté de créer des modèles théoriques qui prédisent la disponibilité du gaz froid ($< 10^4$ K). Ceci est particulièrement important car au-delà d'une masse de halo approximative de $\sim 10^{12}\,M_\odot$, la majorité du gaz devrait être chauffé par choc à des températures virales $\gtrsim 10^6$ K. Cependant, il a été prédit que des courants de gaz froid peuvent encore survivre et pénétrer dans les centres des halos avec du gaz autrement chauffé par choc. Ceci est essentiel pour fournir du gaz qui peut être facilement converti en étoiles dans les galaxies massives centrales. Ce n'est que récemment que nous avons commencé à obtenir des preuves observationnelles qui soutiennent cette théorie. Les deux premiers travaux de cette thèse étudient un tel cas, un groupe de galaxies RO-1001 à z=2.91.

Nous présentons d'abord une analyse bien résolue dans l'infrarouge proche et dans l'inframillimètre des trois galaxies massives à forte formation d'étoiles ($> 10^{11}\,M_\odot$) au cœur du groupe de galaxies RO-1001 à $z = 2.91$. Chacune d'entre elles présente des noyaux d'étoiles compacts à l'échelle du kpc avec des propriétés compatibles avec la formation de bulbes de galaxies, intégrés au centre de disques stellaires étendus et massifs. De manière surprenante, les disques stellaires sont sans ambiguïté à la fois quiescents et sévèrement asymétriques. Par conséquent, la trempe "extérieure" est en cours dans les trois galaxies du groupe. Nous proposons un scénario global dans lequel le fort déséquilibre de masse dans les disques (allant d'un facteur de 1,6 à >3), probablement généré sous l'effet du gaz et des amas accrétés, est responsable de la suppression de la formation d'étoiles, tout en canalisant le gaz vers les noyaux et en créant ainsi les explosions d'étoiles centrales. Le côté asymétrique des disques marque l'emplacement de l'impact des courants d'accrétion, avec des composants supplémentaires de matière (poussière et étoiles) détectés à proximité immédiate, traçant directement la direction du flux entrant. L'interaction avec les amas accrétés, qui peuvent être considérés comme des fusions mineures, conduit les axes principaux des trois galaxies à être étroitement alignés avec les filaments

d'alimentation extérieurs émettant des Lyman-α. Ces résultats fournissent la première preuve observationnelle de l'impact des courants d'accrétion froids sur la formation et l'évolution des galaxies qu'ils alimentent. Dans la phase actuelle, cela prend la forme d'une accumulation rapide de bulbes sous l'effet de l'accrétion, tout en préservant des disques stellaires massifs quiescents et asymétriques, au moins jusqu'à la rencontre d'une fusion majeure violente.

Au sein de la même structure, la quatrième galaxie massive a un âge stellaire pondéré par la masse de $1,6 \pm 0,4$ Gyr. Cette galaxie est l'une des plus anciennes connues à $z \sim 3$, ce qui implique que la plupart de ses 10^{11} $M_{\odot}$ d'étoiles se sont formées rapidement à $z > 6$–8. Il s'agit d'un exemple unique de l'évolution principalement passive d'une galaxie sur au moins $3 < z < 6$ après son extinction à haut redshift et d'un événement de type "smoking gun" indiquant l'empreinte précoce d'une relation âge-environnement. En même temps, étant dans un environnement de groupe dense avec de vastes réservoirs de gaz froid comme le trahit un halo géant de Lyα, l'existence de cette galaxie démontre que l'arrêt de l'accrétion de gaz n'est pas nécessaire pour le quenching et son maintien.

On a découvert que l'un des principaux modes de maintien de la quiescence est la rétroaction radio des AGN. Nous étudions ce phénomène au sein de CLJ1449+0856 à z=2 en utilisant des observations VLA à 3 GHz. Nous étudions les effets de la rétroaction cinétique basée sur le radio-jet à des décalages vers le rouge élevés, qui s'est avérée cruciale dans les amas à faible décalage vers le rouge pour expliquer les propriétés thermodynamiques observées de leur MCI. Nous étudions cette interaction à une époque caractérisée par des niveaux élevés d'activité des AGN et une phase de transition du MCI en ce qui concerne la probabilité d'accrétion résiduelle de gaz froid. Nous mesurons un flux total de $30,6 \pm 3,3$ $^{-}$Jy à partir des 6 jets détectés. Leur contribution en puissance est estimée à $1,2\ (\pm 0,6)\ \times 10^{44}$ ergs s^{-1}, bien que cette valeur puisse atteindre $4,7\ \times 10^{44}$ ergs s^{-1}. Cela représente un facteur $\sim 0,25$ – 1,0 de l'injection d'énergie instantanée précédemment estimée dans le MCI de CLJ1449+0856 à partir des flux sortants des AGN et de la formation d'étoiles, qui se sont déjà avérés suffisants pour compenser globalement les flux de refroidissement dans le cœur de l'amas. En accord avec l'abondance déjà détectée de la formation d'étoiles, ce mode de rétroaction distribué sur plusieurs sites, contrairement à une source centrale unique observée à de faibles décalages vers le rouge, indique une accrétion de gaz dans le centre de l'amas. Cela suggère également un "état stable" de l'amas, avec un comportement différent de celui d'un noyau froid.

La deuxième partie de cette thèse comprend deux travaux sur un amas à décalage vers le rouge intermédiaire pour étudier l'élimination du gaz des galaxies en fusion. Nous présentons et discutons les résultats de la première étude cinématique à résolution spatiale de l'extraction par pression dynamique d'une galaxie massive de type tardif à des décalages vers le rouge intermédiaires. Notre cible, la spectaculaire galaxie "méduse" A1758N_JFG1, a été précédemment identifiée comme un membre en mouvement rapide

de la fusion de masse égale A1758N ($z = 0.28$) avec un taux de formation d'étoiles de 48 M yr^{-1}, bien au-dessus de la séquence principale de la galaxie. Les données IFU que nous avons obtenues confirment sans ambiguïté que le mécanisme physique à l'origine de la morphologie optique et du taux élevé de formation d'étoiles de ce système est l'extraction par pression dynamique, en révélant une émission étendue de [O2]λ3727Å jusqu'à 40 kpc (en projection) en aval, ainsi qu'un champ de vitesse radiale ordonné généré par (a) la conservation du moment angulaire du gaz interstellaire arraché au bord du disque galactique et (b) les forces de traînée exercées par le milieu intra-amas sur les "tentacules" de matière arrachée. Nous ne trouvons aucune preuve d'une activité nucléaire significative dans A1758N_JFG1, bien qu'un AGN puisse, à ce stade précoce du processus d'extraction, être obscurci par les densités de colonne élevées de gaz et de poussière près du noyau galactique. Enfin, notre exploration des trajectoires possibles de A1758N_JFG1 a trouvé des solutions cohérentes avec les notions (a) que la fusion A1758N se déroule le long d'un axe qui est substantiellement incliné par rapport au plan du ciel et (b) que A1758N_JFG1 a participé à la fusion, plutôt que d'avoir été accrété indépendamment du champ.

Suite à la découverte de A1758N_JFG1, un cas spectaculaire de dépouillement par pression dynamique (RPS) dans l'amas de galaxies A1758N, nous étudions les propriétés d'autres galaxies suspectées de subir un RPS dans cette fusion post-collision de masse égale. En exploitant les contraintes dérivées des images du télescope spatial Hubble et de la spectroscopie à longue lumière Keck, nous avons découvert des traînées de débris apparentes et des taux de formation d'étoiles considérablement accrus dans sept autres galaxies candidates au RPS. De manière inattendue, nous constatons que la grande majorité des candidats RPS dans A1758N se déplacent vers nous, et dans une direction commune telle que projetée sur le plan du ciel. Nous supposons que ce biais directionnel est le résultat de deux événements successifs : (1) l'extinction, pendant et après le premier passage du noyau, de la formation d'étoiles dans les galaxies avec une distribution de vitesse approximativement isotrope dans la région centrale de la fusion, et (2) des événements RPS déclenchés dans des galaxies de type tardif tombant dans le système de fusion le long d'un filament, peut-être renforcé par un front de choc s'étendant dans la périphérie du sous-amas sud-est. Puisque cette explication implique que l'axe de fusion de A1758N doit être significativement incliné par rapport au plan du ciel, nos résultats ouvrent la possibilité que les événements RPS deviennent des outils de diagnostic importants pour contraindre la géométrie des collisions d'amas qui, en raison de l'orientation de l'axe de fusion, manquent des signatures observationnelles classiques des fusions face à face.

Contents

Chapter 1

Introduction

PART I

1.1 The cosmic petri dish for galaxies

The observable Universe is a fantastic spectacle of the interactions between various forms of baryonic matter, which in turn are governed by the gravitational potentials set up by the underlying dark matter distribution. The widely-accepted standard Lambda cold dark matter (ΛCDM) cosmological model dictates that this frame-work began with small overdensities incrementally growing into larger 'halos' through collapse under self-gravity while overcoming the expansion of the Universe. This bottom-up 'hierarchical structure formation', expected under ΛCDM, also allows for the creation and evolution of galaxies within these structures, as they feed on the gas readily available to them.

The conventional understanding of galaxy growth within dark-matter halos has been constructed over many decades (Rees and Ostriker, 1977; Silk, 1977; White and Rees, 1978; Fall and Efstathiou, 1980; White and Frenk, 1991; Kauffmann, White, and Guiderdoni, 1993; Cole et al., 1994; Avila-Reese, Firmani, and Hernández, 1998; Mo, Mao, and White, 1998; Somerville and Primack, 1999; Blaizot et al., 2006; Daddi et al., 2010a; Tacconi et al., 2010; Dekel and Krumholz, 2013; Feldmann and Mayer, 2015). This picture suggests gas falling into a dark matter halo potential, created as a result of the hierarchical structure formation model, gets shock heated to virial temperatures $\sim 10^6 (v_{circ}/167\,\mathrm{km\,s^{-1}})$K. The gas thereby reaches a state of quasi-hydrostatic equilibrium featuring a uniformly increasing gas density with decreasing radius from the core of the halo.

The hot gas radiates away its thermal energy through Bremsstrahlung emission, detectable in X-ray, as a result of free-electrons interacting with the hot and hence ionized medium. The efficiency of this process is proportional to the gas density and hence in the central regions of the halos where the density is highest, the gas efficiently collapses, thereby leading to a cooling flow, into galactic disks leading to star formation (e.g., Fabian, 1994). There is a caveat here however. This process needs to be controlled in order to prevent a 'runaway' cooling flow that would otherwise lead to disagreement with

observations of gas (Peterson et al., 2001; Peterson et al., 2003; Sanders et al., 2008), star-formation (McNamara and O'Connell, 1989; Edge and Frayer, 2003) as well as the high luminosity end of the galaxy luminosity functions (Benson et al., 2003). Although there are a variety of processes that can provide the entropy required, like thermal conduction (Kim and Narayan, 2003a; Pope et al., 2006), supernova explosions (Springel and Hernquist, 2003) and turbulent mixing (Kim and Narayan, 2003b; Voigt and Fabian, 2004; Dennis and Chandran, 2005), only active galactic nuclei (AGN)-jet driven feedback is a self-sufficient mechanism to curtail the global cooling. This is expected to be especially critical at higher redshifts (McCarthy et al., 2008; Hatch et al., 2014).

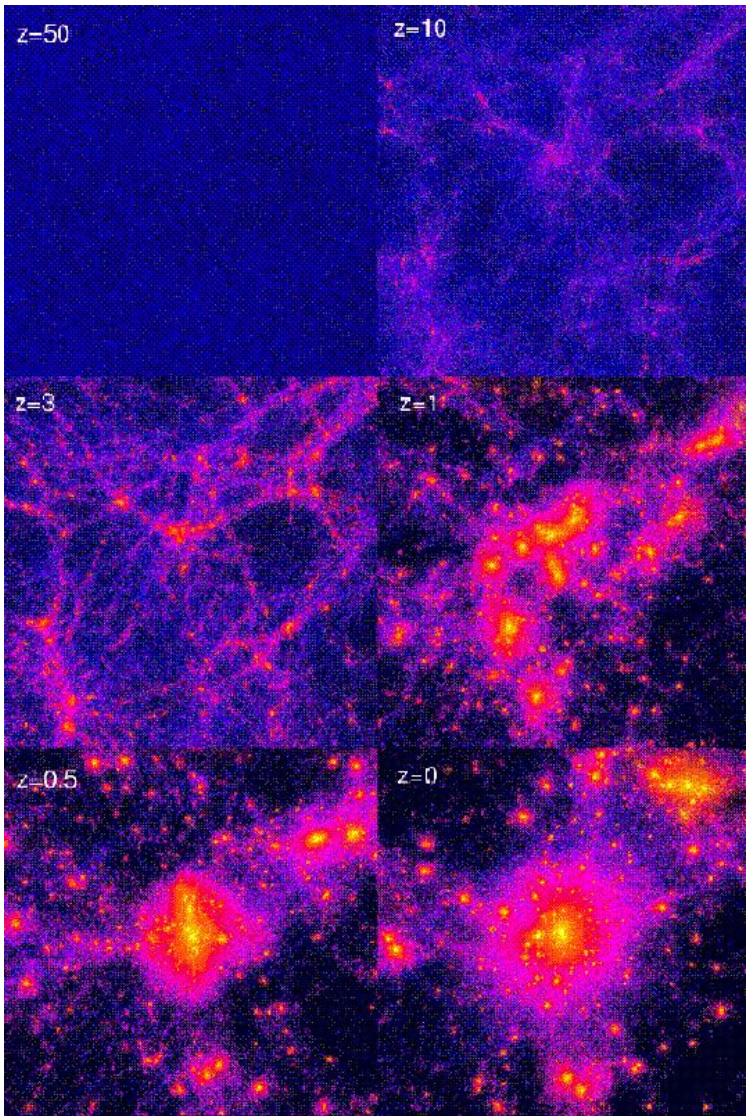

FIGURE 1.1: Figure from (Moore et al., 1998), showing hierarchical evolution in a cosmological simulation leading to the formation of a galaxy cluster within the ΛCDM framework.

FIGURE 1.2: (Left panel) Composite image showing the X-ray (as the purple haze) superimposed on the optical *HST* image of A1689 at z = 0.18. (Right panel) *HST* image of MS0735.6+7421 cluster with the X-ray emission shown in blue, while AGN-jet feedback seen in radio (330 MHz) shown in red.

Although at redshifts ($z < 2$), this is careful balance between shock heating of gas and subsequent cooling of a fraction of that provides the site for galaxy evolution, simulations from the last decade (Kereš et al., 2005; Dekel and Birnboim, 2006; Dekel et al., 2009) have suggested that almost half of the gas accreted by the galaxies within halos never get shock heated to virial temperatures. This is suggested by an approximate agreement over cosmic time between the cosmological accretion rate and the average star formation rate (SFR) of an average star-forming galaxy at the same epoch (Dekel, Sari, and Ceverino, 2009). Hence there would be a large fraction of infalling gas that would remain cold ($\lesssim 10^4$ K) and penetrate into the hot halos to feed the galaxies at the core (Fig. 1.3, left). Moreover, this fraction of cold gas in the accreted material, or the 'cold-gas accretion' depends on the mass of the halo as well as the redshift (Fig. 1.3, right).

1.2 A general overview of galaxy evolution

This thesis is primarily interested in the growth of the massive ($\gtrsim 10^{10}\,M_\odot$) within the cosmic petri dish of hot halos explained above. The available cold gas is accreted to form stars in galaxies. Nevertheless, along with this simple picture of consumption of gas, one also forms and feeds a super massive black hole (SMBH) that provides a gravitational anchor-point especially at the core of the growing galaxy. Furthermore, feedback from the SMBH as well as the star formation itself plays a role in removing available gas, a fraction of which falls back into the galactic potential. The balance between

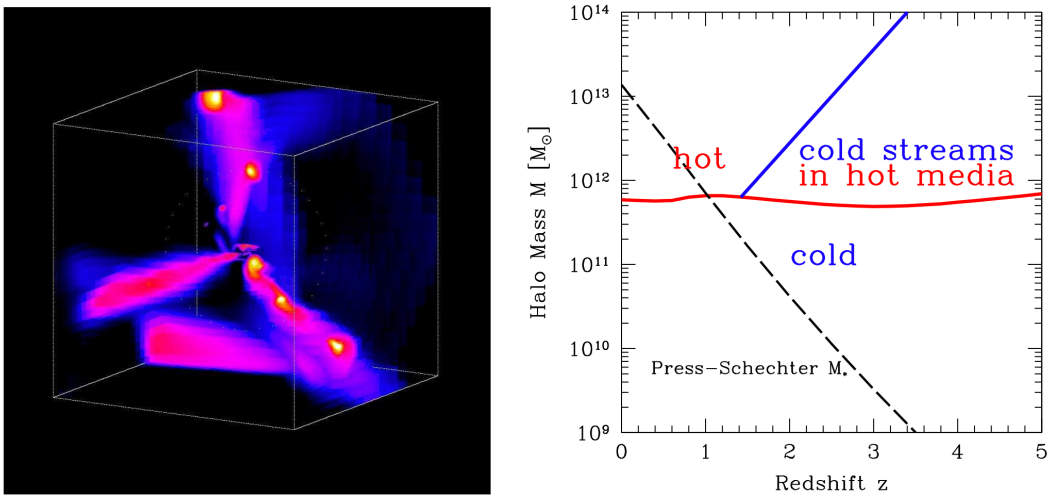

FIGURE 1.3: (Left panel) Cold-gas streams observed in the cosmological MareNostrum simulation — an adaptive-mesh hydrodynamical simulation presented in (Dekel et al., 2009). (Right-panel) Analytic prediction for the regime where cold gas accretion flows (cold in hot) are predicted to survive within the otherwise redshift-independent evolution of halos from cold-gas to shock-heated gas domination (approximately divided at $M_{shock} \sim 10^{12}\,M_{\odot}$)

then facets (Fig. 1.4, from Tumlinson, Peeples, and Werk, 2017) governs the growth and evolution of galaxies, determining their interdependent properties like morphologies and star-formation rates (Bouché et al., 2010; Daddi et al., 2010b; Genzel et al., 2010; Tacconi et al., 2010; Davé, Finlator, and Oppenheimer, 2012; Dekel et al., 2013; Lilly et al., 2013; Feldmann and Mayer, 2015).

A critical empirical model that governs this equilibrium of gas inflow, outflow and consumption is the tight correlation between star-formation rate (SFR) and stellar mass ($M_{\star}$), known as the star-forming main-sequence (MS, Fig. 1.5 from Schreiber et al., 2015). This has been been found to hold with minimum scatter at least upto $z \sim 4$ (e.g., Brinchmann et al., 2004; Daddi et al., 2007; Elbaz et al., 2007; Noeske et al., 2007b; Noeske et al., 2007a; Salim et al., 2007; Whitaker et al., 2012; Speagle et al., 2014; Schreiber et al., 2015). Hence, the star-forming MS can be used to classify galaxies based on their position w.r.t. the MS, as star-bursting (above the 0.2 dex scatter of the MS), star-forming (within the scatter of the MS), the transitioning "green valley" galaxies and passive/quiescent galaxies[1] (below the scatter of MS).

Within this framework, we can now discuss the basic categorization of galaxies based on morphologies: Early-type galaxies (or ETGs which

[1] A specific SFR ($SFR/M_{\star}$) can be used as a distinction between passive and quiescent galaxies (usually $\sim -11\,yr^{-1}$). However, given the purpose of this thesis is primarily to understand drivers of star-formation and quenching, we shall be using these terms interchangeably

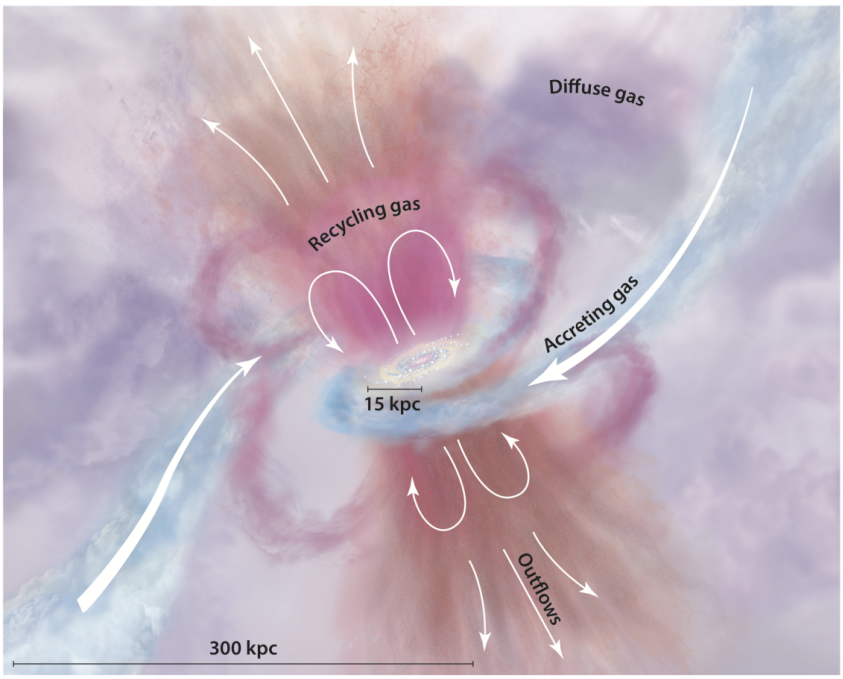

FIGURE 1.4: From Tumlinson, Peeples, and Werk, 2017, a cartoon illustrating the balance between star-formation in a galaxy, gas accretion (in blue) and outflows (in pink and orange).

are pressure supported low-gas systems) and Late-type galaxies (or LTGs predominantly featuring disks and in some cases, bulges, spiral arms and/or bars). However, this classification should rather be considered as the two ends of a continuous distribution, with possible (but debated) evolutionary pathways especially from LTGs to ETGs. This becomes even more complex when one considers the variation over the observed wavelengths which determines which component of the galaxy are we witnessing: young or old stars, hot or cold gas, dust or relativistic electrons (Galliano, Galametz, and Jones, 2018). Moreover, uncertainties in determining morphology also grows with increasing redshift. This is primarily due to detection limits of telescopes at high redshifts, in addition to galaxies being dynamically unstable leading to morphological transformations (Noguchi, 1999; Bournaud, Elmegreen, and Elmegreen, 2007; Dekel et al., 2009; Zolotov et al., 2015; Tacchella et al., 2016) as well as them being progressively more compact with increasing redshift (Fig. 1.6 as shown in van der Wel et al., 2014).

1.2.1 The growth of massive galaxies in dense environments

An attempt at combining the two methods of characterization: star-formation and morphology, leads to a generalized understanding of galaxy evolution over cosmic time. The secular evolution model, characterized by the MS is likely the dominant mode of star-formation at least over the epoch over which the relation holds ($z < 4$). This primarily features the inflow of gas

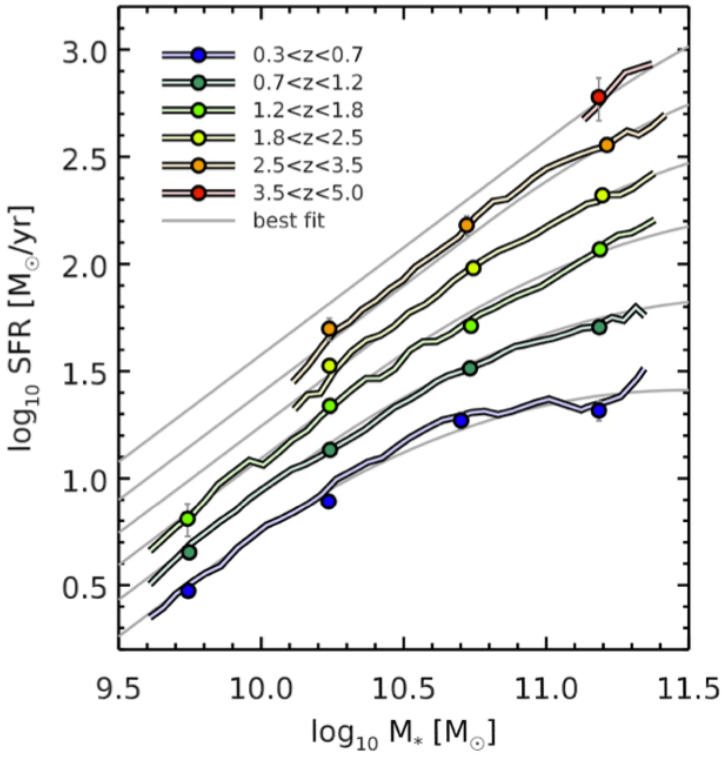

FIGURE 1.5: From Schreiber et al., 2015. Evolution of the average SFR of SFGs with stellar mass and redshift which defines the MS of star formation at different redshifts. The best-fit are shown as light gray curves.

into the galaxies, which is converted to stars with an efficiency (specific SFR or sSFR = SFR/$M_\star$) which is found to increase with increasing redshift. This is thought to result most naturally in disks (e.g., Wuyts et al., 2011) due to the dissipative nature of gas, which in turn leads to a similar stellar morphology. Thin disks, with the ratio of rotational velocity to the velocity dispersion > 5, are expected to be created at $z \lesssim 1$. However, these disks may experience dynamical instabilities at various stages of its evolution, that can lead to a variety of morphological transformations as as summarized in Fig. 1.7.

This is especially pertinent with increasing redshift, which brings along an enhancement of cold-gas accretion (as already discussed in Sec. 1.1). This accretion could be in the form of smooth-gas, as well as 'clumps' that can lead to mergers with a wide range of mass-ratios (from 'minor' to 'major') as predicted in Dekel et al., 2009. These interactions with accreted material, that lead to dynamical instabilities, are the primary drivers of outliers in the otherwise tight correlation of the MS. At the higher sSFR end, we have the star-bursts (or SBs). What causes the elevated sSFR has been a matter of debate: whether it is due to an increased star formation efficiency or SFE = SFR/M_{gas}, an increase in gas content (Scoville et al., 2016) or a combination

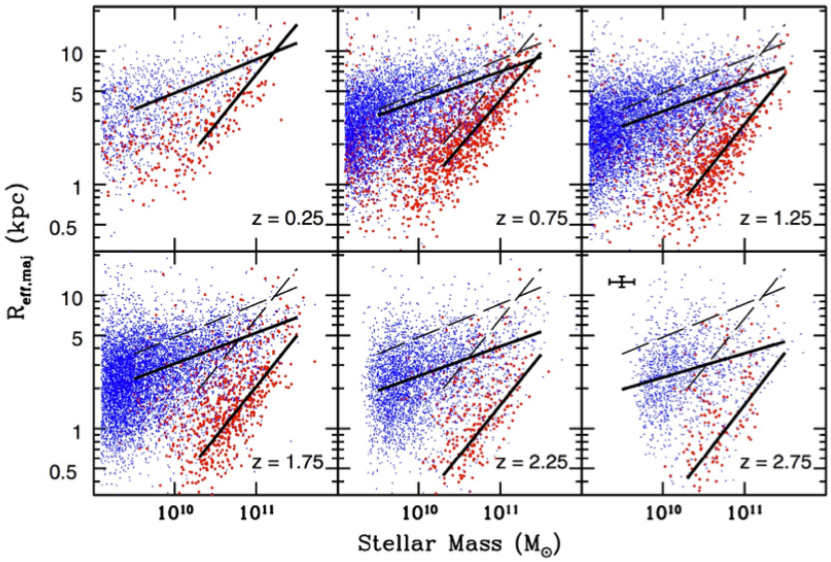

FIGURE 1.6: From van der Wel et al., 2014. Size-stellar mass distribution of SFGs (blue symbols) and QGs (red symbols). The solid lines represent model fits to the SFGs and QGs populations. The dashed lines represent the model fits to the galaxies at $0 < z < 0.5$ as a reference. There is a strong evolution in the intercept of the size-mass relation in QGs and moderate evolution in SFGs. There is no evidence for evolution in the slope.

of both (Magdis et al., 2012; Sargent et al., 2014; Tacconi et al., 2018). Nevertheless, this discussion of SBs (with sSFR of the order of ~ 100 Myr) is critical for understanding the origins of the most massive ETGs within clusters.

Studies show that their progenitors, the distant red galaxies at $z \sim 2$ (Franx et al., 2003) were in fact predominantly compact, with effective radii $\sim 1 - 2$ kpc. The compact quiescent galaxies (cQGs) have been thought to be the originate from compact star-burst like properties that made formed most of their stars in a short epoch within their nuclei (in the form of compact star-forming galaxies or cSFGs), after which they rapidly underwent quenching at $z \sim 2 - 5$. Such intense levels of star-formation is also associated with the high production of dust (Toft et al. 2005; Daddi et al. 2005; Onodera et al. 2012; Kreik et al. 2016). Given that dust absorbs UV-light from young stars which gets re-emitted in far-infrared and sub-millimeter wavelengths, cSFGs can hence be identified as submillimeter galaxies, with the compact highly star-forming/starbursting cores featuring high levels of dust emission.

The formation mechanism of these high-z cSFGs leads us to revisit the evolution due to a range of interaction with accreted materials. To understand the process that leads to the characteristic nuclear starbursts, possible analogs at low redshifts can be invoked. The infrared-compact (Lutz et al. 2016) luminous and ultra-luminous infrared galaxies, LIRGs and ULIRGs respectively (Joseph & Wright 1985, Sanders & Mirabel 1996, Kartaltepe et al.

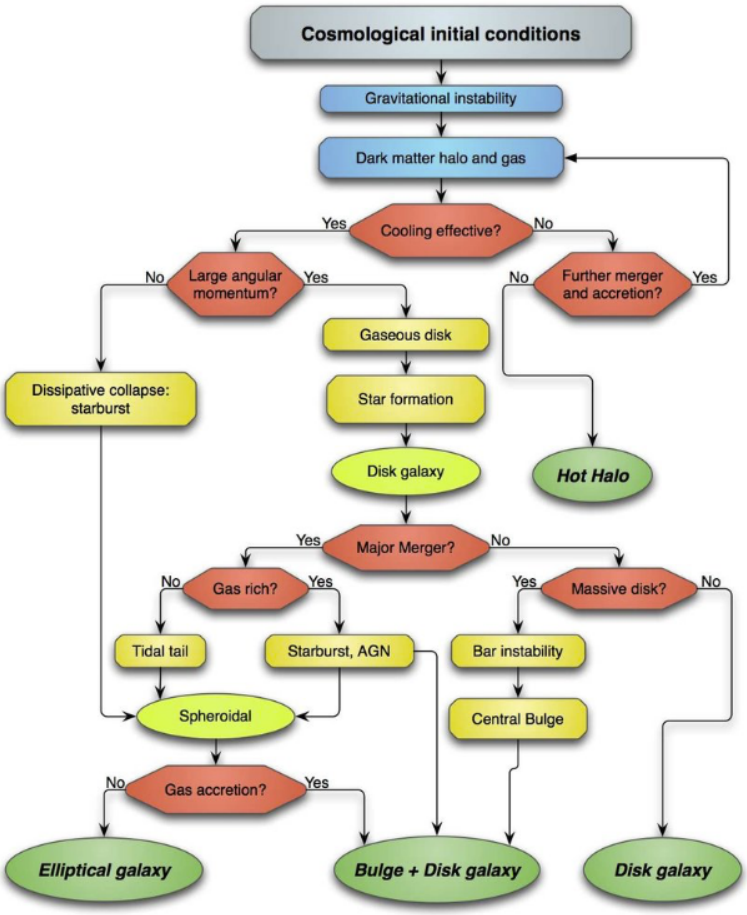

FIGURE 1.7: From Niemi, 2011, a flowchart describing a generalized evolutionary structure leading to formation of galaxies featuring disks, disks with bulges and ellipticals. Each of the variations are primarily driven by dynamical interactions with accreted material, which may vary from smooth gas to major-mergers with other galaxies.

2012), are found to be exclusively associated major-mergers or interacting system. This scenario is further corroborated by simulations reproducing the expected nuclear starbursts (e.g., Barnes & Hernquist 1996; Naab et al. 2006). Hence, gas-rich major-mergers are expected lead to the dynamical instabilities causing the loss of angular momentum and collapse of gas to the nuclear regions leading to high levels of star formation (Cimatti et al., 2008; Fu et al., 2013; Ivison et al., 2013; Toft et al., 2014; Toft et al., 2017; Elbaz et al., 2018). On the contrary, less intense interactions with accreted materials (minor-mergers or smooth-gas accretion) has been suggested to also lead to the formation of cSFGs, as anticipated primarily by simulations along with a few observational studies (Zolotov et al., 2015; Tacchella et al., 2016; Gómez-Guijarro et al., 2018). It can however be surmised that the understanding of

the formation of cSFGs, especially through observational characterisation, is hence in a nascent state. Deeper and well-resolved studies, which will be possible in the JWST era, would be critical in deciphering the relative improtance of the various triggering mechanisms of cSFGs.

1.2.2 Quenching star formation in massive galaxies

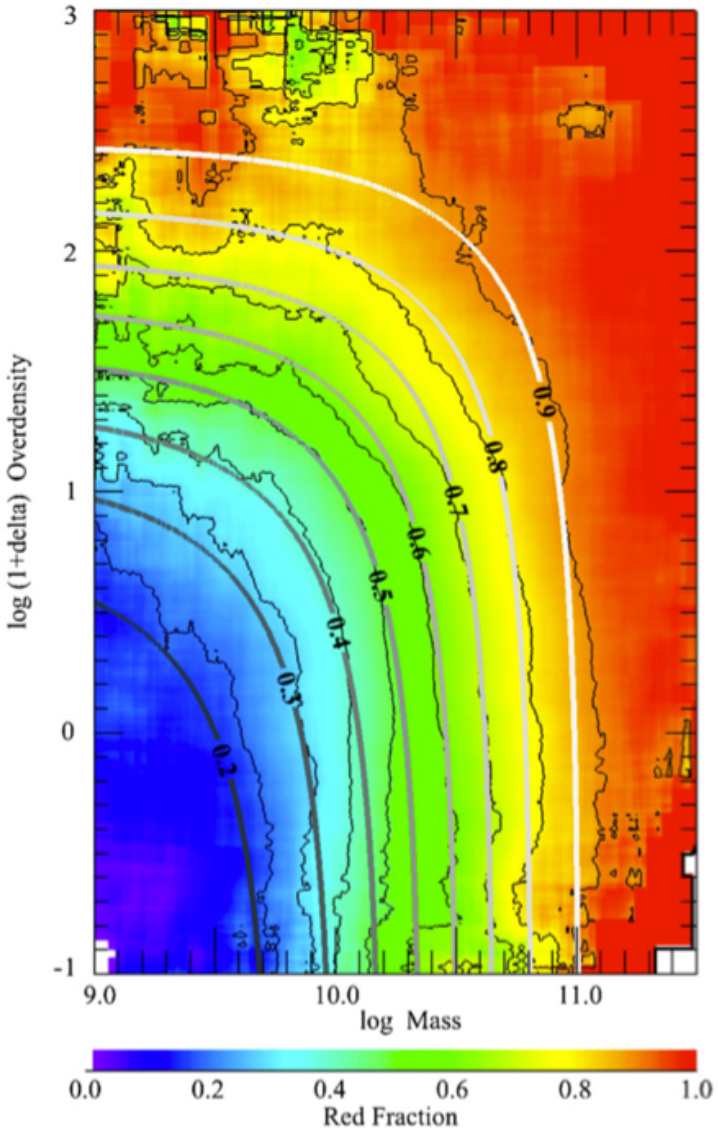

FIGURE 1.8: From Peng et al., 2010b, the red (quenched) fraction of galaxies as a function of stellar mass and overdensity

The second essential question is the mode of quenching of these objects. This ties to the general question of how quenching occurs over cosmic time and whether this is dependent on the mass of galaxies, relevant for the

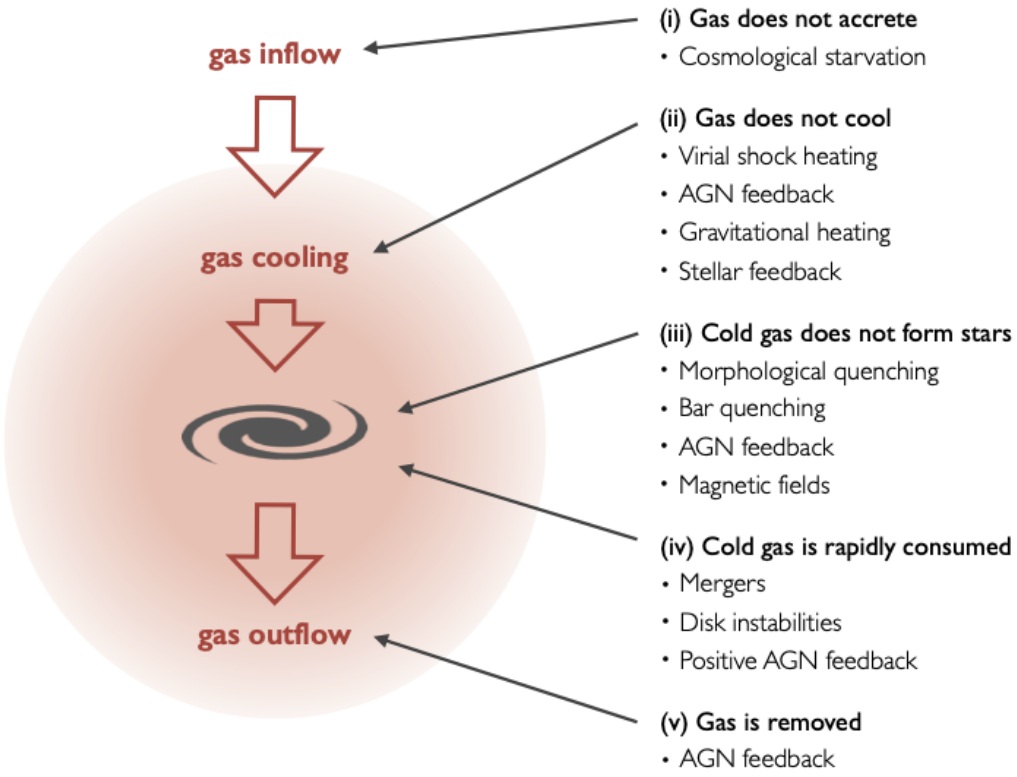

FIGURE 1.9: From Man and Belli, 2018, a schematic diagram of possible quenching mechanisms

massive cSFGs discussed above. Peng et al., 2010b showed that quenching of galaxies (at least up to z $\sim$ 1) with stellar mass $> 10^{11}$ $M_{\odot}$ are more likely to be independent of their environment (Fig. 1.8). Moreover, the dominant 'mass-dependent' quenching is expected to be proportional to the SFR, which could be due to a causal or circumstantial link. There are high levels of ambiguity regarding the dominant quenching modes (summarized in (Man and Belli, 2018) and shown in Fig. 1.9), that may vary on a case by case basis. Nevertheless, it is worth noting that quite a few of these processes are directly (stellar feedback, AGN) or indirectly (mergers, disk instabilities, morphological quenching) related to star-formation.

However, the picture gets far more unclear while considering the origin of the progenitors of the massive cluster galaxies at higher redshifts. Study of this cQG population has led to a large body of research in the current era. Driven by the detection of such galaxies already in place by $z \sim 2$ (Daddi et al., 2005; Gobat et al., 2012; Glazebrook et al., 2017; Schreiber et al., 2018b; Valentino et al., 2020b; Forrest et al., 2020b; Forrest et al., 2020c; D'Eugenio et al., 2020a; Kubo et al., 2021), attempts has been made to make the hierarchical structure formation models compatible with the hence derived number densities, that were initially off by about an order of magnitude (Wellons et al. 2015, Nelson et al. 2015, Steinhardt et al. 2016, Davé et al. 2016, Cecchi et

al. 2019).

Nevertheless, the quenching mechanism invoked during such attempts is usually AGN-driven feedback, which although efficient, is far from being the only possible mode. This is especially critical in regards to the quenching of cSFGs, which already have their high levels of star-formation associated to mergers (e.g., Cimatti et al., 2008; Gómez-Guijarro et al., 2018; Gómez-Guijarro et al., 2019; Puglisi et al., 2019) and violent disk instabilities (e.g., Dekel, Sari, and Ceverino, 2009; Barro et al., 2013; Toft et al., 2014; Zolotov et al., 2015), which in turn can lead to quenching through the rapid consumption of gas. Finally, the rapid build-up of a pressure supported stellar bulge associated with the compact nuclear starbursts observed in cSFGs, can also lead to quiescence. This 'morphological quenching' is also responsible for the maintenance of quiescence in addition to AGN feedback, through the prevention of the gas from being cooled in order to form stars.

1.2.3 Structure of Part I

The first part of this thesis deals with the formation, evolution and quiescence of galaxies within high redshift dense environments. We concentrate on two specific spectroscopically confirmed structures at $z = 2.91$ (a galaxy group RO-1001) and 1.99 (a nascent galaxy cluster CLJ1449+0856). We begin with a detailed study of the stellar and dust emission of three heavily star-forming galaxies at the core of RO-1001, in Chapter 2 (Kalita et al., 2022). We present well-resolved near-IR and sub-mm analysis of the three highly star-forming massive ($> 10^{11}\,M_{\odot}$) galaxies within the core of the galaxy-group. Each of them displays kpc-scale compact star-bursting cores with properties consistent with forming galaxy bulges, embedded at the center of extended, massive stellar disks. Surprisingly, the stellar disks are unambiguously both quiescent, and severely lopsided. Therefore, 'outside-in' quenching is ongoing in the three group galaxies. We propose an overall scenario in which the strong mass lopsidedness in the disks (ranging from factors of 1.6 to >3), likely generated under the effects of accreted gas and clumps, is responsible for their star-formation suppression, while funnelling gas into the nuclei and thus creating the central starbursts. The lopsided side of the disks marks the location of accretion streams impact, with additional matter components (dust and stars) detected in their close proximity directly tracing the inflow direction. The interaction with the accreted clumps, which can be regarded as minor-mergers, leads the major axes of the three galaxies to be closely aligned with the outer Lyman-α-emitting feeding filaments. These results provide the first observational evidence of the impact of cold accretion streams on the formation and evolution of the galaxies they feed.

This is followed by Chapter 3, we proceed towards quenching of massive galaxies. Using deep ALMA and HST observations, we study a quenched massive galaxy within the RO-1001 (Kalita et al., 2021a). With a mass-weighted stellar age of 1.6 ± 0.4 Gyr this galaxy is one of the oldest known

at $z \sim 3$, implying that most of its 10^{11} $M_\odot$ of stars were rapidly formed at $z > 6$–8. This is a unique example of the predominantly passive evolution of a galaxy over at least $3 < z < 6$ following its high-redshift quenching and a smoking-gun event pointing to the early imprint of an age-environment relation. At the same time, being in a dense group environment with extensive cold-gas reservoirs as betrayed by a giant Lyα halo, the existence of this galaxy demonstrates that gas accretion shutdown is not necessary for quenching and its maintenance.

Finally in Chapter 4, we study the effects of AGN kinetic feedback at z $\sim$ 2 (Kalita et al., 2021b). We report the detection of multiple faint radio sources, that we identify as AGN-jets, within CLJ1449+0856 at z=2 using 3 GHz VLA observations. We investigate this interaction at an epoch featuring high levels of AGN activity and a transitional phase of ICM in regards to the likelihood of residual cold-gas accretion. This mode of feedback is found to be distributed over multiple sites within the core of the cluster, contrary to a single central source observed at low redshifts. We suggest that this points to accretion of gas into the cluster centre.

PART II

1.3 Environmental quenching at lower redshifts

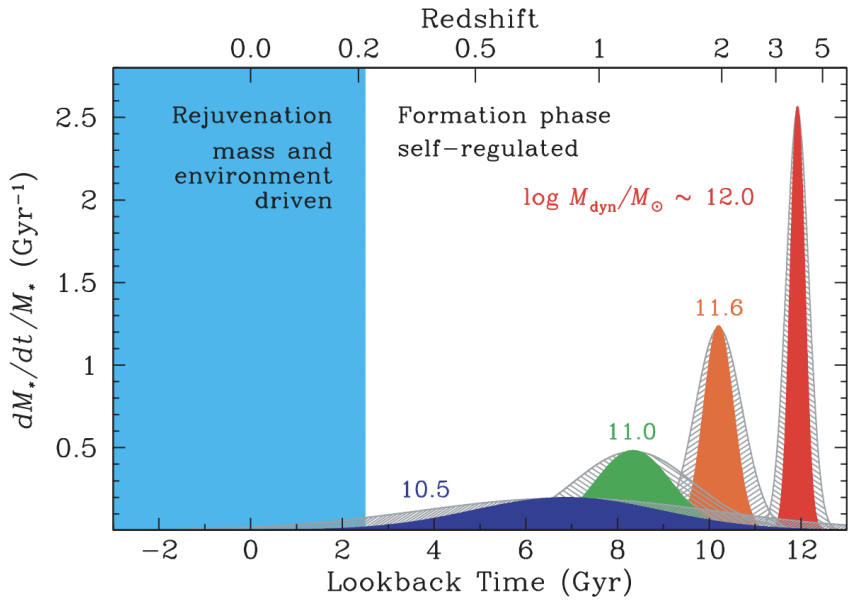

FIGURE 1.10: From Thomas et al., 2010, sSFR as function of look-back time for early-type galaxies of various masses showing the effect of downsizing

One of the crucial developments since early 1970s has been the use of

stellar population models to derive properties from integrated galactic spectra (e.g., Tinsley 1972; Tinsley 1978; Kriek et al. 2009; Schreiber et al. 2018b; Carnall et al. 2019). The use of this method on the quiescent galaxy population has revealed that progressively massive galaxies formed majority of their stars at earlier epochs and over a shorter periods of time (Fig. 1.10 from Thomas et al., 2010; see also Thomas et al. 2005; Gallazzi et al. 2005; Fontanot et al. 2009; Citro et al. 2016). This is known as "downsizing". Hence the most massive of the galaxies, especially found in clusters, had their primary star formation episode at $z \gtrsim 3$, followed by rapid quenching. This can be regarded as one of the major motivations our study of quiescence within dense environments at $z \sim 2-3$ in Part I. However, at lower redshifts ($z \lesssim 1.5$), there is minimal evolution of the high-mass end of stellar mass functions. Meanwhile the lower mass end experiences a rapid rise (Fontana et al., 2004; Cimatti, Daddi, and Renzini, 2006; Arnouts et al., 2007; Drory et al., 2009; Pozzetti et al., 2010; van Dokkum et al., 2014; Gargiulo et al., 2016; Davidzon et al., 2017; Kawinwanichakij et al., 2020).

As suggested in Peng et al., 2010b, the quenching for these lower mass galaxies is primarily driven by environmental effects. Moreover, these effects seem to act in a "one-off" way and there isn't a temporal evolution of the effect of this mode over individual galaxies. These effects are primarily divided into two groups:

- *Gravitational perturbations* due to tidal interactions with other cluster members (e.g., Merritt 1983), or galaxy harassment due to multiple fly-by encounters (e.g., Moore et al. 1996, 1998). This has an effect throughout all galaxy components, that includes stars, gas, dark matter and dust, therefore having the capacity to morphologically alter galaxies.

- *Hydrodynamical interactions* due to the effect of the hot intracluster medium (ICM) on the cold interstellar medium (ISM) of galaxies. This can occur through thermal evaporation (e.g., Cowie & Songaila 1977) or a complete removal through ram-pressure stripping (e.g., Gunn & Gott 1972). This, unlike gravitational interactions, only effect the diffuse ISM (Boselli & Gavazzi 2006), although second order effects such as localized enhancement of star formation or triggering of AGN activity (Poggianti et al., 2017) can also be expected.

Part II of this thesis specifically deals with ram-pressure stripping at a redshift of 0.3 within a merging cluster A1758N. In Chapter 5 (Kalita and Ebeling, 2019), we undertake the first spatially resolved kinematic study of ram-pressure stripping of a massive late-type "jellyfish" galaxy at intermediate redshifts. Integral field unit (IFU) data obtained by us unambiguously confirm ram-pressure stripping as the physical mechanism driving the optical morphology and high star formation rate of this system by revealing extended $[OII]3727$ emission up to 40 kpc (in projection) downstream, as

FIGURE 1.11: From Boselli, Fossati, and Sun, 2022, the pseudo-colour image of part of the Markarian chain of galaxies undergoing ram-pressure stripping in the Virgo cluster obtained using the combination of optical imaging with narrow-band images mapping Hff and [NII]. The latter traces the ionized gas seen as red filamentary structures escaping from the potential of the galaxies.

well as an ordered radial-velocity field generated by (a) conservation of angular momentum of the interstellar gas stripped from the edge of the galactic disk and (b) drag forces exerted by the ICM on the "tentacles" of stripped material. Moreover, our exploration of possible trajectories of the galaxy found solutions consistent with the notions (a) that the A1758N merger proceeds along an axis that is substantially inclined with respect to the plane of the sky and (b) that the jellyfish galaxy participated in the merger, rather than having been accreted independently from the field.

In Chapter 6, prompted by the discovery of the aforementioned massive jellyfish galaxy, we investigate the properties of other galaxies within A1758N suspected to undergo RPS in this equal-mass, post-collision merger (Ebeling and Kalita, 2019). Exploiting constraints derived from Hubble Space Telescope images and Keck longslit spectroscopy, our finding of apparent

debris trails and dramatically enhanced star formation rates in an additional seven RPS candidates support the hypothesis that RPS, and hence rapid galaxy evolution in high-density environments, is intricately linked to cluster collisions. Unexpectedly, we find the vast majority of RPS candidates in A1758N to be moving toward us, and in a shared direction as projected on the plane of the sky. We hypothesize that this directional bias is the result of two successive events: (1) the quenching, during and after the first core passage, of star formation in galaxies with an approximately isotropic velocity distribution within the central region of the merger, and (2) RPS events triggered in late-type galaxies falling into the merging system along a filament, likely as part of a group.

Chapter 2

Bulge formation inside quiescent lopsided stellar disks

This work has been accepted for publication in A & A (Kalita et al., 2022)
(arXiv e-prints, arXiv:2206.05217)

Beginning with the search for signatures of accretion on galaxies within high-z halos, we present the following work that makes use of deep optical, near-IR and sub-mm data. The three highly star-forming galaxies show signs of dynamical instability in the stellar morphology, which have predominantly suppressed star-formation. Meanwhile, the high levels of star formation is rather concentrated in what appears to be the future bulges. We show that interactions with accreted material, be it smooth-gas accretion, minor-mergers or major-mergers, all play a role in the formation of the previously discussed (Sec. 1.2.1) critical population of compact star-forming galaxies.

2.1 Introduction

The formation of massive galaxies ($> 10^{11}\,M_{\odot}$) that happened within the first ~ 3 Gyr after the Big Bang sustained by cold streams (Birnboim and Dekel, 2003; Kereš et al., 2005), is still not fully understood (Somerville and Davé, 2015; Vogelsberger et al., 2020). Cold gas accretion (which includes smooth gas as well as clumpy material) is expected to be ubiquitous in high redshift dense environments (Dekel et al., 2009). Encouraging observational evidence for cold streams was recently obtained for a sample of galaxy groups and clusters at $2.0 < z < 3.3$ and for statistical samples of massive galaxies (Daddi et al., 2022b; Daddi et al., 2022a). Yet there remains a paucity of direct observations of how this critical process affects individual galaxies. In general, the need of gas accretion fueling the star formation in galaxies is abundantly clear, exemplified by the tight correlation between their star formation rates (SFR) and the stellar mass at least up to $z \sim 4 - 6$ (the star-forming main-sequence; Daddi et al., 2007; Elbaz et al., 2007; Whitaker et al., 2012; Speagle et al., 2014; Schreiber et al., 2015). Morphologically, this phase is expected to feature secularly growing disks (Daddi et al., 2010b; Tacconi et al., 2010; Dekel and Krumholz, 2013; Feldmann and Mayer, 2015).

Meanwhile, to accomodate the existence of compact (~ 1 kpc), spheroidal, quiescent galaxies (QGs) observed at $z \sim 2-4$ (e.g., Valentino et al., 2020b; Lustig et al., 2021; D'Eugenio et al., 2021a) in contrast to the relatively more extended star-forming disk galaxies (van der Wel et al., 2014), an intermediate population of compact star-forming galaxies (cSFGs) have been proposed and widely observed (Barro et al., 2013; Barro et al., 2014; van Dokkum et al., 2015; Puglisi et al., 2019; Puglisi et al., 2021) . The feature at the heart of this hypothesis, quite literally, is the compact star-forming core that is expected to form the spheroidal bulge characteristic of the compact QGs. When gas is driven into the central compact region, the increase in the gas surface density results in a rise in star-formation that rapidly builds up the stellar mass of the bulge. However, the mode of formation of these cSFGs has been a matter of debate. On one hand, simulations predict that smooth-gas-accretion driven violent disk instabilities result in the gas being driven to the core of secularly evolving disk-like galaxies, once the galaxy mass reaches $\sim 10^{9.5}\,M_{\odot}$ and thereby creating most of the stellar mass in a compact spheroidal structure (*wet compaction*; Dekel et al., 2013; Zolotov et al., 2015; Tacchella et al., 2016). Whereas observational studies of large statistical samples advocate the rapid effects of major-mergers between galaxies leading to the formation of such objects (Cimatti et al., 2008; Ricciardelli et al., 2010; Fu et al., 2013; Ivison et al., 2013; Toft et al., 2014; Toft et al., 2017; Elbaz et al., 2018; Gómez-Guijarro et al., 2018). Both scenarios have its issues however. Wet compaction predicts the presence of high-gas fractions in cSFGs that is simply not observed (Puglisi et al., 2021; Gómez-Guijarro et al., 2022a; Gómez-Guijarro et al., 2022b). Whereas, a dominance of the merger-driven starbursts (pushing them a factor of $3-4$ above the main sequence) would suggest that the galaxy simply transitions through the star-forming main-sequence on its way to becoming quiescent, making the tight correlation between the SFR and stellar masses difficult to reproduce. Although, Elbaz et al. (2018) does provide an tentative solution through a sub-population of star-bursts 'hidden' within the main-sequence.

The morphology of cSFGs could hold clues to disentangling the processes. Besides their characteristic sub-mm bright highly star-forming cores, the surrounding stellar regions can also provide valuable information, which is only possible through near-IR follow-ups of ALMA (sub-mm) detected cSFGs. In the wet compaction scenario, once the galaxy enters its peak compaction phase at $\sim 10^{9.5}\,M_{\odot}$, the stellar disk (or a 'proto-disk') stays constant or shrinks while the core rapidly builds up mass (Tacchella et al., 2016). Whereas in case of major-mergers between massive galaxies, clear signs of disturbed morphology, especially in the form of clumpy stellar structures (at least during the initial phases) is anticipated (Lotz et al., 2006; Bournaud et al., 2011; Rujopakarn et al., 2019; Calabrò et al., 2019) and extended tidal-tails (e.g., Bridge, Carlberg, and Sullivan, 2010; Wen and Zheng, 2016; Guo et al., 2016). Attempts at characterizing the stellar regions are already underway (e.g., Puglisi et al., 2021; Gómez-Guijarro et al., 2022a), with the narrative

swaying in favour of mergers (Elbaz et al., 2018; Rujopakarn et al., 2019). Nevertheless, it is imperative to determine whether this is a universal trend, especially in regions where galaxies are expected to grow under the influence of high levels of accretion, which might be more conducive for the wet compaction scenario.

Therefore, to attempt a resolution, one will have to specifically investigate high-redshift massive dark-matter halos which are expected to allow the penetration and survival of cold-gas streams into a hot halo (Kereš et al., 2005; Dekel et al., 2009). This is primarily driven by the expected evolution with halo mass ($\propto M_{DM}$) and redshift ($\propto (1+z)^{ff}$ with $\alpha \approx 2.25 - 2.50$). Studying cSFG counterparts within such accretion-rich environments is our best bet at disentangling the effects of accretion and mergers. However, observationally establishing the presence of infalling cold-gas streams in halos has proved to be extremely challenging, with only a handful of convincing cases yet (using Ly-α emission as a tracer; Martin et al., 2015; Martin et al., 2019; Umehata et al., 2019; Daddi et al., 2021a; Daddi et al., 2022b; Daddi et al., 2022a). Following up on one of these cases, we investigate the galaxy-group RO-1001 at $z = 2.91$ presented in Daddi et al. (2021a). The structure hosts three massive ($> 10^{11}\,M_\odot$) star-forming galaxies in its inner core (along with an additional quiescent galaxy; Kalita et al., 2021a), at the center of its $\sim 4 \times 10^{13}\,M_\odot$ dark-matter halo potential well. They are all < 70 kpc ($9''$) from the peak of the giant 300 kpc-wide Lyman-α halo centered on the group, and spectroscopically coincident with the intensity averaged Lyman-α emission within $\pm 500\,km\,s^{-1}$ (Fig.2.1). Finally, the Lyman-α contours provide tentative identification of accretion-streams that are expected to feed the central halo and hence the three star-forming galaxies within.

It needs to be noted that whenever we refer to accretion in this work, we are including both smooth gas as well as clumpy material. The latter is expected to make up $\sim 1/3$ of the accreted matter (Dekel et al., 2009) and its interaction with the galaxies could be observationally characterised as minor-mergers of varying mass-ratios. In this paper, we discuss the observational data in Sec. 2.2, followed by the analysis and results (Sec. 6.5). We then discuss galaxy morphology, star formation and their link to accretion in Sec. 2.4. Finally, we provide the conclusions in Sec.5.8. Throughout, we adopt a concordance ΛCDM cosmology, characterized by $\Omega_m = 0.3$, $\Omega_\Lambda = 0.7$, and $H_0 = 70$ km s^{-1}Mpc^{-1}. We use a Chabrier initial mass function. Magnitudes and colors are on the AB scale. All uncertainties on measured parameters that have been quoted indicate the 90% confidence interval determined from the limits of $\Delta\chi^2 = 2.71$. All images are oriented such that north is up and east is left.

2.2 Observational Data

To study the three star-forming galaxies (A, B and C) in RO-1001 (Fig. 2.1), we make use of *HST/WFC3* imaging in 3 bands (F160W, F125W and F606W)

over a total of 11 orbits during Cycle 27 (Proposal ID: 15190, PI: E. Daddi). The data reduction was executed using the pipeline *grizli* (https://github.com/gbrammer/grizli). The 5σ point-source sensitivities reached are 26.25 (F160W), 26.47 (F125W) and 26.39 (F606W) with a pixel scale of $0.06''$ and a half-power beam-width of $0.24''$ for F160W. Public COSMOS F814W imaging (Scoville et al., 2007) was also incorporated into the analysis. Furthermore, we used the Ks-band image from data release 4 of Ultra-VISTA (McCracken et al., 2012). Finally, IRAC 3.6 μm and 4.5 μm images were taken from the Spitzer Matching Survey of the Ultra-VISTA Deep Stripes (SMUVS; Ashby et al., 2018), while those at 5.7 μm and 7.9 μm are obtained from the public COSMOS database (Laigle et al., 2016).

New Atacama Large Millimetre Array (ALMA) band 7 observations, taken in Cycle 7 (Project ID: 2019.1.00399.S, PI: R.M. Rich) provide the sub-millimeter information of our sources. The data reduction was carried out using the Common Astronomy Software Application (CASA) and a maximum sensitivity of 28 $^{-}$Jy beam^{-1} was reached, with a synthesised beam size of $0.49'' \times 0.46''$. Finally, we utilize NOrthern Extended Millimter Array (NOEMA) spectroscopy data to map the CO$[3-2]$ transition in each of the three galaxies. The synthesized beam size at 88.3 GHz is $4.0'' \times 1.8''$. The spectra creation and analysis is carried out using a GILDAS-based pipeline (http://www.iram.fr/IRAMFR/GILDAS), and has been already discussed in a previous work (Daddi et al., 2021a).

2.3 Analysis

We use the combination of the data listed above (Sec. 2.2) to derive the properties of the three star-forming galaxies in RO-1001. Each of them show extremely compact sub-millimeter bright rotating cores primarily centered on the much more extended $(4-9\times)$ near-IR detected stellar components (Fig.2.1, right panel), with both being co-planar in at least 2/3 cases (Galaxies B and C). The stellar regions also show marked lopsidedness in their emission. We investigate in detail each of these aspects of the galaxies in this section. Given that Galaxy-B is the most extended and hence best resolved, we always begin with the description of its analysis for simplicity. We then proceed to Galaxies A and C, where the same prescription as that for Galaxy-B is used.

2.3.1 Near-IR surface brightness fitting.

We investigate the distribution of rest-frame optical emission in Galaxy-B by model-fitting (Fig. 2.2) the intensity profiles using the software GALFIT (Peng et al., 2002; Peng et al., 2010a). The H-band (F160W) image is used since it has the highest signal-to-noise among the available bands. We find that fitting and subtracting a double Sérsic profile (with indices ~ 0.5) gives the best result, assessed by the maximum fluctuations in the residual image (found to

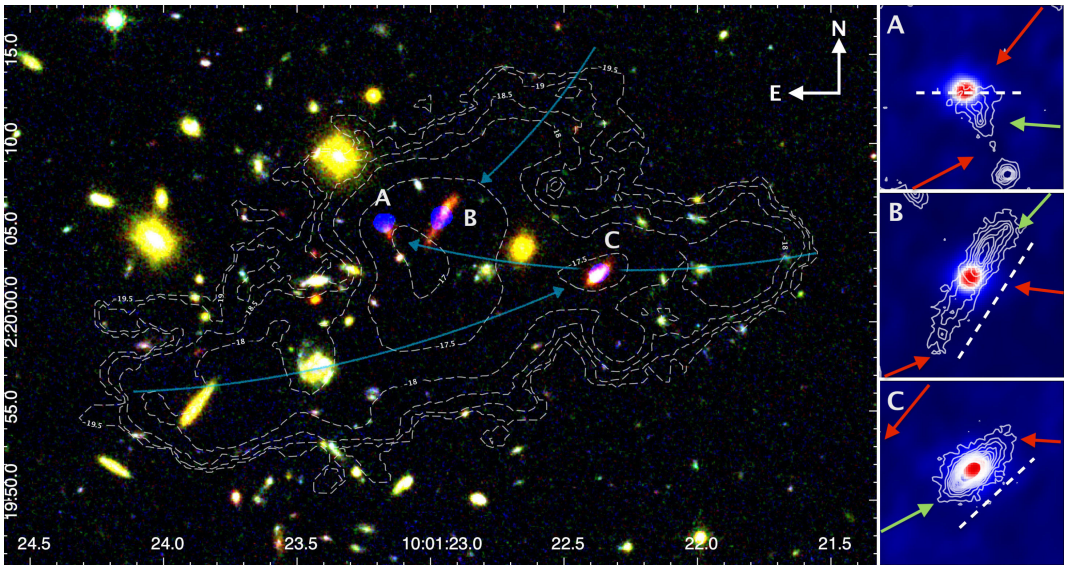

FIGURE 2.1: Location of the massive star-forming galaxies in the network of Lyman-α filaments. (Left) Color image composite of RO-1001, using observations in F160W, F125W and F606W. The ALMA data has been co-added to that in F606W since both trace star-formation, differing based on dust obscuration. The scaling of the ALMA data was done based on its flux to SFR ratio in comparison to the same for that in F606W. The white dashed contours trace the Lyman-α halo whereas the cyan arrows show the tentative directions of the three gas-accretion filaments converging onto the center of the group potential well (the correspondence to the galaxies is discussed in detail in Sec. 2.5.2). (Right) Zoom on the three star-forming galaxies (A, B and C) as seen in ALMA sub-millimeter dust-emission while the white contours trace the F160W flux tracing stellar light. The contours begin at 4σ with increments of 4σ. The arrows indicate the direction of the streams, which are shown in green if they are aligned with the major axis of the galactic disks (in dashed white lines), as discussed in Sec. 2.5.2. Those which are not, are in red. In case of Galaxy-A, we rather show the major axis of the ALMA contour with the white dashed line.

TABLE 2.1: Properties of the star-forming massive galaxies in RO-1001

ID		A	B	C
RA		10:01:23.174	10:01:22.964	10:01:22.369
DEC		02:20:05.57	02:20:05.87	02:20:02.63
$z_{\rm spec}$		2.9214	2.9156	2.9064
$\log \mathrm{M}_\star$ (1)	$\mathrm{M}_\odot$	$11.50^{+0.15}_{-0.19}$	$11.20^{+0.07}_{-0.14}$	$11.26^{+0.14}_{-0.10}$
S_ν(870 μm)	mJy	4.44 ± 0.05	8.69 ± 0.03	4.04 ± 0.11
SFR_{core} (2)	$\mathrm{M}_\odot\ \mathrm{yr}^{-1}$	345 ± 55	674 ± 106	313 ± 50
SFR_{disk_ALMA} (2)	$\mathrm{M}_\odot\ \mathrm{yr}^{-1}$	$< 60^{**}$	$< 19^{**}$	$< 43^{**}$
SFR_{disk_SED} (1)	$\mathrm{M}_\odot\ \mathrm{yr}^{-1}$	66^{+446}_{-49} (3)	42^{+51}_{-37}	94^{+66}_{-94}
t_{50} (1)	Gyr	$1.7^{+0.3}_{-0.7}$	$0.5^{+0.7}_{-0.2}$	$0.2^{+1.3}_{-0.1}$
r_{e_disk}	kpc	3 ± 1	9 ± 2	4 ± 1
$\mathrm{r}_{disk}/\mathrm{r}_{core}$		4 ± 1	9 ± 2	5 ± 1
$\log \mathrm{M}_{mol}$	$\mathrm{M}_\odot$	9.8	10.7	10.6
$\mathrm{FWZV}_{\mathrm{CO[3-2]}}$ (4)	$\mathrm{km\ s}^{-1}$	381	1114	1098
$\log \mathrm{M}_{dyn,tot}$ (5)	$\mathrm{M}_\odot$	10.4	11.1	11.2
A_v		$1.8^{2.1}_{1.3}$	$1.0^{1.2}_{0.4}$	$1.6^{1.8}_{0.4}$

Notes: (1) Estimated from the composite-τ model fitting to optical and near-IR photometry and therefore primarily associated with the disks (2) Derived from the 870μm flux of individual galaxies assuming the same SED shape as for their coaddition (Daddi et al., 2021a). (3) This high upper-limit from the composite-τ model is in agreement with a constant star formation model being within 90% confidence interval (4) Full Width at Zero Velocity as previously reported (Daddi et al., 2021a). (5) Dynamical mass primarily associated with the core, rather than the whole galaxy as described in the main text. ** 3σ upper-limits.

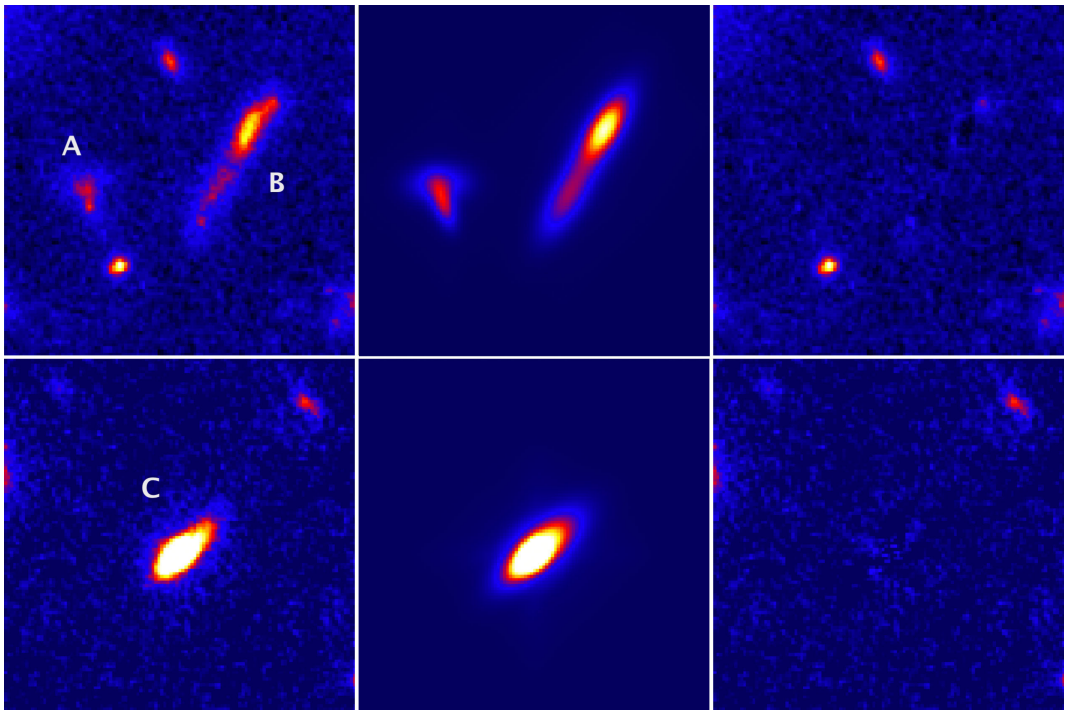

FIGURE 2.2: (Left panel) The HST F160W cutouts of Galaxies-A and B (top) and Galaxy-C (bottom) used for the morphological model fitting. (Middle and right panels) The GALFIT returned models and residuals of the same cutouts. In the latter, only the RO-1001 galaxy models have been subtracted. The rest of the sources, although used during the fit, have been left in the image.

be $< 1\sigma$). Care is taken to simultaneously subtract all nearby sources within $\sim 8''$. We also fit the same profile, convolved with the appropriate point-source-functions (PSFs), to the images in all other observed wavelength windows to ascertain consistency. We find no $> 1\sigma$ fluctuations in the respective residual images. We find that the two Sérsic profiles for Galaxy-B are clearly not spatially coincident with the sub-millimeter bright compact core (discussed below in Sec. 2.3.2), but rather fall $\sim 0.8''$ on either side of it (and hence with a spatial separation of $\sim 0.16''$ between the two Sérsic profile centres). We also find remarkable consistency of the axes ratio and position angles of the two Sérsic profiles, hence likely part of a continuous stellar structure. We repeat this procedure for Galaxies A and C. Galaxy-A is found to have a complex morphology which is fit with a double Sérsic in differing (almost orthogonal) orientations. Galaxy-C on the other hand is found to resemble Galaxy-B in terms of an accordance with two co-aligned Sérsic profiles with low indices (< 1) on either side of sub-millimeter core. But in this case the separation is $\sim 0.2''$, making it more compact than Galaxy-B.

To measure integrated effective radii (r_e) of each of the galaxies, we did an additional round of fitting using single Sérsic profiles. Besides using

TABLE 2.2: Derived morphological Spergel parameters in sub-millimeter

ID		A	B	C
effective radius$^{**}_{major}$	arcsec	0.092 ± 0.004	0.148 ± 0.002	0.122 ± 0.054
	kpc	0.72 ± 0.02	1.15 ± 0.01	0.95 ± 0.42
Ellipticity		0.62 ± 0.03	0.40 ± 0.01	0.47 ± 0.22
Position angle	degrees	-90.6 ± 0.6	-27.4 ± 0.3	-46.4 ± 0.6
Δangle$_{disk,bulge}$ (1)	degrees	–	3.4 ± 1.5	2.9 ± 1.5
Spergel index (2)		-0.6 ± 0.2	0.5 ± 0.3	-0.5 ± 0.3

Notes: (1) The difference between position angles of the stellar disk in HST F160W and that of the sub-millimeter core. The lack of a value in case of Galaxy-A is due to its stellar emission having a complex morphology without a clear position angle for the whole galaxy. (2) Spergel index values 0.5 and -0.6 correspond to Sérsic indices 1 and 4 respectively. $^{**} \sim$ effective radius of the corresponding Sérsic profile, as has been determined through modelling Sérsic and Spergel profiles (Tan et al. in prep.)

the generic version of the Sérsic profile, we also invoke the m $= 1$ Fourier component to account for the lopsidedness of the stellar components. This is due to quantify the emission asymmetry we observe in each of the cases which is later discussed in Sec. 2.5.1. We also measure growth curves using circular apertures with their centers fixed at the ALMA core of the galaxies to independently determine the effective radius. For Galaxy-A, we only use the northern component of its complex near-IR double emission, which we determine as the primary stellar region due to its proximity to the sub-mm emission. We use the average of all three methods that are consistent within $15 - 20\%$, to obtain the final measurements reported in Table 2.1: 3 ± 1 kpc, 9 ± 2 kpc and 4 ± 1 kpc for Galaxies-A, B and C respectively. It is noteworthy that for each galaxy, the single profiles are characterised by Sérsic indices < 1, indicating disk-like morphology (and hence we refer to them as disks throughout this work, a conclusion which will be reinforced in Sec. 2.4.2). The ellipticities measured for the three galaxies are $0.5 \pm 0.1, 0.15 \pm 0.05$ and 0.5 ± 0.2 (A, B and C), indicating an almost edge-on orientation for Galaxy-B.

2.3.2 Sub-millimeter emission analysis

The compact highly star-forming regions of the galaxies are detected thanks to their dust emission using ALMA at 870 μm. It is noteworthy that due to a well characterised PSF and high signal-to-noise, we have the ability to map structures much smaller than the integrated ALMA PSF (Rujopakarn et al., 2019). We begin with a detailed morphological analysis of the emission region in Galaxy-B. Due to the data being distributed over multiple partially

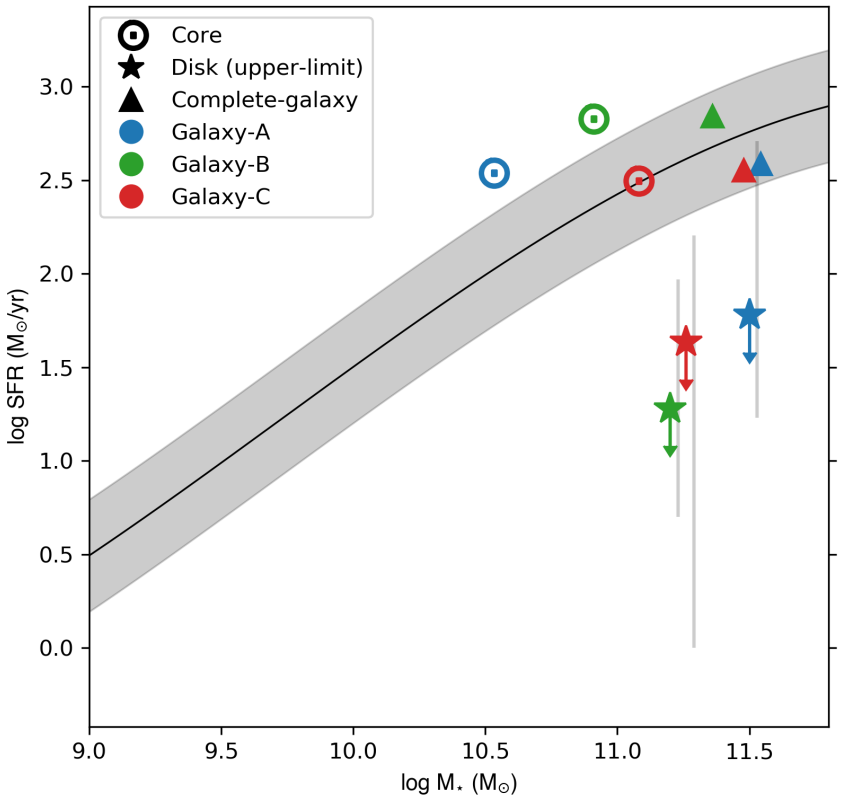

FIGURE 2.3: Components of the three galaxies on the star-forming main-sequence: star-bursting bulges and quiescent disks. The SFR vs stellar-mass values of the star-bursting core, the quiescent stellar disk and the combination of the two placed with respect to the star-forming main-sequence (Schreiber et al., 2015) at z = 3, shown as the black solid line. The shaded region demarcates the 0.3 dex uncertainty in the relation. We use the 3σ ALMA upper-limits as the value for SFR with the associated grey error-bars showing the range allowed by our SED model fitting.The latter have been artificially offset in the x-axis to emphasize the difference in the method of measurement.

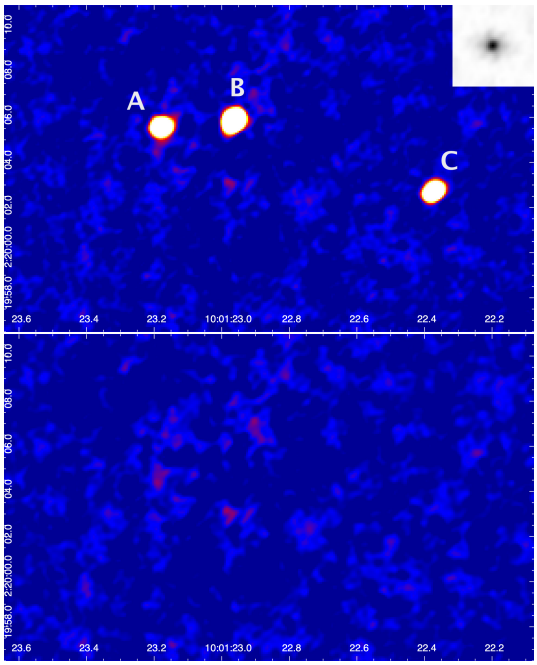

FIGURE 2.4: The top panel shows the ALMA 870 μm image of the core of RO-1001 with the three star-forming galaxies clearly visible. Each of them were fit with intensity profiles which were then subtracted to obtain the residual image displayed in the bottom panel. The ALMA PSF at 870 μm is shown in the inset on the top right.

overlapping pointings, we combine the ones with Galaxy-B within their primary beam. To do so, we follow the procedure outlined in Gómez-Guijarro et al. (2022a), for combination and stacking of individual pointings in ALMA. We phase shift each of them to set the source coordinates at their respective phase center. Finally, the pointings are combined into a single measurement set which provides the maximum sensitivity available with our data.

Since the Sérsic profile, commonly used to study galaxy morphologies, cannot be easily extended to the UV space due to its Fourier transform not being analytically expressible, we use a substitute. We exploit the Spergel profile (Spergel, 2010), recently incorporated within the MAPPING procedure of GILDAS. This has been found to correlate well with the Sérsic profile allowing us to extract Sérsic parameters corresponding to the Spergel parameters we determine. To also determine the robustness of the fitting procedure (Fig. 2.4; Table. 2.2), we perturb the initial parameters within a factor of 5 over a total of $\sim$ 200 times and repeat the fitting. We also artificially inject 1000 times the best fitting model of each galaxy at different empty locations (one at a time) and fit them individually to estimate reliable error for our measurements based on the a-posteriori dispersion of resulting parameters. This procedure also shows that there are no detectable systematic biases in the measured quantities.

For Galaxy-B, we obtain an almost-perfect exponential profile characteristic of a disk of effective radius ~ 1.1 kpc, with a Spergel index of 0.55 ± 0.12 (Sérsic index ~ 1) and an ellipticity of 0.40 ± 0.01. From the model hence returned, we measure the 870 μm observed-frame flux. This is converted to a total-infrared luminosity (L_{IR}; $8 - 1000\,\mu$m) using the integrated SED from the co-added photometry of RO-1001 (Daddi et al., 2021a). This can then be converted to a SFR of $674 \pm 106\,M_\odot\,yr^{-1}$ using the widely adopted conversion relation (Kennicutt, 1998; Daddi et al., 2010a):

$$SFR_{IR}[M_\odot\,yr^{-1}] = 1.0 \times 10^{-10}\,L_{IR}[L_\odot] \tag{2.1}$$

The error for this measurement is determined from the 1σ dispersion in the dust-temperature dependent parameter $< U >$, that is usually invoked during the conversion of the 870 μm flux to L_{IR}. We use this to account for variations in dust temperature of individual galaxies with respect to the average value. This approach of evaluating SFR uncertainties is over-conservative, as it does not take into account that the integrated bolometric IR luminosity (hence SFR) of the 3 galaxies that is known to better than 10% accuracy, given the well sampled IR SED including Herschel (Daddi et al., 2021a).

In Galaxy-A, we obtain a much different Spergel index (-0.61 ± 0.04) that translates to a Sérsic index ~ 4. The situation is similar in Galaxy-C with a Spergel index of -0.48 ± 0.12, although it has an additional point source adjacent to it (at $0.14''$). The sizes of these profiles are very compact with effective radii ~ 0.7 kpc and 0.9 kpc. We measure the SFR using the same prescription as that for Galaxy-B, and estimate values of $345 \pm 55\,M_\odot\,yr^{-1}$ and $313 \pm 50\,M_\odot\,yr^{-1}$ for Galaxies A and C respectively.

2.3.3 Determining the quiescence of the stellar regions

Besides the measurements for the sub-mm bright compact cores, the high resolution 870 μm map (Sec. 2.2) also provides us with constraints on the levels of star formation in the surrounding regions. We are mainly interested in the estimates for the extended stellar regions detected in near-IR, that lack any sub-mm emission. Using the H-band models as fixed priors, we measure 3σ upper-limits for each of the galaxies by simultaneously fitting them along with the primary profiles for the cores in the ALMA data (uv plane). For Galaxy-B, we estimate a 3σ flux upper-limit of 0.25 mJy (corresponding to an SFR upper-limit of $19\,M_\odot\,yr^{-1}$) for the stellar disk, while we obtain 0.77 mJy and 0.55 mJy ($60\,M_\odot\,yr^{-1}$ and $43\,M_\odot\,yr^{-1}$) for galaxies A and C respectively. This provides clear evidence of almost all star formation being concentrated at the core leaving the massive stellar disks devoid of it and well below the star-forming main-sequence (Fig. 2.3).

We note that the estimation of the star formation upper limits in the stellar disks should be considered as overly conservative. This is because the conversion to SFR is done based on the average IR SED in the group

which is driven by the co-addition of the emission from all three sub-mm bright galactic cores in RO-1001 that have a much higher SFR surface density (Σ_{SFR}; e.g., see Fig. 2.8). Hence, the dust temperature in the disks would likely be lower due to a softer radiation field (based on the star-formation surface density vs. dust temperature relation, Valentino et al., 2020a, see also), which would in turn drive our 3σ upper-limit even lower, probably at least by factors of 2–3.

2.3.4 Star formation history modelling

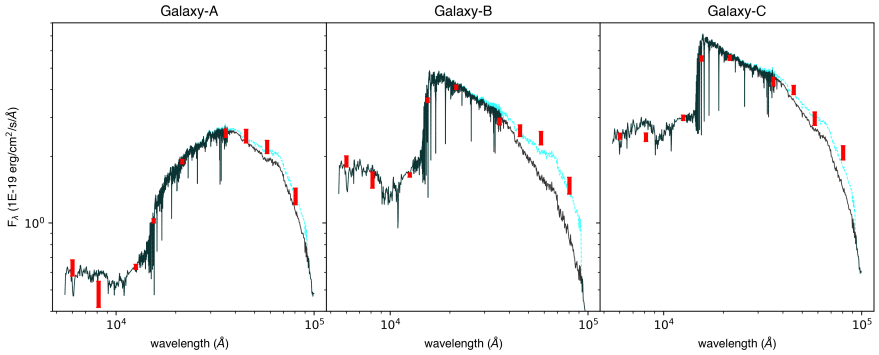

FIGURE 2.5: The best-fit SED models in optical and near-IR for each of the three star-forming galaxies in RO-1001. The photometry with their respective errorbars are shown in red. The cyan contours show a modified SED with an addition of an example 0.1 Gyr old highly obscured ($A_V = 6.5 - 7.5$) constant star-formation history SED in each case. In each case, the resulting stellar-masses are in agreement with our CO$[3-2]$ estimates within 0.1 dex and are hence a representation of contributions of the star-bursting cores.

We make use of the photometry obtained in observed frame optical and near-IR, to estimate a star formation history (SFH) and thereby the age of the stellar population as well as stellar masses. The measurements can primarily be attributed to the stellar disks since the prodigious sub-millimeter flux from the cores is by design at the expense of UV rest-frame flux. However, during our fitting procedure, we do fix an additional core component in each case using positional priors obtained in Sec. 2.3.2. Except in the IRAC bands, all others return fluxes $< 5\%$ of the total galaxy flux. However for IRAC, the PSF is a factor ~ 10 larger than that of HST and a factor ~ 5 compared to Ultra-VISTA. Hence in this case, the sources are unresolved and this leads to the photometry corresponding to the integration over the whole galaxy. Albeit, in each of the cases the stellar mass within the core is expected to be $< 10\%$ (based on estimates discussed in Sec. 2.3.5) that ensures a minimal contribution. Nevertheless, Fig. 2.5 does suggest progressively higher fluxes in the IRAC bands, leading to offsets from SED models. To limit

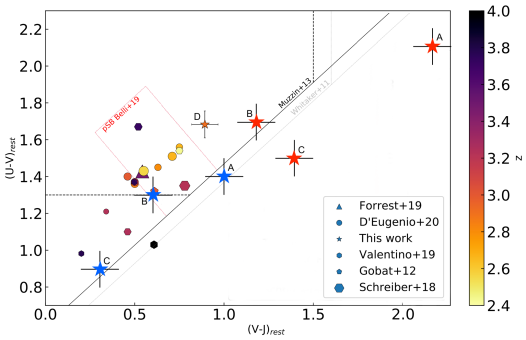

FIGURE 2.6: The UVJ colors of high-z QGs ($z > 2.5$) adapted from D'Eugenio et al. (2020b). The post-star burst region is demarcated with the red box as specified in Belli, Newman, and Ellis (2019). The marker sizes are proportional to the stellar mass. The red and blue stars are the dust uncorrected and corrected measurements of the quiescent stellar disks in the three star-forming galaxies within our sample. The final star in orange marks the location of Galaxy-D, a quiescent galaxy photometrically confirmed to be part of RO-1001 (Kalita et al., 2021a)

the influence of the rapidly star-forming core, primarily in the IRAC bands with insufficient resolution to disentangle the core from the disk, we execute the SED fitting in three stages. The first is done using photometry up to the bands where the galaxies are well-resolved (2.1μm). We then include the remaining 4 bands in pairs of two. We find that the results from the first two stages are almost identical within their errors and hence use the results of the second stage (up to the 4.5μm band; due to better constraints). We show in Fig. 2.5 that the net photometry at the third stage is reproducible using the SED derived at stage-two and an additional highly obscured component for the core.

For a description of the SED model fitting, we refer the readers to Appendix 2.8. The procedure for Galaxy-B returns the lowest reduced χ^2 of 2.0 for the two declining SFH models used (composite-τ and delayed-τ). In case of a constant star-formation model this value is found to be 6.8 that translates to a $\Delta\chi^2 = 38$, making it highly unlikely. Hence, this indicates that the disk in Galaxy-B is undergoing a decline in star-formation, as already conclusively demonstrated by the ALMA upper limts. We also determine this decline to be significant by measuring the age/τ ratio from the delayed-τ models and it is found to be 7 ± 1. Given that the composite-τ models are relatively more robust, we use them to measure the look-back time of half-mass formation ($t_{50} = 0.5^{+0.7}_{-0.2}$ Gyr), that can be considered to be the approximate epoch at which the last major star formation episode had occurred. However, the results from delayed-τ models are also in agreement. Furthermore, we obtain a SFR estimate of $42^{+51}_{-37}\,M_\odot\,yr^{-1}$, consistent with the ALMA 3σ upper-limit.

The picture is slightly less strict in Galaxy-C followed by Galaxy-A. In

the former, the declining models still give the best fit (reduced-$\chi^2 = 1.9$) and a $t_{50} = 0.2^{+1.3}_{-0.1}$ Gyr. But the constant star formation model is relatively less unlikely than for Galaxy-B, with a reduced-χ^2 of 3.7. Galaxy-A on the other hand has values of 0.8 and 1.1 for almost equally plausible declining and constant star formation models, allowing for possible ongoing star formation in the disk. Nevertheless, the SFR in both these cases ($94^{+66}_{-94}\,M_\odot\,yr^{-1}$ for Galaxy-A and $66^{+446}_{-49}\,M_\odot\,yr^{-1}$ for Galaxy-C) are still in general agreement with the much more stringent ALMA 3σ upper-limit.

We also derive UVJ colors (Fig. 2.6) not so much to ascertain quiescence that is already unambiguously demonstrated by ALMA, but rather to compare them to more classical exemples of high redshift quiescent galaxies. Of special interest are the widely studied post-starburst (PSB) galaxies that have experienced quenching of star-formation over the last < 0.8 Gyr and generally show low dust attenuation (Gobat et al., 2012; Schreiber et al., 2018b; Forrest et al., 2020b; D'Eugenio et al., 2020b; Forrest et al., 2020b; Valentino et al., 2020b). The PSB ages are potentially similar to the mass-weighted ages derived for our sample, while attenuation in our case is larger (Table. 2.1). We find that the observed UVJ colors of our quiescent disks are much redder than those of known population of quiescent systems at $z \sim 3$. Also, at least in two cases they are scattered just outside of the formal UVJ-passive boundary. However, when correcting for dust reddening the colors of the three galaxies in RO-1001 more closely resemble those of PSBs as well as of the massive quiescent galaxy with a mass-weighted age > 1 Gyr (Kalita et al., 2021a) within the same group (Fig. 2.6).

Finally for Galaxy-B, we pay special attention to the spatial decomposition of the stellar mass estimates (listed in Table. 2.1) derived from the SED fitting procedure – by obtaining separate photometry of the northern and southern sections of its elongated disk. This is to quantify the lopsidedness in the stellar structure. We hence find the total stellar mass of $1.6 \pm 0.4 \times 10^{11}\,M_\odot$ for the complete stellar region is divided into $1.1 \times 10^{11}\,M_\odot$ and $0.5 \times 10^{11}\,M_\odot$ for the northern and southern segments. It is noteworthy that for this analysis, we only use observations up to the 2.1 μm band beyond which the resolution is too low to spatially disentangle the two parts.

2.3.5 Rotating gas traced by CO[3 − 2] transition.

A direct spectroscopic tracer of the gas content of the galaxies is available in the form of NOEMA CO[3 − 2] transition observations. For Galaxy-B, we use its integrated luminosity ($\log(L'_{CO(3-2)}/(K\,km^{-1}pc^2)) = 10.46$) to estimate a gas mass. This is calculated from the line flux (Daddi et al., 2021a) using the relation prescribed in a recent work (Silverman et al., 2018). Using a standard R31 = 0.5 (Daddi et al. 2015; Valentino et al. 2020; Boogardt et al. 2020), we hence derive $\log(L'_{CO(1-0)}) = 10.76$. The gas mass is finally computed as $M_{mol} = \alpha_{CO} \times L'_{CO(1-0)}$ by adopting a conversion factor $\alpha_{CO} =$

$0.8\,M_\odot(K\,kms^{-1}pc^2)^{-1}$ as expected in starbursts (given location of the cores, with respect to the star-forming main-sequence in Fig. 2.3, and their very high SFR surface densities). This provides values of $4.6\times10^{10}\,M_\odot$, $0.7\times10^{10}\,M_\odot$, $4.2\times10^{10}\,M_\odot$ for Galaxy-B, A and C respectively. Although, we do acknowledge that this estimate is dependent on our choice of conversion factors. Nevertheless, we can place a strict upper-limit on the gas mass using the dynamical mass estimates calculated below (i.e., in the limiting case in which there was no stellar mass nor dark matter in the cores), which is less than $2\times$ above the current values in each case. A Milky-Way-like α_{CO} would have resulted in a factor of 5 higher gas-mass. Hence, these are in direct conflict with the dynamical mass values. Moreover, any increase in gas-mass would also indicate almost a negligible stellar mass, which in turn would place the galaxy-cores at a much higher offset from the star-forming main-sequence. This would suggest even more star-burst-like characteristics.

The width of the emission line in Galaxy-B is used to determine the dynamical mass within the dusty core where the gas is expected to be confined. Given the sub-millimeter emission profile of the core is found to resemble a disk, we measure the M_{dyn,r_e} within the effective radius r_e using the following relation (Daddi et al., 2010b):

$$M_{dyn,r_e} = 1.3\times\frac{r_e\times\left(FWZV_{CO[3-2]}/2\right)^2}{G\sin^2 i}\pm12.5\% \tag{2.2}$$

The effective radius returned from the sub-millimeter emission profile is used in this equation. The width of the line, quantified by the parameter $FWZV_{CO[3-2]}$ is already reported in Table. 2.1, while the inclination angle (i) is determined based on the ellipticity of the sub-millimeter profile. Subsequently, we measure the total dynamical mass, $M_{dyn,tot} = 2\times M_{dyn,r_e} = 1.3\pm0.1\times10^{11}\,M_\odot$. The factor of 2 in invoked since only half of the mass is contained within r_e. We use the same procedure to obtain $M_{dyn,tot} = 2.6\pm0.3\times10^{10}\,M_\odot$ and $1.7\pm0.2\times10^{11}\,M_\odot$ for Galaxies A and C. However, given their cores have morphology closer to a Sérsic index of 4, we re-estimate the $M_{dyn,tot}$ using the following formula applicable to an elliptical galaxy dominated by random motion.

$$M_{dyn,r_e}\approx5.0\,\frac{r_e\,\text{œ}_e^2}{G} \tag{2.3}$$

We measure the total dynamical masses of $\sim2.2\times10^{10}\,M_\odot$ and $2.4\times10^{11}\,M_\odot$ for Galaxies A and C respectively, reasonably consistent with our earlier estimates. Although the relatively high discrepancy in case of Galaxy-C likely points to the rotational-dominance expected in a gas-rich structure. Nevertheless, we do not expect the structures to fully conform to such a dynamical arrangement due to the inherent dissipative nature of gas within them.

Finally, two separate continuum images are created for Galaxies B and C, by dividing the whole spectral range into two segments that are separated by the average location of the CO$[3-2]$ emission of the whole galaxy. The offset between the peaks trace the plane of rotation, which are found to be in agreement with the major axes of the respective galaxies in both sub-millimeter and near-IR (Fig. 2.7). A similar analysis is not possible for Galaxy-A due to a low signal-to-noise of the CO$[3-2]$ detection.

2.4 Results

2.4.1 Compact star-forming cores in extended quiescent stellar disks

The spatial decomposition of surface-brightness profiles of the galaxies reveals extremely compact sub-millimeter bright rotating cores and extended near-IR detected co-planar stellar disks showing varying levels of lopsidedness (Fig.2.1, right panel). The size contrast is evident from the high near-IR to sub-mm radius ratios: $\sim$ 5–8 for Galaxy-B, while in case of Galaxy-A and C it is 4 ± 1 and 5 ± 1. Majority of the star formation is concentrated in the cores, with the IR-based SFR in the cores being a factor of $6-36\times$ higher than the $3\,\sigma$ upper-limits in the disks. The mass concentrations also displays this dichotomy between the cores and the stellar components. Using the difference between the CO$[3-2]$ derived dynamical masses and the gas masses, we obtain approximate stellar masses of the cores for each galaxy ($\approx 2\times10^{10}\,\mathrm{M}_\odot, 8\times10^{10}\,\mathrm{M}_\odot$ and $12\times10^{10}\,\mathrm{M}_\odot$). These are concentrated within the areas $> 60\times$ compact than the extended stellar regions that feature stellar masses of $3.2\pm1.3\times10^{11}\,\mathrm{M}_\odot$, $1.6\pm0.4\times10^{11}\,\mathrm{M}_\odot$ and $1.8\pm0.5\times10^{11}\,\mathrm{M}_\odot$.

2.4.2 Morphological characterisation

The single-peaked profiles point to these galaxies consisting of singular (albeit, lopsided) disks with central cores. This is corroborated by the single Sérsic profile fits (with indices $\lesssim 1$; Sec. 2.3.1) to their near-IR surface-brightness profiles. About $10-40\%$ of the stellar mass is concentrated in the cores occupying $< 1\%$ of the surface area of the whole galaxy. This is illustrated in Fig.2.8 for Galaxy-B, the most extended of the three galaxies. We find comparable contrasts in the other two galaxies (based on their near-IR to sub-mm ratio, Table 2.1). Hence, the cores of these galaxies are likely forming the future stellar bulges. This is characterised by their nuclear location, masses, the extreme compactness similar to $z\sim$ 2–3 passive galaxies (Daddi et al., 2005), and their sub-millimeter surface brightness profiles with Sérsic index $\sim$ 4 for Galaxies-A and C, which is relatively unusual (Barro et al., 2016; Martig and Bournaud, 2008, indicate that the indices should be closer to that

for a disk). Galaxy-B although has an index ~ 1, but the higher ellipticity of the core (0.40 ± 0.01) in comparison to the disk (0.15 ± 0.05) still supports the idea of bulge formation.

For Galaxies B and C, we do not expect their stellar disks to have been perturbed by major-mergers involving equal-mass galaxies (with ratios 1:1 to $\sim$1:3), which have been studied in multiple simulations over the years (e.g., Bendo and Barnes, 2000; Bournaud, Jog, and Combes, 2005; Nevin et al., 2019). Firstly, we conclude a lack of any visible disturbance in the disks from our well resolved and high signal-to-noise HST imaging (Fig. 2.1, right). Had these undergone major-mergers, they would have had to consist of two perfectly aligned disks at a very early stage of collision (pre-coalescence), the probability of which is 0.1% and 0.4% for Galaxies B and C respectively based on the probability of the specific geometrical orientation (having uncertainties equal to the thickness of the disks). Coupled with the concurrence of both these galaxies are detected in the same exact scenario, the probability reduces to a negligible 0.04%. Moreover, the temporal aspect also makes such a scenario even more unlikely – given that both Galaxy-B and C are detected in the same situation within the observation window. Furthermore, had a major-merger been the case, one would have detected a bi-modality in the mass distribution associated with each participating galaxy rather than a centrally peaked profile, especially seen in Galaxy-B (Fig.2.8). An alternate scenario would have been the near-IR detected stellar disk and the sub-millimeter core are actually two separate galaxies. However, we also reject such a scenario due to the sub-millimeter bright segment being perfectly at the geometric center of the stellar emission region in not one but two separate cases within the same group. In Galaxy-A, with its disturbed stellar morphology however, the situation is different from its neighbors. As discussed earlier, the stellar emission can be decomposed into two almost perpendicular orientations. We observe that one of the two (the northern component) is better coinciding with the compact ALMA core, similar to that in Galaxies B and C. We therefore identify it as the primary stellar disk of Galaxy-A. The additional component is likely an in-falling equal-mass galaxy.

In at least two of the galaxies (B and C), the major axes of both the core and the disk are aligned within $\sim 3^{\circ}$, as well as with the major axis implied by the rotational patterns of the gas in the respective cores, determined from the CO$[3-2]$ emission (Fig. 2.7). This is dependent on a reasonable assumption that the gas is confined within the same area as the dust. Hence, we conclude that these two galaxies have co-planar (and possibly co-rotating) stellar-disks and compact cores. The current data does not allow us to measure the major axis direction of the rotational pattern, or the severely lopsided stellar disk (by a factor > 3, towards South) of Galaxy-A. For the latter, we are likely observing only the 'heavier' part of the disk and hence the disk size and shape parameters cannot be satisfactorily determined. For Galaxy C, the ellipticities of the core and the stellar component are found to be in

agreement (within 0.1). But in Galaxy-B, where the stellar component is observed edge-on (with an ellipticity of 0.15 ± 0.05), the core has a larger ellipticity (0.40 ± 0.01). However, it should be noted that all the three cores have values within $0.4 - 0.6$.

2.4.3 Young cores within older disks.

For the three cores, we find short gas-consumption timescales of 20 Myr, 70 Myr and 130 Myr and time taken to build the stellar masses, assuming constant rates of star-formation, $\sim$ 60 Myr, 120 Myr and 400 Myr. However, the short timescales $\sim$ 100 Myr for three such neighbouring objects makes them statistically unlikely to be simultaneously observed. Hence we propose that the extreme star formation levels is rather the culmination of an increase over a larger period of time. The rate and the beginning of this increase cannot be ascertained. Nevertheless, these are still similar or smaller compared to the time scales characterising the decline in star-formation of the stellar components, based on the goodness-of-fit from the best-fit SED composite τ-models(Schreiber et al., 2018b): the look-back times to the epoch of half-mass formation (t_{50}) are $1.7^{+0.3}_{-0.7}$ Gyr, $0.5^{+0.7}_{-0.2}$ Gyr and $0.2^{+1.3}_{-0.1}$ Gyr for Galaxies A, B and C. Hence, the star-bursting cores only started getting built after the disks had already formed about half of their stellar mass and were past their last major episode of star-formation.

2.5 Discussion

In this section, we revisit the key observational results and discuss how their interplay leads to a coherent picture of the evolution of the three star-forming galaxies in RO-1001. Each of them feature extended stellar disks that are lopsided and quiescent, along with highly star-forming compact cores within them.

2.5.1 Lopsidedness and quiescence of the disks

We first begin with the severe lopsidedness of the stellar disks (Fig. 2.1, right panel). For Galaxy-B, the asymmetry in the stellar emission (of a factor of 2.0 in F160W/*HST*) manifests as a mass lopsidedness of 2.2 (Sec. 2.3.4) along the major-axis (Fig. 2.9). In Galaxy-C, the emission asymmetry, also along the major axis, is 1.6. The current data does not allow us to measure the major axis direction of the stellar disk of Galaxy-A, but only the lopsidedness upper limit (> 3) and direction (South), that is nearly perpendicular to the East-West ALMA core major axis (Fig. 2.9). Such asymmetries, not yet recognised at high redshifts, are in fact a common characteristic among spiral galaxies in the local Universe (Sancisi et al., 2008; Rix and Zaritsky, 1995; Zaritsky and Rix, 1997; Reichard et al., 2008), although relatively less

pronounced. Since lopsidedness is usually contributed to tidal interactions and in-situ star-formation asymmetry (Sancisi et al., 2008), we attribute the strong lopsidedness in our sample to the accretion of material onto the galaxies, i.e. asymmetric gas-accretion (Bournaud et al., 2005) (that is reflected by stellar-mass distribution hence created) and/or the tidal interaction (or 'minor-mergers') with in-falling satellite sub-halos (Zaritsky and Rix, 1997; Kazantzidis et al., 2008; Kazantzidis et al., 2009), that may also include their assimilation into the primary galaxy halo. These 'less-severe' interactions (with mass-ratios from 1:4 or lower) are expected to preserve the stellar disks (Bournaud et al., 2005; Hopkins et al., 2009). Only in Galaxy-A, can we also associate the imminent major-merger to also be playing a role.

Meanwhile, the quiescence of the stellar disks (albeit possibly not entirely passive), is the first indication of the presence of an apparent 'outside-in' quenching mode in high-redshift massive galaxy populations, in contradiction to the classic 'inside-out' configuration (Lang et al., 2014; Tacchella et al., 2015; Breda and Papaderos, 2018). We consider various possible modes of quenching. Since we observe the galaxies to be undergoing an outside-in quenching, this could not have primarily occurred due to feedback from active galactic nuclei (AGN; Alatalo et al. 2015), known to quench galaxies inside-out (Tacchella et al., 2018). We also find no evidence of AGN activity from X-ray observations (Daddi et al., 2021a), although a radio excess in Galaxy-C is indicative of weak past AGN activity in that galaxy. The process of morphological quenching (Martig et al., 2009), where the formation of a stellar bulge stabilises the disk against further star-formation, is also improbable. The galaxies are far from being bulge-dominated, essential for this mode of quenching to be applicable, based on their stellar mass distributions. Also unlikely is cosmological starvation (Feldmann and Mayer, 2015) since the availability of gas has already been established in RO-1001. Finally, ram-pressure stripping (RPS; Gunn and Gott, 1972) could be regarded as a possible contributor as it is known to remove gas from external regions of galaxies (Bravo-Alfaro et al., 2000; Vollmer et al., 2001; Fumagalli et al., 2009; Boselli et al., 2014; Loni et al., 2021), therefore resulting in an apparent outside-in quenching (for a review, Boselli, Fossati, and Sun, 2021). It could also lead to compression of the gas in the galaxy which could result in the lopsidedness (although the stellar morphology would not be affected). However, as shown in Appendix 2.8, a conservative lower-limit of the radius up to which RPS can remove gas from the sample in RO-1001 would be $10 - 15$ kpc. This is more than an order of magnitude higher than the kpc-scale cores beyond which the galaxies have suppressed star-formation. Hence we do not expect RPS to be playing a major role.

The only possible scenarios capable of self-sufficiently explaining the observed suppression of star-formation are found to be connected to the aforementioned heavy lopsidedness in the disks. Introduction of such asymmetry, in a differentially rotating disk-like structure induces loss of angular momentum, causing mass to rapidly fall into the central regions (Combes

and Gerin, 1985). This process can be characterised as the triggering of the m = 2 Fourier component, denoting a bar, by the m = 1 component that refers to the asymmetry or lopsidedness (Bournaud et al., 2005), observed in our sample. Bars have already been found to efficiently suppress star-formation up to factors of ~ 10 in the disk (Khoperskov et al., 2018), while driving gas into the core (Carles et al., 2016), albeit on less spectacular scales than what observed here. This could be a possible case of an early-phase bar-formation, which are usually scarce at high redshifts (e.g., Sheth et al., 2008). However, the resolution and sensitivity is not sufficient to confirm it. The accreted clumpy material driving the lopsidedness is also expected to feed the star-forming core, and in the process leading to a stabilization of the disk (Dekel, Sari, and Ceverino, 2009). Therefore the same outside-in quenching can be expected in all scenarios involving lopsidedness and compact star formation.

Moreover, the expected damping time of the lopsidedness is comparable to the Hubble time (Jog and Combes, 2009), explaining their detection throughout our sample and allowing them to act as catalysts of bulge formation under the high redshift accretion conditions. This timescale is not however associated with the gas being funneled into the core, but rather the survival of the asymmetry that drives this process. We propose that accreted material is resulting in the compact star-forming cores within outside-in quenching disks, either directly (mergers) and/or indirectly (lopsidedness funneling gas to the core). The accretion may vary from smooth dust (hence presumably gas) components, to sub-halo stellar 'clumps', as in Galaxies B and C (while preserving the disks in the process), or additional massive stellar structures, observed in Galaxy-A.

2.5.2 Determining the direction of accretion

Due to the confluence of evidence for influence of accretion on the galaxies, we try to discuss possible tracers of this process. In an accreting galaxy, the lopsided part of the disks would be expected to mark the location of impact for the accreted material. Corroborative evidence can be found in our sample when the models of the primary disks in the F160W image and the sub-millimeter bright cores in the ALMA image are subtracted. Residual emission (stars in near-IR emission and dust in sub-mm) is clearly detected in each case (Fig. 2.9). In Galaxy-A, its F160W and the associated ALMA residuals demonstrate the presence of the similarly-massive companion merging into the disk. For Galaxies-B and C, their respective F160W residuals are much fainter (by ~ 3 orders of magnitude) and are likely in-flowing small-mass 'clumps' within or adjacent to the disks.

These are found to be preferentially located in the direction of the lopsidedness of the stellar-disks. We hence suggest that these indicators could be tracing the mass inflow into the core.

2.6 A generalized picture accretion-driven galaxy evolution

In this section, we put forward a way to fit our work within the general framework of high-z massive galaxy evolution. Throughout, we suggest how our results indicating accretion onto galaxies is well suited to provide a general picture of galaxy mass-buildup at these redshifts.

2.6.1 Comparison to high-z compact star-forming galaxies

We start of by making a comparison with the widely studied cSFG population at similar redshifts (Cimatti et al., 2008; Ricciardelli et al., 2010; Fu et al., 2013; Ivison et al., 2013; Toft et al., 2014; Toft et al., 2017; Elbaz et al., 2018; Gómez-Guijarro et al., 2018; Gómez-Guijarro et al., 2019; Puglisi et al., 2019; Puglisi et al., 2021). These cSFGs also feature compact kpc-scale sub-mm bright regions, as is observed in our sample. In fact, Puglisi et al. (2019) already suggested these regions/cores to be above the star-forming main sequence (as seen in our sample, Fig. 2.3). However, the surrounding disks being well below the star-forming main sequence as in our sample (Fig. 2.3), making galaxies appear to be quenching 'outside-in', have not yet been recognized. A similar scenario might hold for post-starbust galaxies (e.g., Baron et al., 2022). Another apparent difference is the average ratio of the near-infrared and sub-millimeter radii for cSFGs, that is ~ 3 (Puglisi et al., 2021; Smercina et al., 2018; Lang et al., 2019). Although this is likely a lower limit due to many cSFGs remaining unresolved in large sample studies. It remains thus unclear if examples like the three galaxies in RO-1001 with ratios $4-9$ could also present among cSFGs. Moreover, simply the size of Galaxy-B being a factor of $2.0-2.5$ above the mass-size relation (van der Wel et al., 2014) for star-forming galaxies at $z=3$, adds to the rarity of our sample, especially with regards to cSFGs. Another characteristic of cSFGs seemingly in conflict with our results is the expectation of major-merger dominance within such samples (Elbaz et al., 2018). Both in galaxies B and C, the stellar disks appear to be well-preserved (Sec. 2.4.2).

We can however provide possible reasons behind these apparent discrepancies. Our high-resolution imaging capabilities in both near-IR and sub-mm for RO-1001 is usually not reached in larger statistical studies of cSFGs. Hence we might have simply been able to resolve the galaxies better to determine their properties. This allowed us to study the lopsidedness, the lack of dynamical perturbations (in galaxies B and C) and the apparent 'outside-in' quenching, based on which we draw the conclusions of our work. Although, we can also hypothesize a physical reasoning. Large statistical samples usually comprise of galaxies in the field which do not experience the high levels of accretion of gas and satellites expected within dense gas-rich environments like RO-1001 (accretion rate increases with halo mass; Dekel et al., 2009). Hence the cSFGs in the regions with less accretion would be more

likely to be results of major-mergers driving gas into compact cores while destroying extended stellar disks. This is further exemplified by our direct visual investigation finding a complete lack of similarly massive galaxies with extended and continuous stellar morphology (like in Galaxy B) in the redshift window of $2.6 < z < 3.2$ in both COSMOS and GOODS-South fields. If this is true, cSFGs with compact star-forming cores and very extended quiescent stellar disks (similar to our sample) might be more easily found in dense accretion-rich regions.

2.6.2 A link to the accretion filaments in RO-1001

Extending on our hypothesis of accretion onto the three star-forming galaxies in RO-1001, it is imperative to associate the discussed properties with the large scale narrative of accretion for the galaxy-group (Daddi et al., 2021a). Any ongoing accretion in RO-1001 would likely be coupled with the established Lyman-α-emitting filaments in RO-1001 (Daddi et al., 2021a). Hydrodynamical simulations predict that massive galaxies evolving under the influence of nearby accretion-streams have their major axes aligned along the stream direction (Dubois et al., 2014; Codis et al., 2018). We observe a consistency with this prediction in our observations (Fig. 2.1, right panel). We quantify this by finding the probability for the chance alignment of the major axis of each galaxy with one of the three filaments. The range of allowed angles is approximated using the centre of the galaxies and the edges of the '-18.0' contour (corresponding to a surface brightness of $10^{-18}\,\mathrm{s}^{-1}\,\mathrm{erg\,cm}^{-2}\,\mathrm{arcsec}^{-2}$) in Fig. 2.1, since it is the highest brightness level at which the Ly-α traced filaments are detected. We also ensure that the tentative direction of the filaments, qualitatively reported in Daddi et al. (2021a), are within this subtended angle ($< \pm 10^{\circ}$). We find total chance probabilities of 13%, 17% and 12%. Additionally, the probability of all three galaxies being aligned with one of the filaments (which is what we observe) is hence $< 1\%$. This alignment, especially in case of disk-like galaxies, is attributable to the process of tidal torquing (Codis, Pichon, and Pogosyan, 2015) by the massive accretion filaments. However, at the core of this lies the tidal interactions the galaxies experience due to infalling satellites (or minor-mergers). Hence, the apparent alignments should be regarded as an indication of the galaxies accreting clumpy material, which has already been suggested in Sec. 2.5.1.

In each case however, we would still expect a level of 'bending' of the accretion streams before the final impact on to the galaxies, revealed by offsets between the direction of accretion (Fig.2.9) and the preferred filament (Fig. 2.1, right panel). We propose a scenario where the Galaxy-A, B and C are being fed by the south-western, northern and south-eastern filaments. The swap of the preferred filament for Galaxies A and C from those in their proximity has been made due to better alignment with the major-axis of the galaxies traced by near-IR and sub-millimeter emissions as well as

the direction of accretion traced by the lopsidedness and residual emission (Fig. 2.9). Otherwise, for Galaxy-C the accretion direction would have been opposite to direction of approach of the filament. Moreover, there is an additional inconsistency of the line-of-sight velocities of the Lyman-α in the south-eastern filament at the galaxy position (Daddi et al., 2021a). For Galaxy-A, it has a large spatial displacement from the direction of the nearest south-western filament. In each case hence, the actual streams of in-falling material would have needed to drastically bend before the final impact onto the galaxies. Nevertheless, even in our preferred scenario there is still a level of bending of the streams necessary as they approach the inner halos of the galaxies. For Galaxy-A, the major axis (measured here from ALMA) versus the lopsidedness and in-falling material direction are nearly orthogonal. Hence the bending is likely occurring in the line-of-sight. The same could also be true in Galaxy-B, where the northern filament with its reduced length likely has a major component along the line-of-sight. Hence, the in-falling stream would need to bend if it has to agree with the expected direction of accretion along the major-axis, on the plane of the sky (Fig. 2.9).

2.6.3 A unified picture of accretion-driven evolution

Based on the results of the three star-forming galaxies in RO-1001, we find evidence of massive disk-like galaxies expected to have secularly evolved featuring compact star-forming regions at their cores. We propose that the massive disks build up lopsidedness under the combined effects of gas and satellite accretion which in turn results in loss of angular momentum of the material. This drives the prodigous star-formation in the central regions. Such a scenario is likely being observed in galaxies B and C. Although, gas can also be driven to the core by much more violent major-mergers (Toft et al., 2017; Elbaz et al., 2018), but this leads to a destruction of the stellar disks which is only anticipated in Galaxy-C. However, we conclude that the *wet compaction* scenario proposed by simulations (Dekel et al., 2013; Zolotov et al., 2015; Tacchella et al., 2016), where compact stellar bulges get rapidly built up as a result of accretion-driven violent disk instabilities, is too extreme to reproduce the observations in RO-1001. Such a compaction simply does not allow for creation of extended and massive stellar disks ($\gtrsim 10^{9.5}\,M_\odot$) while in our sample we are observing them with masses $> 10^{11}\,M_\odot$.

Finally, the presence of massive stellar disks points to the need for a mode of destruction, since they are not usually observed in dense environments at lower redshifts (Bundy et al., 2010). Dynamical disturbances caused by mergers or galaxy harassment can easily be invoked for this (Toth and Ostriker, 1992; Kazantzidis, Zentner, and Kravtsov, 2006; Bullock, Stewart, and Purcell, 2009; Purcell, Kazantzidis, and Bullock, 2009; Bournaud et al., 2011). We might already be observing such a scenario in action in Galaxy-A, with its signs of a forthcoming major-merger. Finally, a possible end product may be the compact quiescent spheroidal galaxy(Kalita et al., 2021a) that

has been photometrically confirmed to also be within the group, although it never grew beyond $10^{11}\,M_{\odot}$. It is curious however, that we have stumbled upon a galaxy-group with three massive galaxies close together with recent gas-rich star-bursting cores created within the last few 100 Myr. From each of their observed properties, they seem to have undergone a recent shift in evolution with a preference for the central region. A possible reason has recently been discussed in Noguchi (2021), where bulges get rapidly built-up in $> 10^{11}\,M_{\odot}$ galaxies within dark-matter halo cores that are accessible to cold-gas filaments (Dekel et al., 2009). This limit is related to the dependence of migration timescales of clumpy accreted material (already suggested in our sample by their lopsidedness, as discussed in Sec. 2.5.1) that feed the central star-forming region on the stellar mass of the galaxy. Hence, the galaxies in RO-1001, all of which are $> 10^{11}\,M_{\odot}$, could simply be experiencing ideal conditions for a rapid buildup of bulges. It should be noted however that we refrain from estimating the timescale of migration of accreted clumps since such a calculation depends on the relative angular momentum of the inflowing material with respect to the disk. This can result in a range between a few tens to a few hundred Myrs, which is highly uncertain and heavily dependent on assumptions that we are not in a position make with the current data.

2.7 Caveats and future prospects

2.7.1 Further investigations

In our study, we are still lacking information about certain facets of the three galaxies in RO-1001. A spatially resolved spectroscopic study of the quiescent stellar regions would be extremely useful to constrain their star-formation histories. A lot of work in this direction has been done for massive QGs (e.g., Schreiber et al., 2018b; Forrest et al., 2020b; Valentino et al., 2020b), with signatures of rapid quenching of star-formation observed in their samples. Although we do determine rapid quenching of the stellar disks in our sample (Sec. 2.3.4), conclusive proof will only be available after obtaining spectroscopic data.

Furthermore, this will also allow the tracing of the metallicity of the stellar disks. It is hypthesized that accreted gas being metal-poor leads to a fall in the metallicity in the accreting galaxy (Lehner et al., 2013; Sánchez Almeida et al., 2013; Sánchez Almeida et al., 2014; Wotta et al., 2019). Hence, RO-1001 could be a test-bed for such theories. Finally, spectroscopy will also provide the kinematics of the stellar disk and determine the level of rotational dominance within the structure. This would be necessary to model the evolution of the galaxies as well as similar galaxies in the future featuring signs of accretion. This is especially of interest since we have suggested the possible prevalence of clumps migrating to the core of the galaxies, driving the high levels of star-formation. The timescales of in-flowing material is

coupled with the rotation timescales of the respective disks (Dekel, Sari, and Ceverino, 2009).

2.7.2 Extending the search to other structures

Asymmetries in the stellar distribution as well as relative position of the sub-mm bright cores of cSFGs are rather common. However, they are mostly associated with galaxy-galaxy interactions (Elbaz et al., 2018; Cibinel et al., 2019; Puglisi et al., 2019). However, we demonstrate that if studied in higher resolution, they might reveal effects of accretion of gas and clumps especially in dark matter halos where cold-gas filaments are expected to survive in spite of the surrounding hot medium (Dekel et al., 2009). Hence, deep observations of star-forming galaxies within dense-environments would be instrumental in establishing a generalised picture of massive galaxy evolution in dense environments. A few examples are in fact already available. CLJ1449+0856 (Gobat et al., 2011; Gobat et al., 2013; Strazzullo et al., 2016; Coogan et al., 2018) has three highly star-forming galaxies that showcase clear offsets between their near-IR and sub-mm/radio contours, with one of them also featuring AGN activity (S7-N7 system; Kalita et al., 2021b). Using unresolved sub-mm data, they were regarded as mergers. However, reconsideration after obtaining high resolution data might reveal the asymmetries to be due to comparable features as those seen in RO-1001. Another such case is the highly star-forming galaxy, GN20, which is part of a proto-cluster at $z = 4.05$ (Daddi et al., 2009; Hodge et al., 2015). This too features a similar offset and is a confirmed member of a high-z dense environment. Additional sources of interest include galaxies within seven other high-z structures with Ly-α halos suggesting abundance of gas (Daddi et al., 2022b; Daddi et al., 2022a). Future well-resolved studies of these and additional structures hold much promise.

2.8 Summary and conclusions

Within a $z = 2.91$ galaxy-group of dark matter halo mass of $\sim 4 \times 10^{13}\,M_\odot$, we observe three massive ($> 10^{11}\,M_\odot$ galaxies (Fig. 2.1). They have a combined star-formation rate of $\sim 1250\,M_\odot\,yr^{-1}$, and are studied here with high resolution near-IR (HST) and sub-mm (ALMA) data. Each of the galaxies have extremely compact (effective radius $\sim$ 1 kpc) sub-millimeter bright cores where almost all of the star-formation and $10 - 40\%$ of the stellar mass is confined. They will likely form the future bulges of their respective galaxies. These are embedded in co-planar stellar disk-like structures which are $4 - 8\times$ more extended in radius. The key new results that emerge from our work are the following:

1. All three galaxies show marked stellar disk lopsidedness of varying degrees (from 1.6 to > 3.0). The stellar morphology of 2/3 galaxies (B

and C) do not show signs of extreme dynamical disturbances however, hence limiting the role of major-mergers. Although, the third (galaxy A) is likely at an initial phase of collision with an equally massive counterpart. These are first, unique cases of high redshift galaxies in which lopsidedness has been recognised to play an important role.

2. Based on ALMA 3σ upper-limits, we also determine that star-formation is suppressed in the disks. They are found to be located > 1 dex below the star-forming main sequence (whose scatter is 0.3 dex), while the star-forming compact cores are mainly located above it (Fig. 2.3). These galaxies are among the first known cases of 'outside-in' quenching observed in the distant Universe.

3. Furthermore, the cores could not have been forming stars beyond earlier than a few 100 Myr, which is the same epoch by which the disks had already formed about 50% of their stellar mass. This bi-modality in star formation and stellar age coincides with the apparent outside-in quenching of the galaxies.

4. We conclude that the lopsidedness is intrinsically connected to gas being driven into the centre of the potential well of the galaxies. The reason of this lopsidedness in at least Galaxies B and C is most likely the combined effect of accreted gas and clumps, the latter of which can be regarded as minor-mergers. In case of Galaxy-A, the imminent major-merger would also play a role.

5. The importance of minor-mergers due to accretion is exemplified by the alignment of the major axes of all three galaxies with one of the accretion streams established through Ly-α halo morphology in Daddi et al. (2021a). This is expected to also result in the lopsidedness as well as any residual stellar and dust emission to converge onto the location of impact of the accretion-stream with the galaxies. We detect these signatures in each of the cases. Hence we make the first direct connection between accretion streams and the morphological transformation of galaxies driving compact star-formation in massive galaxies at high redshifts.

6. We show that in the presence of accretion, galaxies can build-up compact highly star-forming cores without the need of major-mergers and therefore preserving their stellar disks. A key feature however is an asymmetry in the stellar distribution, which needs to be studied in high resolution to determine if it is driven by accretion of gas and clumps or by violent interactions like major-mergers. Future studies of accretion-rich high-z dense environments would prove to be crucial.

Based on our results, we suggest an evolutionary pathway in which a secularly evolving disk within a dense environment with accretion (gas and

clumps), grows substantial mass asymmetry and experiences the creation of a compact star-bursting core at the expense of the star-formation within the disk. This is inevitably followed by some form of disruptive event that leads to the destruction of the quiescent disk (Toft et al., 2017), leaving behind, and also possibly adding to (Elbaz et al., 2018; Puglisi et al., 2021), a stellar bulge. However, the ubiquity of such a scenario can only be revealed with more well-resolved observations of massive galaxies at the heart of well studied high-redshift dense environments – that will likely become more accessible in the upcoming James Webb Telescope era.

Spectral Energy Distribution Model Fitting

In order to fit SFH models to the galaxies, we use the results of the surface brightness distributions in F160W (which also provides the flux in the band) and then obtain the rest of the photometry using the best-fit models as priors in all other bands. We fit this photometry with BC03 stellar population models (Bruzual and Charlot, 2003) to derive the properties of the three massive galaxies (Fig. 2.7). The redshift is fixed to the spectroscopic values previously published for the sources (Daddi et al., 2021a). We use FAST++[1] to determine the best fitting SED templates through a χ^2 minimisation procedure. We fix the metallicity to the solar value as is expected in massive galaxies and implement the Calzetti dust attenuation law(Calzetti et al., 2000), with a range of extinction values, $A_V = 0 - 5$ in steps of 0.02. Finally, the following SFH models are used:

1. Constant star formation models: We use this model featuring no decline in star formation (it remains constant throughout) to check if a high attenuation star-forming scenario is formally consistent with the available photometry.

2. Delayed τ-models: This is an exponentially declining SFH here is characterised as $\propto (t/\tau^2)\, e^{-t/\tau}$ with a peak of star formation at $t = \tau$. The τ varies within [100 Myr, t_{obs}] with steps of 0.1 dex, where t_{obs} is the age of the universe at the redshift of the galaxy.

3. Composite τ-models(Schreiber et al., 2018b): This is similar to the previous model, however with different timescales (τ_{rise} and τ_{decl}) for the rising and declining phases separated by the epoch t_{burst}.

$$\mathrm{SFR}_{base}(t) \propto \begin{cases} e^{(t_{burst}-t)/\tau_{rise}} & \text{for } t > t_{burst} \\ e^{(t-t_{burst})/\tau_{decl}} & \text{for } t \leq t_{burst} \end{cases} \tag{2.4}$$

   Both τ_{rise} and τ_{decl} are varied within the range of [10 Myr, 3 Gyr], while for t_{burst} a grid of [10 Myr, t_{obs}] is used.

[1] https://github.com/cschreib/fastpp

Prevalence of Ram Pressure Stripping

We investigate the effect RPS may have on the three star-forming galaxies in RO-1001. We use the following relation from Domainko et al. (2006) for the minimum radius up to which gas may be stripped from a galaxy (r_{strip}):

$$r_{strip} = 0.5\, r_o \times \ln\left(\frac{G\, M_{star}\, M_{gas}}{\frac{2}{gal}\, æ_{ICM}\, 2ß\, r_o^2}\right) \tag{2.5}$$

Here, the r_o is the scale radius of the galaxies, while M_{star}, M_{gas} corresponds to the gas and stellar mass of the galaxies. $_{gal}$ is the relative velocity between the galaxy and the ICM, for which we use the approximate virial velocity of the galaxies in RO-1001 ($500\,km\,s^{-1}$; Daddi et al., 2021a). Finally, the density of the ICM ($æ_{ICM}$) is determined using (Boselli, Fossati, and Sun, 2021):

$$æ_{ICM} = 1.15\, n_e\, m_p \tag{2.6}$$

We use the value of $10^{-3}\,cm^{-3}$ for the electron density (n_e) as is expected in the core of clusters and groups (Vikhlinin et al., 2009; Sun et al., 2009; Pratt et al., 2010).

We hence get an $r_{strip} = 10 - 15\,kpc$ for the galaxies in RO-1001. However, this should be regarded as a conservative lower-limit since RPS efficiency is expected the steeply decrease at high-redshifts. This is primarily due to the contribution of non-gravitational heating which effectively reduces the ICM content (Fujita, 2001). Moreover, the decreasing efficiency of RPS at high redshifts ($z \gtrsim 2$) is also suggested through simulations in (Pfeffer et al., 2022). Hence, in each of our sample galaxies, the r_{strip} is found to be a factor of $\gtrsim 2$ larger than the stellar disks.

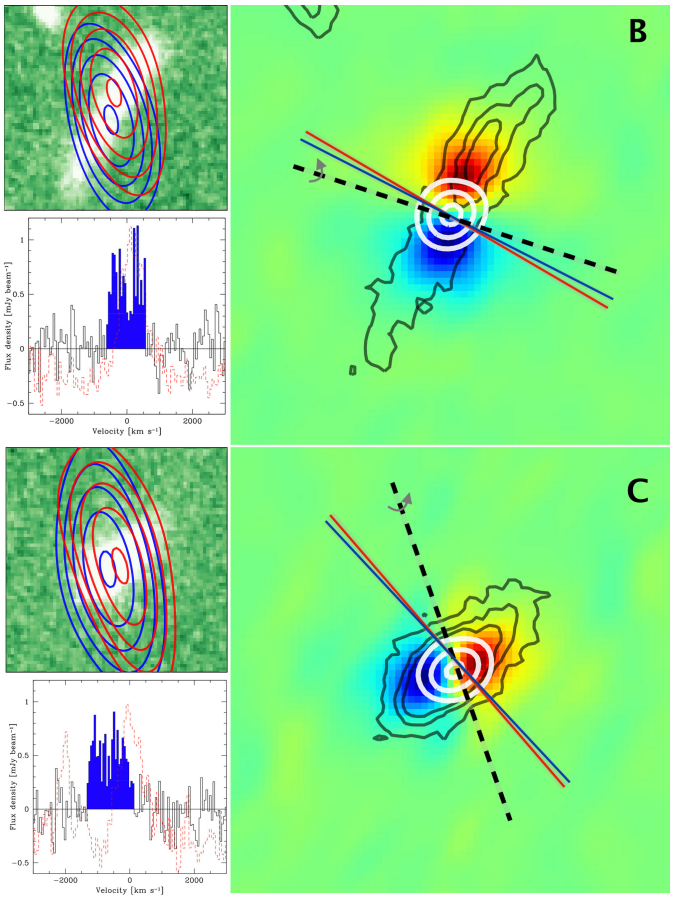

FIGURE 2.7: Two panels showing the rotational properties in Galaxies B and C with three individual sub-images: (top-left) the NOEMA CO$[3-2]$ emission profiles for the *blue* and *red*-shifted sections with respect to the average galaxy profile shown as contours superimposed on the F160W image; (bottom-left) The NOEMA spectra with the CO$[3-2]$ emission line in blue and the local Lyman-α profile in red; (right) The contours of the stellar disk (black; beginning at 8σ with increments of 4σ), the compact core (white; beginning at 100σ with increments of 50σ for Galaxy-B and at 50σ with increments of 25σ for Galaxy-C) and a representation of the *blue* and *red*-shifted CO$[3-2]$ emission locations with the size of the compact core as seen in ALMA. The expected rotational axes have been also been provided for each component – disk in red, core in blue and CO$[3-2]$ emission as black dashed lines. The NOEMA spin axes uncertainties are large enough to make the difference with the other component not statistically significant.

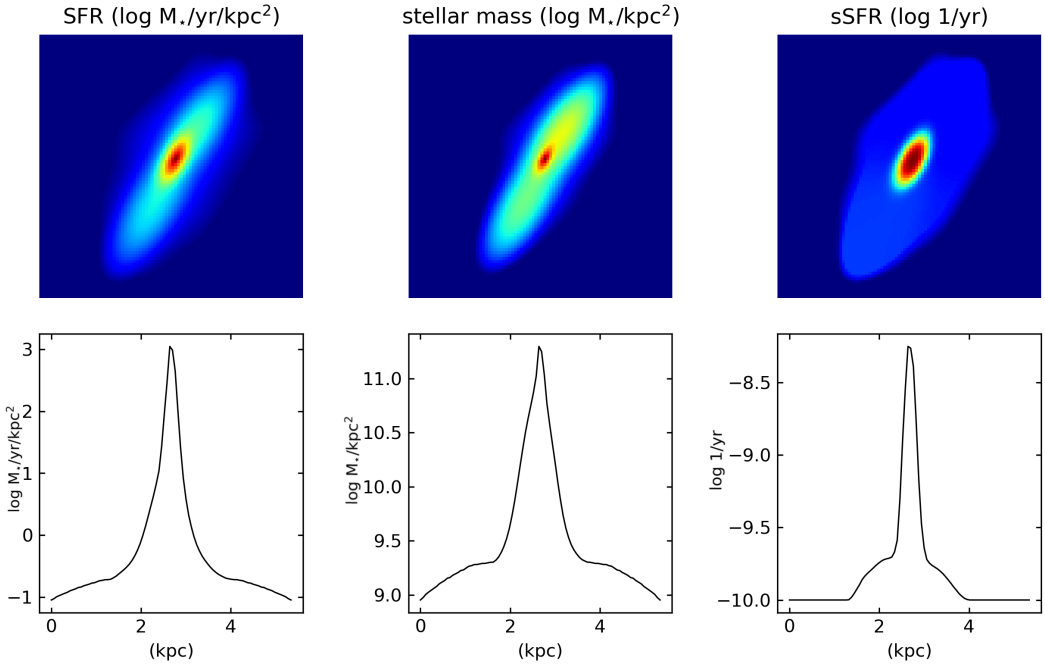

FIGURE 2.8: Spatial distribution of Galaxy-B stellar mass and star formation rates. (Left) The upper panel shows SFR distribution model of Galaxy-B, with the morphology determined by the F160W stellar emission in case of the disk, and the ALMA dust emission for the core. The amplitudes are determined by the SFR of the two components. The lower panel is a 1-D representation of the plot above, after a rotation the make the major axis horizontal. (Middle) The stellar mass distribution following the same procedure. Here the mass in the core is determined from the difference between the dynamical mass and gas-mass determined from the CO$[3-2]$ emission line. (Right) The specific SFR provided by the ratio of the SFR and the stellar mass.

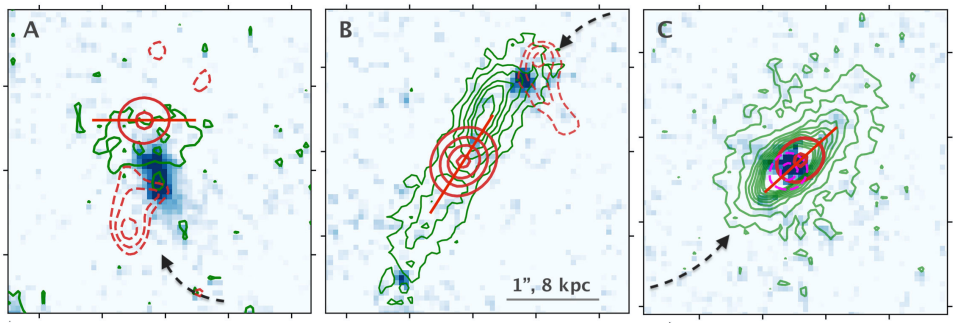

FIGURE 2.9: Additional stellar and dust components tracing the direction of accretion. The three panels showing the three residual F160W images of the galaxies after the subtraction of the primary disks (in green contours; starting at 4σ with increments of 4σ). The red solid contours show the ALMA 870 μm emission with the lines starting at 50σ with increments of 50σ. The red solid lines indicate the respective ALMA major axes. In case of Galaxies A and B, the dashed red contours starting at 3σ with steps of 0.5σ displays the ALMA residual emission after the subtraction of the primary emission regions. In case of Galaxy-C, the same contours show the additional point source adjacent to the core that was found during the fitting procedure. In this case, the contours are at $15, 25\sigma$. Finally, the arrows indicate the likely directions of gas-accretion onto the galaxies based on the asymmetric distribution of all the aforementioned components, which also coincide with the direction in which the disks are lopsided.

Chapter 3

An ancient massive quiescent galaxy found in a gas-rich $z \sim 3$ group

This work has been published in ApJL (Kalita et al., 2021a)
(ApJL, 917.2, p. L17)

Within the same structure where the three star-forming galaxies were observed, we observe a fourth, albeit photometrically confirmed member. However, this galaxy is quiescent and has been so over $> 1\,\mathrm{Gyr}$. We hence illustrate the quiescence of massive high-z galaxies being independent of environment (as discussed in Sec. 1.2.2), especially given that the host group is expected to have large quantities of available cold gas.

3.1 Introduction

Hydro-dynamical simulations and semi-analytical models have found it difficult to reproduce massive ($\gtrsim 10^{11}\,\mathrm{M}_*$) quiescent galaxies (QGs) beyond $\mathrm{z} \gtrsim 3$ (Steinhardt et al., 2016; Schreiber et al., 2018c; Cecchi et al., 2019), while observations have been pushing the redshift boundary by detecting such systems at $\mathrm{z} \sim 3 - 4$ (Gobat et al., 2012; Glazebrook et al., 2017; Schreiber et al., 2018a; D'Eugenio et al., 2020b; Valentino et al., 2020b; Forrest et al., 2020c; Forrest et al., 2020a; Saracco et al., 2020). Most of the systems so far observed belong to a population of recently quenched 'post-starburst' (PSB) galaxies with their last star-formation episode occurring over the last $< 0.8\,\mathrm{Gyr}$. However, we might still be missing a fraction of older ($\gtrsim 1\,\mathrm{Gyr}$) QGs (D'Eugenio et al., 2021b; Forrest et al., 2020a). Moreover, there has not been any insight on the influence of the environment over such galaxies, as most of those studied are field objects.

Studying a younger sub-sample of a larger population of high-z QGs may have influenced our understanding of how quiescence occurs and persists. Currently, for star-formation to be suppressed in the $z > 2$ epoch which usually features gas-rich star-forming galaxies, there are a variety of possible channels. These include merger driven starbursts (Puglisi et al., 2021),

AGN feedback (Brennan et al., 2018), gas strangulation (Peng, Maiolino, and Cochrane, 2015), halo quenching (Feldmann and Mayer, 2015), and morphological quenching (Martig et al., 2009). Hence, further probing the high-z QG population, including those in dense environments, will provide opportunities to investigate the earliest mechanics of quenching.

With this in mind, we report the detection of an extremely red and old quiescent galaxy within a dense environment at $z \sim 3$. Throughout, we adopt a concordance ΛCDM cosmology, characterized by $\Omega_m = 0.3$, $\Omega_\Lambda = 0.7$, and $H_0 = 70$ km s^{-1}Mpc^{-1}. We use a Chabrier initial mass function. Magnitudes and colors are on the AB scale.

3.2 Galaxy-D and RO-1001

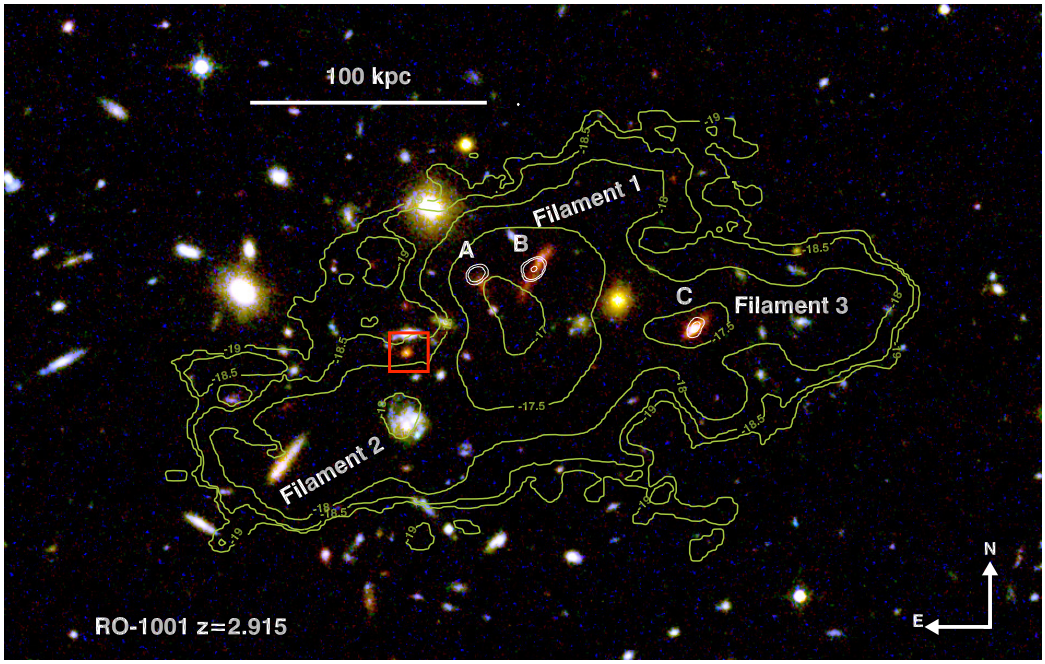

FIGURE 3.1: The core of RO-1001 as seen is HST/WFC3 (F606W, F125W, F160W). The green contours denote the Lyα nebula luminosity with the locations of the associated filaments possibly powered by cold-flow accretion (Daddi et al., 2021b). Galaxy-D is marked with a red square.

Three massive ($\log(M_\star/M_\odot) \gtrsim 11$) galaxies (A, B, and C in Fig. 3.1 and Daddi et al., 2021b) in the $z = 2.91$ RO-1001 group have a combined star formation rate (SFR) $\sim 1250\,M_\odot$ yr^{-1}. NOEMA observations of the CO(3-2) transition showed that they lie at the same redshift of $z = 2.91$. Furthermore, the presence of extensive cold gas reservoirs is suggested by Lyα observations that revealed extended filaments converging onto a single massive halo with a combined luminosity of $1.3 \pm 0.2 \times 10^{44}$ erg s^{-1}, most likely still affected by

cold-accretion persisting in this system with estimated dark matter halo mass of $4 \times 10^{13} M_{\odot}$. These conclusions are based on the observed line profile, the velocity field, and the energetics underlying the Lya emission (Daddi et al., 2021b). Moreover, also pointing to the availability of cold gas is the redshift of the group, which places it in the epoch where cold flow accretion is expected to dominate (Valentino et al., 2015; Overzier, 2016). Galaxy-D was reported earlier as a possible passive member of RO-1001 (Fig. 3.1; Daddi et al., 2021b).

3.3 Observations

3.3.1 Optical and Near-IR imaging

RO-1001 was observed with *HST/WFC3* imaging in 3 bands (F160W, F125W and F606W) over a total of 11 orbits during Cycle 27 (Proposal ID: 15190, PI: E. Daddi). The data reduction was executed using the pipeline *grizli* [1]. The 5σ point-source sensitivities reached are 26.25 (F160W), 26.47 (F125W) and 26.39 (F606W) with a pixel scale of $0.06''$ and a half-power beam-width of $0.24''$ for F160W. An additional image in the F814W band was also incorporated into the analysis. Due to a lack of coverage in z and y-bands, we include Subaru Hyper Suprime-Cam images were from the "COSMOS2015" database (Laigle et al., 2016). Furthermore, we used the Ks band image from data release 4 of Ultra-VISTA. Finally, IRAC 3.6 μm and 4.5 μm images were taken from the Spitzer Matching Survey of the Ultra-VISTA Deep Stripes (SMUVS), while those at 5.8 μm were taken from the COSMOS2015 database.

3.3.2 Sub-mm imaging

To have an estimate of the obscured star formation in Galaxy-D, we also used recently available sub-mm data. Atacama Large Millimetre Array (ALMA) band 7 observations were taken in Cycle 7 (Project ID: 2019.1.00399.S, PI: R.M. Rich). The data reduction was mainly carried out using the Common Astronomy Software Application (CASA). The final mosaics have a maximum sensitivity of 28 $^{-}$Jy beam^{-1}, with a synthesised beam size of $0.49'' \times 0.46''$.

3.4 Analysis and results

3.4.1 Photometry

In the COSMOS2015 catalogue (Laigle et al., 2016) Galaxy-D is blended with a galaxy located $1''$ to the North (Fig. 3.1). Hence, we make new flux measurements for it in each of the wavelength windows we have access to. We first use SExtractor for the 4 HST/WFC3 images since the the resolution

[1] https://github.com/gbrammer/grizli

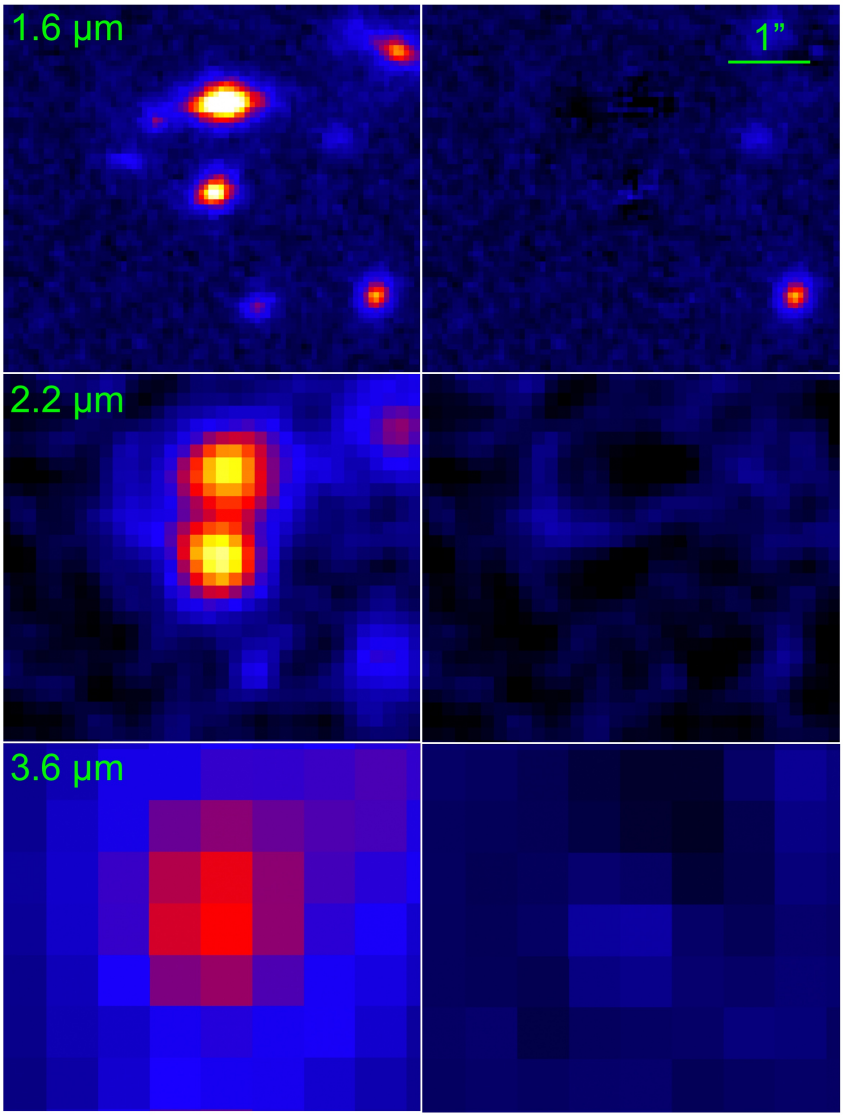

FIGURE 3.2: Panels showing Galaxy-D (at the centre) along with its surrounding foreground galaxies in 3 out of 5 wavelength bands for which GALFIT was used to extract the photometry. As detailed in Sec. 3.4.1, the results of H-band (1.6 ¯m) were used to deblend at the other bands (2.2 ¯m, 3.6 ¯m, 4.5 ¯m, 5.8 ¯m, the first two of which are shown in the middle and lower rows respectively). More sources were fit and subtracted at longer wavelengths due to the increase in PSF size. The residual images are found to not have any fluctuations $> 1\sigma$.

is sufficient to clearly separate galaxy-D from its neighboring foreground galaxy. We use F160W as the detection image to carry out matched aperture photometry using isophotal radii. To ensure equivalent resolutions, we also convolve the F606W, F814W and F125W images with Gaussians such that their respective final point-spread-functions (PSF) have the same size as that in F160W. From the catalogue hence created, we find it to be undetected in F606W and F814W (which therefore provide upper-limits) while F125W and F160W have clear detections with signal-to-noise (S/N) of ~ 25 and 65 respectively. The z and y-bands also return non-detections, which are hence used to set flux upper-limits.

In order to ensure that all the flux from Galaxy-D is accounted for, we use galaxy morphological model fitting with the software GALFIT. Since the 1.6 μm (F160W) image has the highest S/N, we use it for this attempt. We fit sérsic profiles to both Galaxy-D and the foreground galaxy, along with Gaussian profiles to multiple surrounding objects (Fig. 3.2). We measure an AB-magnitude of 24.00 for Galaxy-D and get a sérsic index of 2.0 ± 0.2. The error on the latter value includes the results from a co-addition of the F125W image to the F160W image to improve S/N as well as an independent analysis of the F125W image, all of which are in agreement. The sérsic index suggests that this galaxy might feature a disky component with a significant bulge component, within the scatter expected from high-z QGs (Lustig et al., 2021). The galaxy is also found to be extremely compact with an effective radius, $r_e = 0.14 \pm 0.03''$, which at z=2.9 is 1.1 ± 0.1 kpc. We further use the flux difference between the GALFIT measurement and that from SExtractor, to scale up the catalogue (isophotal) flux measurement at 1.25 μm (F125W) as well as the upper-limits at 0.6 μm (F606W) and 0.8 μm (F814W).

The morphological properties of Galaxy-D determined through the model fitting at 1.6 μm are further used as priors in Ks band (2.1 μm) as well as the IRAC 3.6 μm, 4.5 μm and 5.8 μm. This is done in order to deblend the galaxy from its foreground neighbors, which are also simultaneously fit with models based on 1.6 μm priors (Fig. 3.2). Images beyond this wavelength window do not show a detection, while the implied upper limits are not constraining, and are hence not used.

3.4.2 SED fitting

We fit the photometry derived in the previous section with BC03 stellar population models (Bruzual and Charlot, 2003) to derive the properties of Galaxy-D (Fig. 3.3, left). We use HYPERZ to determine the best fitting spectral energy distribution (SED) templates through a χ^2 minimisation procedure. We investigate a redshift range of $0 - 6$ with a step size of 0.01.For the BC03 templates, a range of metallicities are allowed ($\frac{1}{5}Z_\odot$, $\frac{1}{2}Z_\odot$, $Z_\odot$ and $\frac{5}{2}Z_\odot$). We also implement the Calzetti et al. (2000) along with SMC and LMC laws for dust attenuation, with extinction values, $A_V = 0 - 7$ in steps of 0.1. Finally, a wide variety of star formation histories (SFH) are used:

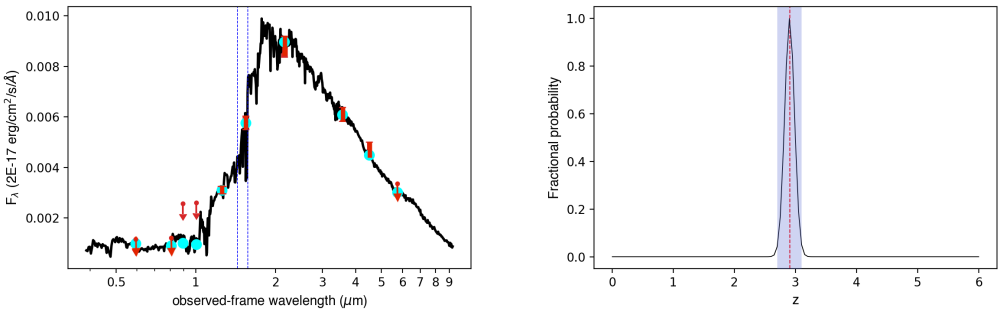

FIGURE 3.3: (Left) The best-fit SED template using the available photometry for Galaxy-D. The red bars show the observed photometry while the cyan points mark the expected values from the SED. The blue dashed-lines mark the locations of the Balmer and 4000 Å breaks. (Right) The probability distribution function for the photometric redshift of Galaxy-D. The red dashed line marks the spectroscopic redshift of RO-1001 while the blue shaded region marks the 90% confidence region of the photometric redshift for Galaxy-D.

1. Simple stellar population (SSP): This is the most basic model with all of the stellar mass formed during an infinitesimal short burst of star formation at $t = 0$.

2. Constant star formation models: Although we have enough evidence for the quiescence of the galaxy (discussed in detail later in Sec. 3.5.1), we use this model featuring no decline in star formation (it remains constant throughout) to check if a high attenuation star-forming scenario is formally consistent with the available photometry.

3. Truncated models: These involve a constant SFR from $t = 0$ up until a t_{stop}, beyond which SFR $= 0\,M_\odot\,yr^{-1}$. The t_{stop} is varied from 0.1 Gyr to a generous upper limit of 5.0 Gyr in steps of 0.1 dex.

4. Delayed τ-models: Finally, we use an SFH that has been widely preferred to model QGs. The exponentially declining SFH here is characterised as $\propto (t/\tau^2)\, e^{-t/\tau}$ with a peak of star formation at $t = \tau$. The τ varies within [0.1, 5.0] Gyr with steps of 0.1 dex.

We investigate the reduced χ^2 values from the fits using the various BC03 models, over the above mentioned grid of A_V. We get the best fit with the delayed τ-models, closely followed by SSP and truncated models. In comparison, we find a complete lack of fit using the constant star formation templates ($\Delta\chi^2 > 30$), with any level of reddening, reinforcing our claim of Galaxy-D being quiescent.

3.4.3 Galaxy Parameters

The photometric redshift (photo-z) determined from the SED fitting is found to be 2.9 ± 0.1 (Fig. 3.3, right), with the limits giving the 1σ confidence interval ($\Delta\chi^2 < 1$). We also derive a stellar mass, $\log(M_*/M_\odot) = 11.0 \pm 0.2$, in agreement with the previous results in Daddi et al. (2021b). Moreover, we find minimum levels of attenuation with the fitting procedure returning a value of $A_V \sim 0.1$.

Following the analysis in similar studies (Gobat et al., 2012; Schreiber et al., 2018c; Valentino et al., 2020b; D'Eugenio et al., 2020b), we define t_{50}, which is the time elapsed since the epoch of "half-mass formation" up until the time of observation. We determine this quantity to be 1.6 ± 0.4 Gyr at 90% confidence, after marginalising on all the unknown parameters (SFH, metallicity, dust attenuation law and A_V, redshift). This is estimated using the combination of all four metallicities mentioned in the previous section, although the solar value gives the best fit (consistent with expectations for massive galaxies; Belli, Newman, and Ellis, 2019). Studying each of the values, we find that t_{50} gets progressively lower as we go from sub-solar to super-solar metallicities. At $z = 2.9$, for $\frac{1}{5}Z_\odot$, we derive a best-fit $t_{50} \sim 2.2$ Gyr which is almost equal to the age of the universe at that redshift, while for the super-solar $\frac{5}{2}Z_\odot$, the t_{50} is found to be ~ 1.0 Gyr. Although these results incorporate all previously mentioned SFH models together, using each model separately we find that the results from delayed-τ and truncated models are in agreement, while those using SSP (which can be considered as the light-weighted age) push the age upper-limit by ~ 0.2 Gyr. Finally, fixing the redshift to that of RO-1001 ($z = 2.91$) returns an age estimate of 1.6 ± 0.5 Gyr (at 90% confidence).

3.4.4 RO-1001 membership

The photo-z measurement of 2.9 ± 0.1 which is in remarkable agreement with the $z_{spec} = 2.91$ of RO-1001, strongly suggests group membership. This is further reinforced by the vanishingly low probability of $\sim 5 \times 10^{-5}$ for a chance alignment of Galaxy-D within $10''$ from the center of the RO-1001 group (as defined by the peak of the Lyα emission). This is estimated by the implied surface density of the 57 galaxies with H-band magnitudes ≤ 24.00, J-H color ≥ 1.1 and H-Ks color ≥ 2.2 over the whole COSMOS area (Laigle et al., 2016).

Hence, it is extremely unlikely that this galaxy is at a redshift different from that of the group RO-1001. Although, it cannot be currently determined with certainty whether Galaxy-D is exactly within the core of RO-1001 or part of the associated large-scale structure. In either case Galaxy-D can still be considered to be within a dense environment.

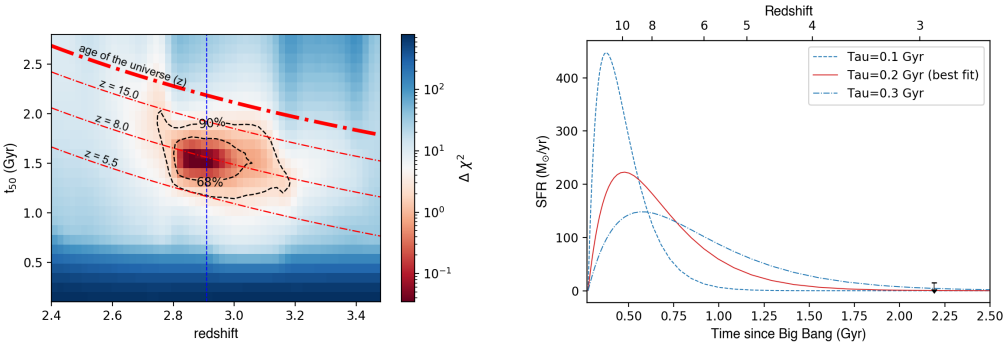

FIGURE 3.4: (Left) The variation of $\Delta\chi^2$ in the stellar population age (t_{50}) vs redshift space. The dot-dash lines demarcate the lookback times for various redshifts along with the thickest of them showing the age of the Universe, all of which are functions of redshift (Right) The best fit delayed τ-model SFH ($\tau = 0.2\,\mathrm{Gyr}$) as a function of age of the universe as well as redshift. Also shown are the SFH models with $\tau = 0.1, 0.3\,\mathrm{Gyr}$ which are within the 90% confidence interval. Finally, the SFR 2σ upper-limit of $13\,\mathrm{M}_\odot\,\mathrm{yr}^{-1}$ derived from the ALMA 870 μm non-detection is shown with the black downward arrow.

3.5 Discussion

3.5.1 Quiescence and the last epoch of star-formation

Confirmation of quiescence at such high redshifts can be challenging (Glazebrook et al., 2017; Schreiber et al., 2017; Simpson et al., 2017). However for galaxy-D, the optical and NIR colors suggest a lack of star-formation based on a complete disagreement with the star-forming SFH models (Sec. 3.4.2). Taking into account all possible SFH models (within 90% confidence interval), we determine a SFR upper-limit of $4\,\mathrm{M}_\odot/\mathrm{yr}$, $\times 30$ below the MS.

The non-detection in our deep ALMA 870 μm data (Sec. 3.3.2) is used to determine a 2σ upper-limit SFR (conservative; fully accounting for its spatial extent of NIR emission of the galaxy based on its Sérsic profile) of $13\,\mathrm{M}_\odot/\mathrm{yr}$ assuming conservatively a main-sequence template appropriate for $z = 3$ (Béthermin et al., 2012). This is already a factor ~ 10 below the main sequence at z ~ 3 (Santini et al., 2017). The limit would be a further factor of 2 deeper if assuming instead a colder IR SED following Gobat et al. (2018), i.e. at $\times 20$ below the MS. Hence, it can be unambiguously concluded that Galaxy-D is truly quiescent, consistently from both the optical and IR side.

Based on the mass-weighted (t_{50}) as well as light-weighted age limits (Sec. 3.4.3), the primary episode of star-formation had already elapsed by $z \gtrsim 6$ and most likely by $z \sim 8$ (Fig. 3.4, left), right after which it likely experienced a rapid decline in its SFR characterised by the best-fit delayed τ-model with $\tau = 0.2\,\mathrm{Gyr}$ (Fig. 3.4, right). However, this should be considered

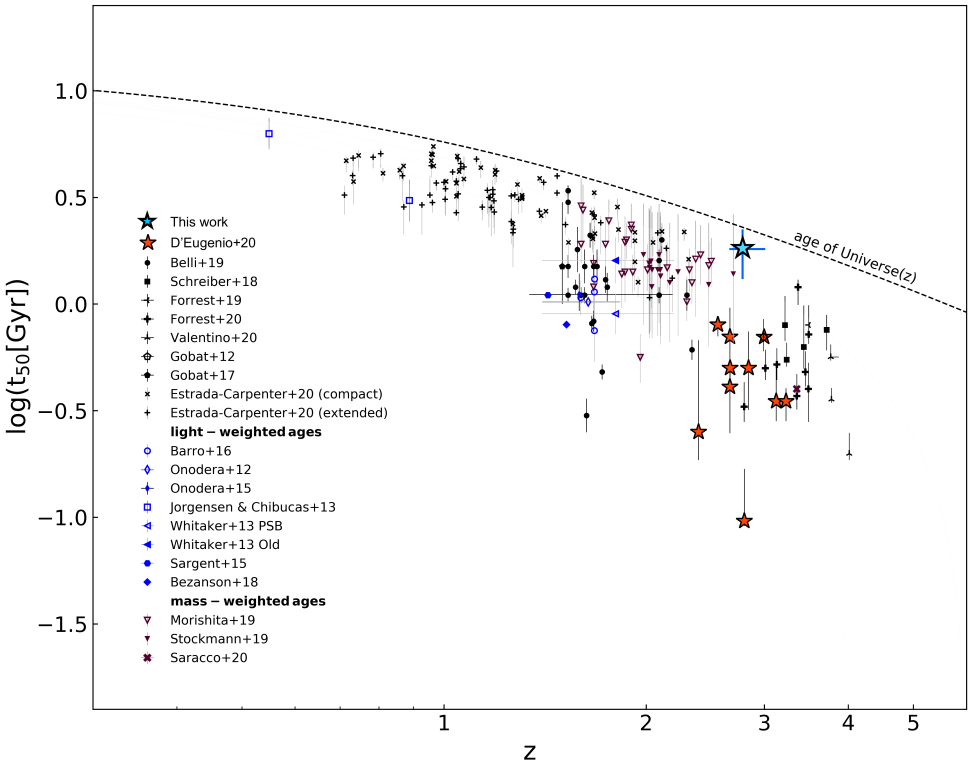

FIGURE 3.5: The stellar population age (t_{50}) vs redshift distribution for $\log(M_*/M_\odot) > 10.5$ QGs adapted from D'Eugenio et al. (2021b), with the references therein. We add Galaxy-D (light-blue star) with the 90% confidence intervals shown as the errorbars for both axes.

as an approximate upper limit, since $\tau = 0.1$ Gyr and the SSP (which has τ equivalent to 0) also return acceptable fits (within an overall $\Delta\chi^2 < 1$ or 68% confidence interval).

This form of rapid quenching has been extensively proposed to explain populations of QGs at z $\sim 3-4$ (e.g., Schreiber et al., 2018c; Forrest et al., 2020c; Forrest et al., 2020a; Valentino et al., 2020b; D'Eugenio et al., 2020b; D'Eugenio et al., 2021b). However, these are usually found to be PSBs, with $t_{50} < 0.8$ Gyr (Fig. 3.5). Such studies usually leave out galaxies similar to Galaxy-D that are expected to have an older (> 1 Gyr) stellar population, due to preferential selection of brighter targets. Forrest et al. (2020a) shows that galaxies with such ages would be considerably less bright (by $\sim 1-2$ magnitudes) in near-IR, compared to PSBs. For example, in comparison to Galaxy-D, the Valentino et al. (2020b) and D'Eugenio et al. (2021b) samples in Ks band are on average brighter by 1.7 and 2.4 magnitudes, respectively. This makes spectroscopic analysis of such very-old galaxies much more difficult, with requirements of extremely long integration times. Possibly as a result, similarly old galaxies at $z \sim 3$ have not yet been spectroscopically studied (Fig. 3.5). We do note however the presence of a population of galaxies at $z \sim 2-2.5$ with seemingly similar ages from Morishita et al. (2019). But their high age estimate can be attributed to systematics, as it would be lowered by a factor of $\sim 1.5-2.0$ if delayed-τ SFH models are employed as in our study (see Fig. 12 in Morishita et al., 2019), further emphasizing the unicity of Galaxy-D in the panorama of known old galaxies at $z \sim 3$.

Larger photometric studies, also with higher uncertainties regarding galaxies being truly quiescent, primarily feature young stellar populations with an extremely small fraction of their samples having ages > 1 Gyr (e.g., Straatman et al., 2014; Carnall et al., 2020). We do have examples of galaxies at lower redshifts $z \sim 0.5$–2 with old enough stellar populations suggesting that they should be already > 1 Gyr old at $z > 3$ (Tacchella et al., 2021, and references therein). Even if those ages inferences are correct (it is increasingly difficult at lower-z to accurately project star formation histories at the earliest times), it is still possible that the progenitors of the lower-z oldest galaxies were not yet hierarchically assembled into a single galaxy by $z \sim 3$ (Mancini et al., 2019). It is hence unclear whether old massive galaxies at $z \sim 3$ are rare due to them experiencing re-accretion of gas and returning back to a star-forming population, to not having yet assembled, or they have simply not yet been detected at these redshifts. Future time-intensive studies would hence be required to complete the mapping of high-z QGs in this regime. A crucial diagnostic for such attempts would be the Balmer and 4000 Å breaks characterised by D_B (Kriek et al., 2006) and D_n4000 (Balogh et al., 1999) respectively. The transition of the D_B/D_n4000 ratio towards values < 1 is a tell-tale sign of ages $\gtrsim 1.0$ Gyr (D'Eugenio et al., 2021b). As an example, we calculate $D_B/D_n4000 = 0.94$ from the best-fit SED template (Fig. 3.3, left), suggesting a small value for D_B. This is in stark contrast to the PSB population, which is usually characterised by much stronger Balmer

breaks and hence higher D_B/D_n4000 ratios (e.g., D'Eugenio et al., 2021b, find an average value of 1.53 for their sample). Future spectroscopy, that should be within reach of JWST, will be needed to validate these inferences.

3.5.2 Tracing the evolution

The short characteristic time-scales (Fig. 3.4) and compact nature of Galaxy-D ($r_e = 1.1 \pm 0.1$ kpc at $z = 2.9$) can be explained by scenarios like mergers (e.g., Puglisi et al., 2021) that drive gas into a compact central region of the galaxy, leading to rapid consumption of gas through star formation. This quickly exhausts the available gas, thereby quenching the system and leaving behind a compact QG. Mergers are already observed in the three primary star-forming galaxies in RO-1001 which are nearly identical in mass and size to galaxy-D (Daddi et al., 2021b, Kalita, B. S. et al. in prep.), but forming over $1000\,M_\odot\ yr^{-1}$ in stars complessively.

Furthermore, with 50% stellar mass ($\sim 5 \times 10^{10}\,M_\odot$) being formed at $z \gtrsim 6$, we can determine whether its progenitor could have existed based on the expected galaxy mass-function, mainly sensitive to star-forming galaxies, at such redshifts. To make a comparison, we estimate a log number density of -9.24 ± 0.5 by assuming a single detection within $2.6 < z < 3.2$ over the COSMOS 1.7 deg $\times$ 1.7 deg area. Then a number density of $> 5 \times 10^{10}\,M_\odot$ possible progenitors at $z > 5.5$ is derived from the results of Grazian et al. (2015). We find the Galaxy-D-based density to be one order of magnitude lower that the latter value determined from the galaxy mass-function. However, it is not yet known whether there are more galaxies with formation epochs at $z \gtrsim 6$ within the COSMOS field at similar redshifts. As discussed in Sect. 4.4, there are potentially up to 50 galaxies in the whole COSMOS with similarly red $J - H$ and $H - K$ colors, among which there could possibly be comparable or even older $z \sim 3$ galaxies. Nevertheless, we conclude that at least 10% of the $z \sim 6$ star-forming galaxies with stellar mass $> 5 \times 10^{10}\,M_\odot$ can be expected to have undergone quenching to form QGs by $z \sim 3$.

3.5.3 Quiescence in a dense environment

Given the estimated t_{50}, not only we need a quenching mechanism that could form it very early, but any galaxy rejuvenation has to be prevented thereafter. This primarily involves curbing accretion of gas or preventing the gas from forming stars. Galaxy-D belongs to RO-1001 or associated sub-halos at $z = 2.91$ (Sec. 3.4.4). This halo is expected to be fed by copious cold gas accretion (Daddi et al., 2021b) still at $z = 2.91$, all the more in its past evolutionary and assembly phases and up to the $z > 6$ quenching of Galaxy-D that inescapably happened in a progenitor halo in which accretion must have been prominent. This shows that one may have quenching and keep fully quenched galaxies (that remain so for over 1 Gyr) even with large amounts of diffuse cold gas and in presence of cold accretion. This is evidence that environmental

quenching scenarios like cosmological starvation (Feldmann and Mayer, 2015) and gas strangulation (Peng, Maiolino, and Cochrane, 2015) do not play a necessary role in quenching and/or maintaining the quiescence of high-z galaxies.

One of the alternative channels for inhibiting star formation would be AGN-driven feedback (Sanders et al., 1988; Di Matteo, Springel, and Hernquist, 2005; Hopkins et al., 2006; McCarthy et al., 2011). Although Galaxy-D is not hosting a detectable AGN (Daddi et al., 2021b), multiple works have suggested that there are enhanced AGN fractions in high-z massive QGs (e.g., Olsen et al., 2013; Aird, Coil, and Georgakakis, 2019). Hence, it is highly likely that this galaxy would have at least experienced episodes of AGN activity in the past, inevitable given its large stellar mass. These AGN episodes might have or not curbed star formation as in QSO-mode quenching. However, AGN radio-mode activity was most likely crucial to allow it to evolve passively for > 1 Gyr, as supported by the high radio detection rate of distant quenched systems (Gobat et al., 2018; D'Eugenio et al., 2021b). Furthermore, other scenarios like morphological quenching (stellar bulges preventing the collapse of gas for star formation; Martig et al., 2009) could also be at play to prevent any significant late-time star formation.

But a question still remains: what sets Galaxy-D apart from the other similarly massive but intensively star-forming galaxies in RO-1001? It appears to be simply at a later evolutionary phase, while its merging counterparts have grown their large stellar masses later and are still undergoing rapid star formation and merging growth. They might have an eventual fate as that of Galaxy-D (similar to the scenario outlined in Puglisi et al., 2021), and be hardly distinguishable in the stellar population properties once reaching $z \sim 0$ more than 10 Gyr later. While Galaxy-D has a mass-weighted age (t_{50}) of 1.6 ± 0.4 Gyr, most other quiescent galaxies at similar redshifts or above are younger PSBs and can predominantly be characterised as field galaxies (due to a lack of association with known overdensities). Therefore, the age difference between Galaxy-D and the currently known PSB population ~ 1.0 Gyr is one of the first known evidences of an age-environment relation at high-z. Interestingly, similar difference of 1 Gyr between clusters and field have also been found for local populations, where this relation has already been established (e.g., Bernardi et al., 2006; Gallazzi et al., 2021). But unlike at low-z, the age offset at $z \gtrsim 3$ is a sizable fraction of the stellar ages themselves, thereby manifesting as much more pronounced observational differences as has already been discussed in Sec. 3.5.1. In any case, Galaxy-D satisfying such a relation suggests a rapid hierarchical buildup of mass in dense environments, earlier than in the field. This in turn leads to the quenching scenarios discussed in the previous sections, mostly driven by mass and internal processes, while still agreeing with our conclusions of direct environment-dependent quenching scenarios not being necessary.

Chapter 4

Multiple faint radio-jets detected in cluster at z=2

This work has been published in MNRAS (Kalita et al., 2021b)
(MNRAS, 503.1, pp. 1174–1186)

As we progress to lower redshifts where the virialized clusters have begun taking shape, additional energy is needed to be injected into the ICM to prevent a runaway cooling through Bremsstrahlung emission (Sec. **??**). Although, singular central AGNs providing jet-driven feedback are found to be responsible for this process, we observe that (using deep radio observations) the AGN feedback maybe distributed over multiple low-powered sites. The net energy injected is still however sufficient to offset the global cooling.

4.1 Introduction

Discoveries brought by steadily increasing, mainly X-ray observing capabilities have generated a debate over the heating and cooling processes shaping the intra-cluster medium (ICM) and, by extension, their respective clusters. If left unhindered, the gravitational collapse and the subsequent cooling via X-ray emission is known to produce a steady inflow of gas into cluster cores (known as the classical cooling flow model; Fabian, 1994). This 'cooling' is characterised by significant loss of energy in a very short time ($\ll 1/H_0$). Although observed in moderate amounts, the high levels of cool gas in cluster cores expected from such a scenario have not been detected (e.g., Peterson et al., 2001; Peterson et al., 2003; Sanders et al., 2008) nor has been the resulting star formation and CO emission (e.g., McNamara and O'Connell, 1989; Edge and Frayer, 2003). Moreover, this would have also led to a galaxy population at the centre of clusters much more massive and brighter than what the well-established truncation of the high-luminosity end of the galaxy luminosity function allows (Benson et al., 2003).

With overwhelming evidence for heating mechanisms to be in place to control the cooling flows and suppress the growth of giant elliptical galaxies in cluster cores, multiple modes of energy injection have been proposed over the years. While thermal conduction (e.g., Kim and Narayan, 2003a; Pope et

al., 2006), supernova explosions (Springel and Hernquist, 2003) and turbulent mixing (e.g., Kim and Narayan, 2003b; Voigt and Fabian, 2004; Dennis and Chandran, 2005) can all be possible heating mechanisms, they have been found to be insufficient on their own (Kravtsov and Yepes, 2000; Borgani et al., 2004; Voigt and Fabian, 2004). However, AGN driven ICM heating provides an ideal self-sustained mechanism sufficient in providing enough entropy to prevent a runaway global cooling of the ICM (McNamara and Nulsen, 2007) and in the process, regulate star formation (**russell19**; Voit et al., 2015; Voit et al., 2017; Tremblay et al., 2018; Olivares et al., 2019). In the nearby universe, the interaction of radio-loud AGN-jets with the X-ray emitting ICM of clusters has been well established using high quality data from Chandra and XMM-Newton (McNamara and Nulsen, 2007; Gitti, Brighenti, and McNamara, 2012, for a review). They revealed X-ray deficit cavities that were created due to the kinetic feedback from AGN-jets from the central brightest cluster galaxy (BCG) in the heart of cluster cores. (e.g., Boehringer et al., 1993; McNamara et al., 2000; Blanton et al., 2001; McNamara et al., 2001; Heinz et al., 2002; Clarke, Blanton, and Sarazin, 2004). These cavities generate shocks which dissipate the internal enthalpy into the surrounding medium in their wakes (Jones et al., 2002; Fabian et al., 2003; Bîrzan et al., 2004). The most typical configuration observed in low redshift clusters are of bipolar jet-like flow of radio-bright plasma manifesting in the form of expanding lobes, emanating from the central dominant (cD) galaxy at the cluster centre.

There has been so far no clear evidence for jet-driven feedback at $z \geq 2$. It is noteworthy that this is a crucial epoch featuring a peak in AGN activity (Heckman and Best, 2014, for a review) along with the collapse of non-virialised 'protoclusters' to form lower-redshift virialised clusters (Overzier, 2016). Although there have been studies on the feedback from powerful radio galaxies at high redshifts (e.g., Miley et al., 2006; Venemans et al., 2007; Nesvadba et al., 2008; Hatch et al., 2009; Nesvadba et al., 2017; Markov et al., 2020) these are usually biased towards the high luminosity end and hence unlikely to be representative of a more general scenario. Complicating matters further, there have been suggestions that the energy required to maintain the ICM of a cluster in its observed thermodynamic form at low-redshifts may be different from that required to bring it to this configuration at the first place (McCarthy et al., 2008).

Keeping in mind the need to further investigate the $z \geq 2$ epoch, we present our results from the study of at a redshift of 1.99 (Gobat et al., 2011; Gobat et al., 2013). We have undertaken a sensitive radio analysis of this high redshift X-ray detected cluster primarily aimed at uncovering feedback mechanisms in place which are likely to play a major role in the evolution of this cluster. Following up on the measurements in Valentino et al. (2016) for the AGN outflows from the two known X-ray cluster AGNs, we aim to address the AGN-jet contribution in this work.

Our paper is structured as follows: after introducing in Sec. 4.2, we

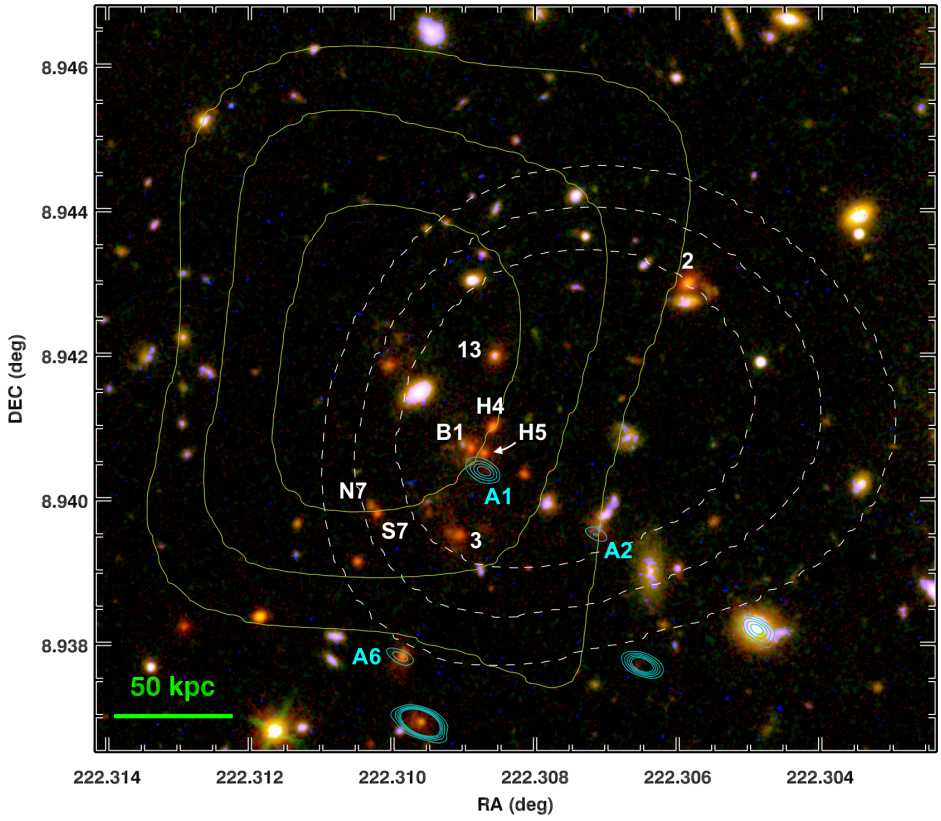

FIGURE 4.1: *HST/WFC3* color composite image of CL J1449+0856. The grey dashed contours represent the X-ray intensity map from Chandra (Valentino et al., 2016) while the extended green contours display the SZ signal tracing the mass distribution (Gobat et al., 2019). The cyan contours are the 870 μm ALMA sources. All galaxies listed in Table 6.1 have been marked.

describe the observations and data analysis in Sec. 6.3. Results regarding radio flux measurements are presented in Sec. 6.6 while their consequences are discussed in Sec. 5.7. Finally, Sec. 4.6 with the conclusions brings this paper to a close. Throughout, we adopt the concordance ΛCDM cosmology, characterized by $\Omega_m = 0.3$, $\Omega_\Lambda = 0.7$, and $H_0 = 70$ km s^{-1}Mpc^{-1}. We use a Chabrier initial mass function (IMF; Chabrier, 2003). All images are oriented such that north is up and east is to the left.

4.2 CL J1449+0856

CL J1449+0856 (Fig. 4.1), is in a phase of galaxy assembly and star formation quenching which will eventually lead to the creation of the dominant population of massive and passive galaxies that characterizes later galaxy clusters (Strazzullo et al., 2016). Unlike the less evolved protoclusters (Overzier, 2016,

ID	RA (deg)	Dec (deg)	z_{CO}	$F_{3\,GHz}$ ($\bar{}$Jy)	$F_{870\bar{}m}$ ($\bar{}$Jy)	$\log(M_*/M_\odot)$	SFR ($M_\odot\ yr^{-1}$)	Description
A2	222.30710	8.93951	1.9951 ± 0.0004	4.2 ± 1.3	515 ± 135	9.93**	94±16	Merger
A1	222.30872	8.94037	1.9902 ± 0.0005	7.8 ± 1.3	1370 ± 140	10.28**	178±19	Merger
13	222.30856	8.94199	1.9944 ± 0.0006	6.6 ± 1.3	248 ± 69	10.46 ± 0.3	39±8	AGN
A6	222.30991	8.93779	1.9832 ± 0.0007	< 2.7	709 ± 75	10.71 ± 0.3	88±11	Prominent bulge
N7	222.31029	8.93989	1.9965 ± 0.0004	< 2.7	217 ± 79	10.07 ± 0.3	31±10	Interacting
B1	222.30891	8.94071	1.9883 ± 0.0070	4.9 ± 1.3	346 ± 69	10.81 ± 0.3	38±8	Merger
3	222.30910	8.93951	1.9903 ± 0.0004	< 2.7	< 141	10.31 ± 0.3	23 ± 9	Quiescent
S7	222.31021	8.93980	$1.982 \pm 0.002^*$	< 2.7	< 150	10.48 ± 0.3	~ 8	AGN, interacting
2	222.30586	8.94297	1.98 ± 0.02	< 2.7	184 ± 73	10.81 ± 0.3	< 24	Prominent bulge
H4	222.30859	8.94100	–	< 2.7	< 135	10.9 ± 0.3	< 22	Quiescent, merger
H5	222.30872	8.94064	–	4.4 ± 1.3	237 ± 95	10.9 ± 0.3	< 27	Quiescent, merger

TABLE 4.1: The confirmed cluster members of . The first seven have molecular gas detection as reported in Coogan et al. (2018) while 2, H4 and H5, which only have photometric redshift confirmations, are additions from Gobat et al. (2011), Valentino et al. (2015), Strazzullo et al. (2016), and Strazzullo et al. (2018). * S7 lacks molecular gas detection, and hence the optical redshift calculated using *HST/WFC3* grism and *MOIRCS* spectroscopy (Gobat et al., 2011; Valentino et al., 2015) has been reported. 2σ upper limits are reported for galaxies lacking $F_{3\,GHz}$ and/or $F_{870\bar{}m}$. The star formation rates (SFR) reported are the average of the estimates from CO[4–3] line flux and the 870$\bar{}$m continuum flux reported in Coogan et al. (2018). *(** Stellar mass measurements from dynamical mass estimates (Coogan et al., 2018))*

for a review) that are more commonly found at z $\geq$ 2, features an extended X-ray emission originating most likely from its hot ICM plasma (as confirmed now by an SZ detection; Gobat et al., 2019) along with an already forming red sequence (Strazzullo et al., 2016). The observed X-ray emission is a signature of a dense ICM environment, similar to what is observed in local galaxy clusters. It also hosts a population of highly star-forming galaxies which suggests a presence of large scale-gas inflow needed for their sustenance (Valentino et al., 2015). We list the various galaxies with sub-mm continuum and/or CO line detection (Coogan et al., 2018; Strazzullo et al., 2016) within the core of in Table 6.1. These will be the galaxies that we will be restricting our work to (in the region r $<$ 200 kpc from the cluster center). However, two additional near-infrared (NIR) detected cluster members identified in the *HST/WFC3* imaging but undetected in the sub-mm observations are also included in this table and the analysis. We now discuss the primary galaxy populations in which we shall be extensively referring to in the following sections:

1. **The assembling BCG:** The two galaxies B1 and H5, detected in NIR and radio continuum, with a third (A1) detected in sub-mm and radio continuum, are expected to contribute to the formation of the future BCG of . Coogan et al. (2018) present a faint detection of the CO[4-3] line for B1 (3.7σ) and a 870μm continuum flux of 346$\pm$69 μJy whereas H5 has only been marginally detected ($\sim$ 2.5σ) at 870μm. Conversely for A1, the CO[4-3] line has been detected at 11.9σ and its 870μm continuum flux has been found to be 1370$\pm$140 μJy. Regarding the dynamics, both Coogan et al. (2018) and Strazzullo et al. (2018) conclude that B1, H5 and A1 (along with H4; Strazzullo et al., 2018) are undergoing a merger at the cluster center. Moreover, B1 and H5 (along with H4) appear to be likely suppressed/quiescent galaxies (lower main-sequence galaxies; Sargent et al., 2014) while A1 has a high SFR of 177.5$\pm$19 $M_\odot$ yr^{-1}, above what is expected from a main sequence galaxy (Fig. 8 in Coogan et al., 2018).

2. **Merging galaxies with X-ray AGN:** One of the two X-ray detected AGNs, S7, originally reported by Brusa et al. (2005) and confirmed by Campisi et al. (2009), is also part of a merging pair with galaxy N7 (with a velocity separation of $\sim$1380 at a projected separation $<$0.5$''$ or $\sim$4 kpc; Coogan et al., 2018). Although the N7-S7 system has a combined 870μm flux measurement of 217$\pm$79 μJy, it can mainly be associated with N7. This leaves S7 with a very low SFR ($\sim$8 $M_\odot$ yr^{-1}, based on a negligible CO[4-3] detection), which could be a result of its AGN activity (with an $L_x = 10^{43.7}$ ergs s^{-1}; Campisi et al., 2009) suppressing star formation (Barger et al., 2015).

3. **Isolated X-ray AGN** The second X-ray detected cluster AGN: 13, like S7, was also reported and confirmed by Brusa et al. (2005) and Campisi

et al. (2009). However unlike S7, it is isolated and features an appreciable 870μm flux of 248$\pm$69 μJy, placing it comfortably among the lower main-sequence star formation suppressed galaxies (Sargent et al., 2014).

Furthermore, there is a vast Lyman-α halo ($\geq$ 100 kpc, Valentino et al., 2016) in the core of , possibly being powered by outflows from the two cluster AGNs along with the SFR in the cluster core (with an estimated net energy outflow rate, $\dot{E}_{kin} \sim 5 \times 10^{44}$ ergs s^{-1}; Valentino et al., 2016). This is 5 times larger than the Lyman-α extended luminosity, thereby opening up a possibility that the rest is being injected into the ICM in order to offset the global radiative cooling in the cluster ICM.

4.3 Data observation and reduction

Our analysis is based on a multi-wavelength dataset that we present below. We combine 3 GHz Very Large Array (VLA) continuum data with *ALMA* sub-mm and *HST/WFC3* NIR observations to extract a complete picture of galaxies irrespective of their levels of dust obscuration. The corresponding flux measurements along with resulting star formation rates (SFR) and stellar mass (M_*) acquired from this data have already been presented in (Coogan et al., 2018) and have been reproduced in table 6.1. However, we revise the 3 GHz flux measurements in column 5 following the re-analysis of the corresponding data, which have been the primary motivation for this work. Furthermore, additional previously unreported low resolution GMRT 325MHz legacy continuum observations are also presented in this work, mainly providing upper limits.

4.3.1 JVLA S-band

Continuum observations centered at 3 GHz were obtained for the cluster using the Karl G. Jansky Very Large Array (JVLA; project code: 12A-188, PI: V. Strazzullo). These observations were carried out between February and November 2012, for a total on-source time of $\sim$ 1.1h in configuration C and $\sim$ 11.4h in configuration A. Quasar J1331+3030 was used for flux calibration in both cases. All data were calibrated and imaged following the standard procedures with the Common Astronomy Software Application (CASA; McMullin et al., 2007). Additional flagging had to be done especially in spectral windows 13, 14 and 15 for low level radio-frequency interference (RFI) which significantly affected the phase of most of the data in both configurations. For cleaning the A-configuration calibrated data, we used the TCLEAN task with a Briggs weighting scheme featuring a robust parameter of 2.0. This was aimed at facilitating the highest sensitivity possible for source detection. However, we also created images with lower sensitivities and therefore higher resolutions, in order to examine any undetected compact sources. We found none. For the masking of sources, we used

the 'auto-threshold' feature in tandem with manual selections. Frequency dependent clean components (with two Taylor terms; `nterms=2`) were also used in imaging to mitigate large-bandwidth effects (Rau and Cornwell, 2011). Additionally, we implemented widefield imaging with 128 projection planes (`wprojplanes=128`) and image deconvolution was carried out with the multi-scale multi-frequency synthesis algorithm on scales of [2,5,10] pixels (Rau and Cornwell, 2011) for improved handling of the extended sources present in the field. A similar procedure was used for C-configuration, however with a robust parameter of 0.5 in order to achieve a balance between the resolution and sensitivity. Moreover, we used the mask created during the A-configuration analysis as a starting point for the masking of strong sources. This was then modified incrementally through a mix of automated and manual cleaning. The primary beam FWHM of the 3 GHz observations was 15', and the FWHM of the synthesised beam at this wavelength was $\sim 0.83'' \times 0.67''$ at PA = -4.17 for the A-configuration data, with an RMS noise of 1.34μJy/beam over an effective bandwidth of 1.5 GHz. In the C-configuration, the synthesised beam was $\sim 7.44'' \times 6.58''$ at PA = 7.80, with an RMS noise of 12.1 μJy/beam over a similar effective bandwidth.

4.3.2 GMRT P-band

Low-frequency radio continuum observations were done using the Giant Metrewave Radio Telescope (GMRT; project code: 23_068, PI: R. Gobat) centered at 325 MHz on 23 May 2013. The bandwidth of these observations was 32 MHz and the total on-source time $\sim$ 4 hours. These data were also reduced using CASA. We executed manual calibration and RFI flagging before initiating the cleaning procedure with the TCLEAN task. In order to achieve the best combination of sensitivity and resolution possible from the data, we used the Briggs weighting scheme with a robust parameter of 0.5. The 'auto-masking' feature was implemented to handle the abundance of bright sources within the field of view. We also executed multiple rounds of phase and amplitude self-calibration due to the presence of a S/N (signal-to-noise) $\sim 10^3$ source within the primary beam. The final synthesised beam was $\sim 7.4'' \times 6.6''$ at PA = 7.8 and the RMS noise of the resulting image was 92 μJy/beam.

4.3.3 Sub-millimeter

Atacama Large Millimetre Array (ALMA) band 4 observations of the cluster were taken in Cycle 3 (Project ID: 2015.1.01355.S, PI: V. Strazzullo) while band 3 and 7 were taken in Cycle 1 (Project ID: 2012.1.00885.S, PI: V. Strazzullo). The details of these observations and the corresponding analysis have already been discussed in Coogan et al. (2018). We borrow their results from the spectral line flux extraction of CO[4-3] and CO[3-2] along with the continuum flux measurements at 870 μm obtained for each of the cluster galaxies listed

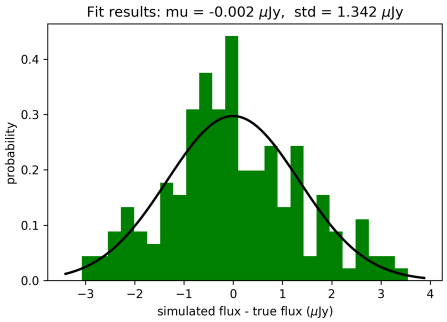

FIGURE 4.2: The histogram created out of the source detection simulation carried out within a distance of $\sim 80''$ from the centre of on the VLA 3 GHz image. The x-axis gives the difference between the measured flux of the simulated sources and their true values, while the y-axis provides a measure of the fractional occurrence. We fit a gaussian, the σ of which is the RMS noise/beam of in the data

in Table 6.1. We also use the corresponding 870 μm continuum image with a sensitivity of 67.6 μJy/beam. We direct the reader to Coogan et al. (2018) for the details of the data reduction and analysis.

Furthermore, ALMA+ACA data of at 92 GHz was presented in Gobat et al. (2019) in cycle 4 (Project ID: 2016.1.01107, PI: R. Gobat). We here make use of their results, including the Sunyaev-Zel'dovich effect (SZ) 5σ signal and the corresponding residual map.

4.3.4 X-ray: soft-band

Brusa et al. (2005) and Campisi et al. (2009) presented deep X-ray soft-band (0.5–2 keV) with *XMM-Newton* and *Chandra* telescopes respectively totalling 80 ks each. After subtraction of the point sources associated with the cluster AGNs detected using *Chandra*, Gobat et al. (2011) detected diffuse X-ray emission in the *XMM-Newton* data for at 3.5σ on scales of 20–30$''$. Valentino et al. (2016) however got an improvement on this having detected the same signal at 4σ with additional *Chandra* data with nominal exposure of 94.81 ks. We shall be henceforth using this result in our work.

4.4 Results

4.4.1 Radio continuum flux measurement

We first estimate the sensitivity reached in the VLA 3 GHz A-configuration, which we mainly use for this analysis. We use the software GALFIT (Peng et al., 2010a) to artificially place point sources (about 200 in number) in an area of $\sim 80''$ in radius centered at the location of the cluster centre. The

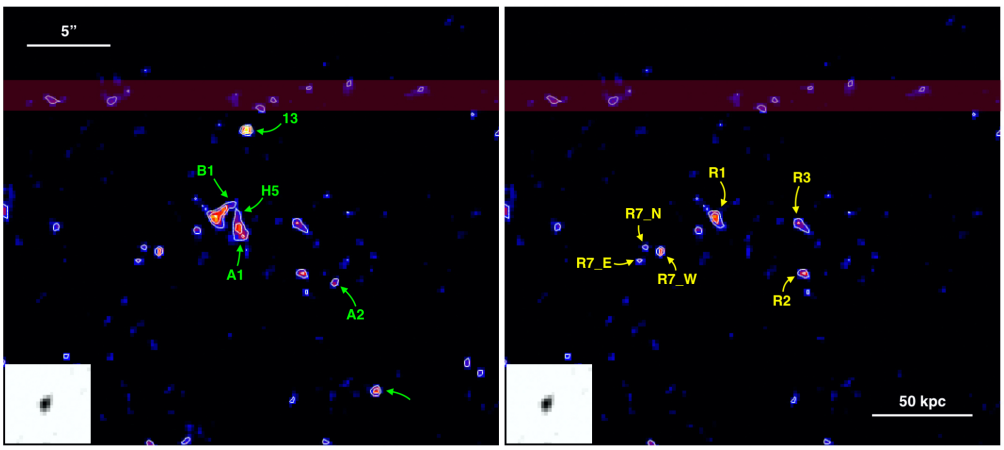

FIGURE 4.3: **(Left)** The VLA 3 GHz image of the cluster core with the galaxies in Table 6.1 detected ($> 3\sigma$) with an additional bright interloper and **(right)** the subsequent residual image after their subtraction, with the remaining major emission regions marked. The sigma contours in white are also provided for each of the images, starting from 3σ with increments of 1σ. Finally, the white boxes show the VLA 3 GHz PSF in the same spatial scale as that in the images. The maroon shaded region highlights a very faint imaging residual spike from the strongest source in the VLA field of view, which contributes to a few spurious $\sim 3\sigma$ peaks. No such systematics are present in the rest of the image.

ID	RA (deg)	Dec (deg)	$F_{3\,GHz}$ ($^{-}$Jy)	$F_{870^{-}m}$ (expected; $^{-}$Jy)	q_{TIR}	Possible galaxy association
R1	222.30911	8.94060	7.4 ± 1.3	570 ± 130	< 1.8	B1, H5, A1
R2	222.30765	8.93966	6.2 ± 1.3	480 ± 130	< 1.9	uncertain
R3	222.30775	8.94050	5.6 ± 1.3	440 ± 130	< 2.0	uncertain
R7_N	222.31031	8.94012	3.4 ± 1.3	260 ± 130	< 2.1	S7, N7
R7_E	222.31041	8.93988	3.4 ± 1.3	270 ± 130	< 2.1	S7, N7
R7_W	222.31006	8.94004	4.6 ± 1.3	360 ± 130	< 2.0	S7, N7

TABLE 4.2: The radio jet detections with their observed 3 GHz flux along with that expected at 870 μm due to star formation if these sources would have been MS galaxies. The penultimate column gives the 3σ upper limits of the q_{TIR}. The final column lists the possible source galaxies from Table 6.1 for each of the jet sources, however such associations have not been possible for R2 and R3.

flux of these sources is randomly chosen within the range 4.5 μJy – 7.5 μJy which is where most of the radio-detected cluster galaxies lie (Coogan et al., 2018). Regions that are within a distance of $1''$ from any $> 4\sigma$ pixel have been ignored during this exercise in order to prevent source confusion. GALFIT is used again on the resulting image to fit these sources with fixed positional priors. The resulting 1σ error in the point-source sensitivity is hence found to be 1.34 μJy (Fig. 4.2), which is a 34% improvement compared to that in Coogan et al. (2018). This can be attributed to the additional flagging that we implemented that would lead to an improvement in the phase solutions and thereby the imaging. Moreover, we used cleaning input parameters more in line with our primary goal of source detection, including a broader synthesised beam. The value 1.34 μJy is also equal to the RMS noise/beam of the 3 GHz image at phase centre (Sec. 4.3.1). We shall therefore be using the terms 'point-source sensitivity' and 'RMS noise/beam' interchangeably for the rest of the paper.

We then measure the 3 GHz continuum fluxes by placing point sources with positional priors from an available *HST/WFC3* image (and in case of optically dark galaxies, the 870 μm continuum ALMA data) for the galaxies listed in Table 6.1 and shown in Fig. 4.1. We choose to use point sources since the size of the galaxies are smaller than the synthesised beam half-power beam width. However, we find that there are multiple additional sources ($\geq 3.5\sigma$) that remain after the fitting and subtraction of the known galaxies at the cluster center (Fig. 4.3). Hence we execute another round of fitting with additional point sources having both position and flux free, besides the ones for the galaxies. The list of sources being fit is incrementally expanded until there are no remaining detectable sources present within the core of . We use the results from the final round of fitting where we incorporate the complete list of sources simultaneously. The resulting flux measurements of the galaxies are listed in Table 6.1, while the additional sources, discussed in detail in the next section, have been recorded in Table 4.2. It is noteworthy that we also fit point sources for two additional sources (R7_N and R7_E) that are at $\leq 3.5\sigma$. This is due to their physical proximity to R7_W and the AGN S7, details of which are discussed in Sec. 4.5.1. Following the final subtraction, we check for any residual emission around the fits. Finding none, we also conclude that all the sources detected are indeed unresolved point sources for the 3 GHz synthesized beam.

We also detect an unresolved emission centered at the region with the assembling BCG and R1 with $\sim 3.8\sigma$ significance in the C-configuration VLA observation. Using the A-configuration detections as positional priors, we attempt to measure individual flux of the sources. However, limited by the high levels of mixing of source fluxes due to a much lower resolution and a noise RMS higher by a factor of ~ 10 compared to the A-configuration image, we simply measure an integrated flux over the aforementioned region. We then use this flux as a constraint for the A-configuration flux measurements. We encounter a similar situation with our new 325 MHz GMRT observations

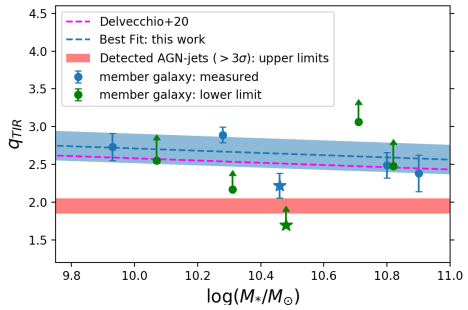

FIGURE 4.4: The total infrared and radio luminosity ratio (q_{TIR}) vs the stellar mass of the member galaxies of (listed in Table. 6.1), with the two AGNs shown with the '⋆' marker. We also plot the best fit along with the 1σ limits. We only provide the lower limit q_{TIR} for the galaxies lacking a radio detection which are obtained using the 2σ upper limits of the 3 GHz VLA data. The slope was fixed to the value determined in Delvecchio et al. (2020), the q_{TIR} vs. M_* relation from which has also been presented for comparison. Finally, the q_{TIR} upper limits of the AGN radio-jets detected ($> 3\sigma$) in this work has also been shown.

(Sec. 4.3.2), with a synthesized beam size $\sim 7''$ and an RMS of 92 μJy/beam, although it also lacks a $> 3\sigma$ detection. We hence use this data to measure an upper limit value of ~ 1.5 for the negative radio spectral index of the sources detected using VLA. We apply this in the estimation of the uncertainty in luminosity measurements in the following sections.

4.4.2 TIR-radio correlation

Using the revised 3 GHz flux values of the cluster core galaxies along with the total-infrared luminosity (L_{IR}; rest-frame 8–1000 μm) that was derived from the 870 μm flux presented in Coogan et al. (2018) using SEDs from Béthermin et al. (2015), we measure the total-infrared (TIR) and radio luminosity ratio (q_{TIR}) using the following relation (Helou et al., 1988):

$$q_{\rm TIR} = \log\left(\frac{L_{\rm IR}[\rm W]}{3.75\times10^{12}\rm Hz}\right) - \log\left(L_{1.4\,\rm GHz}[\rm W\,Hz^{-1}]\right), \tag{4.1}$$

where $L_{1.4\,\rm GHz}$(; $\rm W\,Hz^{-1}$) is the 1.4 GHz rest-frame luminosity measured from the 3 GHz fluxes ($S_{\rm 3GHz}$; $\rm W\,Hz^{-1}\,m^{-2}$) using:

$$L_{\rm 1.4GHz} = \frac{4ßD_{\rm L}^2}{(1+z)^{\alpha+1}}\left(\frac{1.4}{3}\right)^{\alpha} S_{\rm 3GHz}, \tag{4.2}$$

where D_L is the luminosity distance and α is the spectral index. Since in this section we are targeting emission due to star formation, we assume an $\alpha = -0.7$ (Delhaize et al., 2017). We do note however, this value of α is not applicable for all kinds of objects. Additionally, Coogan et al. (2018) presented the stellar mass (M_*) of all but two galaxies (H4 and H5) listed in Table 6.1 that were measured from their respective SEDs. For A1 and A2, this was rather done using their dynamical masses (Coogan et al., 2018, for further details). We use these values to plot q_{TIR} vs. M_* (Fig. 4.4). For those galaxies that are not detected at 870 μm, we use the 2σ limit as the flux in the measurement of L_{IR}.

We also add to this the results from Delvecchio et al. (2020), which is a follow-up study of Main-Sequence star-forming galaxies from Delvecchio et al. (2017) but for an M_*-selected sample from the VLA-COSMOS 3 GHz survey (Smolčić et al., 2017). Their work presents a q_{TIR} vs M_* relation as follows:

$$q_{TIR}\,(M_*, z) = 2.646 \pm 0.024 \cdot A^{(-0.023 \pm 0.008)} - B \cdot (0.148 \pm 0.013)\,,$$

where A = (1+z) and B = (log $M_*/M_\odot$ - 10). Since we just have 10 galaxies to work with, we only fit for the normalisation of the equation for a comparison of our sample with their results. As shown in Fig. 4.4, we see an agreement within 1σ (0.2 dex), although acknowledging the inability of our limited dataset to detect a more subtle digression in the behaviour of q_{TIR}, if it exists.

Furthermore, we measure the q_{TIR} 3σ upper limits (due to a lack of sub-mm detection) for the additional radio sources reported in the previous section and show their range on the y-axis of Fig. 4.4. It is immediately clear that these limits are well below q_{TIR} of the galaxies listed in Table. 6.1, as well as the those expected from the relation derived by Delvecchio et al. (2020) for main-sequence star-forming galaxies. The average q_{TIR} upper limit for the brightest of the additional sources (ignoring R7_N and R7_E due to $< 3\sigma$ radio detection significance) is 1.95, in contrast with the average q_{TIR} of the 3 GHz-detected galaxies, which is ~ 2.5 as expected (Magnelli et al., 2015). This places the radio sources at least 0.5 dex below the general behaviour of galaxies within , making it unlikely that their radio emission is due to star formation.

4.5 Discussion

4.5.1 Origin of the radio emissions

The detection of multiple emission regions that do not overlap with any of the HST or ALMA detected galaxies in the field (Figs. 4.3, 4.5) raises the question of their authenticity and physical origin. To check the former,

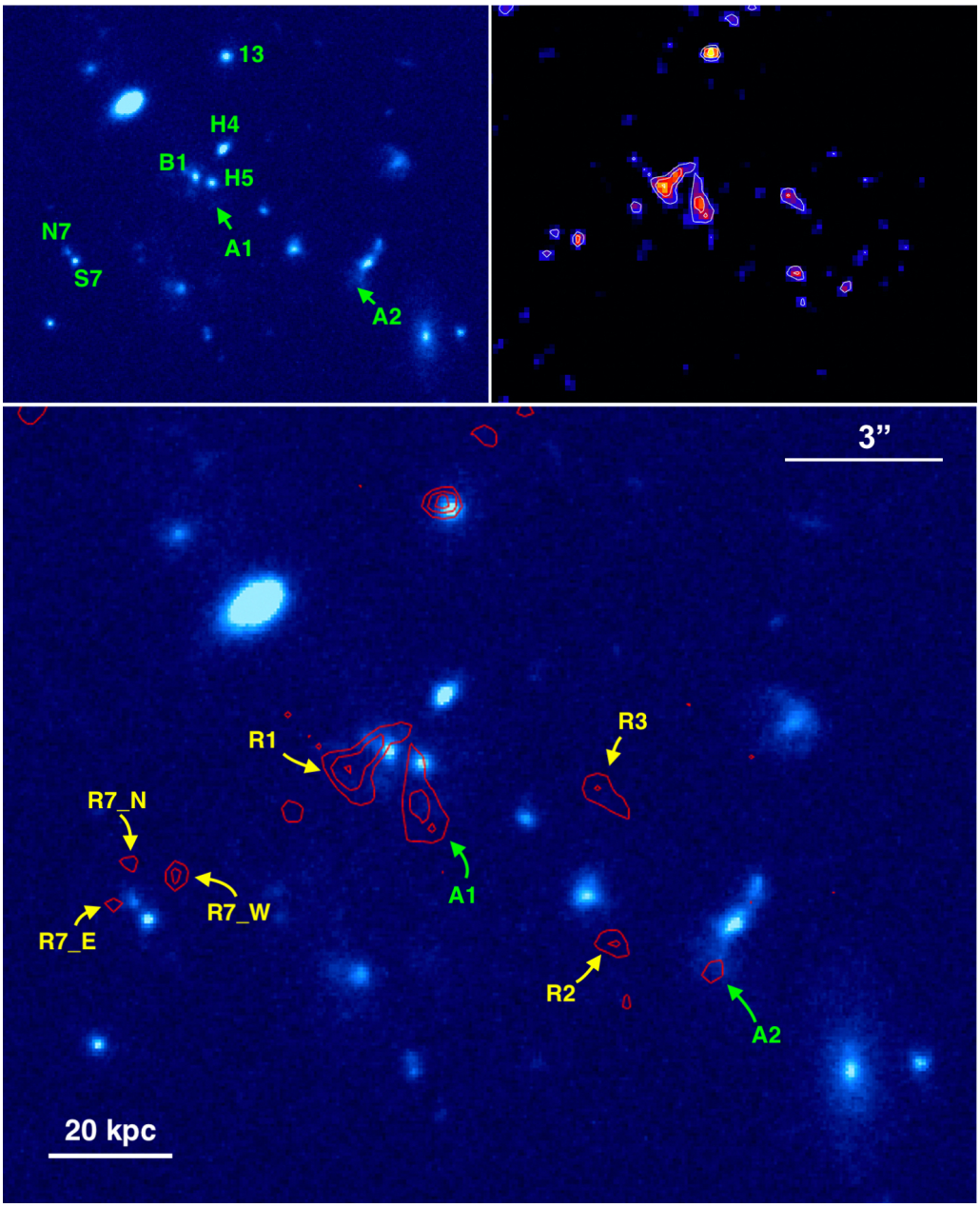

FIGURE 4.5: **(Top-left)** The *HST/WFC3* F140W image with the sources listed in Table 6.1 marked. However, 2 and A6 are not shown as they are outside the area shown and are not relevant to the results presented in this work. **(Top-right)** The 3 GHz VLA image of the region with sigma contours starting at 3σ with 1σ increments, as in Fig. 4.3. **(Bottom)** The same *HST/WFC3* F140W image with the contours of the VLA 3 GHz image along with the AGN-jets listed in Table 4.2 (in yellow) and the two *HST* undetected bright ALMA sources A1 and A2 that are also detected at 3 GHz (in green) marked.

following Jin et al. (2019) we estimate the probability of these sources being due to noise fluctuations as:

$$P = 1 - (P_o)^n$$

where P_o is the probability of finding a point source of a certain sigma within a Gaussian distribution while n is the number of synthesised beams that make up a region with radius $20''$ (or ~ 170 kpc) surrounding the centre of . This area was chosen for being large enough to cover the complete central core of the cluster. The probabilities for the three primary sources (R1, R2 and R3) are found to vary from 5×10^{-5} for R1 to 0.03 for R3. It is noteworthy that these are generous upper limits, having not considered their relative physical proximity to each other and to the known galaxies of . This is however especially important in case of the R7 group (R7_N, R7_W and R7_E) which appear clumped together and adjacent to a known cluster AGN, S7. Hence the possibility of these radio sources being generated due to noise is rather small.

We then move on to the investigation of their possible physical origins. To examine if these are simply undetected galaxies, which would mean that the radio flux could be traced back to star formation. We estimate an expected 870 μm flux for each of them. This is done by first converting the measured 3 GHz fluxes (S_{3GHz}; $W\,Hz^{-1}\,m^{-2}$) into observed frame 1.4 GHz ($S_{1.4GHz}$; $W\,Hz^{-1}\,m^{-2}$), using a spectral index of –0.7 (as expected from star formation; Delhaize et al., 2017). This is then converted to the expected flux at 870 μm using SEDs from Béthermin et al. (2012). From the resulting values listed in column 5 of Table 4.2 and the RMS noise of 67.5 μJy/beam in the 870 μm data (Sec. 4.3.3), it is evident that these sources would have been comfortably detected at $> 4\sigma$ had their emission been due to star formation. Moreover, the measurement of the 870 μm expected flux for the sources is influenced by the assumption of a constant q_{TIR} (2.64; Béthermin et al., 2012). Taking into account redshift evolution (Magnelli et al., 2015; Delhaize et al., 2017) as well as stellar mass dependence (Delvecchio et al., 2020) of q_{TIR}, we expect even higher sub-mm fluxes, making our estimates much more conservative. It is noteworthy that this lack of detected flux has already manifested as the low q_{TIR} upper limits for the radio sources in Sec. 4.4.2.

We also median stack $1.5''$ cutouts of the 870 μm continuum image from the regions of the sources and do not detect any emission even with the resulting sensitivity of 28 μJy/beam. This gives an 3σ upper limit on the average SFR of $\sim 22\ M_\odot yr^{-1}$ within the emission regions, assuming a main-sequence template. With a similar stacking analysis on our HST F140W image we also confirm a lack of stellar presence down to a generous upper limit of AB magnitude of $10^9\ M_\odot$ (for an AB magnitude of 25.9, assuming quiescence; Strazzullo et al., 2016). This eliminates a likelihood of these being galaxy merger driven tidal features, since had this been the case, there would have been structures with either detectable star formation or unobscured stellar emission. This only leaves two likely candidates: AGN

radio-jets or cluster merger driven diffuse emission (radio halos and relics), both resulting from synchrotron emission. Given the concentrated nature of the emission sites, we can reject the latter. During the flux measurements (Sec. 4.4.1), we were able to account for all the detectable flux using PSF fitting, which suggests that the extent of the emission regions are within the A-configuration synthesised beam size of VLA at 3 GHz (FWHM $\sim 0.7''$ or 6 kpc). Moreover, most of these sites are spatially adjacent to either the assembling BCG members (B1, H5 and A1) or the south-eastern X-ray detected cluster AGN, S7 (Fig. 4.5), hence pointing towards the radio-jet case.

We note our reliance on the positional accuracy of our VLA image with respect to the *HST* astrometry. To check for any intrinsic offset between the two, we select all sources detected with $\geq 10\sigma$ significance in VLA and also seen in the *HST/WFC3* F140W image, over a range of distances from the radio-jet sites ($15''$–$70''$). We find nine such objects, which we fit with PSFs/Gaussians to get their positions in each of the images, separately. These are always found to be in agreement for each source within their respective intrinsic positional uncertainty in the VLA image, which can be estimated as $\frac{1}{2}\frac{\mathrm{FWHM}}{(\mathrm{S/N})}$ (Ball, 1975; Condon, 1997). We also repeat the same exercise with respect to the ALMA 870 μm image and draw the same conclusion, although with only 4 sources that are detected at $\gtrsim 6\sigma$ at 3 GHz. Hence, we infer that the positional accuracy of the radio-jets are only limited by their respective positional uncertainties, which in the case of R1 for example is $\sim 0.1''$.

4.5.2 Tracing the sources of the jets

Besides the detection of the radio-jets, the source of the jets are also worth noting if we are to understand better the role they play in the general evolution of the cluster. We have listed the probable location of the source galaxy for each of the jets in the final column of Table 4.2, simply from their respective physical proximity (Fig. 4.5). Starting with the assembling BCG described in detail in Sec. 4.2, it is likely that R1 is originating from one of its members. This could in fact be the progenitor of a possible central radio AGN that is observed in many z=0 clusters. Moreover, there is another faint detection below R1 which could simply be the remnant of a previous phase of jet emission. However, due to the very low significance ($< 2.5\sigma$) and large distance from any of the known cluster galaxies, we have not included it in our analysis.

Moving slightly to the south-east, we have the R7 group surrounding N7 and S7, which is a merging pair with the latter being an X-ray detected AGN (Campisi et al., 2009). Hence it is highly likely that they are hotspots from the jets emerging from S7 with a level of bending that is common for AGNs interacting with the dense medium of cluster cores. Similarly, R2 could be expected to be stemming from A2. On the other hand, for the source R3, although lying within the cluster core, we can only speculate about a yet

undetected highly obscured or a 'switched-off' AGN in a very faint galaxy producing it.

4.5.3 Radio emission: How much do we really have?

To corroborate the radio-jet conclusion, it is important to understand if there is an overall radio excess and therefore an abundance of general AGN-jet activity within . Since we are also aiming to investigate the differences in the mode of operation of radio-jets at higher redshifts compared to their low redshift counterparts, we make a comparison to the results presented in Mittal et al. (2009). Here they use the X-ray flux-limited HIFLUGCS sample (Reiprich and Böhringer, 2002) with a mean $\langle z \rangle \sim 0.05$ in an attempt to understand the coupling between radio-jet based AGN activity and the surrounding hot ICM. For this they measure the total radio luminosity (10 MHz – 10 GHz) from the radio-jets of the centrally placed AGN of each cluster. However in , there seems to be multiple sites of AGN jet emission, the implications of which are discussed in the following section. To make a comparison, we add up the contributions of all the detected jets in place of the jets from a central AGN, which gives us a flux of 30.6 ± 3.3 ⁻Jy and a corresponding integrated radio luminosity (10 MHz–10 GHz rest-frame) of 2.1 (± 0.2) $\times 10^{41}$ ergs s^{-1}.

It is worth noting however that this luminosity calculation is strongly dependent on the radio spectral index which can be anywhere between –0.7 (as expected in case of star formation; Delhaize et al., 2017) to –1.5 (the upper limit we calculate based on our GMRT 325 MHz measurements). However, to use a spectral index within this range, we decide to borrow the results of Hovatta et al. (2014). With a robust sample of 190 extragalactic radio-jets, they find a mean spectral index of -1.04 ± 0.03 that we use in our calculation. This is also extremely close to the average spectral index of -1 measured by Mittal et al. (2009) for their sample. Although, it is worth noting that the limits of –0.7 and –1.5 result in integrated luminosities of 0.8 $\times 10^{41}$ ergs s^{-1} and 15.3 $\times 10^{41}$ ergs s^{-1} respectively. We can also have flux boosting contributions and we estimate a generous upper limit of the resulting overestimation of the jet flux to be $\sim 40\%$, by assuming an additional noise contribution of 1.5σ for each source. However, accounting for this possible contribution does not change the conclusions of this paper.

Finally, with the additional information of the X-ray luminosity (7.2 $\times$ 10^{43} ergs s^{-1}) at 0.1–2.4 keV from the ICM of (Gobat et al., 2011; Valentino et al., 2016), we place this cluster among the other galaxy clusters from the Mittal et al. (2009) HIFLUGCS sample in Fig. 4.6. However the caveats of this comparison should be borne in mind. The HIFLUGCS $\langle z \rangle \sim 0.05$ sample occupies an entirely different epoch and evolutionary status relative to at z = 1.99. Differing from the low redshift clusters dominated by hot ICM plasma, clusters at $z \sim 2$ are rather just transitioning into this phase from an epoch featuring inflow of filamentary cold gas penetrating deep into the hot ICM (Valentino et al., 2015; Overzier, 2016). This difference is crucial

since AGN-jet activity is known to be coupled with the level of accretion the central BH experiences. Moreover, Mittal et al. (2009) employed a cut-off distance between the ICM X-ray peak and the radio BCG based on a study by Edwards et al. (2007) which suggested that only those BCGs that lie within $70h_{71}^{-1}$ kpc of the X-ray peak of a cooling flow cluster have significant line emission and therefore enough activity to counteract the cooling. Although it is uncertain whether this conclusion is still valid at $z \sim 2$, we do point out that the radio-jets detected in are concentrated within a region of $70h_{71}^{-1}$ which includes the assembling BCG. However, we can only estimate a rough peak of the X-ray emission with the limited S/N, which still seems to be within this region.

These caveats also bring with them the points of interest once we make the comparison with the sample of galaxies in Mittal et al. (2009). Although is at a very different redshift, its radio and X-ray luminosities place it at the upper end of the scatter in Fig. 4.6, without showing any stark disparity. One may bring up the aspect of us having integrated over the radio flux of all the observed jets. But repeating the same analysis with the central jet (R1) only brings down the luminosity by a factor of 4, keeping it well within the scatter and still slightly above the average. Moreover, the decentralised and plural nature of the jet emission in may be indicative of the inherent dynamics of the cluster core since these jets are probably coupled to accretion of material into the region. This would be a plausible situation for , given that it is most likely still experiencing cold gas accretion into its core (Valentino et al., 2016).

However, a similar attempt at comparing to clusters (or protoclusters) at high redshifts is much more difficult. Firstly, emission from field radio sources as faint as those in ($L_{1.4\,GHz} \sim 10^{24}\,W\,Hz^{-1}$) at $z \sim 2$ is mainly attributed to star formation, with contributions from AGN activity being minimal and hard to disentangle (for a review; Padovani, 2016). Studies of high redshift clusters with associated radio-jets have been limited to ones with high luminosity radio galaxies ($\gtrsim 10^{27}\,W\,Hz^{-1}$, e.g., Wylezalek et al., 2013; Nesvadba et al., 2017; Noirot et al., 2018; Markov et al., 2020). This makes the detection of faint radio-jets within a cluster at $z \sim 2$ relatively new.

4.5.4 Quantifying the feedback

The X-ray detectable 'cavities' which result from AGN-jet activity usually allow us to quantify the amount of effective heating experienced by the ICM. The energy content of these cavities, E_{cav}, is given by the sum of the product of the pressure and volume (pV), which is work done by the jet to create the cavity, and the internal energy of the radio lobes. This comes out to be $4pV$ under the assumption that the cavity is dominated by relativistic plasma. Taking this into consideration, dividing the E_{cav} by the cavity age, t_{cav}, gives the cavity power, P_{cav}, which can be considered as the lower limit of the total AGN jet power as it gauges only the 'observable' effects of the jets.

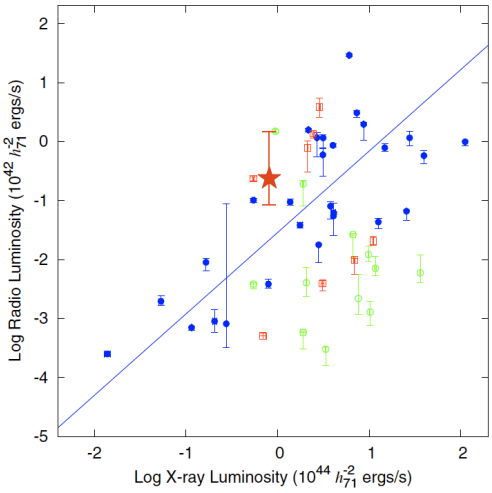

FIGURE 4.6: The total radio luminosity from radio-jets vs X-ray luminosity of the ICM (without any AGN X-ray contribution) plot from Mittal et al. (2009) for strong cool-core ($t_{cool} < 1$ Gyr; filled blue circles), weak cool-core (1 Gyr $< t_{cool} <$ 7.7 Gyr; open green circles) and non cool-core ($t_{cool} > 7$ Gyr; open red squares) clusters, with t_{cool} representing their central cooling times. has been represented here with the red '$\star$'. The observational error bars denote the systematic variation introduced with the change of the α used in the calculation of the radio luminosity. We use 0.7 (the average for star formation) as the lower limit, while for the upper limit we have 1.5 (limit estimated using the 325 MHz GMRT observation).

But such a direct calculation would not be possible in this work as no cavities were detected in the 4σ X-ray diffuse emission (Valentino et al., 2016). However, an alternative method to measure the P_{cav} is given by its observed correlation with the radio luminosity, L_{radio}. Moreover, the use of such a relationship allows us to make measurements directly on the radio data (e.g., Best et al., 2007), thereby avoiding the issue of cavity detectability in shallow X-ray images (which is the case in our work). The aforementioned radio luminosity is usually measured from the jets of the central AGN of the cluster which is observed to be the source of entropy injection in nearby, evolved clusters. is however undergoing rapid evolution with it's central BCG yet to be assembled and lacks a central jet-hosting AGN. It rather features multiple AGN-jet sites distributed over the cluster core. We can hence use the integrated radio luminosity from all these jets (L_{radio}; 10 MHz–10 GHz rest-frame) that can be related to the cavity power (P_{cav}) through the following relation (O'Sullivan et al., 2011):

$$\log P_{cav} = 0.71\,(\pm 0.11)\log L_{radio} + 2.54\,(\pm 0.21)\,, \tag{4.3}$$

where L_{radio} and P_{cav} are in units of 10^{42} ergs s^{-1}. However, one should bear in mind that this relation is still affected by uncertainties due to the assumption of $E_{cav} = 4pV$ and the detectability of cavities within the sample used in O'Sullivan et al. (2011) amongst others, as discussed in their work.

The P_{cav} we estimate for is also dependant on the radio spectral index, α, of the sources. Keeping in mind the caveats discussed in the previous section, we use $\alpha = -1.04$ (from Hovatta et al., 2014) to get L_{radio} = 2.1 $(\pm 0.2) \times 10^{41}$ ergs s^{-1}. We put this in Eq. 4.3 to get a $P_{cav} = 1.14\ (\pm 0.55) \times 10^{44}$ ergs s^{-1}. This power is $\sim$ 0.25 times the already estimated energy injection rate calculated by Valentino et al. (2016) from SFR and AGN outflows ($\sim 5 \times 10^{44}$ ergs s^{-1}). This is a significant addition to the already abundant energy injection being experienced by the core of and would likely also contribute to the Lyff halo through shocks and instabilities (Valentino et al., 2016; Daddi et al., 2021b) besides contributing to the overall entropy of the cluster ICM.

Furthermore, one should also consider the age of the electron population within the jets, which determine the steepness of the spectrum. Although a determination of the age is not possible without a better sampling of the radio spectrum, the fact that we have multiple emission makes the likelihood of the jet activity to have just been 'switched-on' negligible. This could in fact result in a range of spectral indices up to the –1.5 limit we have determined from the 325 MHz data, for the different sources. The details of this distribution, although indeterminable with the current data, have large implications especially since the –1.5 limit results in a $P_{cav} \sim 4.7 \times 10^{44}$ ergs s^{-1}. This is an increase of more than a factor of 4 and would make the AGN-jet feedback almost equal to the rest of the instantaneous

energy injection within . This is especially important since steep spectra ($\alpha > 1$) are more likely in dense environments due to confinement of the relativistic plasma by the inter-galactic environment, which also prevents fading radio-jets from dissipating quickly (e.g., Giacintucci et al., 2011). This makes the aforementioned possibility of multiple jets with a range of (high) spectral indices co-existing even more likely. However, the upper limit of -1.5 may be too high a spectral index based on the compactness of the radio sources ($\lesssim 10$ kpc, Fig. 4.5). A more reasonable upper limit is possibly closer to –1.2 (using the age-size relation presented in Carilli et al., 1991). This gives a $P_{cav} \sim 1.8 \times 10^{44}$ ergs s^{-1}.

4.5.5 Effect of low cluster mass

An additional caveat to the comparison of to other mature clusters with AGN-jet based energy injection (Sec. 4.5.3) is its mass of 5–7 $\times 10^{13}$ $M_{\odot}$ (Valentino et al., 2016), which places it rather in the galaxy group regime. Giodini et al. (2010) demonstrated that the mechanical energy from jets is comparable to the binding energy in galaxy groups, while it is lower by a factor of $\sim 10^2$–10^3 in clusters. This makes jets sufficient in unbinding significant fractions of the intragoup medium. Although the measurement of the binding energy is not possible in due to a low significance detection of the ICM X-ray emission, its galaxy group-like mass could suggest that we are underestimating the consequences of the detected radio-jets on the overall evolution of . Hence, deeper X-ray future observations of the ICM will prove crucial.

4.5.6 Galaxy 13: a possible contributor

During the analysis of the jet driven feedback in , we have ignored galaxy 13 due to a lack of evident jet-like emission. However, it does showcase a high 3 GHz radio flux ($6.6 \pm 1.3\,\mu$Jy) only two-thirds of which can be accounted for by the intrinsic SFR. The rest may still suggest a level of kinetic feedback present in this galaxy with the jets having not been detected due to projection effects. Assuming this to be true, this would only lead to an increment of $\sim$ 6% in the total jet power. Although, this is a small contribution, it is very important to note that this galaxy represents an additional site of AGN activity (with or without jets) which has crucial implications on our understanding of , as described in the conclusion of this work.

4.5.7 The SZ residual

Whenever strong radio-jets occur within dense cluster cores, resulting under-densities are observed due to the gas in the ICM being blown out by the kinetic feedback to form cavities. These cavities are usually spatially co-incident with the lobes of the radio jet and can be observed in X-ray (for

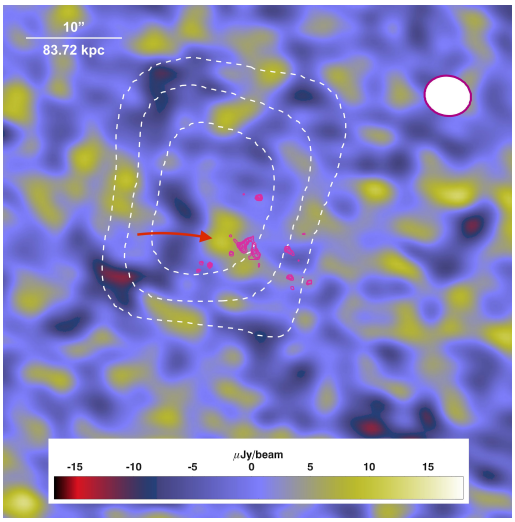

FIGURE 4.7: ALMA 92 GHz residual image of borrowed from Gobat et al. (2019), after subtracting both the point sources and the SZ signal from the cluster (denoted by the white dashed contours). The colour bar at the bottom denotes the residual flux per beam with a positive signal indicating a lack of gas density and vice-versa. This has been overlaid with the radio contours in magenta while the white-filled red ellipse shows the size of the synthesised ALMA beam. The red arrow points to the possible under-density due to the jets.

a review, Fabian, 2012). But with the diffuse X-ray ICM emission having been observed at only 4σ (Valentino et al., 2016), it is not possible to detect variations indicative of cavities. However, in case there are under-densities, they should also manifest in the thermal-SZ map of the cluster as positive signals due to a lack of the SZ decrement (that is otherwise expected from the dense ICM gas; Komatsu and Seljak, 2001) in the 92 GHz flux at z=2. Gobat et al. (2019) presented a detailed study of this for and also generated a residual map after the subtraction of the 5σ SZ signal of the ICM. In Fig. 4.7 we superimpose this map with the location of the radio-jets. Interestingly, there seems to be a hint of an under-density (in the form of a positive signal), albeit of a 2σ significance, between sources R1 and R7_W which are two of the brightest sources and therefore strongest jets in our list. This is suggestive of a marginal decrease in the electron density due to possible presence of jet driven feedback, in line with our conclusions.

4.5.8 Inverse-Compton contribution

Following the detection of radio-jets within , we revisit the detection of diffuse X-ray emission in the cluster (luminosity at 0.1–2.4 keV $= 7.2 \times 10^{43}$ ergs s^{-1}; Gobat et al., 2011; Valentino et al., 2016). This has been attributed to the hot ICM of the cluster. However, it is now imperative to

check any possible contributions from the newly detected jets to the cluster X-ray flux through inverse-Compton (IC) scattering (Worrall, 2009, for a review). The cause of this is the relativistic electron population (already emitting in radio from the jet sites) upscattering the photon-field primarily from the Cosmic Microwave Background. Fabian et al. (2009) demonstrated that radio emission corresponding to IC is best detected at lower frequencies, as higher frequencies like 3 GHz may not be sensitive enough to aging electron populations with steep spectra. Hence we decide to only use the GMRT 325 MHz upper limit for this estimation. Using the equations (4.53) and (4.54) in Tucker (1975), we get an upper limit IC contribution of 6.5 $\times 10^{42}$ ergs s^{-1} ($\sim$ 10% of the X-ray luminosity). This is measured using a Lorentz factor of 10^3–10^5 and a photon index of 2, the reasons for which has been provided in Fabian et al. (2009) who estimate the IC contributions for HDF130 at z=1.99: a case very similar to ours.

Furthermore, we stack the *Chandra* X-ray data at the locations of the jets to observationally confirm a lack of IC X-ray emission. The generous upper limit hence derived from the total counts detected is 2.2 $\times 10^{42}$ ergs s^{-1} or 3% of the ICM X-ray luminosity. We do not include the R7 group in this analysis though, in order to prevent contamination from the X-ray flux of the core of the AGN in the adjacent S7. However, we are certain that we do not miss any contribution to the ICM X-ray luminosity since its value of 7.2 $\times 10^{43}$ ergs s^{-1} was calculated after subtracting the flux from S7 (Gobat et al., 2013; Valentino et al., 2016). Hence, even if there is minimal contribution from the R7 jets, it has already been excluded. Therefore, we conclude that there is no major IC contribution to the cluster X-ray luminosity, which has already been found to trace the cluster mass due to an agreement with the SZ measurements presented in Gobat et al. (2019).

4.6 Summary and Conclusion

We have presented a detailed analysis of the radio behaviour of , motivated by a revised reduction of 3 GHz VLA observations as well as new 325 MHz GMRT data. The main results of this study are as follows:

1. We reach a sensitivity of 1.34 μJy/beam at 3 GHz, which is a $\sim$34% improvement compared to the previous results presented in Coogan et al. (2018). This improved sensitivity allowed us to detect multiple radio emission regions without any counterparts in our *HST/WFC3* NIR as well as 870 μm continuum data. We also use median stacking to check for low levels of star formation or stellar populations at these sites that would result in faint emissions in sub-mm or NIR respectively, and find none within the detection limits. Finally, the possible association with known galaxies due to physical proximity for 4/6 of these objects without any overlap led us to conclude them to be AGN radio-jets.

2. Detection of multiple radio-jet sites in a cluster core is in stark contrast to low redshift counterparts, which predominantly feature centrally placed radio AGN-jets. We furthermore measure a total flux of $30.6 \pm 3.3\,\mu$Jy from all the detected jets. Using a spectral index of –1.04 based on the study by Hovatta et al. (2014) for radio-jets, we determine an integrated radio luminosity (10 MHz – 10 GHz) of 2.1 (± 0.2) $\times 10^{41}$ ergs s^{-1} which places at the radio-bright end of the radio-jets to X-ray luminosity relation for low redshift clusters (Fig. 4.6). Additionally, given that the radio luminosity is measured only from the central dominant AGN-jets in Hovatta et al. (2014), we point out that using only the jet detected at the site of the BCG assembly (R1) for this analysis does not change this conclusion.

3. With the spectral index of –1.04, we further estimate that $\sim$ 20% of the total instantaneous energy injection into the ICM of can be attributed to AGN jets, with a $P_{cav} = 1.14\ (\pm 0.55)\ \times 10^{44}$ ergs s^{-1}. Although, this could be much higher (up to $4.7\ \times 10^{44}$ ergs s^{-1}) given that the multiple sites suggest an extended period of AGN-jet activity which could lead to a spectral index even up to the limit of –1.5 measured from our 325 MHz GMRT data. However, a more realistic upper limit is found to be closer to –1.2, which gives $P_{cav} \sim 1.8\ \times 10^{44}$ ergs s^{-1}. Only deeper low-frequency observations can settle this uncertainty.

4. We make 3 GHz flux measurements to estimate the TIR-radio luminosity ratio (q_{TIR}) of the galaxies within the cluster core. We find agreement within 0.2 dex with the results of Delvecchio et al. (2020) for star-forming main sequence galaxies.

Based on this work, we hence expand our current understanding of . We begin with the revised 3 GHz flux measurements and the subsequent FIR-radio correlation analysis. We find the cluster galaxies to be in agreement with the relation reported in Delvecchio et al. (2020), hence suggesting that galaxies in clusters follow the same FIR-radio correlation. This conclusion also reinforces the use of radio luminosity as an SFR tracer even in dense environments. However, as it is beyond the scope of this work, studies of a larger sample of clusters would be highly encouraged to understand more subtle effects of density on this relation.

Moving on to the detection of multiple sites of AGN jet-like emission which has been the primary focus of this work, we revise our narrative of the cluster galaxies. It is worth noting that showcases an SFR $\sim 1000\ M_{\odot} yr^{-1}$ at its core, which is most likely being driven by residual cold-gas accretion into the cluster core (Valentino et al., 2016). The same accretion could very well be resulting in the presence of the two radiative-mode radio-detected AGNs in the cluster core, at least one of which is featuring clear jets, since they are known to be present in environments with high levels of accretion (Lin et al., 2010) and star formation (Kauffmann et al., 2003; Kauffmann and Heckman,

2009). The situation at the site of the BCG assembly is a little more obscure however. The jet R1 may be stemming from the two massive quiescent bulge-dominated galaxies (B1 and H5) or the highly star-forming A1 which could be hosting a highly obscured AGN core. However in this case as well, the cause of AGN activity can be linked to accretion, especially since the same accretion is most likely driving the star formation in A1 (Valentino et al., 2016). Although, one cannot dismiss an additional contribution from merger activity in (Coogan et al., 2018) towards the triggering of AGN-jet activity. This is especially important since both the assembling BCG and the N7-S7 pair are known to be undergoing mergers and are the sites of R1 and the R7 group respectively.

Regarding the effect of the jets on the hot ICM of , we revisit the results of Valentino et al. (2016) that were motivated by the discovery of a giant 100 kpc extended Lyff nebula in the cluster core. They found the AGN outflows from the two radiative mode AGNs (13 and S7) to be the most likely candidates powering the nebula, thereby disfavouring an established classical cooling flow in the cluster core. Adding to this is the presence of multiple sites of AGN-jet driven energy injection, which has led us to conclude the presence of a dispersed mode of AGN kinetic feedback in . Since the centralised AGN driven feedback at the cores of low redshift CC clusters is crucial for balancing the global cooling (McNamara and Nulsen, 2007, for a review), the peak of which is usually coincident with the AGN itself (Edwards et al., 2007), the lack of such an arrangement would suggest an absence of a classical cooling flow. This is hence in line with the conclusion of Valentino et al. (2016). Moreover, it is highly likely that the jets are also contributing to the powering of the Lyff nebula which is already too high in luminosity (by a factor of 10–1000) for it to be present in a CC cluster. Another conclusion that can be drawn is the improbability of a change in the status-quo with any phases of cooling flow domination in the immediate future of during an absence of AGN activity, since this is unlikely to be allowed given the multiple AGN sites. Hence, we are possibly witnessing a 'steady state' of the cluster ICM due to a rather constant version of the AGN feedback driven loop (McNamara et al., 2005; Rafferty et al., 2006; Gaspari and Sądowski, 2017).

The lack of a classical cooling flow however should not be interpreted as a sign of low overall AGN-jet driven feedback in . We demonstrate that the ratio of the radio luminosity from jets and the ICM X-ray luminosity is higher than what is usually expected even in CC clusters (Fig. 4.6). This is especially crucial considering the sizable contribution of the jets to the total energy injection rate in this cluster which we estimate to be $\sim 20\%$, but could in fact be even higher if one considers possible effects of an older electron population. It is unclear although if this puts on a fast track to becoming a non cool-core cluster (with $t_{cool} > 7$Gyr at the cluster core, Fig. 4.6; Mittal et al., 2009) or could it still end up turning into a CC cluster with a central dominant AGN spewing out relativistic jets and harboring a classical cooling

flow at later stages. Uncovering evolutionary pathways, if they exist, would require a larger sample of galaxy clusters at high redshifts with detailed study of the interaction between jets and their ICM. Deeper ALMA SZ observations tracing the morphology of the ICM of clusters could facilitate such a study in the future. However, a clear picture would most likely only be possible in the 2030's with the coming of ATHENA and with it an era of high sensitivity X-ray observations. Until then, it is imperative that we keep attempting similar studies as that done for to pave the way for future efforts.

Chapter 5

Resolving the kinematics of extreme ram-pressure stripping at $z \sim 0.3$

This work has been published in ApJ (Kalita and Ebeling, 2019)
(ApJ, 887.2, p. 158)

Exploring the effects of environment quenching mechanisms, we concentrate on dynamical characterizing the effects of ram-pressure stripping for the first time in an intermediate redshift of z $\sim$ 0.3. This chapter discusses the analysis of deep optical imaging along with IFU spectroscopy for a spectacular 'jellyfish' late-type galaxy. The results not only show the localized, albeit temporary, enhancement of star-formation due to ram-pressure stripping, but also provides clues to the trajectory of entry of the galaxy into the host cluster.

5.1 Introduction

Galaxy evolution, specifically the transformation from late- to early-type galaxies, has long been known to depend sensitively on environment. Since low relative velocities are conducive to collisions, galaxies inhabiting low-density environments evolve primarily through mergers; by contrast, ram-pressure stripping (Gunn and Gott, 1972) and galaxy harassment (Moore et al., 1996) are key drivers of evolution in groups and clusters of galaxies where environmental effects dominate (e.g., Oemler, 1974; Dressler, 1980; Whitmore, Gilmore, and Jones, 1993; Dressler et al., 1997). Ram-pressure stripping (RPS) in particular has emerged as the perhaps most efficient evolutionary process through which galaxies can lose their gas content, a critically important element of the transformation of gas-rich spirals to gas-devoid ellipticals.

For galaxies traversing the dense, gaseous environment of clusters, the physics of RPS go well beyond the interplay between an external pressure gradient and a restoring gravitational force. In addition to the effects of turbulence and viscous stripping (e.g., Roediger and Brüggen, 2008), the large-scale kinematics of the interstellar medium (ISM) need to be considered if we want

to understand the gradual degradation of spiral-arm features (Bekki, Couch, and Shioya, 2002) or the sequence of stripping, currently understood to start with the loosely bound peripheral ISM, mainly HI (**haines84**; Cayatte et al., 1990; Vollmer et al., 2001; Kenney, van Gorkom, and Vollmer, 2004; Chung et al., 2009; Kenney et al., 2014; Kenney, Abramson, and Bravo-Alfaro, 2015; Jaffé et al., 2015; Jaffé et al., 2016). Whether the molecular gas detected in the wake of galaxies affected by RPS was similarly removed from the disk is much more uncertain; a competing hypothesis posits that it formed *in situ* through collapse of atomic gas clouds (Vollmer et al., 2008; Fumagalli et al., 2009; Boselli et al., 2014; Jáchym et al., 2014; Moretti et al., 2018).

Observations at UV and optical wavelengths of ionized gas that reveal the locations and rate of star formation represent a powerful tool in this context, as they highlight regions in which the collapse of gas clouds during stripping leads to the formation of young stars (Cortese et al., 2007; Yoshida et al., 2008; Hester et al., 2010; Owers et al., 2012; Kenney et al., 2014; Fumagalli et al., 2014; Bellhouse et al., 2017; Jaffé et al., 2018; Vulcani et al., 2018; Poggianti et al., 2019). It remains debated though, both observationally and in numerical simulations, whether RPS-triggered star formation adds significantly (or, in fact, at all) to an increase in the galaxy's overall star formation rate (SFR; Kronberger et al., 2008; Kapferer et al., 2009; Tonnesen and Bryan, 2012; Roediger et al., 2014), and whether any enhancement of the star-formation rate occurs primarily in the disk or in the wake of stripped galaxies.

By revealing the kinematics of the ISM, in both disk and wake of galaxies undergoing RPS, integral-field unit (IFU) observations of RPS cases in the nearby Universe have provided key insights into the complex physical processes governing ram-pressure stripping (e.g Merluzzi et al., 2013; Fossati et al., 2016; Bellhouse et al., 2017; Gullieuszik et al., 2017; Poggianti et al., 2017; Vulcani et al., 2018; Fossati et al., 2019). Extending IFU studies of RPS to higher redshifts, we here attempt a detailed IFU-based characterization of A1758N_JFG1 (Fig. 5.1), a spectacular "jellyfish" galaxy discovered in our recent study of A1758N, an exceptional cluster merger at $z = 0.28$ (Ebeling and Kalita, 2019, hereafter EK19) , as a first step toward a more comprehensive understanding of the impact of cluster environment and relaxation state on RPS events at ever increasing redshifts.

Our paper is structured as follows: after introducing A1758N_JFG1 in Sec. 6.2, we summarize the observations upon which our work is based in Sec. 6.3. Data analysis procedures are discussed in Sec. 6.5, and results presented in Sec. 6.6. We then describe our simple three-body model of the gravitational interactions between A1758N and A1758N_JFG1 in Sec. 5.6, before interpreting and discussing our findings in Sec. 5.7. A summary is provided in Sec. 5.8. Throughout this paper we adopt the concordance ΛCDM cosmology, characterized by $\Omega_m = 0.3$, $\Omega_\Lambda = 0.7$, and $H_0 = 70$ km s^{-1} Mpc^{-1}. All images are oriented such that north is up and east is to the left.

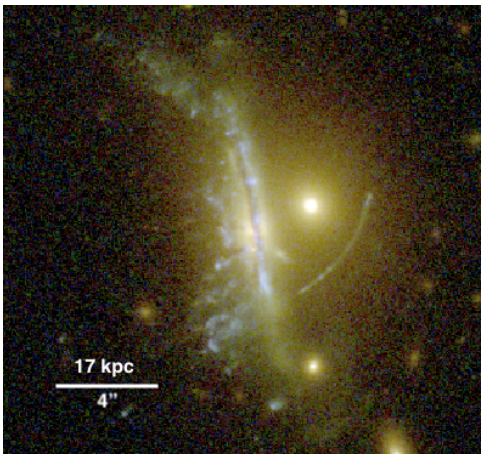

FIGURE 5.1: A1758N_JFG1, a newly discovered spectacular example of ram-pressure stripping in a galaxy cluster at $z > 0.2$ as seen with HST / ACS. Our target is viewed projected onto a cluster elliptical and an associated giant gravitational arc, both visible just west of this textbook "jellyfish" galaxy.

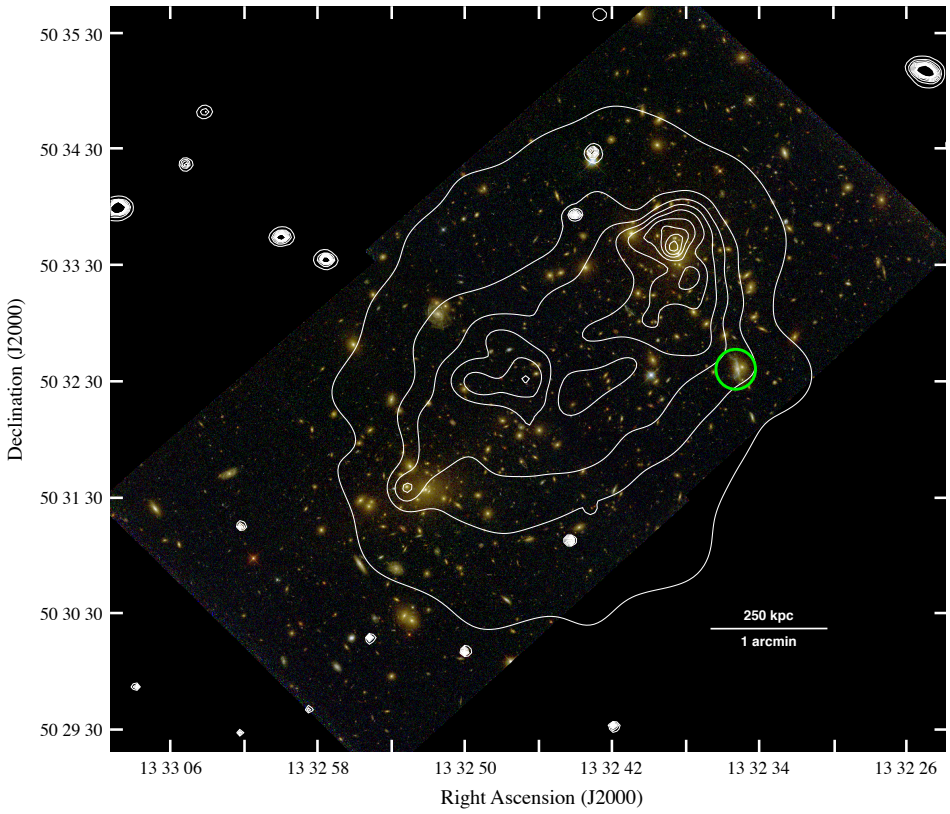

FIGURE 5.2: A1758N as seen with HST / ACS (false-colour composite from F435W, F606W, and F814W images collected for GO-12253). Overlaid in white are linearly spaced contours of the adaptively smoothed X-ray surface brightness in the 0.5–7 keV band as observed with Chandra / ACIS-I. A1758N_JFG1 is marked by a green circle.

5.2 A spectacular case of ram-pressure stripping

The target of this work, A1758N_JFG1 (Fig. 5.1) was first noted by Ragozzine et al. (2012, their Fig. 3) in the context of their weak-lensing analysis of the A1758 double cluster (Abell, 1958). However, focusing entirely on strong-lensing features, these authors made no mention of the spectacular "jellyfish" morphology (Smith et al., 2010; Ebeling, Stephenson, and Edge, 2014; McPartland et al., 2016) of the giant, edge-on spiral which they (most likely erroneously) take to be the lens responsible for the giant arc visible in Fig. 5.1[1]. A1758N_JFG1 was re-discovered by us in 2018 in the course of a visual search for RPS candidates in A1758N, described in detail in EK19.

5.3 Observational Data

Our analysis is based on data previously used by EK19 for their study of RPS events in A1758N, as well as on IFU observations performed specifically for this work. We here provide a brief overview of the former before describing the latter in more detail.

5.3.1 Space-based optical and X-ray observations

Observations of A1758N were performed with the Hubble Space Telescope (HST) for two unrelated projects (GO-12253, PI: Clowe, and GO-14096, PI: Coe) in 2011 and 2016, respectively. We used the resulting high-level science products from the Advanced Camera for Surveys (ACS) publicly available from the MAST archive and refer to EK19 for more details about these observations. A1758 was also observed twice with the Chandra X-ray Observatory (Sequence Number 800152 and Sequence Number 801177, PI: David) in 2001 and 2012, respectively. We only used the data from the second, much deeper observation and again refer to EK19 for additional details. An overlay of the adaptively smoothed X-ray emission (Ebeling, White, and Rangarajan, 2006) on the optical HST image is shown in Fig. 6.2.

5.3.2 Ground-based spectroscopy

Long slit

We observed A1758N_JFG1 (and other RPS candidates in A1758N, see EK19) with the DEIMOS multi-object spectrograph on the Keck-II 10m-telescope in poor conditions in July 2018. The chosen instrumental setup used a 1 slit width and combined the 600 l/mm grating (set to a central wavelength of 6300Å) with the GG455 blocking filter to suppress second-order contributions at $\lambda > 9000$Å.

[1] Ragozzine et al. (2012) describe this source as "a good candidate [...] for being a strong arc and for being lensed by the edge-on spiral to the east".

Integral Field Unit (IFU)

About a year later, on April 29, 2019, we targeted A1758N_JFG1 again, this time with the Keck Cosmic Web Imager (KCWI; Morrissey et al., 2018). In order to cover the entire disk of the galaxy as well as the downstream region while maintaining adequate spatial resolution, we chose the Medium Slicer mode, which provides 0.7 spatial sampling and a 16.5×20 field of view, well matched to the 19×19region shown in Fig. 5.1. Since KCWI's spectral coverage is currently limited to 3500 to 5600Å, we opted for the BM grating and a central wavelength of 5000Å, thereby covering the range from 4550 to 5450Å (approximately 3600–4300Å in the galaxy restframe). This spectral window includes the redshifted location of the [O2]3727Å emission line, an important star-formation diagnostic. We integrated for a total of 260 minutes in variable, but consistently poor seeing of 1.2 to 2. All data were reduced with the python-based data reduction pipeline KDERP.

5.4 Data Analysis

5.4.1 Photometry

We initially obtained photometry in all HST passbands with SExtractor (Bertin and Arnouts, 1996) in dual-image mode and using the F606W image as the detection band, while adopting the same settings and input parameters as employed for GO-14096. Since the resulting photometry proved inadequate for the complex superposition of sources in the immediate vicinity of A1758N_JFG1 (see Fig. 5.1), we obtained custom photometry for this object by subtracting a GALFIT model of the nearby elliptical galaxy (visible to the West in Fig. 5.1) and then adjusting SExtractor's parameters to avoid fragmentation of the object of interest, the edge-on massive spiral. Differential photometry was also applied in order to subtract any remaining contribution from the much fainter elliptical visible near the bottom of Fig. 5.1. The brightness and color of A1758N_JFG1 relative to other galaxies within the HST/ACS field of view is illustrated by Fig. 6.3.

5.4.2 Long-slit spectroscopy

The DEIMOS spectrum was flux calibrated by tying the observed flux to the HST photometry within the same passband and was subsequently extinction corrected. The procedures employed are described in detail in EK19. Note that, as for all studies based on long-slit observations, any galaxy properties derived from the resulting spectrum, shown in Fig. 6.4, implicitly assume that the signal recorded within the DEIMOS slit is representative of that of the entire galaxy.

From the DEIMOS 2d spectrum of A1758N-JFG1 we measured the galaxy's rotational velocity as a function of galactocentric radius by stacking sections

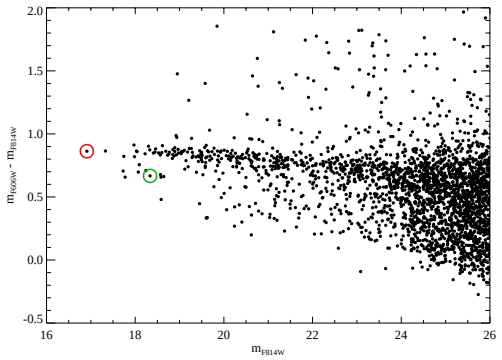

FIGURE 5.3: Color-magnitude diagram of all galaxies within the field of Fig. 6.2. A1758N_JFG1 and the BCG NNE of it (Fig. 6.2) are marked by a green and red circle, respectively.

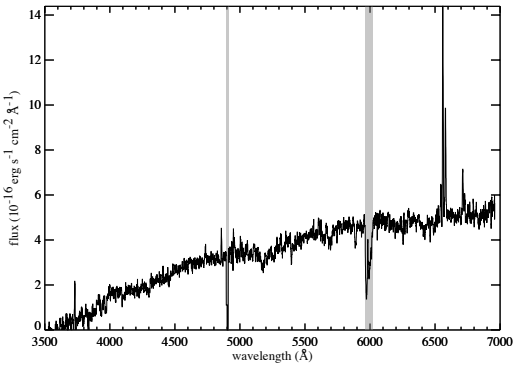

FIGURE 5.4: Rest-frame spectrum of A1758N_JFG1 as obtained with Keck-II/DEIMOS. The DEIMOS chip gap and absorption at 7600Å (about 6000Å in the galaxy rest frame) from water in the atmosphere are greyed out.

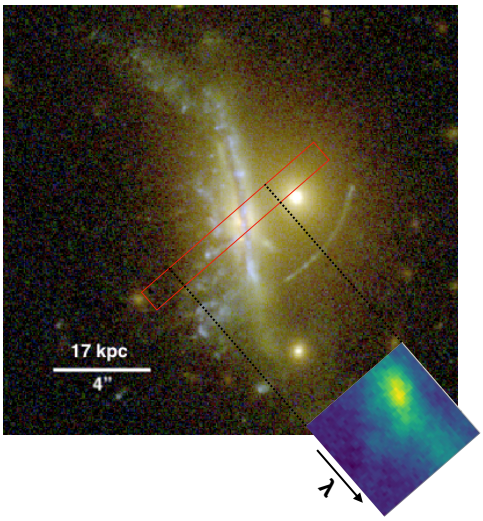

FIGURE 5.5: Stacked 2d spectrum of 20Å-wide regions around each of Hα, [N2], Hβ and [O3]5007Å, superimposed on the HST image of A1758N_JFG1 to illustrate the spatial alignment of spectral and imaging features along the DEIMOS slit. Note the clear slant of the stacked emission lines.

of the 2d spectra around the Hα, [N2]6548Å, [O3]5007Å, and Hβ emission lines (Fig. 5.5). Gaussian profiles were fitted to each of the spatial rows, and the centroids of these Gaussians converted to radial velocities using the Doppler-shift formula. Since the DEIMOS slit runs, by design, through the approximate center of the galaxy at an angle of 58° relative to the plane of the galactic disk, the galactocentric distance of any feature on the slit can be calculated via $d_g = d_s \cos 58°$, where d_g and d_s are the distance from the center of A1758N_JFG1 and the distance along the slit, measured from the center of the continuum emission.

5.4.3 IFU data

As the first step toward analyzing the [O2] emission from A1758N_JFG1, we limited the spectral range of the fully reduced and calibrated KCWI data cube and the associated signal variance (the “icubes" and “vcubes" files, in KDERP parlance) to 80Å centered on 4745Å, the observed wavelength of [O2] at the systemic redshift of our target, as determined from the DEIMOS long-slit spectrum shown in Fig. 6.4. We also binned the cubes by a factor of three in both spatial dimensions to create 0.87 pixels, approximately matched to the 0.7 slit width. We then computed the net [O2] flux at each pixel location as the difference of the signal within a 14Å-wide region centered on [O2] and the sum of the (continuum) flux recorded in 7Å-wide regions at either end of our spectral window. The resulting image of the [O2] emission-line flux is shown in Fig. 5.6.

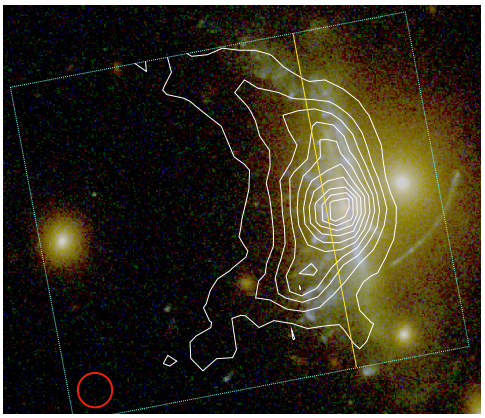

FIGURE 5.6: Contours (linearly spaced) of the [O2]3727Å emission-line flux from A1758N_JFG1 overlaid on the HST image of our target show the stripping of gas from the outer edge of the disk. The dotted, cyan line delineates the KCWI field of view; the red circle has a diameter of 1.5, representing the seeing disk during our Keck-II observation. The yellow line divides the field into a "disk" and "wake" region (see text for details).

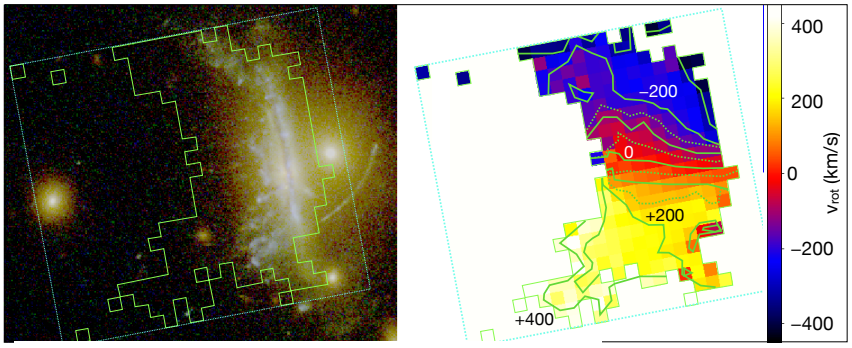

FIGURE 5.7: Right: map of the radial velocity of A1758N_JFG1 as derived from the observed wavelength of the [O2]3727Å emission line. The dotted, cyan line delineates the KCWI field of view; within the shown outlines the line flux is significant at greater than 2σ significance. Left: outlines of the $v_{\rm rot}$ distribution shown on the right, overlaid on the HST image of our target. Note that our measurement probes the velocity field well downstream of the disk, i.e., the jellyfish "tentacles".

R.A. (J2000) Dec	z	m_{435}	m_{606}	m_{814}	$\log(M* M_{\odot}^{-1})$	SFR ($M_{\odot}$ yr^{-1})	Δv_{rad} (km s^{-1})
13 32 35.18 +50 31 36.3	0.2733	19.70	18.58	17.97	10.87±0.02	47.9±11.9	−936

TABLE 5.1: Global properties of A1758N_JFG1: equatorial coordinates, heliocentric redshift, apparent magnitudes in the F435W, F606W and F814W bands, respectively, stellar mass, star formation rate (SFR), and radial velocity relative to the NW BCG of A1758N.

Finally, we measured radial velocities from the location of [O2] in the spectral dimension of the data cube. In order to avoid systematic uncertainties introduced by fitting a Gaussian profile to the unresolved [O2] doublet, we computed the line centroid as the flux-weighted average of the wavelengths within the same 14Å-wide spectral window used before. The results, after conversion to peculiar velocities in the galaxy rest frame and considering only pixels within which [O2] was detected with greater than 2σ significance, are shown in Fig. 5.7.

5.5 Results

5.5.1 Global properties

From the prominent emission lines shown in Fig. 6.4 EK19 measured a heliocentric redshift of $z = 0.2733$ for A1758N_JFG1, significantly less than the redshift of $z = 0.2787$ of the nearby brightest cluster galaxy of the northwest component of A1758N (see Fig. 6.2). As reported by EK19, this redshift difference corresponds to a relative radial velocity of about -940 km s^{-1}, i.e., in addition to its apparent westerly motion in the plane of the sky, A1758N_JFG1 is moving rapidly toward us in the cluster rest frame.

The stellar mass of $(7.4 \pm 0.3) \times 10^{10}$ $M_{\odot}$ and star-formation rate of (48 ± 12) $M_{\odot}$ yr^{-1} measured for A1758N_JFG1 by EK19 place our target far above the galaxy main sequence, about a factor of five above the star formation rates encountered typically in disk galaxies of this mass (EK19; their Fig. 8). Consistent with this observation, EK19 find A1758N_JFG1 to fall within the starburst regime in the BPT diagram (**baldwin81**), albeit just outside the purely star-forming population (EK19; their Fig. 9). While not representative of the field galaxy population in general, the system's high stellar mass (within the top few percent of disk galaxies at $z < 0.5$; Torrey et al., 2015) is accompanied by a commensurate physical size, absolute brightness, and resulting SFR under RPS (see Fig. 8 of EK19), rendering A1758N_JFG1 an ideal target for in-depth study.

Our analysis of the stacked 2D spectrum (Fig. 5.5) from the same DEIMOS observation as used by EK19 yielded a maximal velocity for the ionized ISM

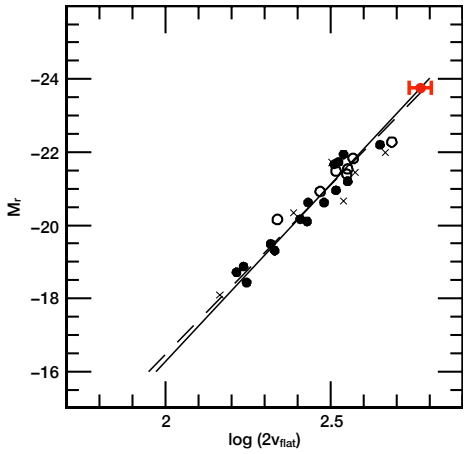

FIGURE 5.8: Locus of A1758N_JFG1 (red symbol) on the R-band Tully-Fisher relation at $z = 0$ (Verheijen, 2001). From the extinction-corrected absolute R-band magnitude of -23.7 (derived from the k-corrected F814W magnitude), the TFR predicts a rotation velocity of approximately 300 km s^{-1} for our textbook "jellyfish" galaxy.

of (143±16) km s^{-1}. For comparison, we also calculated the rotational velocity of A1758N_JFG1 expected from the Tully-Fisher relation (TFR; Tully and Fisher, 1977) as determined by Verheijen (2001). Since the F814W passband at z=0.28 is effectively R-band at $z = 0$, we used our target's F814W magnitude, corrected for Galactic extinction (Sec. 6.5.1), to find V_{flat} = (288±31) km s^{-1} from the R-band TF relation[2] (Fig. 5.8). The discrepancy between this expectation value and the cited, much lower measurement obtained from our DEIMOS observation is entirely anticipated, given that the spectrum recorded through our DEIMOS slit (see Fig. 5.5) probes only the central region of the galaxy, far from the outer reaches of the disk where the rotational-velocity curve flattens.

The global properties of A1758N_JFG1 derived here (or previously by EK19) show our "jellyfish" galaxy to be a massive, star-bursting, fast-rotating, late-type galaxy moving at high velocity through the A1758N cluster merger (Table 6.1). Our target's direction of motion in the plane of the sky is, as for all galaxies, difficult to determine but can be approximately constrained from the orientation and slight N-S asymmetry of the "tentacles" in Fig. 5.1 to be due west or WSW.

5.5.2 Nuclear activity and star-formation rate

Prompted by A1758N_JFG1 falling into the composite region of EK19's BPT diagram, we attempted to constrain the fraction of the Hα luminosity

[2]The effects of a possible redshift evolution of the TF relation (**port07**) amount to at most 10% at the modest redshift of our target and thus do not affect our conclusions.

that can be attributed to LINER/AGN-powered photoionization. Although the absence of diagnostic emission lines (other than [O2]3727Å) within the spectral window (e.g., Poggianti et al., 2019) currently precludes a conclusive determination from our IFU data, an upper limit on any AGN contribution can be obtained from the lack of X-ray emission from A1758N_JFG1, apparent in Fig. 6.2. The 3σ upper limit on the X-ray luminosity of 2×10^{42} erg s^{-1} (2–10 keV) measured by us from the archival Chandra data suggests a negligible AGN contribution of less than 2×10^{41} erg s^{-1} to the observed Hα luminosity of 2×10^{42} erg s^{-1} (Shi et al., 2010).

While the narrow spectral range covered by our KCWI data contains insufficient spectral diagnostics to shed further light on any nuclear activity, the IFU data provide a clear view of the spatial distribution of star formation. Adopting the [OII]3727Å flux as an alternative tracer of star formation (**ken98**), we find star formation to occur not only along the entire galactic disk but also, at steadily declining intensity, well outside the disk, in the downstream region (Fig. 5.6). Indeed the integrated SFR in the galaxy's wake (see dividing line in 5.6) rivals, and in fact exceeds, that observed in the disk region. We also note that the contours of the [OII]3727Å flux shown in Fig. 5.6 exhibit the same asymmetry noted already in Sec. 5.5.1 with reference to the orientation of the tentacles visible in Fig. 5.1.

5.5.3 Gas phase velocities

A conclusive, and much more complex, picture of the rotational velocity of A1758N_JFG1 is painted by the map we derived from the redshift of the [O2] emission line (Fig 5.7). The key insights can be summarized as follows:

1. All lines of constant radial velocity are significantly slanted relative to the galaxy's axis of rotation, in the sense that gas that is farther downstream (i.e., east) of the galactic disk lags behind the galaxy (which is moving toward us, see Sec. 5.5.1).

2. The lag is small near the center of A1758N_JFG1, but increases both toward the outer edges of the disk and eastward, along the debris trail, where offsets of over 200 km s^{-1} are observed.

3. Within the galactic disk, the maximal rotational velocity observed once the mentioned lag is accounted for ($v_{\rm max} \sim \pm 300$ km s^{-1}) is consistent with the TFR expectation value.

5.6 Origin and trajectory within the A1758N merger

From their analysis of the line-of-sight and projected directions of motions of eight RPS candidates in A1758N (one of them A1758N_JFG1) EK19 concluded that these galaxies likely have a common origin, the most plausible scenario

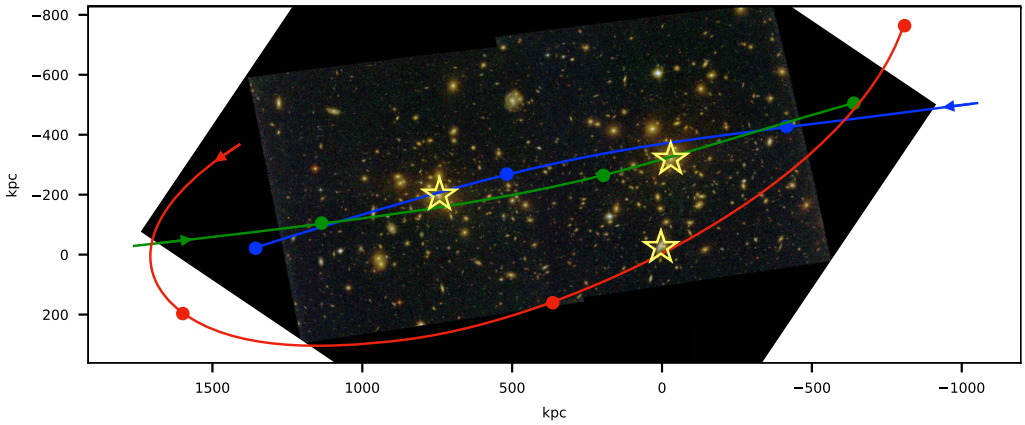

FIGURE 5.9: Example of simulated trajectories for the two subclusters and A1758N_JFG1 that reproduce the observed locations (in projection) of the two BCGs and our jellyfish galaxy (marked by yellow asterisks) as well as the radial velocity and approximate projected direction of motion of the latter. We show the trajectories overlaid on the HST image of A1758N, i.e., as viewed along our line of sight; in three dimensions, the merger axis for which our observational constraints are met is inclined by 58° with respect to the plane of the sky. Solid circles on each trajectory mark time intervals of 667 Myr.

being infall along a wide filament roughly aligned with the cluster merger axis.

To test the validity of this hypothesis we attempted to recover the trajectory of A1758N_JFG1 by creating a simple three-body model of the A1758N collision, constrained by five observational facts: the projected positions of the two BCGs and of A1758N_JFG1, the line-of-sight velocity of our jellyfish galaxy, and its projected, approximately westerly direction of motion.

Since realistic modelling of the complex physics of a cluster merger was well beyond the scope of our conceptual study of plausible orbits of A1758N_JFG1, we simulated the relevant trajectories with GALPY, a python package designed for galactic-dynamics calculations (**bovy14**; **mack18**). The two subclusters in A1758N were assigned spherical NFW mass profiles (**nfw96**) of 1.1×10^{15} $M_{\odot}$ each (based on findings of Ragozzine et al., 2012), whereas A1758N_JFG1 was considered a point mass; in addition, all three bodies were assumed to share the same orbital plane. We adopted the initial conditions of Machado et al. (2015) and **mo17**, i.e., we started our simulations from a subcluster separation of 3 Mpc and assumed an impact parameter of 150 kpc and a relative velocity of 1750 km s^{-1} between the two clusters. The parameter space probed by the initial conditions for A1758N_JFG1 combined distances ranging from 600 kpc to 2 Mpc from each of the two subclusters with an initial velocity vector ranging from 600 to 2400 km s^{-1} and adopting all possible angles within the merger plane. Dynamical friction as well as

hydrodynamical interactions were ignored, a decision that was as much choice as necessity, given our inability to incorporate such physics into GALPY. Neither simplification is likely to have a noticeable impact on our findings though, since the merger is believed to be observed after the first core passage (**mo17**; Machado et al., 2015), i.e., before dynamical friction has a noticeable effect, and that A1758N_JFG1 appears to be in an early phase of the stripping process. For this last reason, and because the stripping timescale is shorter than the dynamical timescale of galaxies within clusters (Quilis, Moore, and Bower, 2000; Steinhauser, Schindler, and Springel, 2016), we also required A1758N_JFG1 not to have previously passed either of the two subcluster cores within a distance of 500 kpc, which is a conservative estimate of the pericenter of orbits of stripped galaxies within clusters (Quilis, Moore, and Bower, 2000). We note that this is the only constraint used that at least implicitly invokes the density of the intra-cluster medium; as stated before, a realistic simulation of the gas densities encountered by A1758N_-JFG1 on its trajectory through this active merger is well beyond the scope of our simple three-body simulation.

The set of observational constraints described above greatly limit the possible trajectories of A1758N_JFG1. Although our simple simulations are far from exhaustive, the results favor a scenario in which the A1758N merger proceeds along an axis that is closer to our line of sight than to the plane of the sky, and in which A1758N_JFG1's trajectory is not dissimilar to that of the subcluster observed today as the NW component of A1758N (see Fig. 5.9).

5.7 Discussion

The discovery of A1758N_JFG1, a spectacular example of ram-pressure stripping in a massive cluster merger, provides a rare opportunity to quantitatively study the physics and kinematics of RPS acting on an exceptionally massive late-type galaxy at the relatively high redshift of $z \sim 0.3$. Viewed edge-on, and exhibiting a debris trail that extends over 40 kpc in projection on the plane of the sky, A1758N_JFG1 would be an even more spectacular sight from a different angle, as evidenced by the system's radial peculiar velocity of close to –1000 km s^{-1} and the unambiguous kinematic signature of stripped ISM trailing behind the galaxy as it approaches along our line of sight (Fig. 5.7). The fortuitous orientation and direction of motion of A1758N_JFG1 provide an edge-on view of the stripping process that minimizes projection effects and clearly reveals the dynamics of both galaxy and stripped ISM. North-South asymmetries clearly visible in both optical imaging (Fig. 5.1) and the distribution of [OII]3727Å flux (Fig. 5.6) strongly suggest that our target's velocity vector, as seen in projection on the plane of the sky, points W or, more likely, WSW.

5.7.1 ISM kinematics

The spatial distribution of line emission from A1758N _JFG1, specifically [O2]3727Å, provides crucial insights into the physics at work in this extreme case of ram-pressure stripping. The continuous and monotonic change of both [O2] flux and velocity gradient, shown in Figs. 5.6 and 5.7, rules out the (remote) possibility of the enhanced star-formation rate and morphology of this galaxy being caused by a merger instead of RPS. More importantly, it shows that, consistent with the findings of studies of RPS in nearby galaxies (e.g., Bellhouse et al., 2017), stripping proceeds gradually from the outer edge of the disk inward. Although results from a single object obtained at only modest spatial resolution are unable to settle the question, the observed distribution of [O2] emission also strongly suggests that the stripped ISM does not start forming stars only within the “tentacles". In other words, enhanced star formation is triggered as ram pressure compresses the ISM in the galaxy-ICM interface, but continues far into the galaxy’s wake, as gas clouds stripped from the disk collapse and form stars *in situ*. Although at this early stage of the stripping process much of the [O2] flux, and hence of the star formation, is still concentrated within, or just downstream of, the galactic disk (in agreement with Kronberger et al., 2008), the balance is likely to shift more heavily toward the wake, as stripping of the ISM proceeds from the outer edges of the disk toward the galaxy’s bulge.

The ISM within the disk exhibits a rotation velocity profile consistent with the TFR prediction of a maximal velocity of approximately 300 km s^{-1}. However, the significant line-of-sight velocity of A1758N_JFG1 adds a characteristic tilt to a velocity gradient that would otherwise run perpendicular to the plane of the galactic disk (Fig. 5.7). This slant, more pronounced toward the edges of the disk, also increases with downstream distance, indicative of drag exerted by the ICM that causes the stripped gas to gradually “fall behind” the galaxy as both move toward us.

5.7.2 Nuclear activity

Some of the Hα luminosity recorded in our long-slit observation of A1758N_-JFG1 (which probed the galaxy’s nucleus) could conceivably be due to nuclear activity, rather than star formation; if so, our target would be expected to harbor a prominent X-ray point source, but no such emission is detected in the existing Chandra data. The almost complete absence of signs of nuclear activity in A1758N_JFG1 (except for the system’s location in the “composite region" of the BPT diagram presented by EK19) is intriguing, given that well established scaling relations (e.g., Reines and Volonteri, 2015) predict the presence of a supermassive black hole ($M_{BH} > 10^8$ $M_\odot$) in this extreme spiral galaxy, and in view of the results of Poggianti et al. (2017) who found RPS to boost nuclear activity in nearby galaxies of high stellar mass ($M_* \geq 4 \times 10^{10}$ $M_\odot$). We note, however, that it remains entirely possible that a heavily obscured AGN resides within the very core of A1758N_JFG1, a region that is

still largely unaffected by RPS and which could be penetrated only by hard X-rays (> 10 keV; see Hickox and Alexander, 2018, for a review).

5.7.3 Origin and trajectory

EK19 propose that the RPS candidates identified within A1758N share their large-scale origin and trajectories with the merging subclusters, i.e., that they enter the cluster environment along a filament that is roughly aligned with the merger axis. In this scenario, the high negative radial velocities of EK19's RPS candidates require the merger axis to be substantially inclined with respect to the plane of the sky. We qualitatively tested this hypothesis with the help of a simple three-body model of the two merging subclusters and A1758N_JFG1. While far from exhaustive, our simulations are not only able to reproduce the observational data; they do so for an orientation of the merger axis that is fully consistent with the geometry proposed by EK19 (Fig. 5.9) and disfavor the accretion of A1758N_JFG1 directly from the field. Although our findings thus support the notion advanced by EK19 that studies of the location and apparent direction of motion of RPS events could become powerful tools to reveal the three-dimensional geometry of cluster collisions, much more sophisticated simulations (far beyond the scope of this paper) are required to fully test the potential of "jellyfish" galaxies as diagnostics of cluster mergers.

5.8 Summary

A1758N_JFG1, a newly discovered textbook "jellyfish" galaxy, offers a rare, clean view of ram-pressure stripping at the relatively high redshift of $z = 0.28$, thanks to the system's edge-on orientation. Adding to the findings of EK19 who report a dramatically enhanced star formation rate, our IFU study of the [O2]3727Å emission line provides a spatially resolved view of the kinematics of the ISM from the galaxy's disk to the end of the visible debris trail. We find unambiguous evidence of a sequence of gradual stripping from the outer edges of the galaxy and drag from the ICM that causes the stripped material to fall behind A1758N_JFG1 along its path through the A1758N merger. The distribution of [O2] emission strongly suggests that the enhanced star formation is the result of both ram-pressure-induced compression at the ISM/ICM interface and subsequent (and independent) *in situ* collapse of ISM clouds in the debris trail.

A1758N_JFG1 exhibits no evidence of nuclear activity, in spite of expectations of a supermassive black hole at its center based on scaling relations. Given the, at this early stage of the stripping process, potentially still very high density of gas obscuring the very core of the system, the absence of observable nuclear actively is, however, not in conflict with previous studies suggesting that RPS boosts AGN activity (Poggianti et al., 2017).

Finally, simplified modelling of the motion of A1758N_JFG1 within the A1758N cluster merger as a three-body problem finds trajectories consistent with EK19's hypothesis of RPS candidates (including A1758N_JFG1) being accreted by the forming cluster from a direction that is aligned with the merger axis and inclined by approximately 60° with respect to the plane of the sky, contrary to the commonly adopted view of the A1758N cluster merger proceeding largely in the plane of the sky (**mo17**; Machado et al., 2015). Although these results are far from definitive, given the simplicity of our simulations, they lend credence to EK19's proposal to investigate the usefulness and power of the spatial and peculiar-velocity distribution of RPS candidates as a tool to study the 3D geometry and dynamics of cluster collisions.

Having demonstrated the feasibility and power of IFU observations of extreme RPS events at intermediate redshifts, our study bodes well for a future, comprehensive kinematic analysis of the environmental dependencies of RPS in truly massive galaxy clusters. By extending the redshift range of in-depth RPS studies, for instance by targeting RPS events in MACS clusters (Ebeling, Edge, and Henry, 2001; Ebeling, Stephenson, and Edge, 2014), we will also increasingly probe dynamically young and actively evolving systems and will eventually reach the era when truly massive clusters only began to form, currently explored only by the recent study of Boselli et al. (2019) at $z = 0.7$.

Chapter 6

Jellyfish: Ram Pressure Stripping as a diagnostic tool in studies of cluster collisions

This work has been published in ApJ (Ebeling and Kalita, 2019)
(ApJ, 882.2, p. 127)

Based on the results shown in the previous chapter, we follow-up additional ram-pressure stripping candidates within the same merging galaxy cluster system. Corroborating the trajectory of the massive jellyfish galaxy into the cluster, we find that it was most probably part of a group of gas-rich star-forming galaxies that also shed light on the overall cluster dynamics.

6.1 Introduction

By providing a physical mechanism to remove both molecular and atomic gas from spiral galaxies moving through the diffuse gas filling the potential wells of massive clusters of galaxies, ram-pressure stripping (hereafter RPS; Gunn and Gott, 1972) has been recognized to play an important (and possibly dominant) role in the transformation of late-type into early-type galaxies. Supported by numerical simulations (e.g., Abadi, Moore, and Bower, 1999; Vollmer et al., 2001; Roediger and Hensler, 2005; McCarthy et al., 2008), observational studies of RPS in nearby clusters have yielded extensive insight into the dynamics and efficiency of RPS (e.g., Kenney, van Gorkom, and Vollmer, 2004; Abramson et al., 2011; Fumagalli et al., 2014) and, more recently, have begun to explore related topics, such as the significance of cluster mergers (e.g., Stroe et al., 2015; McPartland et al., 2016; Deshev et al., 2017) and the interplay of RPS and nuclear activity in galaxies (Poggianti et al., 2017; George et al., 2019).

We here continue our observational investigation of galaxy evolution in the dense environment provided by massive galaxy clusters, focusing on the characterization of ram-pressure stripping events at $z > 0.2$, i.e., at redshifts beyond which the Universe is large enough to contain a significant number of truly massive clusters (see also Cortese et al., 2007; Ebeling, Stephenson,

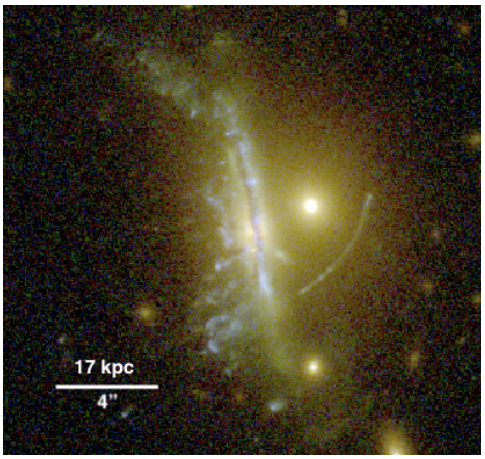

FIGURE 6.1: A1758N_JFG1, a newly discovered spectacular example of ram-pressure stripping in the massive cluster merger A1758N ($z = 0.279$) as viewed by HST/ACS. The unmistakable debris trails and edge-on view of the galactic disk allow an unambiguous determination of this "jellyfish" galaxy's direction of motion relative to the intra-cluster medium. We refer to Kalita and Ebeling (2019) for an in-depth review of the properties of A1758N_JFG1.

and Edge, 2014). The analysis of RPS events and their link to the dynamics and history of cluster mergers described in this paper was triggered by our discovery of a spectacular case of RPS in the merging double cluster A1758N, shown in Fig. 6.1 and discussed in detail in Kalita and Ebeling (2019).

Throughout this paper we adopt the concordance ΛCDM cosmology, characterised by $\Omega_m = 0.3$, $\Omega_\Lambda = 0.7$, and $H_0 = 70$ km s^{-1} Mpc^{-1}. All images are oriented such that north is up and east is to the left.

6.2 Abell 1758

Abell 1758 (Abell, 1958) is a rich cluster of galaxies at $z = 0.28$ found to consist of two components, A1758S and A1758N, separated by about 8 arcmin on the sky. Both components are in turn merging systems that are well studied from X-ray to radio wavelengths (e.g., David and Kempner, 2004; Durret, Laganá, and Haider, 2011; Botteon et al., 2018). Although A1758S and A1758N are bound to merge eventually, no evidence of physical interaction is observed at their current separation of approximately 2 Mpc (in projection). We here focus exclusively on A1758N, an active merger of two similarly massive clusters.

6.3 Observational Data

We here briefly summarize the data used (or referred to) in this work.

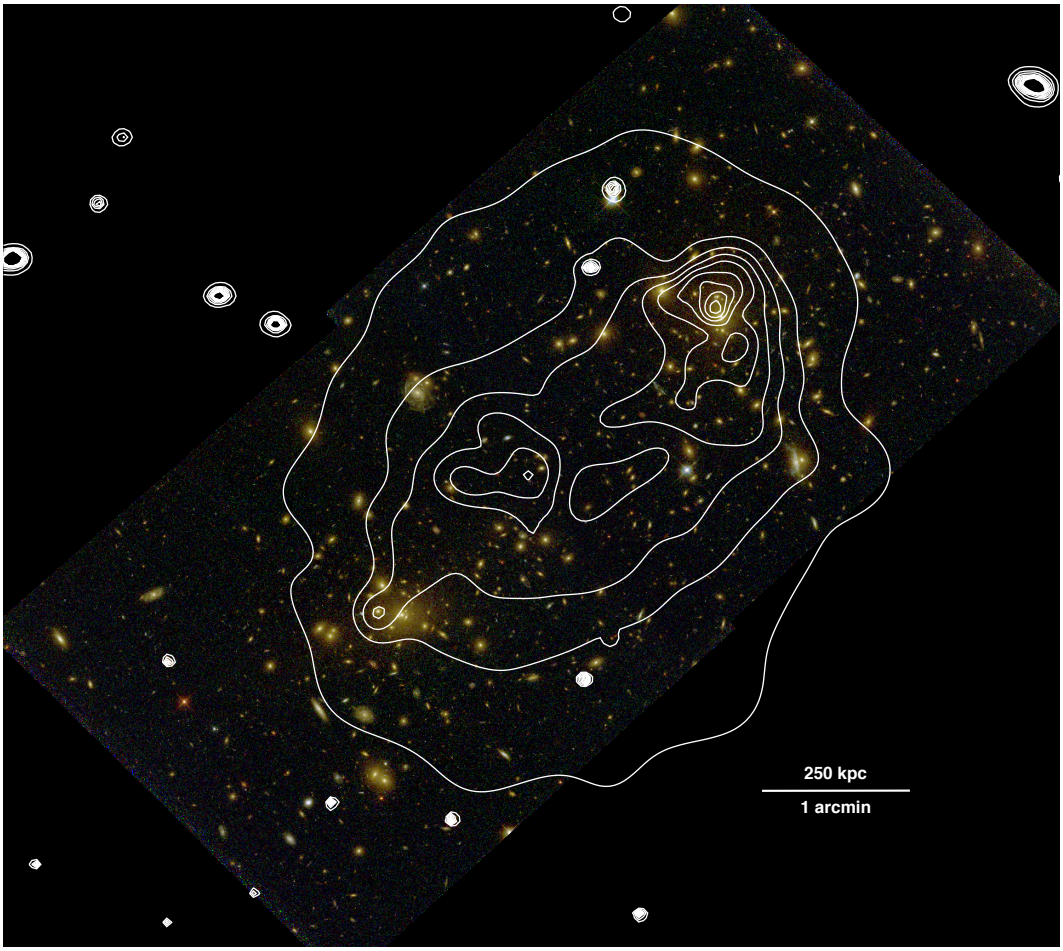

FIGURE 6.2: A1758N as seen with HST / ACS (false-colour composite from F435W, F606W, and F814W images collected for GO-12253). Overlaid in white are linearly spaced contours of the adaptively smoothed X-ray surface brightness in the 0.5–7 keV band as observed with Chandra / ACIS-I.

6.3.1 HST imaging

Observations of A1758N with HST's Advanced Camera for Surveys (ACS; Ford et al., 1998) in the F435W, F606W, and F814W filters were performed for GO-12253 (PI: Clowe) in December 2011 for total exposure times of 2536, 2544, and 5000s, respectively. Two observations of the quoted durations were necessary in each filter to cover both components of this merging cluster. Additional shallow coverage at near-infrared wavelengths, again for both of the subclusters, was added by program GO-14096 (PI: Coe) through short exposures (656s, 331s, 431s, and 1056s) with the Wide Field Camera 3 (WFC3; Kimble et al., 2008) in April and June 2016 in the F105W, F125, F140W, and F160W filters, respectively, as part of the RELICS program (Coe et al., 2019). We use the resulting high-level science products publicly available from the MAST archive; a color image of A1758N based on the cited HST / ACS

observations is shown in Fig. 6.2.

6.3.2 Galaxy spectroscopy

Extensive groundbased spectroscopy of galaxies in the A1758N field was performed by Boschin et al. (2012) and **mo17**. Blissfully unaware of this earlier work, we observed A1758N with the DEIMOS spectrograph on the Keck-II 10m-telescope in poor conditions in July 2018. Three multi-object spectroscopy (MOS) masks were designed to obtain low-resolution spectra of presumed cluster members, potential strong-lensing features, and RPS candidates (see Section 6.5.2 for details of the target selection). All slits were 1 wide; the instrumental setup combined the 600 l/mm grating (set to a central wavelength of 6300Å) with the GG455 blocking filter to suppress second-order contributions at $\lambda > 9000$Å.

Although these observations were later found to have duplicated a significant number of measurements already reported in the literature, they corrected one erroneous literature redshift, added 23 new spectra (and redshifts), and allowed us to test for systematic biases as discussed in Section 6.5.

6.3.3 X-ray imaging spectroscopy

A1758 was observed with the Chandra X-ray Observatory's ACIS-S detector in 2001 (Sequence Number 800152; PI: David) for 58 ks, and with ACIS-I in September and October 2012 (Sequence Number 801177; PI: David) for a total exposure time of 148 ks. All observations were performed in Very Faint mode. We reprocessed and merged all ACIS-I observations using CIAO 4.8, and then adaptively smoothed the emission in the 0.5–7 keV band to 3σ significance using the ASMOOTH algorithm (Ebeling, White, and Rangarajan, 2006). The resulting iso-intensity X-ray surface brightness contours are shown in Fig. 6.2.

The X-ray properties of both A1758S and A1758N as determined from Chandra and XMM-Newton observations, as well as their significance for the interpretation of the extensive merging activity in this system, are discussed by David and Kempner (2004) and Durret, Laganá, and Haider (2011).

6.3.4 Radio observations

Diffuse radio emission from A1758N was first detected in the NVSS and WENSS surveys (Kempner and Sarazin, 2001); investigations conducted with the VLA at 1.4 GHz, the GMRT at 325 MHz, and LOFAR at 144 MHz resolve a giant radio halo extending beyond the X-ray emission and across the full extent of Fig. 6.2 (Giovannini et al., 2009; Venturi et al., 2013; Botteon et al., 2018). No radio relics associated with A1758N were detected.

6.4 Numerical simulations

Smoothed-particle hydrodynamics simulations of the active merger A1758N performed by Machado et al. (2015) found the observed X-ray morphology of the system (Fig. 6.2) to be best replicated by a collision of clusters of equal mass[1] starting from initial conditions characterized by a 3 Mpc separation, an impact parameter of 250 kpc, and a relative velocity of 1500 km s^{-1}. Requiring the observational constraints to be met when the separation of the two subclusters equals the observed (projected) distance of 750 kpc between the BCGs, Machado et al. (2015) report that the best match is attained at t=1.7 Gyr, after the first core passage and just before turnaround, when the relative velocity of the subclusters is 380 km s^{-1}.

Since the simulations assumed that the collision proceeds in the plane of the sky, the relative velocity between the two merger components along our line of sight is essentially zero at all times, although Machado et al. (2015) state that their results remain valid if the collision is viewed at an angle of up to 20 degrees, in which case a relative line-of-sight velocity of up to 130 km s^{-1} is predicted for the two BCGs. As expected for a binary collision of massive clusters, these simulations also predict strong shocks about 600 kpc away from each BCG, propagating outward through the ICM at Mach numbers of at least 6. Consistent findings are reported by **mo17** who refine the simulations by Machado et al. (2015) while retaining the assumption of a plane-of-the-sky merger.

6.5 Data Analysis

6.5.1 Photometry

We use the photometric data provided as a high-level science product by the HST MAST archive at https://archive.stsci.edu/missions/hlsp/relics/abell1758/catalogs/, obtained with SExtractor (Bertin and Arnouts, 1996) in dual-image mode with the F606W image as the detection band and the settings employed for all data acquired for GO-14096.

6.5.2 Spectroscopy

All spectroscopic data, gathered by us with Keck-II/DEIMOS as described in Section 6.3.2, were reduced using a modified version of the DEEP2 pipeline (Cooper et al., 2012; Newman et al., 2013). In the following we describe the selection of galaxy targets and the determination of cluster membership from the resulting redshifts.

[1] Estimates for the total mass of A1758N are compiled in **mo17** and range from 1 to 2×10^{15} M; Machado et al. (2015) adopt $\sim 5 \times 10^{14}$ M for each subcluster.

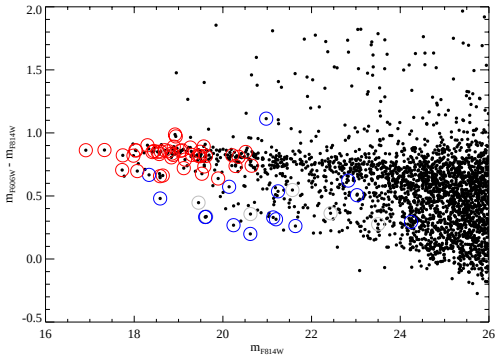

FIGURE 6.3: Color-magnitude diagram of all galaxies within the field of Fig. 6.2. Blue circles mark galaxies targeted in our DEIMOS observations on the grounds of their disturbed morphology; red circles mark ellipticals observed as likely cluster members; fillers (grey) were mainly selected from the population of bright, blue galaxies.

Target selection

The automatically generated SExtractor source catalog referred to in Section 6.5.1 contains a significant number of false detections. We excluded 1092 spurious sources at the field edges and then limited the remaining catalog to objects classified as galaxies and meeting the criterion $m_{\mathrm{F814W}} < 28$. After visual scrutiny of the brightest sources in this list, we removed a further 22 objects with $m_{\mathrm{F814W}} < 24$ as obvious stars. A color-magnitude diagram of the resulting galaxy sample is shown in Fig. 6.3. Highlighted are galaxies selected by us for follow-up spectroscopy either because of their disturbed morphology in the HST image (this subset includes both RPS candidates and potential strong-lensing features), or because their location on the cluster red sequence (clearly visible in Fig. 6.3) makes them likely cluster members.

In the selection of RPS candidates we followed the prescription provided by Ebeling, Stephenson, and Edge (2014) which considers three primary morphological indicators, namely (1) signs of unilateral external forces, (2) brightness or color gradients suggesting triggered star formation, and (3) the presence of debris trails. Similar criteria have been used by other authors to select RPS candidates (e.g., Poggianti et al., 2016).

Redshift measurements and cluster membership

Redshifts were determined for the 66 galaxies marked in Fig. 6.3 through cross-correlation with spectral templates and subsequent correction to the heliocentric frame, using an adaptation of the SpecPro package (Masters and Capak, 2011). This data set, presented in full in Appendix A, includes the brightest cluster galaxy (BCG) of either subcluster. From these redshifts, the ROSTAT statistics package (Beers, Flynn, and Gebhardt, 1990) measures a

systemic cluster redshift of $z = 0.2775$ for A1758N and a velocity dispersion of $\sigma = 1780^{+140}_{-160}$ km s^{-1} from 51 concordant redshifts.

Spatial cross-correlation of our sample with the positions of 203 galaxies with spectroscopic redshifts listed in **mo17** identified 43 objects as in common. For all but one galaxy[2], our redshift measurements are in excellent agreement with the literature values ($\langle \Delta z \rangle = -0.0001 \pm 0.0005$).

Our final sample of spectroscopically confirmed cluster members thus comprises 159 galaxies, 51 observed by us and 118 from the compilation by **mo17**.

6.5.3 Calibration and extinction correction

The DEIMOS spectra were flux calibrated by first dividing the observed spectra by the spectrograph's response function for the grating, blocking filter, and central wavelength used during our observations (see Section 6.3.2 for details) and then scaling the integrated signal within the ACS/F606W passband such that it matches the observed HST photometry in the same filter, i.e.,

$$f(\lambda) = \frac{f_{\lambda,\mathrm{F606W}}}{\int s(\lambda) T_{\mathrm{F606W}}(\lambda) d\lambda \ / \ 2235.5} \, s(\lambda), \tag{6.1}$$

where $f_{\lambda,\mathrm{F606W}}$ is the flux density derived from the galaxy's isophotal magnitude in the ACS/F606W image, and $f(\lambda)$ and $s(\lambda)$ are the flux-calibrated and the response-corrected observed spectrum, respectively. $T_{\mathrm{F606W}}(\lambda)$ and 2235.5Å are the effective throughput and bandwidth (cumulative throughput width, CTW95) of the ACS/F606W filter, respectively. For all spectra that fully contain both the F606W and F814W bandpasses we computed the flux calibration factor of Eqn. 6.1 for either filter and found the results to be consistent within 6%.

We subsequently corrected the spectra for interstellar extinction in the Milky Way following Seaton (1979) and adopting the E(B–V) reddening coefficient of 0.0118 measured by Schlafly and Finkbeiner (2011) in the direction of our cluster target.

Note that this calibration procedure implicitly assumes that the spectrum recorded within each DEIMOS slit is representative of that of the entire galaxy.

6.5.4 Emission-Line Ratios, Star-Formation Rates, Stellar Masses

We measured (net) emission-line fluxes for the thermally excited Hα and Hβ lines, as well as for the collisionally excited [N2] and [O3] lines, from the calibrated DEIMOS spectra, where possible. The resulting ratios [N2]λ6583/Hα and [O3]λ5007/Hβ will be used as diagnostics in Section 6.6.3.

[2]The exception is the foreground spiral at $(\alpha, \delta) = (13\ 32\ 56.1, +50\ 30\ 17)$ (J2000) for which our emission-line redshift of 0.1038 supersedes the erroneous literature value of 0.2764.

Star-formation rates (SFR) for our RPS candidates were derived from the Hα emission-line luminosity, using the scaling relation

$$\mathrm{SFR}[\mathrm{M}_\odot \mathrm{yr}^{-1}] = 9.9 \times 10^{-42} L(\mathrm{H}\alpha)\ [\mathrm{erg\ s}^{-1}]$$

(Kennicutt, 1998), where $L(\mathrm{H}\alpha)$ is the net luminosity of the Hα emission line, corrected for intrinsic extinction as determined from the Balmer decrement following Calzetti et al. (2000).

Finally, we obtained stellar masses with the SED fitting package PROSPECTOR (Leja et al., 2017), using both the HST photometry (ACS and WFC3 where available) and the calibrated DEIMOS spectrum as observational constraints. Like the DEIMOS spectra (see Section 6.5.3), the HST photometry too was corrected for Galactic extinction.

6.6 Results

6.6.1 Nature of ram-pressure stripping candidates

Of the fifteen galaxies targeted by us with DEIMOS because of their disturbed optical morphology, two were found to be foreground galaxies, and five are potentially gravitationally lensed background objects at $z = 0.6 - 1.3$; the remaining eight are cluster members. All of the latter show emission lines, as do four additional cluster members, three of which were targeted because of their red-sequence color. The DEIMOS spectra of the sample of 12 line emitters are shown in Fig. 6.4, their HST images are presented in Fig. 6.5, and their location within the cluster is indicated in Fig. 6.6.

6.6.2 A1758N: radial-velocity distribution

The 159 spectroscopically confirmed cluster members in the combined data set yield a cluster redshift of $z = 0.2785$ and a velocity dispersion of $\sigma = 1553^{+80}_{-100}$ km s^{-1}. While the redshift distribution of A1758N's galaxy population (presented in Fig. 6.7) shows no sign of bimodality, splitting the galaxy sample, as viewed in projection on the sky, at the midpoint between the two BCGs results in redshift distributions that differ at the 3σ confidence level according to a two-sided Kolmogorov-Smirnov test, suggesting a significant, albeit small, line-of-sight velocity of two subclusters relative to each other. Since this simplistic split of the overall galaxy population based on projected position in the sky does not cleanly separate the populations of the two subclusters, regardless of the orientation of the merger axis, the observed velocity difference is merely a qualitative indication of relative motions along our line of sight. Complex velocity substructure was also reported by Boschin et al. (2012) in a study based on 92 cluster members which, however, did not find a significant difference in the systemic redshifts of the two subclusters

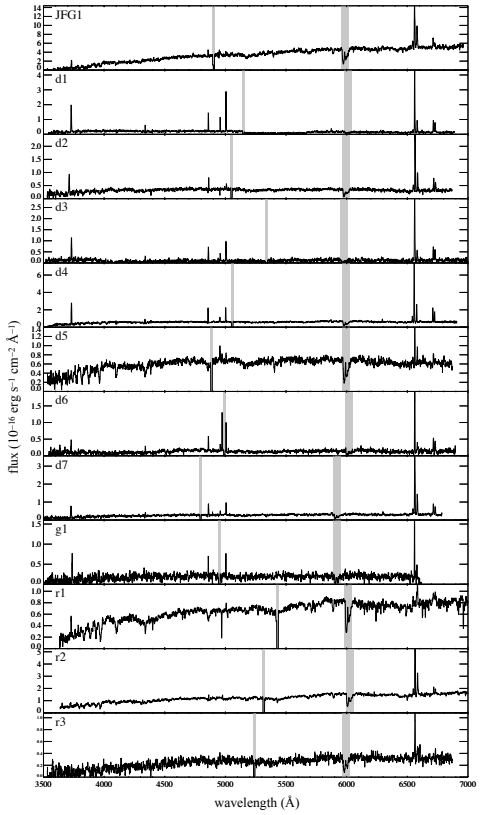

FIGURE 6.4: Rest-frame spectra of the galaxies shown in Fig. 6.5. The DEIMOS chip gap and absorption at 7600Å from water in the atmosphere are greyed out.

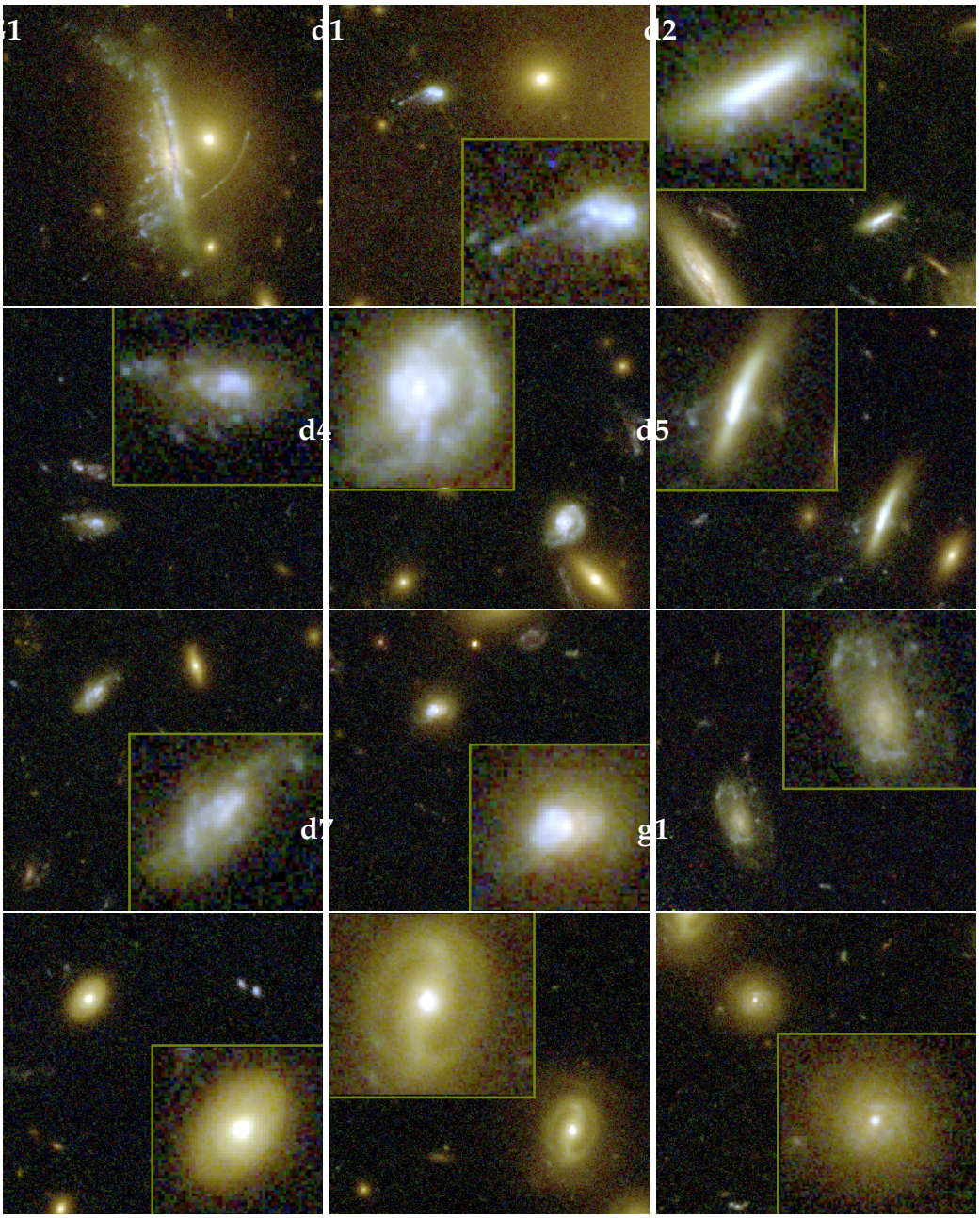

FIGURE 6.5: Close-up view of the galaxies exhibiting Hα emission in our DEIMOS spectra. The first eight are JFG1 and seven additional galaxies targeted because their disturbed morphology suggested ongoing ram-pressure stripping (d1 to d7). The final three (r1 to r3) were selected for observation as likely cluster members because of their color, which is consistent with the cluster red sequence. All images span 17 arcsec on a side; where present, insets show a magnified view of the observed galaxy. The resulting DEIMOS spectra are shown in Fig. 6.4.

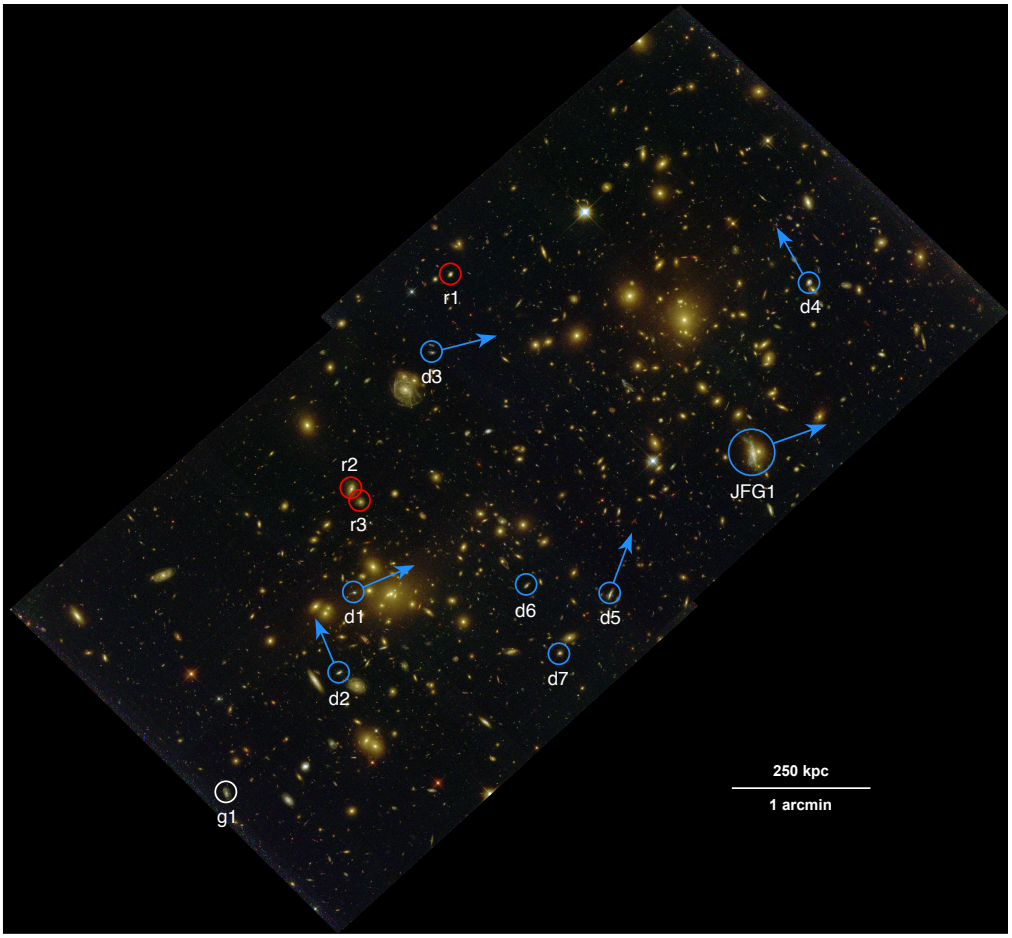

FIGURE 6.6: As Fig. 6.2 but with all galaxies from Fig. 6.5 marked; color coding as in Fig 6.3. Arrows indicate the deduced approximate direction of motion in the plane of the sky for RPS candidates with discernible debris tails.

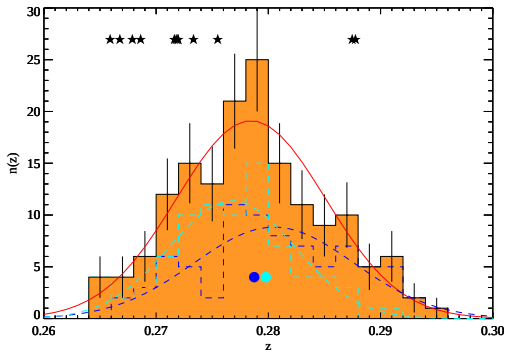

FIGURE 6.7: Redshift histogram for 159 spectroscopically confirmed members of A1758N. Although the data are well described by a single Gaussian, overlaid in red, the redshift distribution in the NW half of the field (dashed blue) differs significantly from that in the SE half (dashed cyan). The locations of the respective BCGs, and of all EL galaxies in the DEIMOS data set, are marked at the bottom and top, respectively.

of A1758N, consistent with the small radial velocity difference of 180 km s^{-1} between the BCGs (see Fig. 6.7).

6.6.3 The emission-line subsample: physical properties

A clear physical division within the sample of emission-line galaxies becomes apparent when we examine star formation as a function of stellar mass. As shown in Fig. 6.8, all of the eight galaxies targeted because of morphological signs of RPS in the HST images (see Fig. 6.5) lie well above even the outermost confines of the so-called main sequence (e.g., Lee et al., 2015), most of them dramatically so. By contrast, the three emission-line galaxies appearing morphologically undisturbed and featuring colors consistent with the cluster red sequence show no elevated star formation[3] (and neither does g1, observed as a “filler" on our DEIMOS masks).

Used as diagnostics in the BPT diagram (Fig. 6.9), the emission line ratios [N2]λ6583/Hα and [O3]λ5007/Hβ place all of the galaxies of our emission-line subsample (see Figs. 6.4, 6.5, 6.6) within the star-formation regime (Kewley et al., 2001). Dividing this regime further, following Kauffmann et al. (2003), we find the two most massive galaxies targeted because of their disturbed morphology (JFG1, discussed in detail by Kalita and Ebeling 2019, and d05, see Table 6.1 and Fig. 6.8) to lie in the “composite" region occupied by galaxies that show both star formation and additional nuclear

[3]We note that our determination of the star-formation rate of r01 remains a lower limit because of our inability to obtain a credible estimate of the Hβ flux and hence of the Balmer decrement.

name	$\log(M_\star M_\odot^{-1})$	SFR ($M_\odot$ yr^{-1})	$\Delta v_{\rm rad}$ (km s^{-1})
JFG1	10.87±0.02	47.9	−936
d1	8.47±0.06	5.6	−1933
d2	9.50±0.03	5.9	−1355
d3	8.39±0.04	6.0	−739
d4	9.83±0.06	15.1	−1174
d5	10.10±0.05	16.6	−1410
d6	8.88±0.02	4.8	−2257
d7	9.78±0.01	13.8	1320
g1	9.47±0.01	1.6	1370
r1	10.46±0.10	$> 1.1^\star$	−1885
r2	10.62±0.12	12.3	−2409
r3	10.02±0.06	6.0	−1381

TABLE 6.1: Stellar mass, star formation rate, and radial velocity relative to the (in projection) closest BCG of all galaxies in our DEIMOS sample that show Hα emission (see Fig. 6.5). Galaxy coordinates and redshifts can be found in Appendix A. We assign a name to the only indisputable case of RPS and denote the provenance of all other galaxies in our line-emitter sample by a leading "d" (for disturbed), "r" (for red sequence), and "g" (for other galaxies).

* *lower limit since negligible Hβ emission prevents computation of the Balmer decrement and hence correction for dust extinction*

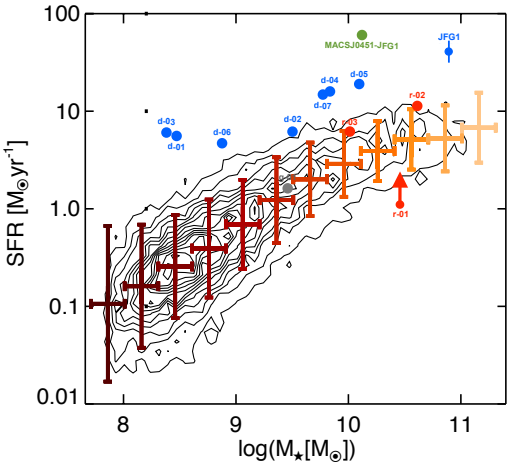

FIGURE 6.8: The loci of the 12 galaxies shown in Fig. 6.5 overplotted on the SFR vs M_* relation (figure adapted from Lee et al. 2015). Also shown for reference is MACSJ0451-JFG1 (in green), a textbook example of ram-pressure stripping at $z = 0.43$ (Ebeling, Stephenson, and Edge, 2014, Ebeling et al. in prep).

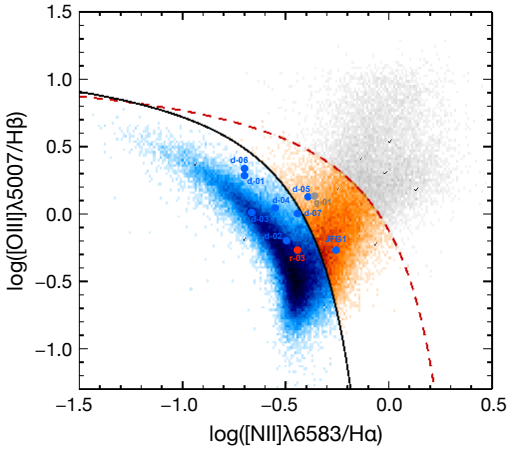

FIGURE 6.9: Location of the RPS candidates shown in Fig 6.5 in the BPT diagram (adapted from Lara-López et al. 2010). The solid line shows the empirical division between star-forming and composite galaxies from Kauffmann et al. (2003); the dashed line represents the starburst limit from Kewley et al. (2001).

activity. Note that not all galaxies from Table 6.1 and Fig. 6.8 are shown in Fig. 6.8 since some lack measurable intensities in the required emission lines.

6.7 Discussion

In the previous section we summarized the properties of the eight RPS candidates in A1758N selected by us for spectroscopic follow-up. Remarkably, they share characteristics that not only strongly support the notion that these systems are indeed undergoing ram-pressure stripping; their dynamical properties also suggest a bulk flow of galaxies that, if real, casts doubt on the merger geometry and dynamics widely adopted for A1758N in the past. In this section we interpret the findings presented in Section 6.6.

6.7.1 Triggered star formation and nuclear activity

Fig. 6.8 and Fig. 6.9 demonstrate that all eight RPS candidates observed by us are undergoing a period of intense star formation. In addition, the location of the most massive galaxies among our targets in the composite region of the BPT diagram (Fig. 6.9) is consistent with modest nuclear activity, in agreement with interplay and possibly a causal link between RPS and AGN as pointed out by Poggianti et al. (2017) and George et al. (2019). A caveat regarding classifications based on the BPT diagram is in order though: our RPS candidate d07 (just outside the composite region in Fig. 6.9) is found to be an X-ray bright point source in the archival Chandra data (Fig. 6.2), which

unambiguously identifies this galaxy as an AGN. Nonetheless, the combination of these systems' disturbed morphology and extreme star-formation rates strongly supports our initial RPS hypothesis for most of our targets, in particular since galaxy mergers, the only other plausible physical process that could explain the observational evidence, are highly improbable due to the very low cross section for galaxy collisions at the high peculiar velocities encountered in massive clusters.

6.7.2 Direction of motion

While the spatial distribution (as projected onto the plane of the sky) of our eight RPS galaxies does not exhibit any obvious pattern, their projected direction of motion, as deduced from their debris trails (where discernible), shows a clear tendency to point toward the NW, as indicated in Fig. 6.6 (six out of eight[4], a ratio that has a probability of 10.9% of occurring by chance in an isotropic distribution). Moreover, all of them also feature high radial velocities relative to both BCGs, and for most of them (seven out of eight) these peculiar velocities are negative (Table 6.1 and Fig. 6.7), indicative of a rapid motion toward us. The probability of this distribution occurring by chance in a radial velocity distribution centered on the systemic cluster redshift is 3.1%. Since the radial and transverse velocity components are statistically independent, the combined probability of the observed distribution of velocity vectors being a coincidence is 3×10^{-3}. While this number (which formally corresponds to 2.9σ significance) ought to be taken with a grain of salt, primarily because of the subjective interpretation of the orientation of the potential debris trails, the observed distribution of velocities for the sample of emission-line galaxies is clearly far from isotropic. The implications of this result are discussed in Section 6.7.3. We further note that, since at least four of the RPS candidates (JFG1, d1, d2, and d3) feature clearly visible and credible debris trails, the significant (but unknown) velocity component in the plane of the sky of these systems makes their total three-dimensional velocities in the cluster restframe even higher than the observed radial velocities of 700 to 2000 km s^{-1}. Moreover, the observed large radial peculiar velocities imply that the debris trails of these systems are likely to be much longer in three dimensions than the observed, projected lengths of 10 to 30 kpc (see Fig. 6.5), rendering these galaxies potentially extreme cases of RPS akin to ESO 137-001 in the nearby Universe (Sun, Donahue, and Voit, 2007; Fumagalli et al., 2014). Although unambiguous evidence of ongoing RPS events is lacking (or less compelling) for the remaining four candidates, the location of all eight galaxies in the SFR vs M_* plane (Fig. 6.8) is indicative

[4]Note that, while our estimate of the direction of motion as indicated in Fig. 6.6 is somewhat subjective, we here only consider the velocity component along the line connecting the two BCGs of A1758N; i.e., our classification is a binary one: toward the NW or toward the SE.

of vigorous starbursts that are consistent with, but greatly exceed, SFR enhancements found for RPS events in less massive clusters (Vulcani et al., 2018).

6.7.3 The impact of cluster mergers

The observed strong bias in favor of negative peculiar velocities highlighted in Section 6.7.2 (see also Table 6.1) is noteworthy, since it effectively rules out two possible scenarios regarding the dynamics and origin of the RPS population in A1758N, both of which should result in a largely symmetric velocity distribution. They are: (a) isotropic infall of late-type galaxies from the surrounding field, and (b) stripping of gas-rich cluster members caused by the high velocities created by a merger proceeding in, or very close to, the plane of the sky (the geometry assumed by all previous studies of this system, including the simulations by Machado et al. 2015 and **mo17**).

Although the lopsided distribution and high amplitudes of radial velocities of our RPS candidates heavily disfavor the specific merger geometry adopted historically for A1758N, the observational evidence nonetheless strongly supports a causal link between RPS and merger events in clusters. Previous studies found two opposing effects of such a link: Stroe et al. (2015) and Stroe et al. (2017) and Ruggiero et al. (2019) report evidence of RPS triggered by merger-induced shocks, while other studies (Pranger et al., 2014; Deshev et al., 2017) find the fraction of star-forming galaxies in mergers reduced compared to non-merging clusters, possibly after a preceding short starburst phase. Although seemingly in conflict with each other at face value, these findings might be reconciled as part of a bigger picture in which RPS events in mergers first trigger an initial burst of star formation, and then reduce or completely quench star formation as the supply of atomic and molecular gas is either exhausted or removed from the affected galaxies. The prominence and duration of either phase are, however, likely to depend on details of the merging systems, such as mass, time since first core passage, and collision geometry. In the following section we describe how a combination of both of these effects can explain the phase-space distribution of RPS candidates in the A1758N merger.

6.7.4 RPS as a diagnostic tool: A history of A1758N?

For the majority of clusters, it is primarily the infall of gas-rich galaxies from the surroundings that gives rise to RPS events. In the absence of pronounced filaments, the resulting velocity distribution is expected to be approximately isotropic, an expectation that clearly is not met by A1758N. Since galaxy infall from the field is unavoidable for a cluster as massive as A1758N, the resulting isotropic RPS distribution is either not well enough sampled to contribute

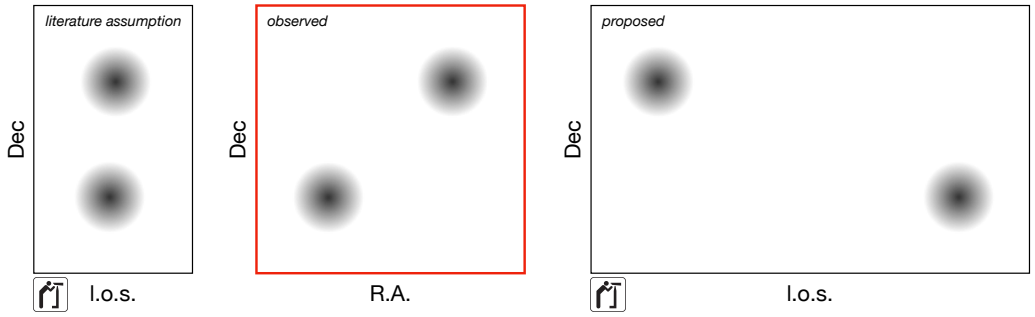

FIGURE 6.10: Center: schematic sketch of the observed locations of the two subclusters of the A1758N merger as seen in projection on the sky. The panels on either side show a rotated view that reveals the two components' separation along our line of sight (l.o.s.); the geometry shown in the left panel corresponds to a merger in the plane of the sky, as assumed in the literature; the one on the right illustrates the scenario proposed by use here, in which the merger (observed near turnaround) proceeds along an axis that is substantially inclined with respect to the plane of the sky.

discernibly to our small sample[5], or the A1758N collision is sufficiently advanced for merger-driven shocks to have quenched star formation in the pre-merger RPS population (Deshev et al., 2017). The latter possibility finds additional support in the findings by Haines et al. (2009) who report the presence of a significant and distinct population of passive spiral galaxies in their infrared study of this system.

While the absence of an isotropic velocity distribution in the RPS population of A1758N thus may (but need not) be a direct consequence of the system's merger history, the cause of the specific, observed directional velocity bias is almost certainly tied to the three-dimensional geometry and environment of the ongoing collision, more specifically to the only preferred direction in this system: the merger axis. Since late-type (gas-rich) galaxies are rare in massive clusters, the population undergoing RPS in A1758N must originate from a much less dense environment, suggesting infall along a filament (rather than isotropically from the general field). However, as the orientation of large-scale filaments determines and indicates the direction along which clusters accrete matter at the vertices of the cosmic web, the direction of the bulk flow of the RPS population of A1758N also marks the most probable orientation of the merger axis. It follows that the latter must be strongly inclined with respect to the plane of the sky, with the feeding filament extending behind and to the SE of the cluster center, as illustrated in Fig. 6.10.

[5]Since observational limitations, such as magnitude limit and angular resolution, pose challenges to the identification of RPS events, study of a single cluster may not yield a large enough sample to robustly probe the velocity distribution.

In this scenario, A1758N is not merging in the plane of the sky (as assumed so far in the literature based on the argument that the absence of a significant difference in redshift between the subclusters is evidence of them moving perpendicular to our line of sight) but, in a geometry not unlike that of MACSJ0553.4−3342 (Ebeling, Qi, and Richard, 2017) along a greatly inclined axis, rendering the observed projected distance between the BCGs of 750 kpc a severe underestimate of their true three-dimensional separation (Fig. 6.10). In this scenario, the lack of a pronounced difference in radial velocity between the subclusters and their BCG represents strong evidence of the merger being observed near turnaround.

6.8 Summary

Following the discovery of A1758N_JFG1 (Kalita and Ebeling, 2019), we identified over a dozen other promising RPS candidates in HST/ACS images of the massive cluster merger A1758N, seven of which were spectroscopically confirmed as cluster members in our DEIMOS observation. Spanning almost three orders of magnitude in stellar mass, all galaxies in the resulting sample of eight feature very high star-formation rates well outside the range observed in regular late-type galaxies. Although only half of these RPS candidates exhibit credible debris trails (an unambiguous sign of ram-pressure stripping), the observed starbursts are unlikely to be the result of minor mergers even for the remaining four, considering the high relative velocities of galaxies (and thus low cross-section for collisions) in this massive cluster merger. Our findings thus lend strong observational support to the notion that RPS, at least in the extreme environment provided by a collision of massive clusters, does not merely displace pre-existing star-forming regions, but in fact triggers powerful starbursts.

Our sample of galaxies undergoing RPS in A1758N exhibits a highly anisotropic velocity distribution, both along the line of sight and in projection of the sky, suggesting a bulk motion of galaxies relative to the intra-cluster medium along an axis that is strongly inclined with respect to the plane of the sky. The physically most plausible causes for such a pronounced directional bias are galaxy infall along an attached filament or (less compelling, since acting only for a short time) a shock front traveling along the merger axis. Either scenario (or a combination of both) implies that, contrary to all assumptions made to date in the literature, the merger axis of A1758N does not lie in (or close to) the plane of the sky, and that the observed small difference in radial velocity between the subclusters is instead indicative of a collision along a highly inclined merger axis being viewed near turnaround.

Extending our findings and conclusions to cluster mergers in general, we advance the hypothesis that measurements of the peculiar velocities of RPS candidates could be used to constrain the three-dimensional orientation of the merger axis in cluster collisions. Systematic study of the velocities of

morphologically disturbed galaxies in other cluster mergers will allow us to test the validity of our hypothesis.

Radial velocities

We list in Table 6.2 the coordinates and redshifts of all galaxies observed by us with Keck-II/DEIMOS. Details of the instrumental setup are summarized in Section 6.3.2.

name	R.A. (J2000)	Declination (J2000)	z	dz
	13:32:27.373	+50:34:03.48	0.3787	0.0002
d7	13:32:44.222	+50:31:07.66	0.2875	0.0001
	13:32:27.900	+50:34:06.00	0.3886	0.0003
	13:32:44.934	+50:31:57.23	0.2806	0.0005
	13:32:29.199	+50:34:10.10	0.2785	0.0002
	13:32:44.956	+50:34:05.82	0.2886	0.0002
	13:32:32.075	+50:32:52.75	0.3901	0.0002
	13:32:45.327	+50:33:24.70	0.2862	0.0002
d4	13:32:32.582	+50:33:52.49	0.2720	0.0002
d6	13:32:45.744	+50:31:37.79	0.2668	0.0002
	13:32:32.624	+50:34:27.88	0.1771	0.0001
	13:32:45.913	+50:32:04.74	0.2672	0.0002
	13:32:34.350	+50:32:11.28	0.2676	0.0008
	13:32:46.977	+50:32:02.01	0.2808	0.0003
	13:32:34.468	+50:33:18.54	0.2830	0.0002
	13:32:48.696	+50:31:21.69	0.2776	0.0002
	13:32:34.932	+50:32:37.28	0.2800	0.0001
	13:32:48.890	+50:34:09.58	0.2746	0.0002
JFG1	13:32:35.169	+50:32:36.43	0.2733	0.0003
r1	13:32:49.296	+50:33:56.02	0.2679	0.0003
	13:32:35.357	+50:32:52.63	0.6188	0.0004
d3	13:32:50.138	+50:33:21.22	0.2755	0.0002
	13:32:35.476	+50:34:51.52	0.6330	0.0004
	13:32:50.992	+50:33:08.86	0.2817	0.0003
	13:32:35.720	+50:33:28.64	1.0349	0.0001
	13:32:51.958	+50:31:47.65	0.2800	0.0008
	13:32:36.486	+50:32:34.79	0.2711	0.0004
BCG-E	13:32:52.065	+50:31:33.98	0.2798	0.0001
	13:32:36.619	+50:32:06.65	0.2693	0.0010
	13:32:52.815	+50:30:26.44	0.2823	0.0002
	13:32:36.700	+50:33:59.24	0.3280	0.0001
	13:32:52.901	+50:31:46.05	0.2659	0.0006
	13:32:37.560	+50:33:05.77	0.2744	0.0002
	13:32:53.293	+50:31:13.77	1.0809	0.0001
	13:32:38.305	+50:31:30.22	0.2886	0.0006
r3	13:32:53.488	+50:32:14.98	0.2718	0.0003
BCG-W	13:32:38.395	+50:33:35.72	0.2787	0.0001
	13:32:53.652	+50:30:53.32	0.3299	0.0003
	13:32:38.448	+50:31:41.49	0.2838	0.0003
d1	13:32:53.785	+50:31:34.65	0.2686	0.0001
	13:32:38.550	+50:33:43.93	0.2792	0.0005
	13:32:53.900	+50:29:57.62	0.2738	0.0003
	13:32:39.413	+50:34:45.08	0.2776	0.0002
r2	13:32:53.918	50:32:20.56	0.2659	0.0003

	13:32:39.526	+50:34:32.00	0.2936	0.0002
	13:32:54.387	+50:33:34.25	0.2723	0.0004
	13:32:39.553	+50:34:00.20	0.2842	0.0002
d2	13:32:54.475	50:30:59.13	0.2719	0.0002
	13:32:39.759	+50:32:41.07	0.2789	0.0002
	13:32:54.785	+50:30:27.78	0.1753	0.0001
	13:32:40.481	+50:35:39.69	0.2727	0.0001
	13:32:55.064	+50:32:04.84	0.2751	0.0004
	13:32:40.640	+50:34:51.46	1.2823	0.0001
	13:32:55.122	+50:31:25.43	0.2838	0.0001
	13:32:40.939	+50:33:46.29	0.2788	0.0001
	13:32:55.975	+50:32:49.03	0.2646	0.0001
d5	13:32:41.868	+50:31:33.58	0.2716	0.0001
	13:32:56.058	+50:30:17.36	0.1038	0.0000
	13:32:42.021	+50:34:34.77	0.2923	0.0004
	13:32:56.875	+50:30:02.76	0.1504	0.0002
	13:32:43.364	+50:33:05.26	1.2472	0.0001
	13:32:57.024	+50:32:13.14	0.2851	0.0003
	13:32:43.415	+50:33:28.68	0.2853	0.0003
	13:32:57.701	+50:31:13.23	0.2804	0.0002
	13:32:43.764	+50:31:14.63	0.2778	0.0002
g1	13:32:59.725	+50:30:05.24	0.2878	0.0006

TABLE 6.2: Positions and redshifts (with associated uncertainties) of all galaxies observed by us with Keck-II/DEIMOS. The 12 emission-line galaxies are labelled.

Chapter 7

Conclusion and Future Work

Part I of this thesis (chapters 2, 3, 4) attempts to provide conclusions on the interdependence of the formation, evolution and quenching of massive galaxies and their environments at $z \sim 2-3$. This epoch is expected to feature an overlap between the effects of cold-gas accretion and the rapid evolution of the star-forming progenitors (cSFGs) of the massive cluster ETGs in the local universe. We revisit each of them and attempt to provide a direction for future research.

Part II (chapters 5, 6), deals with the first fully resolved study of ram-pressure stripping at intermediate redshifts (z $\sim$ 0.3). We show that this also provides information regarding the large scale dynamics of clusters/groups on the plane of the sky, which otherwise cannot be obtained. We discuss the possibility of exploiting the conclusions from the study to investigate pre-processing of galaxies at intermediate redshifts, through environmental quenching mechanisms.

PART I

7.1 Cold-gas accretion in dense environments

We initially dive into the formation of the most massive galaxies that were forming at what would likely be the heart of future clusters (Kalita et al., 2022), a galaxy-group RO-1001 at z=2.91. Although theoretically, cold gas accretion streams are expected to feed the star-formation in these systems, we are far from fully recognizing the direct effects of this process on their evolution due to a lack of direct observational evidence in the galaxies. We have hence used a combination of resolved UV, optical, near-IR and sub-mm data to provide a cohesive picture of how accretion maybe leading to the structural evolution of galaxies driven by the sites of star-formation.

Until now, research has mainly been directed at the global evolution of cold-gas accretion into halos. The current understanding based on theoretical studies along with hydrodynamical simulations indicates that above the M_{shock} limit ($\sim 10^{12}\,M_{\odot}$) of halos (Kereš et al., 2005; Dekel and Birnboim, 2006), where the gas within them are expected to be shock heated to virial temperatures $\sim 10^{6}$ K, collimated streams of cold-gas are capable of

efficiently penetrating into the halo cores and feed member galaxies at high redshits (Kereš et al., 2005; Dekel et al., 2009). This phenomenon is governed by an redshift-dependent halo mass upper-limit (M_{stream}) which is above the M_{shock} limit for $z \gtrsim 1.5$; allowing efficient feeding of SFGs within halos that fall within this regime (Fig. 7.1). This boundary is found to progressively increase with redshift, having a value $\sim 10^{12.5}\,M_\odot$ at z=2, which becomes $\sim 10^{13.5}\,M_\odot$ at z=3.

The rate at which the baryons are channeled by the filaments would be dictated by the cosmological growth rate of host dark matter halos. This can be calculated as:

$$\dot{M} = 6.6\,M_{12}^{1.12}\;(1+z)^{2.25}\;f_b\,M \odot\; yr^{-1} \tag{7.1}$$

Dekel et al., 2009 shows that the $\dot{M}(z)$ is just sufficient to feed the highly star-forming galaxies at high redshifts (using the star-forming galaxy main sequence as a representative measure). This consistency provides further support that the incoming baryons, which firstly needs to be predominantly gas, do in fact penetrate deep into the halos and leads to fueling of star-formation.

Nevertheless, how this accreted gas streaming in through filaments is converted to stars within the galaxies is still unclear. Recently obtained evidence is still limited to consistencies in integrated star-formation rates with theoretical predictions of cold-gas accretion: Popesso et al., 2019; Popesso et al., 2022 showing that the bending of the main-sequence follows the M_{shock} boundary at z=0, while Daddi et al., 2022b shows a similar agreement with the M_{stream} boundary at $z > 2$. In other words, the star-formation in galaxies is regulated by the levels of cold-gas accretion onto the host halos. Nevertheless, the direct link between the cold-gas falling into halos and how it is being fed to the galaxies is still a scientific 'blind-spot'.

7.1.1 Building massive galaxies through accretion

Our work presented in Chapter 2 attempts to bridge the gap between global cold-gas accretion streams and galaxy properties. But this analysis of RO-1001 requires to be part of a larger study of similar structures. The ideal sample has already been put forward in Daddi et al., 2022a: 9 galaxy clusters and groups within a redshift range of $1.98 < z < 3.27$. Their Lyman-α halo luminosities are consistent with the theoretically expected evolution of cold-gas accretion over mass and redshift. The integrated star-formation rate in the core of these structures also seems to follow the same evolutionary trend, although with a temporal offset (Daddi et al., 2022b), suggesting the anticipated link between cold-gas accretion and star-formation.

However, the galaxies in only three of the 9 structures (Fig. 7.1) in Daddi et al., 2022b have yet been studied at high-resolution. The results fail to converge towards a consistent narrative of galaxy evolution. On one hand, CLJ1449+0856 (at $z = 1.99$; Gobat et al., 2012; Strazzullo et al., 2016; Coogan

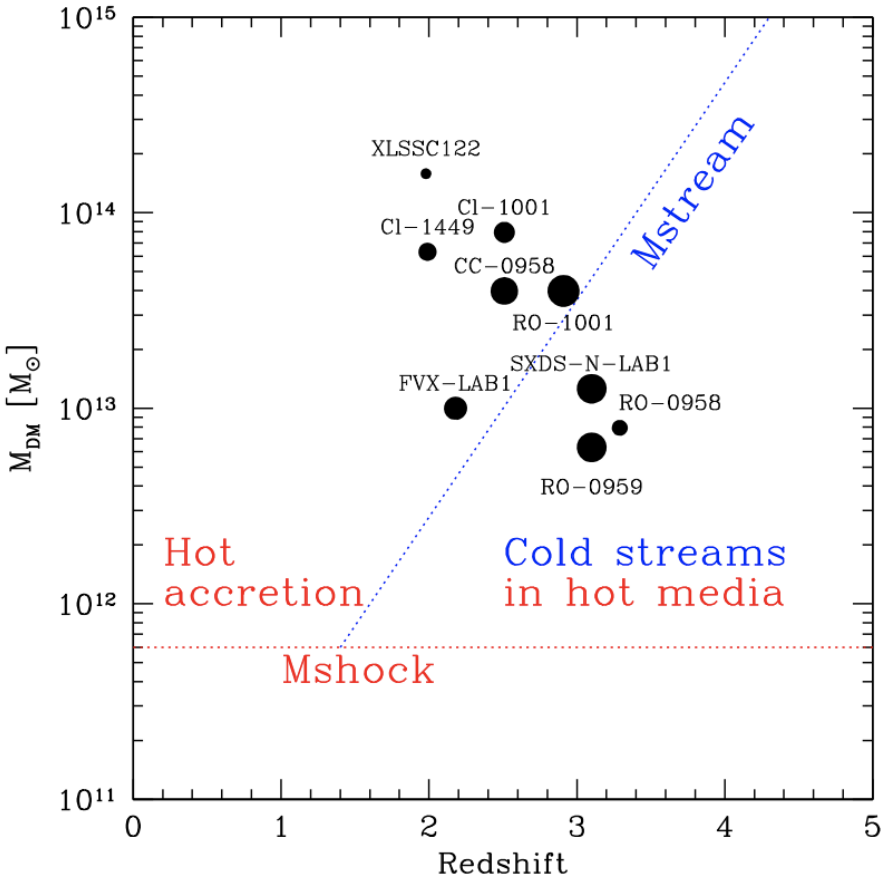

FIGURE 7.1: The M_{halo} vs redshift diagram that we showed previously in Fig. 1.3, that was initially presented in Dekel and Birnboim, 2006. We show the sample of 9 galaxy cluster/groups discussed in Daddi et al., 2022b within this diagram (which includes both RO-1001 and CLJ1449+0856 that were studied in this thesis), each of which are expected to either be within the cold-gas accretion regime or be transitioning out of it.

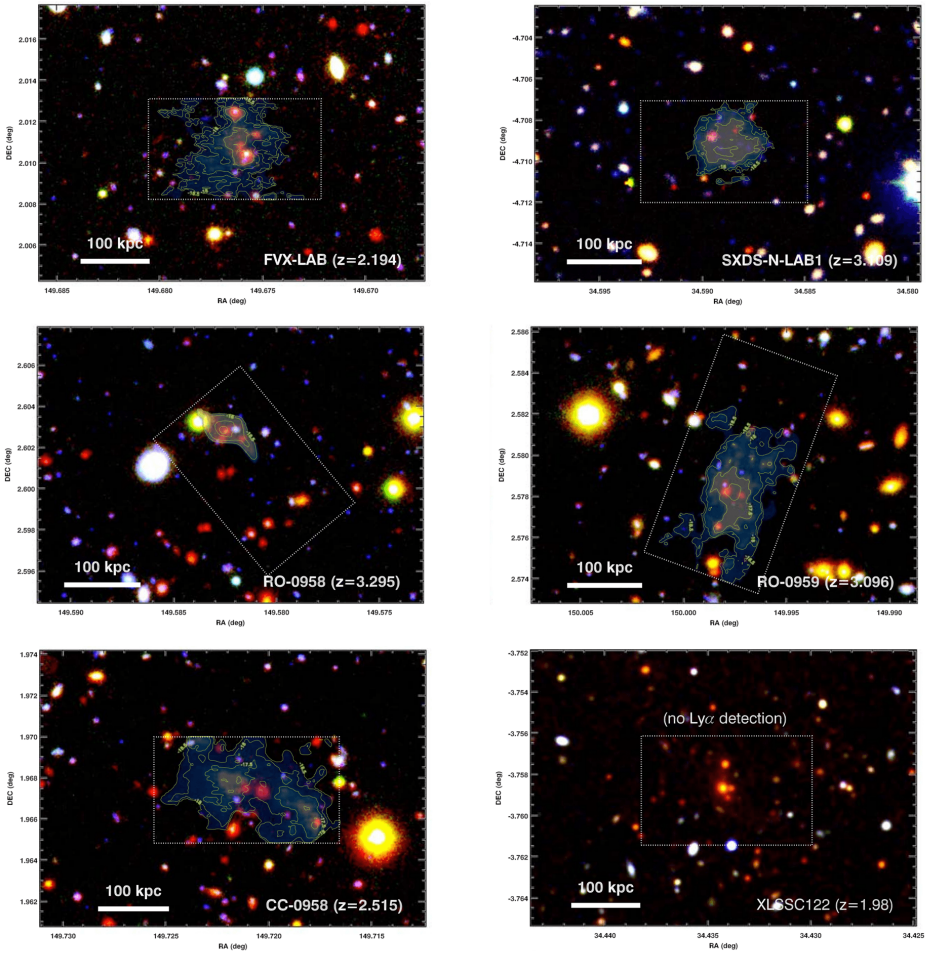

FIGURE 7.2: BzK color images for the six structures of the nine structures shown for illustration purposes. The green contours show the Ly-α halo in each case, while the cyan circles demarcate the sub-mm detected star-forming galaxies. The total log(SFR) contained within the galaxies are $2.1\,M_{\odot}\,yr^{-1}$, $2.2\,M_{\odot}\,yr^{-1}$, $3.2\,M_{\odot}\,yr^{-1}$, $3.2\,M_{\odot}\,yr^{-1}$, $2.3\,M_{\odot}\,yr^{-1}$, and $< 2.3\,M_{\odot}\,yr^{-1}$ for FVX-LAB, SXDS-N-LAB1, RO-0958, RO-0959, CC-0958 and XLSC122 respectively

et al., 2018) and CL1001+0220 (at z = 2.51; Wang et al., 2016) show high levels of major-merger driven star-burst like activity, clearly detected in sub-mm dust emission, in their massive star-forming galaxies. They primarily galaxies have disturbed morphologies and/or appear as merging pairs. This is in line with blind survey studies of sub-mm bright (usually compact) massive galaxies, previously discussed as the crucial population of cSFGs, which conclude that major-mergers result in the star-burst like activity (Cimatti et al., 2008; Fu et al., 2013; Ivison et al., 2013; Toft et al., 2014; Toft et al., 2017; Elbaz et al., 2018).

However, as discussed in chapter 2, our high-resolution HST imaging of the group RO-1001 (at z = 2.91; Daddi et al., 2021a) with 3 spectroscopically confirmed $> 10^{11}\,M_{\odot}$ highly star-forming galaxies (A, B and C; Fig. 2.1), finds a lack of disturbed morphology in 2/3 of them (B and C), and therefore a lack of major-merger evidence. Although, the third (galaxy A) is likely at an initial phase of collision with an equally massive counterpart. This is indicative of sub-mm bright galaxies, especially in accretion-rich sites to be growing under the effects of smooth-gas or clumpy material accretion.

This ambiguity bolsters further the need to study the rest of the 6 structures (Fig. 7.2) with similar detail. The primary objective would be to resolve the stellar emission in search for morphological signatures, along the same lines as done for RO-1001. Moreover, parallel ALMA based sub-mm studies would be indispensable to obtain the dust-obscured star-forming regions. A combined study not only provides key suggestions regarding the morphological state of the galaxies that is critically linked to how the cold-gas from the filaments are interacting with the galaxies, but also indicates how, and especially where within the galaxies, is it enhancing as well as suppressing star-formation.

Hence, such a study has the potential of answering crucial questions about galaxy evolution:

- What effect does accretion have on morphology and star formation in galactic scales?
- How and when does bulges-formation, that manifests as star-forming compact cores, occur in massive galaxies? Are they connected to accreted cold-gas (smooth and/or clumpy) or major-mergers?

It would also be critical to undertake follow-up spectroscopic studies of the sources. A critical parameter to investigate is the relation between the matter accretion and star formation is gas-phase metallicity (e.g., Lilly et al., 2013). At least in the field environment at $z \lesssim 2.5$, it is known that there is a tight relation among stellar mass, gas-phase metallicity, and star formation rate, forming a surface in the 3-dimensional space (e.g., Mannucci et al., 2010). This can be explained by a self-regulation of star formation with gas accretion, gas consumption by star formation, and outflow (e.g., Lilly et al., 2013; Onodera et al., 2016). On the other hand, whether the stellar mass–metallicity–SFR relation is similar in overdense regions or not is not

clear. Valentino et al., 2015 reported a deficit of gas-phase metallicity of star-forming galaxies in the X-ray emitting CLJ1449+0856, relative to field counterparts. Although CLJ1449+0856 is located relatively far from the transition line and in the hot-accretion-dominated regime (Fig 7.1)), this result suggests that the accretion of cold gas may still play an important role to enhance star formation activity and dilute enriched gas. However, since the number of clusters/groups with measured gas accretion rate and reliable galaxy physical properties such as SFR and metallicity based on rest-frame optical emission lines is quite limited, studying more regions is crucial to investigate the galaxy evolution during this critical stage.

One of the major traits of the evolution in the accretion-fed galaxies of RO-1001 is the rapid build-up of bulges within massive stellar disks. However, this is deduced indirectly through the sub-millimeter observations of high levels of star-formation in the compact cores of the galaxies. The only direct method to gauge the stellar mass within the cores is to observe at rest-frame near-IR wavelengths where dust attenuation is minimal. However, one has to currently rely on *Spitzer* IRAC with a point-spread-function (HPBW $\sim 1.8''$) nowhere close to the $\sim 0.2''$ spatial sampling required to study the kpc-scale compact cores of these galaxies. One expects a complete revolution with the upcoming James Webb Space Telescope (JWST) that has an ideal resolution of $0.1 - 0.2''$ (HPBW) in the same regime. Furthermore, RO-1001 along with 4/8 of the candidate sources fall within the COSMOS 2-square-degree field, which is being covered by guaranteed time observation programs within the first cycle. With the data being likely available by the end of 2022, this will be a perfect opportunity to study the stellar-bulge-formation in accretion-fed galaxies within these structures.

7.2 Quenching mechanisms

Discussions on accretion-fed massive galaxies would be incomplete without tackling the question of quenching of star formation. However, one needs to acknowledge that the term 'quenching' or the resulting 'quiescence' refer to either or both the initial cessation of star formation in galaxies as well as the maintenance of the quiescence. The processes responsible (Man and Belli, 2018) might also be effective for both these definitions of 'quenching'.

As has been already discussed in the introduction of this thesis, an interplay between a variety of processes might be leading to the cessation of star-formation, and their relative importance would change based on galaxy mass and redshift (Thomas et al., 2010; Peng et al., 2010b). However, such in depth analysis has only been possible at z$1 - 1.5$, which leaves the explanation of the quiescence of massive ($> 10^{11}\,M_{\odot}$) QGs at z $\sim 3 - 4$ in a highly speculative stage. Currently, studies in this regime mainly depend on the modeling of galaxy star-formation histories, which has predominantly indicated a rapid decline in star-formation (e.g., Schreiber et al., 2018c; Valentino et al., 2020b; Forrest et al., 2020b; Forrest et al., 2020a; D'Eugenio et al., 2020a).

However, the caveat here is that most of these galaxies are recently quenched post-starbursts and their environment is unknown, barring a few cases (Kubo et al., 2021; McConachie et al., 2022). Even in these cases however, only the fact that they are associated in overdense regions is known. Hence, we might still be missing a fraction of older ($\gtrsim 1$ Gyr) QGs which are also expected to be fainter in magnitude by $\sim 1-2$ in near-IR (Forrest et al., 2020b).

In Kalita et al., 2021a, we find a galaxy that has been quiescent for > 1 Gyr and is photometrically confirmed to be within the gas-rich region of RO-1001. This is likely one of the first steps at these redshifts, towards systematically studying the relation between a well-characterised environment and the galaxies living within them. However, investigation of similar structures need to be done to reveal any general trends, beginning with the sample of clusters/groups in Daddi et al., 2022a. This would involve a reassessment of the photometric redshifts (with spectroscopic follow-ups) and stellar ages of possible members, followed by investigation of star-formation rates through a combination of optical/near-IR as well as mid-IR/sub-mm data to be sensitive to both obscured and unobscured star-formation.

A study of quenching at such high redshifts with regards to dense clusters or groups is also critical in exploring the possibility raised by detailed stellar age analysis of quiescent galaxies found in clusters at $z = 1.0-1.5$: galaxies in overdensities undergo quenching at $z > 3$ in an accelerated rate. However, understanding the modes of quenching at work would only be possible after a substantial database of quiescent systems in dense environments is created, and then compared to their field counterparts. As previously discussed, most of the studies at these redshifts primarily investigate the post-starburst population using SFH model-fitting. These indicated that gas within high-z QGs are rapidly consumed in likely major-mergers. However, the possible bias against older (> 1 Gyr) and hence less bright galaxies (Forrest et al., 2020a), may have skewed this conclusion. It is therefore unclear whether all massive quiescent galaxies at these redshifts undergo similarly rapid quenching driven by gas-rich major-mergers. After resolving this possible bias, the next step would then be to investigate whether such rapid quenching is preferred in dense environments.

The cause and sustenance of quiescence can also be intrinsically related to the morphology of the galaxy. Investigating whether major-mergers are the primary cause of quiescence would also manifest as a lack of disks, as they are bound to be destroyed in such violent interactions (e.g., Bendo and Barnes, 2000; Bournaud, Jog, and Combes, 2005; Nevin et al., 2019). Therefore, if one takes into account the expected transformation based on some morphological studies of quiescent high-z galaxies (e.g., Bell et al., 2012; Lustig et al., 2021; Lang et al., 2014; Tacchella et al., 2015; Mowla et al., 2019), we would still be expecting these objects to undergo a violent interaction at some point. On the other hand, other studies suggest that QGs at $z > 2$ are increasingly disk-like (e.g., van der Wel et al., 2011; Wuyts et al., 2011; Bruce et al., 2012; Hill et al., 2019). This would indicate that

they do not undergo violent interactions and retain their structure from their respective star-forming era. The difference may simply be driven by separate evolutionary trajectories because of varying levels of interaction with accreted material, which in turn will depend on the environment.

Our results in Kalita et al., 2022 and Kalita et al., 2021a, pave a path towards a systematic disentanglement of these two channels. In Kalita et al., 2022, we clearly show that star-forming galaxies within a accretion-rich dense group at $z = 2.91$ do feature disk-like morphologies, along with a compact highly star-forming cores. Whereas, the $> 1\,\mathrm{Gyr}$ old galaxy, likely within the same structure features a ellipsoidal structure with no indication of a disk. This illustrates the need to investigate quiescent galaxies in such high-z structures which are known to feature accretion. It needs to be noted however that those in less-dense environments (or field) may also experience low levels of accretion (the accretion rate is proportional to the halo mass), albeit without the high levels of violent interactions which are more prevalent in dense high redshift environments. Hence, such a study would have the potential to investigate what role major interactions have in quenching galaxies, through a comparison of their star formation history as well as stellar morphology.

One of the primary results of Kalita et al., 2021a, is however the sustenance of the quiescence for $\sim 1\,\mathrm{Gyr}$, in spite of the available cold-gas in RO-1001. This can hence be related to the mode of preventing star-formation where 'the gas is not allowed to cool' (Man and Belli, 2018). As discussed in Kalita et al., 2021a, AGN-driven feedback is highly efficient at inhibiting star formation (Sanders et al., 1988; Di Matteo, Springel, and Hernquist, 2005; Hopkins et al., 2006; McCarthy et al., 2011). Out of the two AGN modes, the radiative-feedback, usually detected in X-ray and mid-IR, is capable of expelling gas from galaxies to initially quench them. However, it is the kinetic mode radio-AGN feedback that is capable of injecting entropy into the inter-galactic medium surrounding the galaxies, allowing them to evolve passively for longer stretches of time. This has already been suggested by the high fraction of radio-AGN occurrence in distant quenched systems (Olsen et al., 2013; Aird, Coil, and Georgakakis, 2019; Gobat et al., 2018; D'Eugenio et al., 2021b).

But the consequences of radio AGN activity reaches much further than locally inhibiting star-formation. The entropy imparted by the jets have been found to be self-sufficient in preventing a run-away global cooling of the ICM in the nearby universe, which in turn regulates star-formation and prohibits the formation of anomalously massive cluster galaxies. Although, this kinetic mode feedback mechanism has been well studied at lower redshifts, there is a paucity of observations characterising AGN feedback in nascent clusters/protoclusters at $z \sim 2$. This is expected to have heavy impact on the evolutionary trajectories of the cluster ICM (Martig and Bournaud, 2008; Hatch et al., 2014).

However, studies of radio-jets in clusters at high-redshifts have primarily

been limited to the high-luminosity end (Miley et al., 2006; Venemans et al., 2007; Nesvadba et al., 2008; Hatch et al., 2009; Nesvadba et al., 2017; Markov et al., 2020) and may not reflect a general scenario. Moreover, one key feature of such studies is the presence of singular massive radio AGNs at the center of the cluster environment, similar to lower redshifts (e.g., McNamara and Nulsen, 2007). In Kalita et al., 2021b, we find however that there possibly exists multiple sites of low-power radio-AGN feedback in the core of a nascent galaxy cluster CLJ1449+0856 at $z = 1.99$. The intergrated power from these jets are within the expectations for local clusters with single central radio-AGNs (Mittal et al., 2009), although spatially distributed AGN feedback as in CLJ1449+0856 could be more efficient at offsetting global cooling (Pellisier et al. in prep).

The way forward would be to systematically study radio-AGN activity within dense environments, to check for similarly low-powered multiple radio-AGN feedback in place. This venture can be built on the COSMOS 3 GHz survey data (Smolčić et al., 2017), on which multiple works have already analyzed radio AGN activity upto $z \sim 3$. Hence, follow-up of overdensities in search of radio excess can be initiated with already available data.

7.2.1 Where and how quenching occurs over cosmic time

Understanding quenching within dense environments at high redshifts is incomplete without investigating the transition into lower redshifts. This is one of the avenues opened up by studying the quenching of galaxies we propose in the previous section. Investigating the location of populations of recently quenched galaxies (post-starbursts) along with older but fainter (mass-weighted ages > 1 Gyr similar to that reported in Kalita et al., 2021a), with respect to overdensities, has the potential of directly observing where and how quenching occurs over various cosmic times. This is primarily linked to the three possible quenching scenarios that can lead to a difference of mass-weighted age between QGs within and outside dense environments observed (Wetzel et al., 2013; Balogh et al., 2016; Fossati et al., 2017; Foltz et al., 2018):

- They are 'pre-processed' (e.g., Zabludoff and Mulchaey, 1998; Fujita, 2004; McGee et al., 2009; De Lucia et al., 2012; Pallero et al., 2019) before infall into clusters
- Quenching primarily occurs post-infall into clusters through processes like ram-pressure stripping, harassment and tidal stripping (Gunn and Gott, 1972; Moore et al., 1996; Dressler et al., 1997).
- The galaxies in dense environments simply get a jump-start in their evolution their formation epochs being earlier than field galaxies.

As discussed previously in Chapter 1, the dominant mechanism may be dependent on the epoch of formation, which in turn is dependent on the mass of the galaxies. At higher redshifts ($z1$) one likely expects quenching processes independent of environment (e.g., Balogh et al., 2016). However, at low to intermediate redshifts ($z < 1$), with lower mass galaxies being primarily quenching, environmental effects become a major player, which are suggested to be quenched pre-infall. In other words, they are pre-processed (e.g., Oemler et al., 2013; Haines et al., 2015; Bianconi et al., 2018; Just et al., 2019). However, in the studies suggesting that, pre-processing is inferred from distribution of star-formation estimates, red-fractions or star-formation history modellings. Although this is conclusive, it is unclear which of the environmental processes are actually playing a role due to a lack of high resolution analysis of infalling groups of galaxies.

In order to investigate pre-processing better, especially at higher redshifts, we follow a similar line of inquiry as done in Fossati et al., 2016; Fossati et al., 2019 for $z << 0.1$. We basically propose to extend this search for direct evidence of pre-processing towards intermediate redshifts, bolstered by our study of ram-pressure stripping (one of the dominant environmental processes) at $z \sim 3$ (Ebeling and Kalita, 2019; Kalita and Ebeling, 2019). For this purpose, we exploit the high resolution optical BUFFALO survey data of clusters at $z \sim 0.31 - 0.55$. This most valuable part of this venture would be to use the parallel fields offset from the clusters by a few times the virial radius. This allows us to search for infalling groups and identify signatures of ram-pressure stripping, as well as other environmental effects (Fig. 7.3).

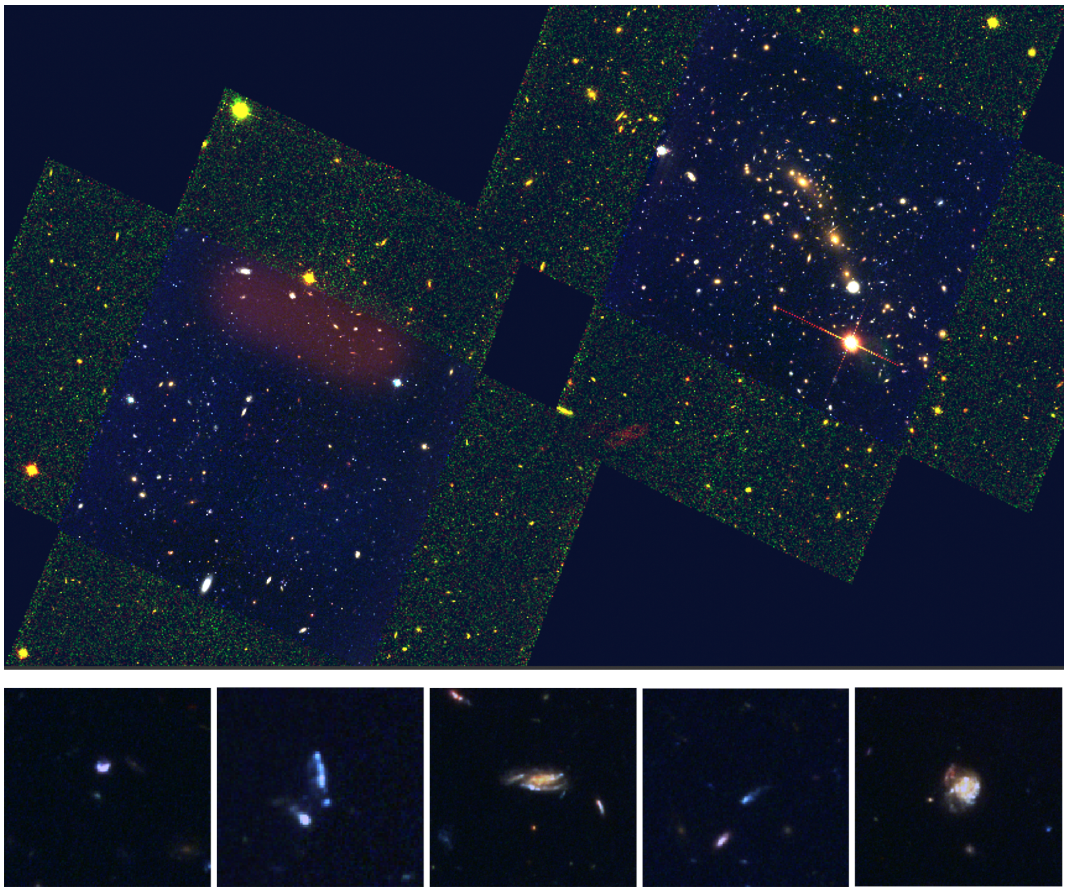

FIGURE 7.3: (Top panel) The optical color image of MACS0416 ($z = 0.396$), part of the BUFFALO sample. It is made up of two parts, the one on the right covers the galaxy cluster, while the other is the parallel field offset by ~ 3 Mpc. (Lower panel) Possible candidates of ram-pressure stripping or other dynamical disturbance in the parallel field (highlighted in the top panel with a red halo), possible part of an infalling group. These are currently awaiting spectroscopic confirmations, a DEIMOS proposal for which has been submitted.

Bibliography

Abadi, Mario G., Ben Moore, and Richard G. Bower (Oct. 1999). "Ram pressure stripping of spiral galaxies in clusters". In: *MNRAS* 308.4, pp. 947–954.

Abell, George O. (May 1958). "The Distribution of Rich Clusters of Galaxies." In: *ApJS* 3, p. 211.

Abramson, Anne et al. (May 2011). "Caught in the Act: Strong, Active Ram Pressure Stripping in Virgo Cluster Spiral NGC 4330". In: *AJ* 141.5, 164, p. 164.

Aird, J., A. L. Coil, and A. Georgakakis (Apr. 2019). "X-rays across the galaxy population - III. The incidence of AGN as a function of star formation rate". In: *MNRAS* 484.3, pp. 4360–4378.

Alatalo, Katherine et al. (Jan. 2015). "Suppression of Star Formation in NGC 1266". In: *ApJ* 798.1, 31, p. 31.

Ashby, M. L. N. et al. (Aug. 2018). "Spitzer Matching Survey of the UltraVISTA Ultra-deep Stripes (SMUVS): Full-mission IRAC Mosaics and Catalogs". In: *ApJS* 237.2, 39, p. 39.

Avila-Reese, Vladimir, Claudio Firmani, and Xavier Hernández (Sept. 1998). "On the Formation and Evolution of Disk Galaxies: Cosmological Initial Conditions and the Gravitational Collapse". In: *ApJ* 505.1, pp. 37–49.

Ball, J. A. (Jan. 1975). "Computations in radio-frequency spectroscopy." In: *Methods in Computational Physics* 14, pp. 177–219.

Balogh, Michael L. et al. (Dec. 1999). "Differential Galaxy Evolution in Cluster and Field Galaxies at z$_\sim$0.3". In: *ApJ* 527.1, pp. 54–79.

Balogh, Michael L. et al. (Mar. 2016). "Evidence for a change in the dominant satellite galaxy quenching mechanism at z = 1". In: *MNRAS* 456.4, pp. 4364–4376.

Barger, A. J. et al. (Mar. 2015). "The Host Galaxies of X-Ray Quasars are Not Strong Star Formers". In: *ApJ* 801.2, 87, p. 87.

Baron, Dalya et al. (Jan. 2022). "Multiphase outflows in post-starburst E+A galaxies - I. General sample properties and the prevalence of obscured starbursts". In: *MNRAS* 509.3, pp. 4457–4479.

Barro, G. et al. (Aug. 2016). "Sub-kiloparsec ALMA Imaging of Compact Star-forming Galaxies at z $\sim$2.5: Revealing the Formation of Dense Galactic Cores in the Progenitors of Compact Quiescent Galaxies". In: *ApJL* 827.2, L32, p. L32.

Barro, Guillermo et al. (Mar. 2013). "CANDELS: The Progenitors of Compact Quiescent Galaxies at z $\sim$2". In: *ApJ* 765.2, 104, p. 104.

Barro, Guillermo et al. (Nov. 2014). "Keck-I MOSFIRE Spectroscopy of Compact Star-forming Galaxies at z >∼2: High Velocity Dispersions in Progenitors of Compact Quiescent Galaxies". In: *ApJ* 795.2, 145, p. 145.

Beers, Timothy C., Kevin Flynn, and Karl Gebhardt (July 1990). "Measures of Location and Scale for Velocities in Clusters of Galaxies—A Robust Approach". In: *AJ* 100, p. 32.

Bekki, Kenji, Warrick J. Couch, and Yasuhiro Shioya (Oct. 2002). "Passive Spiral Formation from Halo Gas Starvation: Gradual Transformation into S0s". In: *ApJ* 577.2, pp. 651–657.

Bell, Eric F. et al. (July 2012). "What Turns Galaxies Off? The Different Morphologies of Star-forming and Quiescent Galaxies since z ∼2 from CANDELS". In: *ApJ* 753.2, 167, p. 167.

Bellhouse, C. et al. (July 2017). "GASP. II. A MUSE View of Extreme Ram-Pressure Stripping along the Line of Sight: Kinematics of the Jellyfish Galaxy JO201". In: *ApJ* 844.1, 49, p. 49.

Belli, Sirio, Andrew B. Newman, and Richard S. Ellis (Mar. 2019). "MOSFIRE Spectroscopy of Quiescent Galaxies at 1.5 < z < 2.5. II. Star Formation Histories and Galaxy Quenching". In: *ApJ* 874.1, 17, p. 17.

Bendo, George J. and Joshua E. Barnes (Aug. 2000). "The line-of-sight velocity distributions of simulated merger remnants". In: *MNRAS* 316.2, pp. 315–325.

Benson, A. J. et al. (Dec. 2003). "What Shapes the Luminosity Function of Galaxies?" In: *ApJ* 599.1, pp. 38–49.

Bernardi, Mariangela et al. (Mar. 2006). "Evolution and Environment of Early-Type Galaxies". In: *AJ* 131.3, pp. 1288–1317.

Bertin, E. and S. Arnouts (June 1996). "SExtractor: Software for source extraction." In: *A&AS* 117, pp. 393–404.

Best, P. N. et al. (Aug. 2007). "On the prevalence of radio-loud active galactic nuclei in brightest cluster galaxies: implications for AGN heating of cooling flows". In: *MNRAS* 379.3, pp. 894–908.

Béthermin, Matthieu et al. (Oct. 2012). "A Unified Empirical Model for Infrared Galaxy Counts Based on the Observed Physical Evolution of Distant Galaxies". In: *ApJL* 757.2, L23, p. L23.

Béthermin, Matthieu et al. (Jan. 2015). "Evolution of the dust emission of massive galaxies up to z = 4 and constraints on their dominant mode of star formation". In: *A&A* 573, A113, A113.

Bianconi, M. et al. (Jan. 2018). "LoCuSS: pre-processing in galaxy groups falling into massive galaxy clusters at z = 0.2". In: *MNRAS* 473.1, pp. L79–L83.

Birnboim, Yuval and Avishai Dekel (Oct. 2003). "Virial shocks in galactic haloes?" In: *MNRAS* 345.1, pp. 349–364.

Bîrzan, L. et al. (June 2004). "A Systematic Study of Radio-induced X-Ray Cavities in Clusters, Groups, and Galaxies". In: *ApJ* 607.2, pp. 800–809.

Blaizot, Jérémy et al. (July 2006). "GALICS - V: Low- and high-order clustering in mock Sloan Digital Sky Surveys". In: *MNRAS* 369.3, pp. 1009–1020.

Blanton, Elizabeth L. et al. (Sept. 2001). "Chandra Observation of the Radio Source/X-Ray Gas Interaction in the Cooling Flow Cluster Abell 2052". In: *ApJL* 558.1, pp. L15–L18.

Boehringer, H. et al. (Oct. 1993). "A ROSAT HRI study of the interaction of the X-ray emitting gas and radio lobes of NGC 1275." In: *MNRAS* 264, pp. L25–L28.

Borgani, S. et al. (Mar. 2004). "X-ray properties of galaxy clusters and groups from a cosmological hydrodynamical simulation". In: *MNRAS* 348.3, pp. 1078–1096.

Boschin, W. et al. (Apr. 2012). "Abell 1758N from an optical point of view: new insights on a merging cluster with diffuse radio emission". In: *A&A* 540, A43, A43.

Boselli, A., M. Fossati, and M. Sun (Sept. 2021). "Ram Pressure Stripping in High-Density Environments". In: *arXiv e-prints*, arXiv:2109.13614, arXiv:2109.13614.

Boselli, A. et al. (Apr. 2014). "Cold gas properties of the Herschel Reference Survey. III. Molecular gas stripping in cluster galaxies". In: *A&A* 564, A67, A67.

Boselli, A. et al. (Nov. 2019). "Evidence for ram-pressure stripping in a cluster of galaxies at z = 0.7". In: *A&A* 631, A114, A114.

Boselli, Alessandro, Matteo Fossati, and Ming Sun (Dec. 2022). "Ram pressure stripping in high-density environments". In: 30.1, 3, p. 3.

Botteon, A. et al. (July 2018). "LOFAR discovery of a double radio halo system in Abell 1758 and radio/X-ray study of the cluster pair". In: *MNRAS* 478.1, pp. 885–898.

Bouché, N. et al. (Aug. 2010). "The Impact of Cold Gas Accretion Above a Mass Floor on Galaxy Scaling Relations". In: *ApJ* 718.2, pp. 1001–1018.

Bournaud, F., C. J. Jog, and F. Combes (July 2005). "Galaxy mergers with various mass ratios: Properties of remnants". In: *A&A* 437.1, pp. 69–85.

Bournaud, F. et al. (Aug. 2005). "Lopsided spiral galaxies: evidence for gas accretion". In: *A&A* 438.2, pp. 507–520.

Bournaud, Frédéric, Bruce G. Elmegreen, and Debra Meloy Elmegreen (Nov. 2007). "Rapid Formation of Exponential Disks and Bulges at High Redshift from the Dynamical Evolution of Clump-Cluster and Chain Galaxies". In: *ApJ* 670.1, pp. 237–248.

Bournaud, Frédéric et al. (Mar. 2011). "Hydrodynamics of High-redshift Galaxy Collisions: From Gas-rich Disks to Dispersion-dominated Mergers and Compact Spheroids". In: *ApJ* 730.1, 4, p. 4.

Bravo-Alfaro, H. et al. (Feb. 2000). "VLA H I Imaging of the Brightest Spiral Galaxies in Coma". In: *AJ* 119.2, pp. 580–592.

Breda, Iris and Polychronis Papaderos (June 2018). "The continuous rise of bulges out of galactic disks". In: *A&A* 614, A48, A48.

Brennan, Ryan et al. (June 2018). "Momentum-driven Winds from Radiatively Efficient Black Hole Accretion and Their Impact on Galaxies". In: *ApJ* 860.1, 14, p. 14.

Bridge, C. R., R. G. Carlberg, and M. Sullivan (Feb. 2010). "The CFHTLS-Deep Catalog of Interacting Galaxies. I. Merger Rate Evolution to z = 1.2". In: *ApJ* 709.2, pp. 1067–1082.

Brinchmann, J. et al. (July 2004). "The physical properties of star-forming galaxies in the low-redshift Universe". In: *MNRAS* 351.4, pp. 1151–1179.

Bruce, V. A. et al. (Dec. 2012). "The morphologies of massive galaxies at 1 < z < 3 in the CANDELS-UDS field: compact bulges, and the rise and fall of massive discs". In: *MNRAS* 427.2, pp. 1666–1701.

Brusa, M. et al. (Mar. 2005). "XMM-Newton observations of Extremely Red Objects and the link with luminous, X-ray obscured quasars". In: *A&A* 432.1, pp. 69–81.

Bruzual, G. and S. Charlot (Oct. 2003). "Stellar population synthesis at the resolution of 2003". In: *MNRAS* 344.4, pp. 1000–1028.

Bullock, James S., Kyle R. Stewart, and Chris W. Purcell (Mar. 2009). "Mergers and Disk Survival in ΛCDM". In: *The Galaxy Disk in Cosmological Context*. Ed. by Johannes Andersen et al. Vol. 254, pp. 85–94.

Bundy, Kevin et al. (Aug. 2010). "The Rise and Fall of Passive Disk Galaxies: Morphological Evolution Along the Red Sequence Revealed by COSMOS". In: *ApJ* 719.2, pp. 1969–1983.

Calabrò, Antonello et al. (Dec. 2019). "Merger induced clump formation in distant infrared luminous starburst galaxies". In: *A&A* 632, A98, A98.

Calzetti, Daniela et al. (Apr. 2000). "The Dust Content and Opacity of Actively Star-forming Galaxies". In: *ApJ* 533.2, pp. 682–695.

Campisi, M. A. et al. (July 2009). "On the nature of red galaxies: the Chandra perspective". In: *A&A* 501.2, pp. 485–494.

Carilli, C. L. et al. (Dec. 1991). "Multifrequency Radio Observations of Cygnus A: Spectral Aging in Powerful Radio Galaxies". In: *ApJ* 383, p. 554.

Carles, Christian et al. (Nov. 2016). "The mass dependence of star formation histories in barred spiral galaxies". In: *MNRAS* 463.1, pp. 1074–1087.

Carnall, A. C. et al. (July 2020). "Timing the earliest quenching events with a robust sample of massive quiescent galaxies at 2 < z < 5". In: *MNRAS* 496.1, pp. 695–707.

Cayatte, V. et al. (Sept. 1990). "VLA Observations of Neutral Hydrogen in Virgo Cluster Galaxies. I. The Atlas". In: *AJ* 100, p. 604.

Cecchi, Rachele et al. (July 2019). "Quiescent Galaxies at $z \gtrsim 2.5$: Observations versus Models". In: *ApJL* 880.1, L14, p. L14.

Chabrier, Gilles (July 2003). "Galactic Stellar and Substellar Initial Mass Function". In: *PASP* 115.809, pp. 763–795.

Chung, Aeree et al. (Dec. 2009). "VLA Imaging of Virgo Spirals in Atomic Gas (VIVA). I. The Atlas and the H I Properties". In: *AJ* 138.6, pp. 1741–1816.

Cibinel, A. et al. (June 2019). "Early- and late-stage mergers among main sequence and starburst galaxies at $0.2 \leq z \leq 2$". In: *MNRAS* 485.4, pp. 5631–5651.

Cimatti, A. et al. (Apr. 2008). "GMASS ultradeep spectroscopy of galaxies at $z \sim 2$. II. Superdense passive galaxies: how did they form and evolve?" In: *A&A* 482.1, pp. 21–42.

Clarke, T. E., Elizabeth L. Blanton, and Craig L. Sarazin (Nov. 2004). "The Complex Cooling Core of A2029: Radio and X-Ray Interactions". In: *ApJ* 616.1, pp. 178–191.

Codis, S. et al. (Dec. 2018). "Galaxy orientation with the cosmic web across cosmic time". In: *MNRAS* 481.4, pp. 4753–4774.

Codis, Sandrine, Christophe Pichon, and Dmitry Pogosyan (Oct. 2015). "Spin alignments within the cosmic web: a theory of constrained tidal torques near filaments". In: *MNRAS* 452.4, pp. 3369–3393.

Coe, Dan et al. (Oct. 2019). "RELICS: Reionization Lensing Cluster Survey". In: *ApJ* 884.1, 85, p. 85.

Cole, S. et al. (Dec. 1994). "A recipe for galaxy formation." In: *MNRAS* 271, pp. 781–806.

Combes, F. and M. Gerin (Sept. 1985). "Spiral structure of molecular clouds in response to bar forcing: a particle simulation." In: *A&A* 150, pp. 327–338.

Condon, J. J. (Feb. 1997). "Errors in Elliptical Gaussian Fits". In: *PASP* 109, pp. 166–172.

Coogan, R. T. et al. (Sept. 2018). "Merger-driven star formation activity in Cl J1449+0856 at z = 1.99 as seen by ALMA and JVLA". In: *MNRAS* 479.1, pp. 703–729.

Cooper, Michael C. et al. (Mar. 2012). *spec2d: DEEP2 DEIMOS Spectral Pipeline*. Astrophysics Source Code Library, record ascl:1203.003.

Cortese, L. et al. (Mar. 2007). "The strong transformation of spiral galaxies infalling into massive clusters at $z \sim 0.2$". In: *MNRAS* 376.1, pp. 157–172.

Daddi, E. et al. (June 2005). "Passively Evolving Early-Type Galaxies at $1.4 <\sim z <\sim 2.5$ in the Hubble Ultra Deep Field". In: *ApJ* 626.2, pp. 680–697.

Daddi, E. et al. (Nov. 2007). "Multiwavelength Study of Massive Galaxies at $z \sim 2$. I. Star Formation and Galaxy Growth". In: *ApJ* 670.1, pp. 156–172.

Daddi, E. et al. (Apr. 2009). "Two Bright Submillimeter Galaxies in a z = 4.05 Protocluster in Goods-North, and Accurate Radio-Infrared Photometric Redshifts". In: *ApJ* 694.2, pp. 1517–1538.

Daddi, E. et al. (May 2010a). "Different Star Formation Laws for Disks Versus Starbursts at Low and High Redshifts". In: *ApJL* 714.1, pp. L118–L122.

Daddi, E. et al. (Apr. 2010b). "Very High Gas Fractions and Extended Gas Reservoirs in z = 1.5 Disk Galaxies". In: *ApJ* 713.1, pp. 686–707.

Daddi, E. et al. (May 2021a). "Three Lyman-α-emitting filaments converging to a massive galaxy group at z = 2.91: discussing the case for cold gas infall". In: *A&A* 649, A78, A78.

— (May 2021b). "Three Lyman-α-emitting filaments converging to a massive galaxy group at z = 2.91: discussing the case for cold gas infall". In: *A&A* 649, A78, A78.

Daddi, E. et al. (Feb. 2022a). "Evidence for Cold-stream to Hot-accretion Transition as Traced by Lyα Emission from Groups and Clusters at 2 < z < 3.3". In: *ApJL* 926.2, L21, p. L21.

Daddi, E. et al. (Mar. 2022b). "The bending of the star-forming main sequence traces the cold- to hot-accretion transition mass over 0<z<4". In: *arXiv e-prints*, arXiv:2203.10880, arXiv:2203.10880.

Davé, Romeel, Kristian Finlator, and Benjamin D. Oppenheimer (Mar. 2012). "An analytic model for the evolution of the stellar, gas and metal content of galaxies". In: *MNRAS* 421.1, pp. 98–107.

David, Laurence P. and Joshua Kempner (Oct. 2004). "Chandra and XMM-Newton Observations of the Double Cluster A1758". In: *ApJ* 613.2, pp. 831–840.

De Lucia, Gabriella et al. (June 2012). "The environmental history of group and cluster galaxies in a Λ cold dark matter universe". In: *MNRAS* 423.2, pp. 1277–1292.

Dekel, A. et al. (Jan. 2009). "Cold streams in early massive hot haloes as the main mode of galaxy formation". In: 457.7228, pp. 451–454.

Dekel, A. et al. (Oct. 2013). "Toy models for galaxy formation versus simulations". In: *MNRAS* 435.2, pp. 999–1019.

Dekel, Avishai and Yuval Birnboim (May 2006). "Galaxy bimodality due to cold flows and shock heating". In: *MNRAS* 368.1, pp. 2–20.

Dekel, Avishai and Mark R. Krumholz (June 2013). "Steady outflows in giant clumps of high-z disc galaxies during migration and growth by accretion". In: *MNRAS* 432.1, pp. 455–467.

Dekel, Avishai, Re'em Sari, and Daniel Ceverino (Sept. 2009). "Formation of Massive Galaxies at High Redshift: Cold Streams, Clumpy Disks, and Compact Spheroids". In: *ApJ* 703.1, pp. 785–801.

Delhaize, J. et al. (June 2017). "The VLA-COSMOS 3 GHz Large Project: The infrared-radio correlation of star-forming galaxies and AGN to $z \lesssim 6$". In: *A&A* 602, A4, A4.

Delvecchio, I. et al. (June 2017). "The VLA-COSMOS 3 GHz Large Project: AGN and host-galaxy properties out to $z \lesssim 6$". In: *A&A* 602, A3, A3.

Delvecchio, I. et al. (Mar. 2020). "The Evolving AGN Duty Cycle in Galaxies Since $z \sim 3$ as Encoded in the X-Ray Luminosity Function". In: *ApJ* 892.1, 17, p. 17.

Dennis, Timothy J. and Benjamin D. G. Chandran (Mar. 2005). "Turbulent Heating of Galaxy-Cluster Plasmas". In: *ApJ* 622.1, pp. 205–216.

Deshev, Boris et al. (Nov. 2017). "Galaxy evolution in merging clusters: The passive core of the "Train Wreck" cluster of galaxies, <ASTROBJ>A 520</ASTROBJ>". In: *A&A* 607, A131, A131.

D'Eugenio, C. et al. (Mar. 2020a). "The Typical Massive Quiescent Galaxy at $z \sim 3$ is a Post-starburst". In: *ApJL* 892.1, L2, p. L2.

— (Mar. 2020b). "The Typical Massive Quiescent Galaxy at z $\sim$ 3 is a Post-starburst". In: *ApJL* 892.1, L2, p. L2.
D'Eugenio, C. et al. (Sept. 2021a). "HST grism spectroscopy of z $\sim$ 3 massive quiescent galaxies. Approaching the metamorphosis". In: *A&A* 653, A32, A32.
— (Sept. 2021b). "HST grism spectroscopy of z $\sim$ 3 massive quiescent galaxies. Approaching the metamorphosis". In: *A&A* 653, A32, A32.
Di Matteo, Tiziana, Volker Springel, and Lars Hernquist (Feb. 2005). "Energy input from quasars regulates the growth and activity of black holes and their host galaxies". In: 433.7026, pp. 604–607.
Domainko, W. et al. (June 2006). "Enrichment of the ICM of galaxy clusters due to ram-pressure stripping". In: *A&A* 452.3, pp. 795–802.
Dressler, A. (Mar. 1980). "Galaxy morphology in rich clusters: implications for the formation and evolution of galaxies." In: *ApJ* 236, pp. 351–365.
Dressler, Alan et al. (Dec. 1997). "Evolution since z = 0.5 of the Morphology-Density Relation for Clusters of Galaxies". In: *ApJ* 490.2, pp. 577–591.
Dubois, Y. et al. (Oct. 2014). "Dancing in the dark: galactic properties trace spin swings along the cosmic web". In: *MNRAS* 444.2, pp. 1453–1468.
Durret, F., T. F. Laganá, and M. Haider (May 2011). "The merging cluster Abell 1758 revisited: multi-wavelength observations and numerical simulations". In: *A&A* 529, A38, A38.
Ebeling, H., A. C. Edge, and J. P. Henry (June 2001). "MACS: A Quest for the Most Massive Galaxy Clusters in the Universe". In: *ApJ* 553.2, pp. 668–676.
Ebeling, H., J. Qi, and J. Richard (Nov. 2017). "Fully stripped? The dynamics of dark and luminous matter in the massive cluster collision MACSJ0553.4-3342". In: *MNRAS* 471.3, pp. 3305–3322.
Ebeling, H., L. N. Stephenson, and A. C. Edge (Feb. 2014). "Jellyfish: Evidence of Extreme Ram-pressure Stripping in Massive Galaxy Clusters". In: *ApJL* 781.2, L40, p. L40.
Ebeling, H., D. A. White, and F. V. N. Rangarajan (May 2006). "ASMOOTH: a simple and efficient algorithm for adaptive kernel smoothing of two-dimensional imaging data". In: *MNRAS* 368.1, pp. 65–73.
Ebeling, Harald and Boris S. Kalita (Sept. 2019). "Jellyfish: Ram Pressure Stripping As a Diagnostic Tool in Studies of Cluster Collisions". In: *ApJ* 882.2, 127, p. 127.
Edge, Alastair C. and David T. Frayer (Sept. 2003). "Resolving Molecular gas in the Central Galaxies of Cooling Flow Clusters". In: *ApJL* 594.1, pp. L13–L17.
Edwards, Louise O. V. et al. (July 2007). "Line emission in the brightest cluster galaxies of the NOAO Fundamental Plane and Sloan Digital Sky Surveys". In: *MNRAS* 379.1, pp. 100–110.
Elbaz, D. et al. (June 2007). "The reversal of the star formation-density relation in the distant universe". In: *A&A* 468.1, pp. 33–48.

Elbaz, D. et al. (Aug. 2018). "Starbursts in and out of the star-formation main sequence". In: *A&A* 616, A110, A110.

Fabian, A. C. (Jan. 1994). "Cooling Flows in Clusters of Galaxies". In: 32, pp. 277–318.

— (Sept. 2012). "Observational Evidence of Active Galactic Nuclei Feedback". In: 50, pp. 455–489.

Fabian, A. C. et al. (Sept. 2003). "A deep Chandra observation of the Perseus cluster: shocks and ripples". In: *MNRAS* 344.3, pp. L43–L47.

Fabian, A. C. et al. (May 2009). "The extended X-ray emission around HDF130 at z = 1.99: an inverse Compton ghost of a giant radio source in the Chandra Deep Field-North". In: *MNRAS* 395.1, pp. L67–L70.

Fall, S. M. and G. Efstathiou (Oct. 1980). "Formation and rotation of disc galaxies with haloes." In: *MNRAS* 193, pp. 189–206.

Feldmann, Robert and Lucio Mayer (Jan. 2015). "The Argo simulation - I. Quenching of massive galaxies at high redshift as a result of cosmological starvation". In: *MNRAS* 446.2, pp. 1939–1956.

Foltz, R. et al. (Oct. 2018). "The Evolution of Environmental Quenching Timescales to z $\sim$ 1.6: Evidence for Dynamically Driven Quenching of the Cluster Galaxy Population". In: *ApJ* 866.2, 136, p. 136.

Ford, Holland C. et al. (Aug. 1998). "Advanced camera for the Hubble Space Telescope". In: *Space Telescopes and Instruments V*. Ed. by Pierre Y. Bely and James B. Breckinridge. Vol. 3356. Society of Photo-Optical Instrumentation Engineers (SPIE) Conference Series, pp. 234–248.

Forrest, Ben et al. (Feb. 2020a). "An Extremely Massive Quiescent Galaxy at z = 3.493: Evidence of Insufficiently Rapid Quenching Mechanisms in Theoretical Models". In: *ApJL* 890.1, L1, p. L1.

Forrest, Ben et al. (Nov. 2020b). "The Massive Ancient Galaxies at z > 3 NEar-infrared (MAGAZ3NE) Survey: Confirmation of Extremely Rapid Star Formation and Quenching Timescales for Massive Galaxies in the Early Universe". In: *ApJ* 903.1, 47, p. 47.

— (Nov. 2020c). "The Massive Ancient Galaxies at z > 3 NEar-infrared (MAGAZ3NE) Survey: Confirmation of Extremely Rapid Star Formation and Quenching Timescales for Massive Galaxies in the Early Universe". In: *ApJ* 903.1, 47, p. 47.

Fossati, M. et al. (Feb. 2017). "Galaxy Environment in the 3D-HST Fields: Witnessing the Onset of Satellite Quenching at z $\sim$ 1-2". In: *ApJ* 835.2, 153, p. 153.

Fossati, Matteo et al. (Jan. 2016). "MUSE sneaks a peek at extreme ram-pressure stripping events - II. The physical properties of the gas tail of ESO137-001". In: *MNRAS* 455.2, pp. 2028–2041.

Fossati, Matteo et al. (Apr. 2019). "MUSE sneaks a peek at extreme ram-pressure stripping events - IV. Hydrodynamic and gravitational interactions in the Blue Infalling Group". In: *MNRAS* 484.2, pp. 2212–2228.

Franx, Marijn et al. (Apr. 2003). "A Significant Population of Red, Near-Infrared-selected High-Redshift Galaxies". In: *ApJL* 587.2, pp. L79–L82.

Fu, Hai et al. (June 2013). "The rapid assembly of an elliptical galaxy of 400 billion solar masses at a redshift of 2.3". In: 498.7454, pp. 338–341.

Fujita, Yutaka (Apr. 2001). "Ram-Pressure Stripping of Galaxies in High-Redshift Clusters and the Influence of Intracluster Medium Heating". In: *ApJ* 550.2, pp. 612–621.

— (Feb. 2004). "Pre-Processing of Galaxies before Entering a Cluster". In: 56, pp. 29–43.

Fumagalli, Michele et al. (June 2009). "Molecular Hydrogen Deficiency in H I-poor Galaxies and its Implications for Star Formation". In: *ApJ* 697.2, pp. 1811–1821.

Fumagalli, Michele et al. (Dec. 2014). "MUSE sneaks a peek at extreme ram-pressure stripping events - I. A kinematic study of the archetypal galaxy ESO137-001". In: *MNRAS* 445.4, pp. 4335–4344.

Gallazzi, Anna R. et al. (Apr. 2021). "Galaxy evolution across environments as probed by the ages, stellar metallicities, and [α /Fe] of central and satellite galaxies". In: *MNRAS* 502.3, pp. 4457–4478.

Galliano, Frédéric, Maud Galametz, and Anthony P. Jones (Sept. 2018). "The Interstellar Dust Properties of Nearby Galaxies". In: 56, pp. 673–713.

Gaspari, Massimo and Aleksander Sądowski (Mar. 2017). "Unifying the Micro and Macro Properties of AGN Feeding and Feedback". In: *ApJ* 837.2, 149, p. 149.

Genzel, R. et al. (Oct. 2010). "A study of the gas-star formation relation over cosmic time". In: *MNRAS* 407.4, pp. 2091–2108.

George, K. et al. (Aug. 2019). "GASP XVIII: star formation quenching due to AGN feedback in the central region of a jellyfish galaxy". In: *MNRAS* 487.3, pp. 3102–3111.

Giacintucci, Simona et al. (May 2011). "A Combined Low-radio Frequency/X-ray Study of Galaxy Groups. I. Giant Metrewave Radio Telescope Observations at 235 MHz AND 610 MHz". In: *ApJ* 732.2, 95, p. 95.

Giodini, S. et al. (May 2010). "Radio Galaxy Feedback in X-ray-selected Groups from COSMOS: The Effect on the Intracluster Medium". In: *ApJ* 714.1, pp. 218–228.

Giovannini, G. et al. (Dec. 2009). "Radio halos in nearby (z < 0.4) clusters of galaxies". In: *A&A* 507.3, pp. 1257–1270.

Gitti, Myriam, Fabrizio Brighenti, and Brian R. McNamara (Jan. 2012). "Evidence for AGN Feedback in Galaxy Clusters and Groups". In: *Advances in Astronomy* 2012, 950641, p. 950641.

Glazebrook, Karl et al. (Apr. 2017). "A massive, quiescent galaxy at a redshift of 3.717". In: 544.7648, pp. 71–74.

Gobat, R. et al. (Feb. 2011). "A mature cluster with X-ray emission at z = 2.07". In: *A&A* 526, A133, A133.

Gobat, R. et al. (Nov. 2012). "The Early Early Type: Discovery of a Passive Galaxy at $z_{spec} \sim 3$". In: *ApJL* 759.2, L44, p. L44.

Gobat, R. et al. (Oct. 2013). "WFC3 GRISM Confirmation of the Distant Cluster Cl J1449+0856 at langzrang = 2.00: Quiescent and Star-forming Galaxy Populations". In: *ApJ* 776.1, 9, p. 9.

Gobat, R. et al. (Jan. 2018). "The unexpectedly large dust and gas content of quiescent galaxies at z > 1.4". In: *Nature Astronomy* 2, pp. 239–246.

Gobat, R. et al. (Sept. 2019). "Sunyaev-Zel'dovich detection of the galaxy cluster Cl J1449+0856 at z = 1.99: The pressure profile in uv space". In: *A&A* 629, A104, A104.

Gómez-Guijarro, C. et al. (Apr. 2018). "Starburst to Quiescent from HST/ALMA: Stars and Dust Unveil Minor Mergers in Submillimeter Galaxies at z $\sim$ 4.5". In: *ApJ* 856.2, 121, p. 121.

Gómez-Guijarro, C. et al. (Dec. 2019). "Compact Star-forming Galaxies as Old Starbursts Becoming Quiescent". In: *ApJ* 886.2, 88, p. 88.

Gómez-Guijarro, C. et al. (Feb. 2022a). "GOODS-ALMA 2.0: Source catalog, number counts, and prevailing compact sizes in 1.1 mm galaxies". In: *A&A* 658, A43, A43.

Gómez-Guijarro, C. et al. (Mar. 2022b). "GOODS-ALMA 2.0: Starbursts in the main sequence reveal compact star formation regulating galaxy evolution prequenching". In: *A&A* 659, A196, A196.

Grazian, A. et al. (Mar. 2015). "The galaxy stellar mass function at 3.5 $\leq$z $\leq$ 7.5 in the CANDELS/UDS, GOODS-South, and HUDF fields". In: *A&A* 575, A96, A96.

Gullieuszik, Marco et al. (Sept. 2017). "GASP. IV. A Muse View of Extreme Ram-pressure-stripping in the Plane of the Sky: The Case of Jellyfish Galaxy JO204". In: *ApJ* 846.1, 27, p. 27.

Gunn, James E. and III Gott J. Richard (Aug. 1972). "On the Infall of Matter Into Clusters of Galaxies and Some Effects on Their Evolution". In: *ApJ* 176, p. 1.

Guo, Rui et al. (July 2016). "The Role of Major Gas-rich Mergers on the Evolution of Galaxies from the Blue Cloud to the Red Sequence". In: *ApJ* 826.1, 30, p. 30.

Haines, C. P. et al. (July 2009). "LoCuSS: luminous infrared galaxies in the merging cluster Abell1758 at z = 0.28". In: *MNRAS* 396.3, pp. 1297–1307.

Haines, C. P. et al. (June 2015). "LoCuSS: The Slow Quenching of Star Formation in Cluster Galaxies and the Need for Pre-processing". In: *ApJ* 806.1, 101, p. 101.

Hatch, N. A. et al. (May 2009). "The growth and assembly of a massive galaxy at z $\sim$2". In: *MNRAS* 395.1, pp. 114–125.

Hatch, N. A. et al. (Nov. 2014). "Why z > 1 radio-loud galaxies are commonly located in protoclusters". In: *MNRAS* 445.1, pp. 280–289.

Heckman, Timothy M. and Philip N. Best (Aug. 2014). "The Coevolution of Galaxies and Supermassive Black Holes: Insights from Surveys of the Contemporary Universe". In: 52, pp. 589–660.

Heinz, Sebastian et al. (Apr. 2002). "Chandra ACIS-S Observations of Abell 4059: Signs of Dramatic Interaction between a Radio Galaxy and a Galaxy Cluster". In: *ApJL* 569.2, pp. L79–L82.

Helou, George et al. (Oct. 1988). "IRAS Observations of Galaxies in the Virgo Cluster Area". In: *ApJS* 68, p. 151.

Hester, Janice A. et al. (June 2010). "IC 3418: Star Formation in a Turbulent Wake". In: *ApJL* 716.1, pp. L14–L18.

Hickox, Ryan C. and David M. Alexander (Sept. 2018). "Obscured Active Galactic Nuclei". In: 56, pp. 625–671.

Hill, Allison R. et al. (Jan. 2019). "High-redshift Massive Quiescent Galaxies Are as Flat as Star-forming Galaxies: The Flattening of Galaxies and the Correlation with Structural Properties in CANDELS/3D-HST". In: *ApJ* 871.1, 76, p. 76.

Hodge, J. A. et al. (Jan. 2015). "The Kiloparsec-scale Star Formation Law at Redshift 4: Widespread, Highly Efficient Star Formation in the Dust-obscured Starburst Galaxy GN20". In: *ApJL* 798.1, L18, p. L18.

Hopkins, Philip F. et al. (Mar. 2006). "A Unified, Merger-driven Model of the Origin of Starbursts, Quasars, the Cosmic X-Ray Background, Supermassive Black Holes, and Galaxy Spheroids". In: *ApJS* 163.1, pp. 1–49.

Hopkins, Philip F. et al. (Aug. 2009). "The effects of gas on morphological transformation in mergers: implications for bulge and disc demographics". In: *MNRAS* 397.2, pp. 802–814.

Hovatta, Talvikki et al. (June 2014). "MOJAVE: Monitoring of Jets in Active Galactic Nuclei with VLBA Experiments. XI. Spectral Distributions". In: *AJ* 147.6, 143, p. 143.

Ivison, R. J. et al. (Aug. 2013). "Herschel-ATLAS: A Binary HyLIRG Pinpointing a Cluster of Starbursting Protoellipticals". In: *ApJ* 772.2, 137, p. 137.

Jáchym, Pavel et al. (Sept. 2014). "Abundant Molecular Gas and Inefficient Star Formation in Intracluster Regions: Ram Pressure Stripped Tail of the Norma Galaxy ESO137-001". In: *ApJ* 792.1, 11, p. 11.

Jaffé, Yara L. et al. (Apr. 2015). "BUDHIES II: a phase-space view of H I gas stripping and star formation quenching in cluster galaxies". In: *MNRAS* 448.2, pp. 1715–1728.

Jaffé, Yara L. et al. (Sept. 2016). "BUDHIES - III: the fate of H I and the quenching of galaxies in evolving environments". In: *MNRAS* 461.2, pp. 1202–1221.

Jaffé, Yara L. et al. (June 2018). "GASP. IX. Jellyfish galaxies in phase-space: an orbital study of intense ram-pressure stripping in clusters". In: *MNRAS* 476.4, pp. 4753–4764.

Jin, S. et al. (Dec. 2019). "Discovery of Four Apparently Cold Dusty Galaxies at z = 3.62-5.85 in the COSMOS Field: Direct Evidence of Cosmic Microwave Background Impact on High-redshift Galaxy Observables". In: *ApJ* 887.2, 144, p. 144.

Jog, Chanda J. and Francoise Combes (Feb. 2009). "Lopsided spiral galaxies". In: 471.2, pp. 75–111.

Jones, C. et al. (Mar. 2002). "Chandra Observations of NGC 4636-an Elliptical Galaxy in Turmoil". In: *ApJL* 567.2, pp. L115–L118.

Just, Dennis W. et al. (Nov. 2019). "Preprocessing among the Infalling Galaxy Population of EDisCS Clusters". In: *ApJ* 885.1, 6, p. 6.

Kalita, Boris S. and Harald Ebeling (Dec. 2019). "Jellyfish: Resolving the Kinematics of Extreme Ram-pressure Stripping at z $\sim$ 0.3". In: *ApJ* 887.2, 158, p. 158.

Kalita, Boris S. et al. (Aug. 2021a). "An Ancient Massive Quiescent Galaxy Found in a Gas-rich z 3 Group". In: *ApJL* 917.2, L17, p. L17.

Kalita, Boris S. et al. (May 2021b). "Feedback factory: multiple faint radio jets detected in a cluster at z = 2". In: *MNRAS* 503.1, pp. 1174–1186.

Kalita, Boris S. et al. (June 2022). "Bulge formation inside quiescent lopsided stellar disks: connecting accretion, star formation and morphological transformation in a z $\sim$3 galaxy group". In: *arXiv e-prints*, arXiv:2206.05217, arXiv:2206.05217.

Kapferer, W. et al. (May 2009). "The effect of ram pressure on the star formation, mass distribution and morphology of galaxies". In: *A&A* 499.1, pp. 87–102.

Kauffmann, G., S. D. M. White, and B. Guiderdoni (Sept. 1993). "The formation and evolution of galaxies within merging dark matter haloes." In: *MNRAS* 264, pp. 201–218.

Kauffmann, Guinevere and Timothy M. Heckman (July 2009). "Feast and Famine: regulation of black hole growth in low-redshift galaxies". In: *MNRAS* 397.1, pp. 135–147.

Kauffmann, Guinevere et al. (May 2003). "Stellar masses and star formation histories for 10^5 galaxies from the Sloan Digital Sky Survey". In: *MNRAS* 341.1, pp. 33–53.

Kazantzidis, Stelios, Andrew R. Zentner, and Andrey V. Kravtsov (Apr. 2006). "The Robustness of Dark Matter Density Profiles in Dissipationless Mergers". In: *ApJ* 641.2, pp. 647–664.

Kazantzidis, Stelios et al. (Nov. 2008). "Cold Dark Matter Substructure and Galactic Disks. I. Morphological Signatures of Hierarchical Satellite Accretion". In: *ApJ* 688.1, pp. 254–276.

Kazantzidis, Stelios et al. (Aug. 2009). "Cold Dark Matter Substructure and Galactic Disks. II. Dynamical Effects of Hierarchical Satellite Accretion". In: *ApJ* 700.2, pp. 1896–1920.

Kempner, Joshua C. and Craig L. Sarazin (Feb. 2001). "Radio Halo and Relic Candidates from the Westerbork Northern Sky Survey". In: *ApJ* 548.2, pp. 639–651.

Kenney, Jeffrey D. P., Anne Abramson, and Hector Bravo-Alfaro (Aug. 2015). "Hubble Space Telescope and HI Imaging of Strong Ram Pressure Stripping in the Coma Spiral NGC 4921: Dense Cloud Decoupling and Evidence for Magnetic Binding in the ISM". In: *AJ* 150.2, 59, p. 59.

Kenney, Jeffrey D. P., J. H. van Gorkom, and B. Vollmer (June 2004). "VLA H I Observations of Gas Stripping in the Virgo Cluster Spiral NGC 4522". In: *AJ* 127.6, pp. 3361–3374.

Kenney, Jeffrey D. P. et al. (Jan. 2014). "Transformation of a Virgo Cluster Dwarf Irregular Galaxy by Ram Pressure Stripping: IC3418 and Its Fireballs". In: *ApJ* 780.2, 119, p. 119.

Kennicutt Robert C., Jr. (May 1998). "The Global Schmidt Law in Star-forming Galaxies". In: *ApJ* 498.2, pp. 541–552.

Kereš, Dušan et al. (Oct. 2005). "How do galaxies get their gas?" In: *MNRAS* 363.1, pp. 2–28.

Kewley, L. J. et al. (July 2001). "Theoretical Modeling of Starburst Galaxies". In: *ApJ* 556.1, pp. 121–140.

Khoperskov, S. et al. (Jan. 2018). "Bar quenching in gas-rich galaxies". In: *A&A* 609, A60, A60.

Kim, Woong-Tae and Ramesh Narayan (Oct. 2003a). "Thermal Instability in Clusters of Galaxies with Conduction". In: *ApJ* 596.2, pp. 889–902.

— (Oct. 2003b). "Turbulent Mixing in Clusters of Galaxies". In: *ApJL* 596.2, pp. L139–L142.

Kimble, Randy A. et al. (July 2008). "Wide Field Camera 3: a powerful new imager for the Hubble Space Telescope". In: *Space Telescopes and Instrumentation 2008: Optical, Infrared, and Millimeter*. Ed. by Jr. Oschmann Jacobus M., Mattheus W. M. de Graauw, and Howard A. MacEwen. Vol. 7010. Society of Photo-Optical Instrumentation Engineers (SPIE) Conference Series, 70101E.

Komatsu, E. and U. Seljak (Nov. 2001). "Universal gas density and temperature profile". In: *MNRAS* 327.4, pp. 1353–1366.

Kravtsov, Andrey V. and Gustavo Yepes (Oct. 2000). "On the supernova heating of the intergalactic medium". In: *MNRAS* 318.1, pp. 227–238.

Kriek, Mariska et al. (Oct. 2006). "Spectroscopic Identification of Massive Galaxies at z $\sim$2.3 with Strongly Suppressed Star Formation". In: *ApJL* 649.2, pp. L71–L74.

Kronberger, T. et al. (Apr. 2008). "On the influence of ram-pressure stripping on the star formation of simulated spiral galaxies". In: *A&A* 481.2, pp. 337–343.

Kubo, Mariko et al. (Sept. 2021). "A Massive Quiescent Galaxy Confirmed in a Protocluster at z = 3.09". In: *ApJ* 919.1, 6, p. 6.

Laigle, C. et al. (June 2016). "The COSMOS2015 Catalog: Exploring the 1 < z < 6 Universe with Half a Million Galaxies". In: *ApJS* 224.2, 24, p. 24.

Lang, Philipp et al. (June 2014). "Bulge Growth and Quenching since z = 2.5 in CANDELS/3D-HST". In: *ApJ* 788.1, 11, p. 11.

Lang, Philipp et al. (July 2019). "Revealing the Stellar Mass and Dust Distributions of Submillimeter Galaxies at Redshift 2". In: *ApJ* 879.1, 54, p. 54.

Lara-López, M. A. et al. (Sept. 2010). "Study of star-forming galaxies in SDSS up to redshift 0.4. II. Evolution from the fundamental parameters: mass, metallicity and star formation rate". In: *A&A* 519, A31, A31.

Lee, Nicholas et al. (Mar. 2015). "A Turnover in the Galaxy Main Sequence of Star Formation at $M_* \sim 10^{10} M_\odot$ for Redshifts $z < 1.3$". In: *ApJ* 801.2, 80, p. 80.

Lehner, N. et al. (June 2013). "The Bimodal Metallicity Distribution of the Cool Circumgalactic Medium at $z <\sim 1$". In: *ApJ* 770.2, 138, p. 138.

Leja, Joel et al. (Mar. 2017). "Deriving Physical Properties from Broadband Photometry with Prospector: Description of the Model and a Demonstration of its Accuracy Using 129 Galaxies in the Local Universe". In: *ApJ* 837.2, 170, p. 170.

Lilly, Simon J. et al. (Aug. 2013). "Gas Regulation of Galaxies: The Evolution of the Cosmic Specific Star Formation Rate, the Metallicity-Mass-Star-formation Rate Relation, and the Stellar Content of Halos". In: *ApJ* 772.2, 119, p. 119.

Lin, Yen-Ting et al. (Nov. 2010). "On the Populations of Radio Galaxies with Extended Morphology at $z < 0.3$". In: *ApJ* 723.2, pp. 1119–1138.

Loni, A. et al. (Apr. 2021). "A blind ATCA HI survey of the Fornax galaxy cluster. Properties of the HI detections". In: *A&A* 648, A31, A31.

Lotz, Jennifer M. et al. (Jan. 2006). "The Rest-Frame Far-Ultraviolet Morphologies of Star-forming Galaxies at $z \sim 1.5$ and 4". In: *ApJ* 636.2, pp. 592–609.

Lustig, Peter et al. (Feb. 2021). "Compact, bulge-dominated structures of spectroscopically confirmed quiescent galaxies at z 3". In: *MNRAS* 501.2, pp. 2659–2676.

Machado, R. E. G. et al. (Aug. 2015). "Simulating the shocks in the dissociative galaxy cluster Abell 1758N". In: *MNRAS* 451.3, pp. 3309–3320.

Magdis, Georgios E. et al. (Nov. 2012). "The Evolving Interstellar Medium of Star-forming Galaxies since $z = 2$ as Probed by Their Infrared Spectral Energy Distributions". In: *ApJ* 760.1, 6, p. 6.

Magnelli, B. et al. (Jan. 2015). "The far-infrared/radio correlation and radio spectral index of galaxies in the SFR-M_* plane up to $z\sim 2$". In: *A&A* 573, A45, A45.

Man, Allison and Sirio Belli (Sept. 2018). "Star formation quenching in massive galaxies". In: *Nature Astronomy* 2, pp. 695–697.

Mancini, Chiara et al. (Oct. 2019). "Rejuvenated galaxies with very old bulges at the origin of the bending of the main sequence and of the 'green valley'". In: *MNRAS* 489.1, pp. 1265–1290.

Mannucci, F. et al. (Nov. 2010). "A fundamental relation between mass, star formation rate and metallicity in local and high-redshift galaxies". In: *MNRAS* 408.4, pp. 2115–2127.

Markov, Vladan et al. (Sept. 2020). "Massive molecular gas reservoir around the central AGN in the CARLA J1103 + 3449 cluster at $z = 1.44$". In: *A&A* 641, A22, A22.

Martig, M. and F. Bournaud (Mar. 2008). "Triggering of merger-induced starbursts by the tidal field of galaxy groups and clusters". In: *MNRAS* 385.1, pp. L38–L42.

Martig, Marie et al. (Dec. 2009). "Morphological Quenching of Star Formation: Making Early-Type Galaxies Red". In: *ApJ* 707.1, pp. 250–267.

Martin, D. Christopher et al. (Aug. 2015). "A giant protogalactic disk linked to the cosmic web". In: 524.7564, pp. 192–195.

Martin, D. Christopher et al. (July 2019). "Multi-filament gas inflows fuelling young star-forming galaxies". In: *Nature Astronomy* 3, pp. 822–831.

Masters, D. and P. Capak (May 2011). "SpecPro: An Interactive IDL Program for Viewing and Analyzing Astronomical Spectra". In: *PASP* 123.903, p. 638.

McCarthy, I. G. et al. (Jan. 2008). "Ram pressure stripping the hot gaseous haloes of galaxies in groups and clusters". In: *MNRAS* 383.2, pp. 593–605.

McCarthy, I. G. et al. (Apr. 2011). "Gas expulsion by quasar-driven winds as a solution to the overcooling problem in galaxy groups and clusters". In: *MNRAS* 412.3, pp. 1965–1984.

McConachie, Ian et al. (Feb. 2022). "Spectroscopic Confirmation of a Protocluster at z = 3.37 with a High Fraction of Quiescent Galaxies". In: *ApJ* 926.1, 37, p. 37.

McCracken, H. J. et al. (Aug. 2012). "UltraVISTA: a new ultra-deep near-infrared survey in COSMOS". In: *A&A* 544, A156, A156.

McGee, Sean L. et al. (Dec. 2009). "The accretion of galaxies into groups and clusters". In: *MNRAS* 400.2, pp. 937–950.

McMullin, J. P. et al. (Oct. 2007). "CASA Architecture and Applications". In: *Astronomical Data Analysis Software and Systems XVI*. Ed. by R. A. Shaw, F. Hill, and D. J. Bell. Vol. 376. Astronomical Society of the Pacific Conference Series, p. 127.

McNamara, B. R. and P. E. J. Nulsen (Sept. 2007). "Heating Hot Atmospheres with Active Galactic Nuclei". In: 45.1, pp. 117–175.

McNamara, B. R. et al. (May 2000). "Chandra X-Ray Observations of the Hydra A Cluster: An Interaction between the Radio Source and the X-Ray-emitting Gas". In: *ApJL* 534.2, pp. L135–L138.

McNamara, B. R. et al. (Dec. 2001). "Discovery of Ghost Cavities in the X-Ray Atmosphere of Abell 2597". In: *ApJL* 562.2, pp. L149–L152.

McNamara, B. R. et al. (Jan. 2005). "The heating of gas in a galaxy cluster by X-ray cavities and large-scale shock fronts". In: 433.7021, pp. 45–47.

McNamara, Brian R. and Robert W. O'Connell (Dec. 1989). "Star formation in cooling flows in clusters of galaxies." In: *AJ* 98, pp. 2018–2043.

McPartland, Conor et al. (Jan. 2016). "Jellyfish: the origin and distribution of extreme ram-pressure stripping events in massive galaxy clusters". In: *MNRAS* 455.3, pp. 2994–3008.

Merluzzi, P. et al. (Feb. 2013). "ACCESS - V. Dissecting ram-pressure stripping through integral-field spectroscopy and multiband imaging". In: *MNRAS* 429.2, pp. 1747–1773.

Miley, George K. et al. (Oct. 2006). "The Spiderweb Galaxy: A Forming Massive Cluster Galaxy at z ∼2". In: *ApJL* 650.1, pp. L29–L32.
Mittal, R. et al. (July 2009). "AGN heating and ICM cooling in the HIFLUGCS sample of galaxy clusters". In: *A&A* 501.3, pp. 835–850.
Mo, H. J., Shude Mao, and Simon D. M. White (Apr. 1998). "The formation of galactic discs". In: *MNRAS* 295.2, pp. 319–336.
Moore, B. et al. (May 1998). "Resolving the Structure of Cold Dark Matter Halos". In: *ApJL* 499.1, pp. L5–L8.
Moore, Ben et al. (Feb. 1996). "Galaxy harassment and the evolution of clusters of galaxies". In: 379.6566, pp. 613–616.
Moretti, A. et al. (Oct. 2018). "GASP - X. APEX observations of molecular gas in the discs and in the tails of ram-pressure stripped galaxies". In: *MNRAS* 480.2, pp. 2508–2520.
Morishita, T. et al. (June 2019). "Massive Dead Galaxies at z $\sim$ 2 with HST Grism Spectroscopy. I. Star Formation Histories and Metallicity Enrichment". In: *ApJ* 877.2, 141, p. 141.
Morrissey, Patrick et al. (Sept. 2018). "The Keck Cosmic Web Imager Integral Field Spectrograph". In: *ApJ* 864.1, 93, p. 93.
Mowla, Lamiya A. et al. (July 2019). "COSMOS-DASH: The Evolution of the Galaxy Size-Mass Relation since z $\sim$ 3 from New Wide-field WFC3 Imaging Combined with CANDELS/3D-HST". In: *ApJ* 880.1, 57, p. 57.
Nesvadba, N. P. H. et al. (Nov. 2008). "Evidence for powerful AGN winds at high redshift: dynamics of galactic outflows in radio galaxies during the "Quasar Era"". In: *A&A* 491.2, pp. 407–424.
Nesvadba, N. P. H. et al. (Apr. 2017). "Gas kinematics in powerful radio galaxies at z 2: Energy supply from star formation, AGN, and radio jets". In: *A&A* 600, A121, A121.
Nevin, R. et al. (Feb. 2019). "Accurate Identification of Galaxy Mergers with Imaging". In: *ApJ* 872.1, 76, p. 76.
Newman, Jeffrey A. et al. (Sept. 2013). "The DEEP2 Galaxy Redshift Survey: Design, Observations, Data Reduction, and Redshifts". In: *ApJS* 208.1, 5, p. 5.
Niemi, Sami-Matias (Sept. 2011). "Properties of Galaxies and Groups: Nature versus Nurture". PhD thesis. University of Turku, Finland.
Noeske, K. G. et al. (May 2007a). "Star Formation in AEGIS Field Galaxies since z=1.1: Staged Galaxy Formation and a Model of Mass-dependent Gas Exhaustion". In: *ApJL* 660.1, pp. L47–L50.
Noeske, K. G. et al. (May 2007b). "Star Formation in AEGIS Field Galaxies since z=1.1: The Dominance of Gradually Declining Star Formation, and the Main Sequence of Star-forming Galaxies". In: *ApJL* 660.1, pp. L43–L46.
Noguchi, Masafumi (Mar. 1999). "Early Evolution of Disk Galaxies: Formation of Bulges in Clumpy Young Galactic Disks". In: *ApJ* 514.1, pp. 77–95.

— (Dec. 2021). "Formation of galactic bulges from the cold gas filaments in high-redshift dark matter halos". In: *arXiv e-prints*, arXiv:2112.01803, arXiv:2112.01803.

Noirot, Gaël et al. (May 2018). "HST Grism Confirmation of 16 Structures at 1.4 < z < 2.8 from the Clusters Around Radio-Loud AGN (CARLA) Survey". In: *ApJ* 859.1, 38, p. 38.

Oemler Augustus, Jr. (Nov. 1974). "The Systematic Properties of Clusters of Galaxies. Photometry of 15 Clusters". In: *ApJ* 194, pp. 1–20.

Oemler Augustus, Jr. et al. (June 2013). "The IMACS Cluster Building Survey. III. The Star Formation Histories of Field Galaxies". In: *ApJ* 770.1, 63, p. 63.

Olivares, V. et al. (Nov. 2019). "Ubiquitous cold and massive filaments in cool core clusters". In: *A&A* 631, A22, A22.

Olsen, Karen P. et al. (Feb. 2013). "Evidence for Widespread Active Galactic Nucleus Activity among Massive Quiescent Galaxies at z ∼2". In: *ApJ* 764.1, 4, p. 4.

Onodera, M. et al. (May 2016). "ISM Excitation and Metallicity of Star-forming Galaxies at z 3.3 from Near-IR Spectroscopy". In: *ApJ* 822.1, 42, p. 42.

O'Sullivan, E. et al. (July 2011). "Heating the Hot Atmospheres of Galaxy Groups and Clusters with Cavities: The Relationship between Jet Power and Low-frequency Radio Emission". In: *ApJ* 735.1, 11, p. 11.

Overzier, Roderik A. (Nov. 2016). "The realm of the galaxy protoclusters. A review". In: 24.1, 14, p. 14.

Owers, Matt S. et al. (May 2012). "Shocking Tails in the Major Merger Abell 2744". In: *ApJL* 750.1, L23, p. L23.

Padovani, Paolo (Sept. 2016). "The faint radio sky: radio astronomy becomes mainstream". In: 24.1, 13, p. 13.

Pallero, Diego et al. (Sept. 2019). "Tracing the quenching history of cluster galaxies in the EAGLE simulation". In: *MNRAS* 488.1, pp. 847–858.

Peng, Chien Y. et al. (July 2002). "Detailed Structural Decomposition of Galaxy Images". In: *AJ* 124.1, pp. 266–293.

— (June 2010a). "Detailed Decomposition of Galaxy Images. II. Beyond Axisymmetric Models". In: *AJ* 139.6, pp. 2097–2129.

Peng, Y., R. Maiolino, and R. Cochrane (May 2015). "Strangulation as the primary mechanism for shutting down star formation in galaxies". In: 521.7551, pp. 192–195.

Peng, Ying-jie et al. (Sept. 2010b). "Mass and Environment as Drivers of Galaxy Evolution in SDSS and zCOSMOS and the Origin of the Schechter Function". In: *ApJ* 721.1, pp. 193–221.

Peterson, J. R. et al. (Jan. 2001). "X-ray imaging-spectroscopy of Abell 1835". In: *A&A* 365, pp. L104–L109.

Peterson, J. R. et al. (June 2003). "High-Resolution X-Ray Spectroscopic Constraints on Cooling-Flow Models for Clusters of Galaxies". In: *ApJ* 590.1, pp. 207–224.

Pfeffer, Joel et al. (Mar. 2022). "The age gradients of galaxies in EAGLE: outside-in quenching as the origin of young bulges in cluster galaxies". In: *MNRAS* 511.1, pp. 1072–1084.

Poggianti, B. M. et al. (Mar. 2016). "Jellyfish Galaxy Candidates at Low Redshift". In: *AJ* 151.3, 78, p. 78.

Poggianti, Bianca M. et al. (Aug. 2017). "Ram-pressure feeding of supermassive black holes". In: 548.7667, pp. 304–309.

Poggianti, Bianca M. et al. (Feb. 2019). "GASP XIII. Star formation in gas outside galaxies". In: *MNRAS* 482.4, pp. 4466–4502.

Pope, Edward C. D. et al. (Apr. 2006). "Heating rate profiles in galaxy clusters". In: *MNRAS* 367.3, pp. 1121–1131.

Popesso, P. et al. (Mar. 2019). "The main sequence of star-forming galaxies - I. The local relation and its bending". In: *MNRAS* 483.3, pp. 3213–3226.

Popesso, P. et al. (Mar. 2022). "The Main Sequence of star-forming galaxies across cosmic times". In: *arXiv e-prints*, arXiv:2203.10487, arXiv:2203.10487.

Pranger, Florian et al. (Oct. 2014). "Abell 2384: the galaxy population of a cluster post-merger". In: *A&A* 570, A40, A40.

Pratt, G. W. et al. (Feb. 2010). "Gas entropy in a representative sample of nearby X-ray galaxy clusters (REXCESS): relationship to gas mass fraction". In: *A&A* 511, A85, A85.

Puglisi, A. et al. (June 2019). "The Main Sequence at z $\sim$ 1.3 Contains a Sizable Fraction of Galaxies with Compact Star Formation Sizes: A New Population of Early Post-starbursts?" In: *ApJL* 877.2, L23, p. L23.

Puglisi, Annagrazia et al. (Dec. 2021). "Submillimetre compactness as a critical dimension to understand the main sequence of star-forming galaxies". In: *MNRAS* 508.4, pp. 5217–5238.

Purcell, Chris W., Stelios Kazantzidis, and James S. Bullock (Apr. 2009). "The Destruction of Thin Stellar Disks Via Cosmologically Common Satellite Accretion Events". In: *ApJL* 694.2, pp. L98–L102.

Quilis, Vicent, Ben Moore, and Richard Bower (June 2000). "Gone with the Wind: The Origin of S0 Galaxies in Clusters". In: *Science* 288.5471, pp. 1617–1620.

Rafferty, D. A. et al. (Nov. 2006). "The Feedback-regulated Growth of Black Holes and Bulges through Gas Accretion and Starbursts in Cluster Central Dominant Galaxies". In: *ApJ* 652.1, pp. 216–231.

Ragozzine, B. et al. (Jan. 2012). "Weak-lensing Results for the Merging Cluster A1758". In: *ApJ* 744.2, 94, p. 94.

Rau, U. and T. J. Cornwell (Aug. 2011). "A multi-scale multi-frequency deconvolution algorithm for synthesis imaging in radio interferometry". In: *A&A* 532, A71, A71.

Rees, M. J. and J. P. Ostriker (June 1977). "Cooling, dynamics and fragmentation of massive gas clouds: clues to the masses and radii of galaxies and clusters." In: *MNRAS* 179, pp. 541–559.

Reichard, Timothy A. et al. (Apr. 2008). "The Lopsidedness of Present-Day Galaxies: Results from the Sloan Digital Sky Survey". In: *ApJ* 677.1, pp. 186–200.

Reines, Amy E. and Marta Volonteri (Nov. 2015). "Relations between Central Black Hole Mass and Total Galaxy Stellar Mass in the Local Universe". In: *ApJ* 813.2, 82, p. 82.

Reiprich, Thomas H. and Hans Böhringer (Mar. 2002). "The Mass Function of an X-Ray Flux-limited Sample of Galaxy Clusters". In: *ApJ* 567.2, pp. 716–740.

Ricciardelli, E. et al. (July 2010). "The evolutionary sequence of submillimetre galaxies: from diffuse discs to massive compact ellipticals?" In: *MNRAS* 406.1, pp. 230–236.

Rix, Hans-Walter and Dennis Zaritsky (July 1995). "Nonaxisymmetric Structures in the Stellar Disks of Galaxies". In: *ApJ* 447, p. 82.

Roediger, E. and G. Hensler (Apr. 2005). "Ram pressure stripping of disk galaxies. From high to low density environments". In: *A&A* 433.3, pp. 875–895.

Roediger, E. et al. (Sept. 2014). "Star formation in shocked cluster spirals and their tails." In: *MNRAS* 443, pp. L114–L118.

Roediger, Elke and Marcus Brüggen (July 2008). "Ram pressure stripping in a viscous intracluster medium". In: *MNRAS* 388.1, pp. L89–L93.

Ruggiero, Rafael et al. (Mar. 2019). "Galaxy cluster mergers as triggers for the formation of jellyfish galaxies: case study of the A901/2 system". In: *MNRAS* 484.1, pp. 906–914.

Rujopakarn, W. et al. (Sept. 2019). "ALMA 200 pc Resolution Imaging of Smooth Cold Dusty Disks in Typical z $\sim$ 3 Star-forming Galaxies". In: *ApJ* 882.2, 107, p. 107.

Salim, Samir et al. (Dec. 2007). "UV Star Formation Rates in the Local Universe". In: *ApJS* 173.2, pp. 267–292.

Sánchez Almeida, J. et al. (Apr. 2013). "Local Tadpole Galaxies: Dynamics and Metallicity". In: *ApJ* 767.1, 74, p. 74.

Sánchez Almeida, J. et al. (Mar. 2014). "Metallicity Inhomogeneities in Local Star-forming Galaxies as a Sign of Recent Metal-poor Gas Accretion". In: *ApJ* 783.1, 45, p. 45.

Sancisi, Renzo et al. (June 2008). "Cold gas accretion in galaxies". In: 15.3, pp. 189–223.

Sanders, D. B. et al. (May 1988). "Warm Ultraluminous Galaxies in the IRAS Survey: The Transition from Galaxy to Quasar?" In: *ApJL* 328, p. L35.

Sanders, J. S. et al. (Apr. 2008). "Cool X-ray emitting gas in the core of the Centaurus cluster of galaxies". In: *MNRAS* 385.3, pp. 1186–1200.

Santini, Paola et al. (Sept. 2017). "The Star Formation Main Sequence in the Hubble Space Telescope Frontier Fields". In: *ApJ* 847.1, 76, p. 76.

Saracco, Paolo et al. (Dec. 2020). "The Rapid Buildup of Massive Early-type Galaxies: Supersolar Metallicity, High Velocity Dispersion, and Young Age for an Early-type Galaxy at z = 3.35". In: *ApJ* 905.1, 40, p. 40.

Sargent, M. T. et al. (Sept. 2014). "Regularity Underlying Complexity: A Redshift-independent Description of the Continuous Variation of Galaxy-scale Molecular Gas Properties in the Mass-star Formation Rate Plane". In: *ApJ* 793.1, 19, p. 19.

Schlafly, Edward F. and Douglas P. Finkbeiner (Aug. 2011). "Measuring Reddening with Sloan Digital Sky Survey Stellar Spectra and Recalibrating SFD". In: *ApJ* 737.2, 103, p. 103.

Schreiber, C. et al. (Mar. 2015). "The Herschel view of the dominant mode of galaxy growth from z = 4 to the present day". In: *A&A* 575, A74, A74.

Schreiber, C. et al. (Mar. 2017). "The ALMA Redshift 4 Survey (AR4S). I. The massive end of the z = 4 main sequence of galaxies". In: *A&A* 599, A134, A134.

Schreiber, C. et al. (Jan. 2018a). "Dust temperature and mid-to-total infrared color distributions for star-forming galaxies at $0 < z < 4$". In: *A&A* 609, A30, A30.

Schreiber, C. et al. (Mar. 2018b). "Jekyll & Hyde: quiescence and extreme obscuration in a pair of massive galaxies 1.5 Gyr after the Big Bang". In: *A&A* 611, A22, A22.

Schreiber, C. et al. (Oct. 2018c). "Near infrared spectroscopy and star-formation histories of $3 \leq z \leq 4$ quiescent galaxies". In: *A&A* 618, A85, A85.

Scoville, N. et al. (Sept. 2007). "The Cosmic Evolution Survey (COSMOS): Overview". In: *ApJS* 172.1, pp. 1–8.

Scoville, N. et al. (Apr. 2016). "ISM Masses and the Star formation Law at Z = 1 to 6: ALMA Observations of Dust Continuum in 145 Galaxies in the COSMOS Survey Field". In: *ApJ* 820.2, 83, p. 83.

Seaton, M. J. (Jan. 1979). "Interstellar extinction in the UV." In: *MNRAS* 187, p. 73.

Sheth, Kartik et al. (Mar. 2008). "Evolution of the Bar Fraction in COSMOS: Quantifying the Assembly of the Hubble Sequence". In: *ApJ* 675.2, pp. 1141–1155.

Shi, Yong et al. (May 2010). "Unobscured Type 2 Active Galactic Nuclei". In: *ApJ* 714.1, pp. 115–129.

Silk, J. (Feb. 1977). "On the fragmentation of cosmic gas clouds. I. The formation of galaxies and the first generation of stars." In: *ApJ* 211, pp. 638–648.

Silverman, J. D. et al. (Nov. 2018). "The Molecular Gas Content and Fuel Efficiency of Starbursts at $z \sim 1.6$ with ALMA". In: *ApJ* 867.2, 92, p. 92.

Simpson, J. M. et al. (July 2017). "An Imperfectly Passive Nature: Bright Submillimeter Emission from Dust-obscured Star Formation in the z = 3.717 "Passive" System, ZF 20115". In: *ApJL* 844.1, L10, p. L10.

Smercina, A. et al. (Mar. 2018). "After the Fall: The Dust and Gas in E+A Post-starburst Galaxies". In: *ApJ* 855.1, 51, p. 51.

Smith, Russell J. et al. (Nov. 2010). "Ultraviolet tails and trails in cluster galaxies: a sample of candidate gaseous stripping events in Coma". In: *MNRAS* 408.3, pp. 1417–1432.

Smolčić, V. et al. (June 2017). "The VLA-COSMOS 3 GHz Large Project: Continuum data and source catalog release". In: *A&A* 602, A1, A1.

Somerville, Rachel S. and Romeel Davé (Aug. 2015). "Physical Models of Galaxy Formation in a Cosmological Framework". In: 53, pp. 51–113.

Somerville, Rachel S. and Joel R. Primack (Dec. 1999). "Semi-analytic modelling of galaxy formation: the local Universe". In: *MNRAS* 310.4, pp. 1087–1110.

Speagle, J. S. et al. (Oct. 2014). "A Highly Consistent Framework for the Evolution of the Star-Forming "Main Sequence" from z ∼0-6". In: *ApJS* 214.2, 15, p. 15.

Spergel, David N. (Nov. 2010). "Analytical Galaxy Profiles for Photometric and Lensing Analysis". In: *ApJS* 191.1, pp. 58–65.

Springel, Volker and Lars Hernquist (Feb. 2003). "The history of star formation in a Λ cold dark matter universe". In: *MNRAS* 339.2, pp. 312–334.

Steinhardt, Charles. L. et al. (June 2016). "The Impossibly Early Galaxy Problem". In: *ApJ* 824.1, 21, p. 21.

Steinhauser, Dominik, Sabine Schindler, and Volker Springel (June 2016). "Simulations of ram-pressure stripping in galaxy-cluster interactions". In: *A&A* 591, A51, A51.

Straatman, Caroline M. S. et al. (Mar. 2014). "A Substantial Population of Massive Quiescent Galaxies at z ∼4 from ZFOURGE". In: *ApJL* 783.1, L14, p. L14.

Strazzullo, V. et al. (Dec. 2016). "The Red Sequence at Birth in the Galaxy Cluster Cl J1449+0856 at z = 2". In: *ApJL* 833.2, L20, p. L20.

Strazzullo, V. et al. (July 2018). "Deciphering the Activity and Quiescence of High-redshift Cluster Environments: ALMA Observations of Cl J1449+0856 at z = 2". In: *ApJ* 862.1, 64, p. 64.

Stroe, Andra et al. (June 2015). "The rise and fall of star formation in z ∼ 0.2 merging galaxy clusters". In: *MNRAS* 450.1, pp. 646–665.

Stroe, Andra et al. (Mar. 2017). "A large Hα survey of star formation in relaxed and merging galaxy cluster environments at z ∼ 0.15-0.3". In: *MNRAS* 465.3, pp. 2916–2935.

Sun, M., M. Donahue, and G. M. Voit (Dec. 2007). "Hα Tail, Intracluster H II Regions, and Star Formation: ESO 137-001 in Abell 3627". In: *ApJ* 671.1, pp. 190–202.

Sun, M. et al. (Mar. 2009). "Chandra Studies of the X-Ray Gas Properties of Galaxy Groups". In: *ApJ* 693.2, pp. 1142–1172.

Tacchella, S. et al. (Apr. 2015). "Evidence for mature bulges and an inside-out quenching phase 3 billion years after the Big Bang". In: *Science* 348.6232, pp. 314–317.

Tacchella, S. et al. (May 2018). "Dust Attenuation, Bulge Formation, and Inside-out Quenching of Star Formation in Star-forming Main Sequence Galaxies at z ∼ 2". In: *ApJ* 859.1, 56, p. 56.

Tacchella, Sandro et al. (May 2016). "Evolution of density profiles in high-z galaxies: compaction and quenching inside-out". In: *MNRAS* 458.1, pp. 242–263.

Tacchella, Sandro et al. (Apr. 2021). "Fast, Slow, Early, Late: Quenching Massive Galaxies at z $\sim$ 0.8". In: *Extragalactic Spectroscopic Surveys: Past, Present and Future of Galaxy Evolution (GALSPEC2021)*, p. 59.

Tacconi, L. J. et al. (Feb. 2010). "High molecular gas fractions in normal massive star-forming galaxies in the young Universe". In: 463.7282, pp. 781–784.

Tacconi, L. J. et al. (Feb. 2018). "PHIBSS: Unified Scaling Relations of Gas Depletion Time and Molecular Gas Fractions". In: *ApJ* 853.2, 179, p. 179.

Thomas, Daniel et al. (June 2010). "Environment and self-regulation in galaxy formation". In: *MNRAS* 404.4, pp. 1775–1789.

Toft, S. et al. (Feb. 2014). "Submillimeter Galaxies as Progenitors of Compact Quiescent Galaxies". In: *ApJ* 782.2, 68, p. 68.

Toft, Sune et al. (June 2017). "A massive, dead disk galaxy in the early Universe". In: 546.7659, pp. 510–513.

Tonnesen, Stephanie and Greg L. Bryan (May 2012). "Star formation in ram pressure stripped galactic tails". In: *MNRAS* 422.2, pp. 1609–1624.

Torrey, Paul et al. (Dec. 2015). "An analysis of the evolving comoving number density of galaxies in hydrodynamical simulations". In: *MNRAS* 454.3, pp. 2770–2786.

Toth, G. and J. P. Ostriker (Apr. 1992). "Galactic Disks, Infall, and the Global Value of Omega". In: *ApJ* 389, p. 5.

Tremblay, G. R. et al. (Sept. 2018). "A Galaxy-scale Fountain of Cold Molecular Gas Pumped by a Black Hole". In: *ApJ* 865.1, 13, p. 13.

Tucker, Wallace (1975). *Radiation processes in astrophysics*.

Tully, R. B. and J. R. Fisher (Feb. 1977). "A new method of determining distances to galaxies." In: *A&A* 54, pp. 661–673.

Tumlinson, Jason, Molly S. Peeples, and Jessica K. Werk (Aug. 2017). "The Circumgalactic Medium". In: 55.1, pp. 389–432.

Umehata, H. et al. (Oct. 2019). "Gas filaments of the cosmic web located around active galaxies in a protocluster". In: *Science* 366.6461, pp. 97–100.

Valentino, F. et al. (Mar. 2015). "Metal Deficiency in Cluster Star-Forming Galaxies At Z = 2". In: *ApJ* 801.2, 132, p. 132.

Valentino, F. et al. (Sept. 2020a). "CO emission in distant galaxies on and above the main sequence". In: *A&A* 641, A155, A155.

Valentino, Francesco et al. (Sept. 2016). "A Giant Lyα Nebula in the Core of an X-Ray Cluster at Z = 1.99: Implications for Early Energy Injection". In: *ApJ* 829.1, 53, p. 53.

Valentino, Francesco et al. (Feb. 2020b). "Quiescent Galaxies 1.5 Billion Years after the Big Bang and Their Progenitors". In: *ApJ* 889.2, 93, p. 93.

van der Wel, A. et al. (June 2014). "3D-HST+CANDELS: The Evolution of the Galaxy Size-Mass Distribution since z = 3". In: *ApJ* 788.1, 28, p. 28.

van der Wel, Arjen et al. (Mar. 2011). "The Majority of Compact Massive Galaxies at z ∼2 are Disk Dominated". In: *ApJ* 730.1, 38, p. 38.

van Dokkum, Pieter G. et al. (Nov. 2015). "Forming Compact Massive Galaxies". In: *ApJ* 813.1, 23, p. 23.

Venemans, B. P. et al. (Jan. 2007). "Protoclusters associated with z > 2 radio galaxies . I. Characteristics of high redshift protoclusters". In: *A&A* 461.3, pp. 823–845.

Venturi, T. et al. (Mar. 2013). "Low frequency follow up of radio haloes and relics in the GMRT Radio Halo Cluster Survey". In: *A&A* 551, A24, A24.

Verheijen, Marc A. W. (Dec. 2001). "The Ursa Major Cluster of Galaxies. V. H I Rotation Curve Shapes and the Tully-Fisher Relations". In: *ApJ* 563.2, pp. 694–715.

Vikhlinin, A. et al. (Feb. 2009). "Chandra Cluster Cosmology Project. II. Samples and X-Ray Data Reduction". In: *ApJ* 692.2, pp. 1033–1059.

Vogelsberger, Mark et al. (Jan. 2020). "Cosmological simulations of galaxy formation". In: *Nature Reviews Physics* 2.1, pp. 42–66.

Voigt, L. M. and A. C. Fabian (Feb. 2004). "Thermal conduction and reduced cooling flows in galaxy clusters". In: *MNRAS* 347.4, pp. 1130–1149.

Voit, G. Mark et al. (July 2015). "Precipitation-regulated Star Formation in Galaxies". In: *ApJL* 808.1, L30, p. L30.

Voit, G. Mark et al. (Aug. 2017). "A Global Model for Circumgalactic and Cluster-core Precipitation". In: *ApJ* 845.1, 80, p. 80.

Vollmer, B. et al. (Nov. 2001). "Ram Pressure Stripping and Galaxy Orbits: The Case of the Virgo Cluster". In: *ApJ* 561.2, pp. 708–726.

Vollmer, B. et al. (Nov. 2008). "Ram-pressure stripped molecular gas in the Virgo spiral galaxy NGC 4522". In: *A&A* 491.2, pp. 455–464.

Vulcani, Benedetta et al. (Oct. 2018). "Enhanced Star Formation in Both Disks and Ram-pressure-stripped Tails of GASP Jellyfish Galaxies". In: *ApJL* 866.2, L25, p. L25.

Wang, Tao et al. (Sept. 2016). "Discovery of a Galaxy Cluster with a Violently Starbursting Core at z = 2.506". In: *ApJ* 828.1, 56, p. 56.

Wen, Zhang Zheng and Xian Zhong Zheng (Nov. 2016). "Merging Galaxies with Tidal Tails in COSMOS to z = 1". In: *ApJ* 832.1, 90, p. 90.

Wetzel, Andrew R. et al. (June 2013). "Galaxy evolution in groups and clusters: satellite star formation histories and quenching time-scales in a hierarchical Universe". In: *MNRAS* 432.1, pp. 336–358.

Whitaker, Katherine E. et al. (Aug. 2012). "The Star Formation Mass Sequence Out to z = 2.5". In: *ApJL* 754.2, L29, p. L29.

White, S. D. M. and M. J. Rees (May 1978). "Core condensation in heavy halos: a two-stage theory for galaxy formation and clustering." In: *MNRAS* 183, pp. 341–358.

White, Simon D. M. and Carlos S. Frenk (Sept. 1991). "Galaxy Formation through Hierarchical Clustering". In: *ApJ* 379, p. 52.

Whitmore, Bradley C., Diane M. Gilmore, and Christine Jones (Apr. 1993). "What Determines the Morphological Fractions in Clusters of Galaxies?" In: *ApJ* 407, p. 489.

Worrall, D. M. (Jan. 2009). "The X-ray jets of active galaxies". In: 17, pp. 1–46.

Wotta, Christopher B. et al. (Feb. 2019). "The COS CGM Compendium. II. Metallicities of the Partial and Lyman Limit Systems at z $\lesssim$ 1". In: *ApJ* 872.1, 81, p. 81.

Wuyts, Stijn et al. (Dec. 2011). "Galaxy Structure and Mode of Star Formation in the SFR-Mass Plane from z $\sim$2.5 to z $\sim$0.1". In: *ApJ* 742.2, 96, p. 96.

Wylezalek, Dominika et al. (May 2013). "Galaxy Clusters around Radio-loud Active Galactic Nuclei at 1.3 < z < 3.2 as Seen by Spitzer". In: *ApJ* 769.1, 79, p. 79.

Yoshida, Michitoshi et al. (Dec. 2008). "Strange Filamentary Structures ("Fireballs") around a Merger Galaxy in the Coma Cluster of Galaxies". In: *ApJ* 688.2, pp. 918–930.

Zabludoff, Ann I. and John S. Mulchaey (Mar. 1998). "The Properties of Poor Groups of Galaxies. I. Spectroscopic Survey and Results". In: *ApJ* 496.1, pp. 39–72.

Zaritsky, Dennis and Hans-Walter Rix (Mar. 1997). "Lopsided Spiral Galaxies and a Limit on the Galaxy Accretion Rate". In: *ApJ* 477.1, pp. 118–127.

Zolotov, Adi et al. (July 2015). "Compaction and quenching of high-z galaxies in cosmological simulations: blue and red nuggets". In: *MNRAS* 450.3, pp. 2327–2353.